



HAL
open science

Direct Synthesis of Light Olefins Using CO and CO₂ Hydrogenation Reactions

Alan Josue Barrios Medina

► **To cite this version:**

Alan Josue Barrios Medina. Direct Synthesis of Light Olefins Using CO and CO₂ Hydrogenation Reactions. Other. Centrale Lille Institut; Universiteit Gent, 2021. English. NNT : 2021CLIL0030 . tel-03987841

HAL Id: tel-03987841

<https://theses.hal.science/tel-03987841>

Submitted on 14 Feb 2023

HAL is a multi-disciplinary open access archive for the deposit and dissemination of scientific research documents, whether they are published or not. The documents may come from teaching and research institutions in France or abroad, or from public or private research centers.

L'archive ouverte pluridisciplinaire **HAL**, est destinée au dépôt et à la diffusion de documents scientifiques de niveau recherche, publiés ou non, émanant des établissements d'enseignement et de recherche français ou étrangers, des laboratoires publics ou privés.

THESE

Présentée en vue
d'obtenir le grade de

DOCTEUR

en

Spécialité : Molécules et Matière Condensée et Doctor of Chemical Engineering

Par

Alan Josue Barrios Medina

**DOCTORAT délivré conjointement par CENTRALE LILLE et
l'UNIVERSITE de GAND**

Titre de la thèse :

**Synthèse Directe d'Oléfines Légères par des Réactions
d'Hydrogénation du CO et du CO₂**

**Direct Synthesis of Light Olefins Using CO and CO₂
Hydrogenation Reactions**

Soutenue le 10 décembre 2021 devant le jury d'examen :

Président : SCHUURMAN Yves, Directeur de Recherche, CNRS

Co-présidente : DE SCHEPPER Hennie, Prof., Université de Gand

Rapporteure : ROGER Anne-Cécile, Prof., Université de Strasbourg

Rapporteure: VENVIK Hilde, Prof., Université Norvégienne des Sciences et Technologie

Membre : MAMEDE Anne-Sophie, Maître de conférence, Centrale Lille

Membre : STEFANIDIS Georgios, Prof., Université de Gand

Co-encadrante : VIRGINIE Mirella, Maître de conférence, Centrale Lille

Co-directeur de thèse : THYBAUT Joris, Prof., Université de Gand

Directeur de thèse : KHODAKOV Andrei, Directeur de Recherche, CNRS

Thèse préparée au laboratoire UCCS, UMR CNRS 8181, École doctorale SMRE 104 et au
Laboratoire de Technologie Chimique, Technologiemark 125.



Contents

Chapter 1 Literature review	22
1.1. General Introduction.....	22
1.1.1. Plastic waste and its recycling.....	24
1.1.2. Gasification	27
1.1.3. Main components and impurities in syngas produced by gasification.....	30
1.1.4. Syngas purification.....	31
1.2. CO hydrogenation and CO ₂ hydrogenation	33
1.2.1. Thermodynamics.....	33
1.2.2. Kinetics.....	35
1.2.3. Mechanism.....	37
1.2.3.1 Mechanism for CO hydrogenation.....	37
1.2.3.2 Mechanism for CO ₂ hydrogenation	42
1.2.4. Reaction conditions	44
1.2.5. Reactors	45
1.2.6. Catalysts for CO and CO ₂ hydrogenation	50
1.2.7 Light olefins synthesis	52
1.3. Iron catalysts for CO and CO ₂ hydrogenation	54
1.3.1 Iron catalysts for CO hydrogenation	54
1.3.1.1 Active phases and promoters	55
1.3.1.2 Bulk and Supported catalysts.....	59
1.3.1.3 Role of catalyst activation.....	62
1.3.1.4. Light olefin selectivity	63
1.3.2 Iron catalysts for CO ₂ hydrogenation	64
1.3.2.1 Active phases, promoters, selectivity, and supports	65
1.3.2.2 Catalysts activation for CO ₂ Hydrogenation	69
1.4. Catalyst deactivation.....	70
1.4.1 Catalyst deactivation during CO hydrogenation.....	70
1.4.2. Catalyst deactivation during CO ₂ hydrogenation.....	72
1.4.3. Catalyst regeneration.....	73
1.5. High throughput experimentation for catalysts screening.....	74
1.6. Challenges and objectives of the thesis.....	76
1.7. Outline of the thesis.....	77
1.8. References	79

Chapter 2 Catalysts and experiments 86

2.1. Catalysts preparation	86
2.1.1. Silica supported catalysts.....	86
2.1.2. Silica supported catalysts prepared by mechanical mixing	87
2.1.3. Zirconia supported catalysts	87
2.2. Evaluation of catalytic performance	88
2.2.1. Evaluation of Fe-based catalysts in fixed-bed reactors	88
2.2.2. Avantium high throughput equipment for determination of suitable promoters	90
2.3. Analysis method.....	91
2.4. Catalysts characterization	93
2.4.1. X-Ray diffraction.....	93
2.4.2. X-Ray fluorescence.....	94
2.4.3. Surface area and porosity	95
2.4.4. Transmission electron microscopy	95
2.4.5. Temperature programmed reduction	97
2.4.6 Thermogravimetric analysis.....	97
2.4.7 Temperature programme desorption.....	98
2.4.8. X-Ray photoelectron spectra	98
2.4.9. Near Ambient Pressure – X-Ray photoelectron spectra	99
2.4.10. In-situ magnetic characterization	100
2.4.11. Mössbauer spectroscopy	100
2.4.12. In-situ X-ray absorption spectroscopy	101
2.5. References	102

Chapter 3 Identification of efficient promoters and selectivity trends in high temperature Fischer-Tropsch synthesis over supported iron catalysts 103

3.1. Introduction	104
3.2. Results and discussion	106
3.2.1. Silica supported iron catalysts promoted with 29 elements	106
3.2.1.1. Conversion and reaction rate	106
3.2.1.2 Selectivity trends in high temperature FT synthesis.....	107
3.3.1. Characterization of the promoted catalysts	112
3.3.2. In-situ catalyst characterization.....	115
3.3.3. Catalytic performance of the Sn-, Sb-, Bi and Pb-promoted catalysts.....	124
3.4. Conclusions	129

3.5 References	131
Chapter 4 Active phases for high temperature Fischer-Tropsch synthesis in the silica supported iron catalysts promoted with antimony and tin	134
4.1. Introduction	135
4.2. Results.....	137
4.2.1. Ex-situ characterization.....	137
4.2.2. In-situ Mossbauer measurements	149
4.2.3. In-situ XAS characterization of the Sn and Sb promoters.....	152
4.3. Catalytic performance.....	158
4.4. Discussion.....	161
4.5. Conclusions	167
4.6 References	168
Chapter 5 Efficient promoters and reaction paths in the CO₂ hydrogenation to light olefins over zirconia supported iron catalysts.....	170
5.1. Introduction	171
5.2. Results.....	173
5.2.1. CO ₂ hydrogenation on SiO ₂ -supported catalysts	173
5.2.2. Optimization of potassium load for iron-based catalysts.....	174
5.2.3. HTE evaluation of the promoted iron catalysts	176
5.2.3.1. Catalyst activity and iron time yield.....	176
5.2.3.2. Product selectivity at different conversions	177
5.3. Catalyst characterization	184
5.4. Discussion.....	197
5.5. Conclusions	202
5.6. Reference.....	203
Chapter 6 General conclusions and perspectives	206
6.1. General conclusion.....	206
6.2. Perspectives	208

List of figures

Figure 1-1. Non-oil-based carbon resources via syngas convert to chemicals.....	22
Figure 1-2. Some chemicals obtained from CO ₂ hydrogenation process.....	23
Figure 1-3. World production of plastics (reproduced from Plastics Europe).....	25
Figure 1-4. Routes for chemical valorization of plastic waste.....	26
Figure 1-5. ΔG comparison for different products of CO hydrogenation.....	34
Figure 1-6. Variation of Gibbs free energy with reaction temperature.....	35
Figure 1-7. Carbide mechanism by insertion of methylene (CH ₂).....	39
Figure 1-8. Mechanism of hydroxycarbene intermediates formation and chain growth pattern during FT synthesis.....	40
Figure 1-9. Mechanism of hydroxycarbene intermediates formation and chain growth pattern during FT synthesis.....	41
Figure 1-10. Hydrocarbon selectivity as function of the chain growth probability.....	42
Figure 1-11. Hydrocarbons selectivity during CO and CO ₂ hydrogenation.....	42
Figure 1-12. Possible routes for CO ₂ hydrogenation.....	43
Figure 1-13. Hydrocarbons selectivity during CO and CO ₂ hydrogenation.....	44
Figure 1-14. Multi-tubular fixed bed reactor.....	46
Figure 1-15. Slurry phase reactor.....	47
Figure 1-16. a) fixed fluidized bed (FFB) reactor and b) circulating fluidized bed (CFB) reactor.....	48
Figure 1-17. Microreactors for FTS: a) monolith microstructured catalyst reactor; b) microchannel reactor; c) milli-fixed bed reactor.....	50
Figure 1-18. Processes for the transformation of synthesis gas into light olefins.....	53
Figure 1-19. Effect of promotion with soldering atoms on FT synthesis.....	59
Figure 1-20. Stabilization of iron supported nanoparticles vs bulk iron catalyst.....	60
Figure 1-21. Representation of CO ₂ hydrogenation to lower olefins.....	65
Figure 1-22. Schematic illustrations of the two principal sintering mechanisms.....	71
Figure 2-1. High pressure catalytic set-up for CO and CO ₂ hydrogenation.....	89
Figure 2-2. Flowrence Avantium High Through put Experiment unit.....	91
Figure 2-3. Bruker AXS D8 diffractometer.....	93
Figure 2-4. Micro-X-ray Fluorescence spectrometer M4 TORNADO (Bruker).....	94
Figure 2-5. Micromeritics Tristar II PLUS Surface Area and Porosimetry analyzer.....	95
Figure 2-6. Micromeritics Auto Chem II 2920 equipment.....	97
Figure 2-7. SDT Q600 V20.9 Build 20 Thermogravimetric Analyzer.....	97
Figure 2-8. X-Ray Photoelectron Spectra (XPS) Kratos AXIS UltraDLD spectrometer.....	99
Figure 2-9. Near Ambient Pressure X-Ray Photoelectron Spectroscopy at Charles University.....	100
Figure 3-1. Carbon monoxide conversion measured over the promoted silica supported iron catalysts at iso-WHSV: T=350°C, H ₂ /CO=1, P=10 bar, WHSV=3.4 L/g.h.....	107
Figure 3-2. Light olefin selectivity versus carbon monoxide conversion. Promoted Fe/SiO ₂ catalysts. Fe/P=100:2, H ₂ /CO=1, WHSV=2.25-6.75 L/g.h, P=10 bar.....	108
Figure 3-3. Selectivity versus carbon monoxide conversion: a) CO ₂ selectivity, b) methane selectivity, c) light paraffin selectivity, d) C ₅₊ hydrocarbon selectivity. Promoted Fe/SiO ₂ catalysts. Fe/P=100:2, H ₂ /CO=1, WHSV=2.25-6.75 L/g.h, P=10 bar.....	110

Figure 3-4. Surface polymerization paths in high temperature FT synthesis over iron catalysts.	112
Figure 3-5. XRD patterns of the catalysts after calcination (a) and after FT reaction (b).	114
Figure 3-6. H ₂ -TPR profiles of reference and promoted catalysts with Sn, Sb, Bi and Pb. ...	115
Figure 3-7. Variation of magnetization during exposure of silica supported iron catalysts to CO as a function of temperature (a- Fe/SiO ₂ , b- FeSn/SiO ₂ ; c- FeSb/SiO ₂ , d- SbFe/SiO ₂).....	117
Figure 3-8. Variation of magnetization during exposure of silica supported iron catalysts activated in pure CO to syngas (H ₂ /CO=1) as a function of temperature (a- Fe/SiO ₂ , b- FeSn/SiO ₂ ; c- FeSb/SiO ₂ , d- SbFe/SiO ₂).	118
Figure 3-9. Fe 2p NAP-XPS spectra measured in CO and syngas at different temperatures: a) FeBi/CNT; b) Fe/CNT+Bi/CNT	119
Figure 3-10. Bi 4f NAP-XPS spectra measured in CO and syngas at different temperatures: a) FeBi/CNT; b) Fe/CNT+Bi/CNT	122
Figure 3-11. TEM images of Bi/CNT (2 wt.%) after calcination in nitrogen (a), after the pretreatments in CO at 250°C (b) and at 350°C (c).....	124
Figure 3-12. CO conversion as a function of time for iron catalysts promoted with Sn, Sn, Bi and Pb. Reaction conditions: P = 10 bar, H ₂ /CO = 1, WHSV = 3.6 L/g.h.	127
Figure 3-13. Selectivity conversion curves for silica supported iron catalysts promoted with Bi, Pb, Sn, Sb and reference iron catalysts	128
Figure 4-1. XRD patterns of the catalysts after calcination (a) and after FT reaction (b).	139
Figure 4-2. STEM-HAADF and SEM-EDX mapping of the Fe/SiO ₂ catalyst: (a) after calcination; (b) after activation in CO.	138
Figure 4-3. STEM-HAADF and SEM-EDX mapping of the FeSn/SiO ₂ catalyst: (a) after calcination; (b) after activation in CO.	140
Figure 4-4. STEM-HAADF and SEM-EDX mapping of the FeSb/SiO ₂ catalyst: (a) after calcination; (b) after activation in CO showing the formation of Fe-Sb core-shell structures.	141
Figure 4-5. Histograms of iron nanoparticles distribution in silica supported catalysts activated in CO at 350 °C: a) Fe/SiO ₂ , b) FeSn/SiO ₂ , c) FeSb/SiO ₂	142
Figure 4-6. H ₂ -TPR profiles of Fe(20%)/SiO ₂ , FeSb/SiO ₂ (m) and FeSn/SiO ₂ (m) prepared by mechanical mixing.....	143
Figure 4-7. Thermogravimetric analysis (TGA) curves for activated (a) and spent catalysts (b).	145
Figure 4-8. XPS spectra after calcinations and exposure to carbon monoxide: (a) Fe 2p XPS spectra of the FeSb/SiO ₂ catalyst, (b) Fe 2p XPS spectra of the FeSn/SiO ₂ catalyst, (c) Sb 4d XPS spectra of the FeSb/SiO ₂ catalyst, (d) Sn 3d XPS spectra of the FeSn/SiO ₂ catalyst.	147
Figure 4-9. Mössbauer spectra obtained for fresh (a) impregnated and (b) mixed catalysts at -153 °C.....	149
Figure 4-10. Mössbauer spectra after reaction for impregnated and mixed catalysts at -153 °C.....	150
Figure 4-11. Evolution of the Sb K and Sn absorption edges during the heating in carbon monoxide: a) FeSb/SiO ₂ ; b) FeSb/SiO ₂ (m), c) FeSn/SiO ₂ ; d) FeSn/SiO ₂ (m).....	153
Figure 4-12. Evolution of the Sb and Sn phase compositions during heating in CO and exposure to syngas at 350 °C: a) FeSb/SiO ₂ ; b) FeSb/SiO ₂ (m), c) FeSn/SiO ₂ ; d) FeSn/SiO ₂ (m).	155

Figure 4-13. EXAFS Fourier transform moduli of iron catalysts: a) FeSb/SiO ₂ , b) FeSb/SiO ₂ (m), c) FeSn/SiO ₂ and d) FeSn/SiO ₂ (m) after activation in CO, FT reaction and cooling down to ambient temperature.	157
Figure 4-14. CO conversion as a function of time for iron catalysts promoted with Sn and Sb prepared by co-impregnation and mechanical mixture. Reaction conditions: T = 350 °C, P = 10 bar, H ₂ /CO = 1, WHSV = 3.6 L/g.h.	158
Figure 4-15. Selectivity patterns over Fe/SiO ₂ , FeSb/SiO ₂ and FeSn/SiO ₂ measured at the CO conversion of 10 - 13 %.	159
Figure 4-16. Tin-enriched areas in the close proximity of iron nanoparticles in the activated FeSn/SiO ₂ catalyst.	166
Figure 5-1. CO ₂ conversion as a function of time for iron catalysts promoted with Bi, Sn and Sb. Reaction conditions: T = 350 °C, P = 10 bar, H ₂ /CO ₂ = 3, GHSV = 10.2 L/g.h.	174
Figure 5-2. Iron- based catalysts activity promoted with different amounts of potassium. ...	175
Figure 5-3. Carbon dioxide conversion and activity measured over the promoted zirconia supported iron catalysts T=350 °C, H ₂ /CO ₂ =3, p=10 bar.	177
Figure 5-4. CO selectivity versus carbon dioxide conversion for Fe/ZrO ₂ promoted catalysts. H ₂ /CO=3, WHSV=4.67-18.19 L/ g.h, P=10 bar.	178
Figure 5-5. Methane selectivity versus carbon dioxide conversion for Fe/ZrO ₂ promoted catalysts. H ₂ /CO ₂ =3, WHSV=4.67-18.19 L/ g.h, P=10 bar.	179
Figure 5-6. Light olefin selectivity versus carbon dioxide conversion for Fe/ZrO ₂ promoted catalysts. H ₂ /CO ₂ =3, WHSV=4.67-18.19 L/ g.h, P=10 bar.	180
Figure 5-7. C ₂ -C ₄ paraffins selectivity versus carbon dioxide conversion for Fe/ZrO ₂ promoted catalysts. H ₂ /CO ₂ =3, WHSV=4.67-18.19 L/ g.h, P=10 bar.	181
Figure 5-8. C ₅₊ selectivity versus carbon dioxide conversion for Fe/ZrO ₂ promoted catalysts. H ₂ /CO ₂ =3, WHSV=4.67-18.19 L/ g.h, P=10 bar.	182
Figure 5-9. CO ₂ conversion as a function of time for iron catalysts promoted with K, Ga, Mo, Ce, Cs, and Cu. Reaction conditions: T = 350 °C, P = 10 bar, H ₂ /CO ₂ = 3, WHSV = 9.25 L/g.h.	183
Figure 5-10. XRD patterns of the catalysts after calcination (a) and after reaction (b).	186
Figure 5-11. CO ₂ TPD profiles adsorbed over ZrO ₂ and iron catalysts.	187
Figure 5-12. CO ₂ -TPD curves deconvolution for different ZrO ₂ -supported catalysts.	188
Figure 5-13. H ₂ -TPR profiles of reference and promoted catalysts with K, Cs, Ce, Ga, Mo, and Cu.	190
Figure 5-14. STEM-HAADF, SEM-EDX mapping and histograms of iron nanoparticle sizes for the activated Fe/ZrO ₂ (a), FeK/ZrO ₂ (b), FeKGa/ZrO ₂ (c) and FeKMo/ZrO ₂ (d) catalysts. ...	192
Figure 5-15. Mössbauer spectra after activation measured at -153 °C.	193
Figure 5-16. Mössbauer spectra after reaction measured at -153 °C.	195
Figure 5-17. Thermogravimetric analysis (TGA) curves of the spent catalysts.	197
Figure 5-18. Reaction paths in CO ₂ hydrogenation over promoted iron catalysts with (a) and without (b) potassium.	199
Figure 6-1. Activity of iron-promoted catalysts with different load of Sb.	208

List of tables

Table 1-1. Contaminants present after gasification of plastics and their maximum values for FT synthesis.....	31
Table 1-2. Relative cost of the catalysts.....	51
Table 1-3. Iron oxide phases.....	56
Table 1-4. Iron oxide phases involved during CO ₂ hydrogenation process.....	66
Table 1-5. Some suitable catalysts for hydrogenation of CO ₂	69
Table 3-1. Physical properties of supported Fe catalysts.....	113
Table 3-2. Relative intensities of NAP-XPS peaks measured in the presence of carbon monoxide and syngas.....	120
Table 3-3. Catalytic performance of iron catalysts promoted with soldering metals in FT synthesis measured in a conventional fixed bed reactor at iso-GHSV (10 bar, 350 °C, H ₂ /CO= 1/1, WHSV = 3.6 L/g.h, TOS = 48h).....	125
Table 4-1. Physical properties of supported Fe catalysts.....	138
Table 4-2. XPS ratio before and after activation.....	148
Table 4-3. The Mössbauer fitted parameters of fresh and spent catalysts, obtained at -153 °C.....	151
Table 4-4. Catalytic performance of iron catalysts promoted with Sn and Sb in FT synthesis measured in a conventional fixed bed reactor at iso-WHSV (10 bar, 350oC, H ₂ /CO = 1/1, WHSV = 3.6 L/g.h, TOS = 24h).....	161
Table 5-1. Catalytic performance of iron catalysts promoted with different K amount for CO ₂ hydrogenation reaction (10 bar, 350 °C, H ₂ /CO ₂ = 3, GHSV = 9.25 L/g.h, TOS = 48 h).....	176
Table 5-2. Catalytic performance of iron catalysts promoted with K, Cs, Cu, Ga, Mo and Ce for CO ₂ hydrogenation reaction measured in a fixed bed reactor (10 bar, 350 °C, H ₂ /CO ₂ = 3, GHSV = 9.25 L/g.h, TOS = 48 h).....	183
Table 5-3. Physical properties of supported Fe catalysts.....	185
Table 5-4. The Mössbauer fitted parameters of the ZrO ₂ -based catalysts, obtained at 120 K.....	194

Abstract

Fischer-Tropsch (FT) synthesis is an attractive way to convert non-petroleum and renewable feedstocks such as biomass, plastic and organic waste into fuels and chemicals. Additionally, carbon dioxide is the most important industrial pollutant and is also the major reason of the global climate changes. Rapidly growing the CO₂ concentration in the atmosphere can be addressed on the one hand, by reducing the CO₂ emission from human activities and on the other hand, by carbon dioxide removal from the atmosphere, using carbon capture and storage (CCS) and carbon capture and utilization (CCU). Iron catalysts are the catalysts of choice for CO and CO₂ hydrogenation aiming the production of olefins. Activity, selectivity to light olefins and catalyst stability are major challenges of these reaction over Fe catalysts. CO and CO₂ hydrogenation reaction on Fe catalysts involves iron carbide phases. Catalyst activation which transforms iron oxide nanoparticles into small nanoparticles of iron carbide occurring in CO or syngas is an important step in the catalyst design often strongly affecting the overall catalytic performance. Catalyst doping with small amounts of different elements is one of the common approaches to improve the performance of iron catalysts.

This thesis was performed in the framework of the Interreg PSYCHE Project which aims at the production of base chemicals (olefins) starting from plastic waste which could be reused within the chemical industry. Our contribution to the project focuses on the catalytic transformation of the obtained syngas (CO + H₂) and CO₂ towards base chemicals via the FT process and CO₂ hydrogenation reaction.

In this thesis, we synthesized different iron-based catalysts for both CO and CO₂ hydrogenation. For CO hydrogenation, silica was used as support, while for CO₂

hydrogenation reaction zirconia supported catalysts presented the most encouraging results. Catalysts were synthesized by impregnation methods and characterized using different techniques, such as: XRD, XRF, BET, TEM, TGA, TPR, XPS, NAP-XPS, In-situ magnetic Mössbauer spectroscopy and In-situ X-ray absorption spectroscopy (XAS).

In chapter 3, we relied on High Throughput Experimentation (HTE) to identify among 29 promoters the most efficient ones for FT synthesis at the same time that different selectivity trends were evaluated. For the Cr-, Nb-, Ga-, Pd-, Co-, In-, Mo-, Zn-promoted catalysts carbon monoxide conversion was insignificant. On the other hand, Bi-, Pb-, Sn- and Sb-promoted catalysts displayed an enhanced catalytic activity. HTE tests allowed us to clearly identify these metals as the most promising promoters in order to obtain iron catalysts with higher activity in FT synthesis. Additionally, we observed a CO₂ selectivity increase as function of conversion over all catalysts and it reaches the stoichiometric value of 50% at the CO conversion over 30%. Higher methane selectivities were observed at rather low carbon monoxide conversion (<10%). The lowest methane selectivity was observed over the Pb and Bi-promoted catalysts and the highest over the Sn- and Zr-promoted counterparts. Finally, we obtained that selectivity to light olefins is reduced at higher CO conversion levels. On the other hand, a light olefin selectivity close to 60 % is observed at the relatively low CO conversion (< 2-3 %), while C₂-C₄ paraffins were not much affected by CO conversion.

In chapter 3, characterization also allowed elucidation of the evolution of the catalyst (Fe/SiO₂, FeBi/SiO₂, FePb/SiO₂, FeSn/SiO₂ and FeSb/SiO₂) structure during activation and reaction. For promoted catalysts, the main iron phase detected was the Hägg carbide (Fe₅C₂). Under the conditions of catalyst activation and reaction, it was

observed that metallic bismuth migrated over the catalyst surface forming larger spherical bismuth droplet and strongly interacted with iron carbide species which enhanced catalytic activity and olefins production. Finally, two kinds of promotion were observed. The incorporation of Sn and Sb resulted in the enhancement of the FT reaction rate, while the light olefin selectivity is not much affected. The incorporation of Bi and Pb enhanced both the FT reaction rate and selectivity to light olefins.

In chapter 4, we focused on studying the strong promoting effects of antimony and tin on the catalytic performance of silica supported iron FT catalysts using a combination of advanced and in-situ techniques. TEM in the activated FeSn/SiO₂ catalyst showed highly dispersed Sn nanoparticles on the silica support. On the other hand, activated FeSb/SiO₂ catalyst showed a core-shell morphology, with the core rich in Sb and the shell constituted mainly by iron. Thermogravimetric analysis (TGA) results showed that spent Sn- and Sb-promoted catalysts prepared by co-impregnation show ~60% and 30% less significant carbon deposition respectively compared to the reference non-promoted Fe/SiO₂ catalyst. This smaller amount of carbon deposition is crucial for better stability of the Sn- and Sb-promoted catalysts in FT reaction. Additionally, EXAFS and In-situ XANES showed the presence of Fe-Sb alloy species, formed during reaction conditions, the Fe-Sb intimate contact was claimed responsible for the higher catalytic activity observed. For FeSn/SiO₂ catalyst, the better activity was related to the effect of electron charge transfer and polarization, which can occur, because of localization of mostly tin oxide species in the proximity to iron carbide nanoparticles as revealed by TEM analysis.

In chapter 5, we focused on the identification of the most efficient promoters for zirconia supported iron catalysts and elucidation of the reaction paths using the benefits of high throughput experimentation facility for CO₂ hydrogenation reaction.

We observed the most pronounced increase in the reaction rate for the potassium and cesium promoted catalysts. In this study, the CO selectivity decreased as a function of CO₂ conversion and those catalysts containing potassium, showed higher CO selectivity at similar CO₂ conversion compared to the promoted iron catalysts without potassium. Light olefins selectivity was higher for the catalysts promoted with alkali metals (K or Cs). HTE clearly showed that the presence of potassium was essential to achieve higher light olefin selectivity. In addition to potassium, Mo, Cu, Cs, Ce and Ga were identified as possible promoters to further increase the selectivity of CO₂ hydrogenation to this fraction. The results analysis provided valuable information about possible reaction paths in CO₂-FT synthesis over iron catalysts. The first step is CO₂ hydrogenation to CO followed by formation of C₁ adsorbed monomers. These monomers can be either hydrogenated to yield methane or to undergo oligomerization to different C_n adsorbed species. Desorption of C₂-C₄ adsorbed species should produce light olefins, while their hydrogenation produces light paraffins. Finally, further reactions of adsorbed C₂-C₄ species with C₁ monomer produce longer-chain hydrocarbons. It was proposed that enhancement of activity and selectivity towards light olefins could be due to improvement of reverse water gas shift reaction, changes in catalyst basicity determined by CO₂-TPD.

The work performed during this thesis allowed to design new catalysts for CO and CO₂ hydrogenation reaction that could be easily implemented at industrial level and provided valuable information about the reaction mechanism. Catalysts studied for both reactions showed improvement of activity, selectivity, and stability.

Key words: Fischer-Tropsch synthesis, CO₂ hydrogenation, iron catalysts, light olefins, High Throughput Experimentation, promoter.

Samenvatting

Fischer-Tropsch (FT) synthese is een aantrekkelijke manier om niet op aardolie gebaseerde en hernieuwbare grondstoffen zoals biomassa, plastic en organisch afval om te zetten in brandstoffen en chemicaliën. Daarnaast is koolstofdioxide één van de meest vervuilende industrieel geproduceerde stoffen en tevens de hoofdoorzaak van de wereldwijde klimaatveranderingen. De snel toenemende CO₂-concentratie in de atmosfeer kan enerzijds worden aangepakt door de antropogene CO₂-uitstoot te verminderen en anderzijds door koolstofdioxide uit de atmosfeer te verwijderen, met behulp van koolstof-afvang en -opslag (CCS) en koolstof-afvang en -gebruik (CCU). Doorgaans zijn ijzerkatalysatoren de katalysatoren bij uitstek voor de hydrogenering van CO en CO₂ met het oog op de productie van olefinen. Hierbij zijn de activiteit, de selectiviteit naar lichte olefinen en de katalysatorstabiliteit de belangrijkste uitdagingen van deze reacties op Fe-katalysatoren. Bij de CO- en CO₂-hydrogenatiereactie met behulp van Fe-katalysatoren treedt ijzercarbide op als katalytisch actieve fase. Tijdens het activeren van de katalysator worden nanopartikels ijzeroxide omgezet in kleine nanodeeltjes ijzercarbide met behulp van de koolstof aanwezig in CO of syngas. Dit is een belangrijke stap in het katalysatorontwerp en heeft vaak een sterke invloed op de totale katalytische prestaties. Het doteren van een katalysator met verschillende elementen is één van de gebruikelijke benaderingen om de prestaties van een ijzerkatalysator te verbeteren.

Dit proefschrift past in het kader van het Interreg PSYCHE project dat zich richt op de productie van basischemicaliën (olefinen) uit plastic afval dat zo kan worden hergebruikt in de chemische industrie. Onze bijdrage aan het project richt zich op de katalytische omzetting van het daaruit verkregen syngas (CO + H₂) en CO₂ naar basischemicaliën via het FT proces en de CO₂ hydrogeneringsreactie.

In dit proefschrift hebben we verschillende ijzerhoudende katalysatoren gesynthetiseerd voor zowel CO als CO₂ hydrogenering om zeer selectieve, actieve en stabiele katalysatoren te verkrijgen die bruikbaar zijn onder industrieel relevante reactieomstandigheden. Voor de CO hydrogenering werd silica als drager gebruikt, terwijl voor de CO₂ hydrogeneringsreactie zirkonium-ondersteunde katalysatoren de meest belovende resultaten opleverden. De katalysatoren werden gesynthetiseerd door eenvoudige impregnatiemethoden en vervolgens gekarakteriseerd met behulp van verschillende technieken, zoals: XRD, XRF, BET, TEM, TGA, TPR, XPS, NAP-XPS, in-situ magnetische Mössbauer spectroscopie en in-situ röntgenabsorptiespectroscopie (XAS).

In hoofdstuk 3 hebben we gebruik gemaakt van High Throughput Experimentation (HTE) om uit 29 promotoren de meest efficiënte voor FT synthese te identificeren terwijl verschillende selectiviteitstrends werden geëvalueerd. Voor de Cr-, Nb-, Ga-, Pd-, Co-, In-, Mo-, Zn-gedoteerde katalysatoren was de omzetting van koolmonoxide niet significant. Omgekeerd vertoonden de Bi-, Pb-, Sn- en Sb-gedoteerde katalysatoren een verhoogde katalytische activiteit. HTE-campagnes stelden ons in staat deze metalen duidelijk te identificeren als de meest veelbelovende promotoren voor ijzerkatalysatoren op basis van een hogere activiteit in de FT-synthese. Bovendien zagen we bij alle katalysatoren een toename van de CO₂-selectiviteit als functie van de conversie en deze bereikte de stoichiometrische waarde van 50% bij een CO-conversie van meer dan 30%. Hogere methaanselectiviteiten werden waargenomen bij een vrij lage koolmonoxideconversie (<10%). De laagste selectiviteit voor methaan werd waargenomen bij de Pb- en Bi-gedoteerde katalysatoren en de hoogste bij de katalysatoren waaraan Sn- en Zr was toegevoegd. Ten slotte hebben we vastgesteld dat de selectiviteit voor lichte olefinen afneemt bij

hogere CO-conversies. Anderzijds werd een selectiviteit voor lichte olefinen van bijna 60% waargenomen bij een relatief lage CO-conversie (< 2-3%), terwijl de C₂-C₄-paraffines niet sterk beïnvloed werden door de CO-conversie.

In dit hoofdstuk kon door karakterisering de evolutie van de katalysatorstructuur (Fe/SiO₂, FeBi/SiO₂, FePb/SiO₂, FeSn/SiO₂ en FeSb/SiO₂) tijdens activering en reactie worden onderzocht. Bij de gedoteerde katalysatoren werd de belangrijkste ijzerfase geïdentificeerd als het zogenaamde Hägg-carbide (Fe₅C₂). Onder de omstandigheden van katalysatoractivering en -reactie werd waargenomen dat metallisch bismut over het katalysatoroppervlak migreert en grotere bolvormige bismutdruppels vormt; de toename van de katalytische activiteit en de daaruit voortkomende olefinenproductie kon worden toegeschreven aan de interactie tussen dit metallisch bismut en de verschillende ijzercarbidesoorten. Tenslotte werden twee soorten effecten waargenomen als gevolg van dotering. De incorporatie van Sn en Sb resulteerde in de verhoging van de FT-reactiesnelheid, terwijl de reactieselectiviteit naar lichte olefinen niet veel werd beïnvloed. Het toevoegen van Bi en Pb verbeterde zowel de FT-reactiesnelheid als de selectiviteit voor lichte olefinen.

In hoofdstuk 4 hebben we ons gericht op het bestuderen van de sterk bevorderende effecten van antimoon en tin op de katalytische prestaties van silica ondersteunde ijzer-gebaseerde FT katalysatoren met behulp van een combinatie van geavanceerde en in-situ analysetechnieken. TEM op de geactiveerde FeSn/SiO₂-katalysator toonde de sterk verspreide Sn-nanopartikels op de silica drager. Anderzijds vertoonde de geactiveerde FeSb/SiO₂-katalysator een core-shell-morfologie, waarbij de kern rijk was aan Sb en de schil voornamelijk uit ijzer bestond. Thermogravimetrische analyse (TGA) toonde aan dat gebruikte Sn- en Sb-gedoteerde katalysatoren, bereid door co-impregnatie, respectievelijk ~60% en 30% minder

afzetting vertoonden dan de referentie (i.e., niet-gedoteerde) Fe/SiO₂-katalysator. Deze kleinere hoeveelheid koolstofafzetting is cruciaal voor een hogere stabiliteit van de Sn- en Sb-gedoteerde katalysatoren in de FT-reactie. Bovendien toonden EXAFS en in-situ XANES de aanwezigheid van verschillende types Fe-Sb legeringen. Deze werden gevormd als gevolg van de aangewende reactieomstandigheden en de toegenomen katalytische activiteit werd toegeschreven aan het nauw contact tussen beide metalen. Voor FeSn/SiO₂ katalysatoren was de betere activiteit gerelateerd aan het effect van elektronentransfer en polarisatie. Deze fenomenen kunnen optreden als gevolg van de aanwezigheid van (voornamelijk) tinoxides in de nabijheid van de ijzercarbide nanodeeltjes. Dit laatste werd bevestigd door middel van TEM analyse.

In hoofdstuk 5 richtten we ons op de identificatie van de meest efficiënte promotoren voor zirkonium-ondersteunde ijzerkatalysatoren en de identificatie van de courante reactiepaden in de CO₂ hydrogeneringsreactie door middel van high throughput experimenten. De meest uitgesproken verhoging van de reactiesnelheid werd waargenomen bij de met kalium en cesium gedoteerde katalysatoren. In deze studie nam de CO-selectiviteit af naarmate de CO₂-conversie toenam en de katalysatoren die kalium bevatten, vertoonden een hogere CO-selectiviteit bij een vergelijkbare CO₂-conversie in vergelijking met de gedoteerde ijzerkatalysatoren zonder kalium. De selectiviteit voor lichte olefinen was hoger voor de katalysatoren die met alkalimetalen (K of Cs) werden gedoteerd. HTE toonde duidelijk aan dat de aanwezigheid van kalium essentieel is om een hogere selectiviteit richting lichte olefinen te bereiken. Naast kalium werden Mo, Cu, Cs, Ce en Ga geïdentificeerd als mogelijke promotoren om de selectiviteit van CO₂ hydrogenering naar deze fractie verder te verhogen. Analyse van de resultaten maakte het mogelijk de relevante reactiepaden te identificeren in de ijzer-gekatalyseerde CO₂-FT synthese. De eerste

stap is de hydrogenering van CO₂ tot CO, gevolgd door de vorming van geadsorbeerde C₁-monomeren. Deze monomeren kunnen ofwel gehydrogeneerd worden tot methaan ofwel een oligomerisatie ondergaan tot verschillende geadsorbeerde C_n-soorten. Desorptie van de C₂-C₄ geadsorbeerde soorten leidt tot de vorming van lichte olefinen, terwijl hun hydrogenering aanleiding geeft tot de vorming van lichte paraffinen. Tot slot leveren verdere reacties van geadsorbeerde C₂-C₄-soorten met een C₁-monomeer koolwaterstoffen met langere ketens op. Voorgesteld werd dat de verhoging van de activiteit en selectiviteit ten opzichte van lichte olefinen te wijten zou kunnen zijn aan de verbetering van de omgekeerde water-gas-shift-reactie en veranderingen in de basiciteit van de katalysator, zoals bepaald door CO₂-TPD.

Het werk dat voor dit proefschrift werd verricht resulteerde in het ontwerp van nieuwe katalysatoren voor CO en CO₂ hydrogeneringsreacties, die bovendien vrij gemakkelijk op industriële schaal kunnen worden geïmplementeerd. De katalysatoren die voor beide reacties werden bestudeerd, vertoonden een verbetering op de drie belangrijkste aspecten, nl. katalysatoractiviteit, -selectiviteit, en -stabiliteit.

Trefwoorden: Fischer-Tropsch synthese, CO₂ hydrogenering, ijzerkatalysatoren, lichte olefinen, High Throughput Experimentation, promotor.

Résumé

La synthèse Fischer-Tropsch (FT) est une voie intéressante de conversion des matières premières non pétrolières et renouvelables telles que la biomasse, le plastique et les déchets organiques, en carburants et en produits chimiques. Le dioxyde de carbone est un polluant industriel. Des changements climatiques mondiaux sont attribués à son implication dans l'effet de serre. L'augmentation rapide de concentration de CO₂ dans l'atmosphère peut être limitée, d'une part, en réduisant les émissions de CO₂ dues aux activités humaines et, d'autre part, en éliminant le dioxyde de carbone de l'atmosphère grâce à son captage et à son stockage (Carbon capture and storage, CSC) ou au captage et à l'utilisation du carbone (Carbon capture and utilization CCU). Les catalyseurs à base de fer sont les catalyseurs de choix pour l'hydrogénation du CO et du CO₂ visant la production d'oléfines. L'activité, la sélectivité en oléfines légères, ainsi que la stabilité du catalyseur sont des défis majeurs de ces réactions. La réaction d'hydrogénation du CO et du CO₂ sur ces catalyseurs implique des phases de carbure de fer. L'activation du catalyseur par le CO ou le gaz de synthèse, qui transforme les nanoparticules d'oxyde de fer en petites nanoparticules de carbure de fer, est une étape importante qui affecte souvent de manière significative la performance catalytique globale. Le dopage du catalyseur à base de fer avec de petites quantités de différents éléments est l'une des approches courantes pour améliorer sa performance.

Cette thèse a été réalisée dans le cadre du projet Interreg PSYCHE qui a pour objectif de synthétiser des produits chimiques de base à haute valeur ajoutée (oléfines) à partir de déchets plastiques ;. Notre contribution au projet porte sur la transformation catalytique du gaz de synthèse (CO + H₂) et du CO₂ obtenus via le procédé FT et la réaction d'hydrogénation du CO₂ en oléfines.

Dans cette thèse, nous avons synthétisé différents catalyseurs à base de fer pour l'hydrogénation du CO et du CO₂. Pour l'hydrogénation du CO, la silice a été utilisée comme support tandis que pour la réaction d'hydrogénation du CO₂, les catalyseurs supportés par la zircone ont présenté les résultats les plus encourageants. Les catalyseurs ont été synthétisés par la méthode d'imprégnation et caractérisés en utilisant différentes techniques, telles que : XRD, XRF, BET, TEM, TGA, TPR, XPS, NAP-XPS, spectroscopie Mössbauer magnétique in-situ et spectroscopie d'absorption des rayons X (XAS) in-situ.

Dans le chapitre 3, nous nous sommes appuyés sur l'expérimentation à haut débit (EHD) pour identifier parmi 29 éléments testés, les promoteurs les plus efficaces pour la synthèse de FT en évaluant également les différentes tendances de sélectivité. Les catalyseurs promus par Bi-, Pb-, Sn- et Sb ont montré une activité catalytique accrue. Les tests EHD nous ont permis d'identifier clairement ces métaux comme les promoteurs les plus prometteurs qui permettent d'obtenir des catalyseurs ferreux avec une plus grande activité pour la synthèse de FT. De plus, nous avons observé une augmentation de la sélectivité en CO₂ en fonction de la conversion sur tous les catalyseurs et elle atteint la valeur stœchiométrique de 50% à une conversion du CO supérieure à 30%. Des sélectivités plus élevées en méthane ont été observées à une conversion plutôt faible du monoxyde de carbone (<10%). La plus faible sélectivité en méthane a été observée sur les catalyseurs promus par Pb et Bi et la plus élevée sur les catalyseurs équivalents promus par Sn- et Zr. Enfin, nous avons également observé que la sélectivité en oléfines légères est faible lorsque les valeurs de conversion du CO sont élevées. Ainsi, une sélectivité en oléfines légères proche de 60 % est observée à un taux de conversion du CO relativement bas, alors que la sélectivité en paraffines C₂-C₄ n'est pas influencée par la conversion du CO.

Dans le chapitre 3, les techniques de caractérisation ont permis d'élucider l'évolution de la structure des catalyseurs (Fe/SiO_2 , FeBi/SiO_2 , FePb/SiO_2 , FeSn/SiO_2 et FeSb/SiO_2) pendant l'activation et lors de la réaction. Pour les catalyseurs promus, la principale phase de fer détectée était le carbure de Hägg (Fe_5C_2). Dans les conditions d'activation et de test catalytique, le bismuth métallique migre à la surface du catalyseur en formant des gouttelettes de bismuth sphériques qui interagissent fortement avec les espèces de carbure de fer, et améliore l'activité catalytique et la production d'oléfines. L'incorporation de Sn et de Sb a entraîné une augmentation de la vitesse de réaction de synthèse FT, tandis que la sélectivité en oléfines légères n'en pas impactée. L'incorporation de Bi et de Pb a amélioré à la fois la vitesse de réaction FT et la sélectivité en oléfines légères.

Dans le chapitre 4, nous nous sommes concentrés sur l'étude des promoteurs antimoine et étain, sur la performance catalytique des catalyseurs à base de fer supportés sur silice, en utilisant une combinaison de techniques avancées et in-situ. Les images MET du catalyseur FeSn/SiO_2 activé ont montré des nanoparticules de Sn hautement dispersées sur le support de silice. D'autre part, le catalyseur activé FeSb/SiO_2 a montré une morphologie cœur-coquille, avec le cœur riche en Sb et la coquille constituée principalement de fer. Les résultats de l'analyse thermogravimétrique (ATG) ont montré que les catalyseurs après tests promus par Sn- et Sb et préparés par co-imprégnation présentent respectivement ~60% et 30% de dépôt de carbone moins par rapport au catalyseur de référence non promu Fe/SiO_2 . Cette plus petite quantité de dépôt de carbone est cruciale pour leur meilleure stabilité dans la réaction FT. De plus, l'EXAFS et le XANES in-situ ont montré la présence d'espèces d'alliage Fe-Sb, formées pendant les conditions de réaction, ce contact intime est considéré comme responsable de la meilleure activité catalytique observée.

Pour le catalyseur FeSn/SiO₂, la meilleure activité était liée à l'effet du transfert de charge et de la polarisation des électrons, qui peut se produire en raison de la localisation des espèces d'oxyde d'étain à proximité des nanoparticules de carbure de fer, comme le révèle l'analyse MET.

Dans le chapitre 5, nous avons identifié des promoteurs les plus efficaces pour les catalyseurs de fer supportés sur zircone et élucidé des étapes principales d'hydrogénation du CO₂ en utilisant les avantages de l'expérimentation à haut débit. Nous avons observé une nette augmentation de la vitesse de réaction pour les catalyseurs promus par le potassium et le césium. La sélectivité en CO diminue en fonction de l'augmentation de la conversion du CO₂ et les catalyseurs contenant du potassium ont montré une plus grande sélectivité en CO pour une conversion similaire du CO₂ par rapport aux catalyseurs de fer promus sans potassium. La sélectivité en oléfines légères est plus élevée pour les catalyseurs promus avec des métaux alcalins (K ou Cs). Le EHD a clairement montré que la présence de potassium est essentielle pour obtenir une plus grande sélectivité en oléfines légères. En plus du potassium, le Mo, Cu, Cs, Ce et Ga ont été identifiés comme des promoteurs capables d'augmenter davantage la sélectivité en oléfines. La première étape de la réaction CO₂-FT est l'hydrogénation du CO₂ en CO, suivie de la formation de monomères adsorbés en C₁. Ces monomères peuvent être soit hydrogénés pour donner du méthane, soit subir une oligomérisation en différentes espèces adsorbées C_n. La désorption des espèces adsorbées C₂-C₄ devrait produire des oléfines légères, tandis que leur hydrogénation produit des paraffines légères. Enfin, d'autres réactions des espèces C₂-C₄ adsorbées avec le monomère C₁ produisent des hydrocarbures à chaîne plus longue. L'amélioration de l'activité et de la sélectivité envers les oléfines légères pourrait être

due à la réaction reverse du gaz à l'eau, des changements dans la basicité des catalyseurs déterminées par CO₂-TPD.

Le travail effectué au cours de cette thèse a permis de concevoir de nouveaux catalyseurs pour la réaction d'hydrogénation du CO et du CO₂ qui pourraient être mis en œuvre au niveau industriel, ainsi que d'obtenir des informations importantes sur le mécanisme de ces réactions. Les catalyseurs étudiés pour les deux réactions ont montré une amélioration de trois aspects clés : l'activité, la sélectivité et la stabilité.

Mots clés : Synthèse de Fischer-Tropsch, hydrogénation du CO₂, catalyseurs à base de fer, oléfines légères, expérimentation à haut débit, promoteur.

Chapter 1 Literature review

1.1. General Introduction

Nowadays, increasing attention to global climate change, energy demand, and depleting oil reserves made exploration of clean energies one of the most important topics for people around the world. Currently, oil, coal, and natural gas constitute the main energy source worldwide. Likewise, among the problems caused, it stands out that these resources are not renewable and they have a huge environmental impact. Their treatment involves the release of greenhouse gases that contribute to climate change, in addition, they generate fuels that could be highly contaminated with cancerogenic aromatic compounds, sulphur, or metallic particles.

At the present time, direct conversion of non-petroleum carbon resources (coal, natural gas, shale gas, and biogas) into valuable chemicals continues to be challenging. One of the main strategies for the transformation of non-petroleum carbon resources is the production of synthesis gas ($\text{CO}+\text{H}_2$) by gasification in the first step, followed by production of liquid fuels or building-block chemicals from the syngas produced in previous step (**Figure 1-1**). Typically, two groups of products (hydrocarbons and organic oxygenates), can be obtained depending on the catalyst and conditions used for the conversion of syngas^{1,2}.

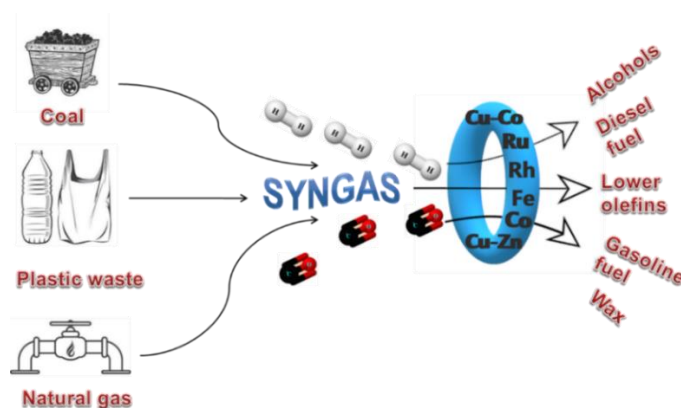


Figure 1-1. Non-oil-based carbon resources via syngas convert to chemicals.

In addition to the CO use, CO₂ is an abundant and vital carbon resource that can serve for various chemical and material synthesis via photocatalysis^{3,4}, electrocatalysis⁵, and thermocatalysis⁶. Thermocatalytic CO₂ hydrogenation to value-added chemicals such as light olefins is a potential pathway due to its scalability. CO₂ is an economical, non-toxic, and renewable carbon source. The employment of CO₂ as feedstock for production of chemicals (**Figure 1-2**) is not only motivating to diminish the greenhouse gases emissions, but a fascinating challenge to study new concepts and new chances for catalysis and chemical industry^{2,7}.

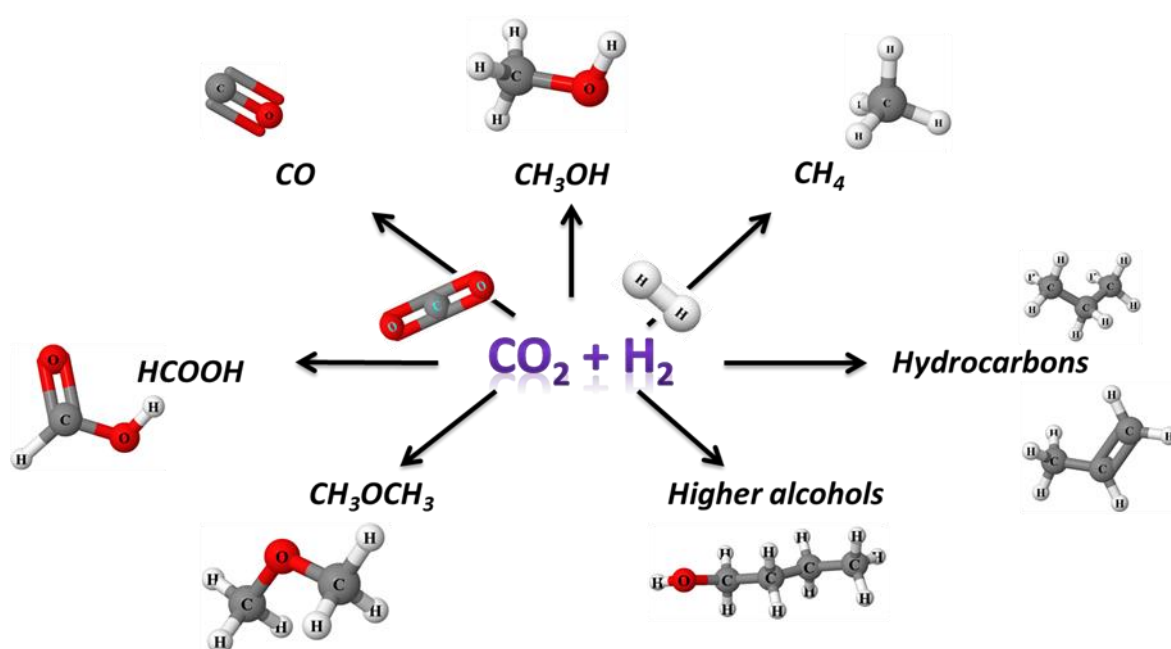


Figure 1-2. Some chemicals obtained from CO₂ hydrogenation process.

Besides CO and CO₂, hydrogen is an important energy carrier that can help to support sustainable energy development, if it is produced from renewable feedstock. At the moment, more than 95% of the hydrogen in the world is produced by steam reforming or partial oxidation of hydrocarbons with the inevitable production of carbon dioxide⁸. Because of this, actions to decrease greenhouse gases emissions have to contemplate hydrogen generation from sustainable energy sources, that is, so-called

green hydrogen production methods⁹. These green hydrogen production methods are expected to supply hydrogen to be employed directly as fuel, to produce synthetic fuels, to upgrade heavy oils (like oil sands), and to generate other chemicals¹⁰.

In this context, CO and CO₂ hydrogenation are promising ways for obtaining light olefins which are basic platform molecules for production of polymers, chemical intermediates, and solvents. For this reason, it is necessary to develop new catalysts for efficiently produce high valuables hydrocarbons that can meet current standard regulations^{11,12,13}.

1.1.1. Plastic waste and its recycling

Plastics are key and omnipresent materials in our economy and daily lives¹⁴ because of their affordable prices and a wide range of convenient properties, such as low density, strength, durability, user-friendly design and resistance to corrosion. In many areas, plastics have caused a displacement of conventional materials, like wood, metals, and ceramics¹⁵. In fact, over the last five decades, global production of plastics has steadily increased (**Figure 1-3**), arriving to 359 million tons (Mt) in 2018. Moreover, the worldwide production of plastics is expected to double again during the next 20 years¹⁴.

Plastic waste management represents a huge challenge that has to be urgently addressed¹⁶. In the past, plastic materials were not recycled due to elevated costs. Nevertheless, new environmental laws have generated the imperious necessity of looking for novel alternatives as a replacement for storage in landfills, which in the year 2000 was the final destiny of 75% plastic in Europe¹⁷.

Around the world, plastic waste gathered from the solid garbage stream is an impure, diverse mixture of various polymer materials. The aforementioned makes their

cataloging, separation, and purification quite challenging⁷. In the plastics waste stream, polyethylene represents the greatest portion. Lower quantities of a mixture of other plastics can also be identified in the plastics waste stream.

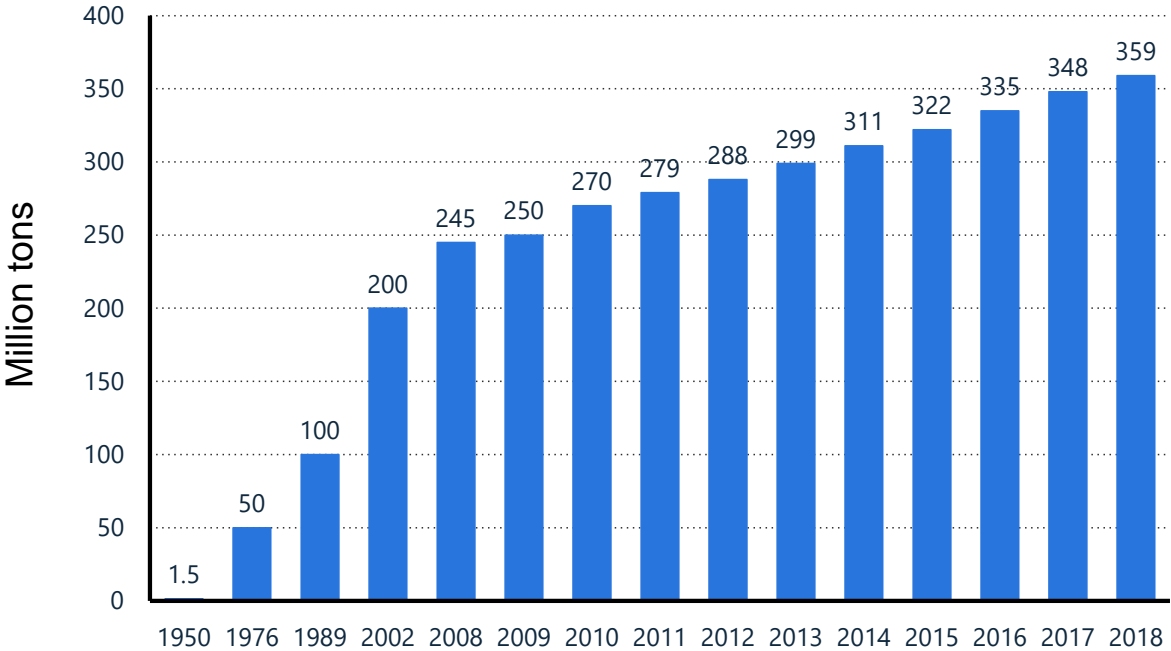


Figure 1-3. World production of plastics (reproduced from *Plastics Europe*).

Among the plastic waste management, the cheapest and most used is dumping. However, since the plastic material degrades very slowly, it is not a sustainable way out because of the limited landfill space and environmental consequences, including groundwater pollution, vegetation damage and air pollution. An alternative to dumping can be direct energy usage of plastics, for example, for heat or energy generation via incineration. Because of the great energy value of plastic materials, this method can produce electricity with high efficiency^{17,18}. Additionally, this method hugely decreases the amount of garbage by about 90–95%. Unfortunately, toxic emission produced during plastics incineration considerably hinders use of this technology¹⁹.

Another way to manage plastic waste is to recycle it. Several approaches have been considered and implemented over the years (**Figure 1-4**). The primary plastics

recycling, also named re-extrusion, is the re-introduction of wastes in order to generate products of the similar quality. This type of reutilization is just possible with semi-clean waste. Therefore, making it an unpopular choice.

On the other hand, the secondary mechanical recycling comprises collection, sorting, washing, and granulation of the waste, is one of the most attractive recycling strategies, since it permits plastics to be used as raw materials in other recycling processes. Plastics must be sorted before the mechanical recycling. Different technologies are being applied to sort plastics, employing different approaches like X-ray fluorescence, infrared spectroscopy, electrostatics, and flotation. Directly after the categorization, the plastics can be straightly melted down and molded into a new form, or melted down right after being shredded into flakes and then processed into granules²⁰. Nonetheless, the latter mentioned kind of recycling is just viable in the materials made by single-polymer plastic (polyethylene, polypropylene, polystyrene, etc). As general rule, if the mixture of plastic waste is complex and presents a lot of contaminants, more problematic will be its mechanical recycling^{17,7,20}.

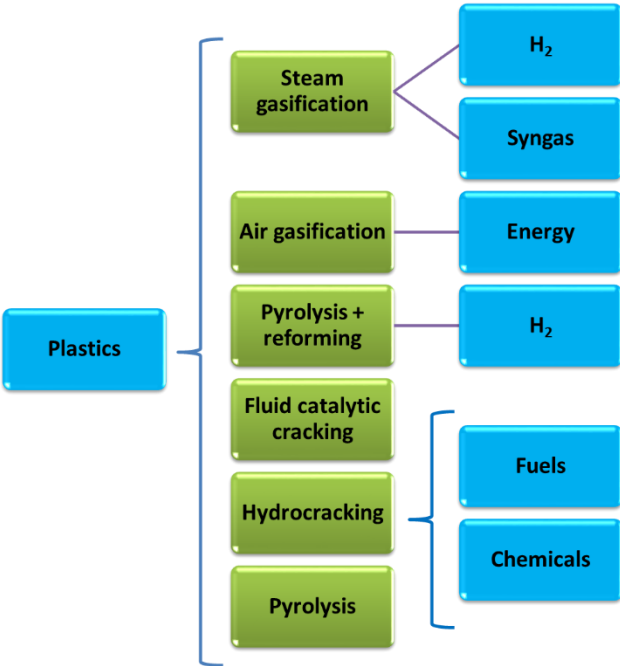


Figure 1-4. Routes for chemical valorization of plastic waste²¹.

In addition to mechanical recycling, chemical (tertiary) recycling allows the production of small molecules from plastic materials. Among these small molecules, liquids and gases are the most typical, which were appropriate for using them as raw material for generation of new fuels, petrochemicals, and plastics making this process an alternative to landfilling and incineration²². Lately, investigations have been focused on chemical recycling (mostly pyrolysis, hydrogenation, and gasification) as a practical way of producing different hydrocarbon fractions from plastic solid waste²³. Even though chemical recycling is expensive and needs a lot of used plastics to process to be economically feasible, it has a greater flexibility over composition and is more tolerant to contaminants than mechanical recycling²⁰.

Finally, gasification process has recently been attracting increased attention as thermo-chemical recycling technique. Its major advantage is the possibility of treating heterogeneous and contaminated polymers with limited use of pre-treatment, whilst the production of syngas creates different applications in synthesis reactions or energy utilization. Gasification has been broadly studied and applied for biomass²⁸ and coal²⁹, with results reported and published in literature. The application for the treatment of plastic solid waste is less documented, although the number of publications increases exponentially.

1.1.2. Gasification

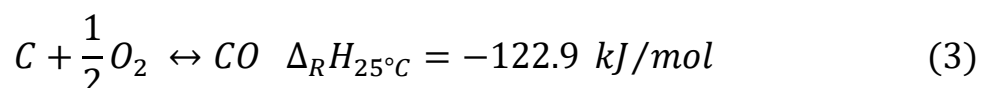
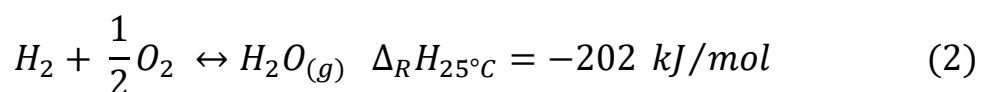
Nowadays, feedstock recycling, which converts plastic materials into helpful basic chemicals, has been recognized as an advanced technology process. Gasification process has the great advantage of allowing the treatment of contaminated waste or unsorted plastic waste. This technology is completely different to, for example, incineration of plastic which focuses on just eliminating the plastic waste or to generate electricity. The gasification process apart from being a way for

electricity generation it also allows fuels production and gives more flexible manners to store energy. Besides, it produces lower amounts of contaminants (nitrogen oxides and sulfur). Most common gasification technologies use reactors that operate in high temperature (generally in the range 800 °C to 1000 °C or even higher)²⁴. This process converts almost every feed composed of organic materials into a combustible gas, composed of CO, CO₂, CH₄, H₂, and other light hydrocarbons^{25,26}.

During gasification process the main reactions need energy supply to occur. This energy is, normally, provided by the combustion of part of feed. In general, gasification can be considered as a series of several steps. The major steps of this process are:

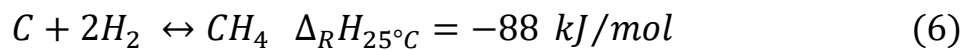
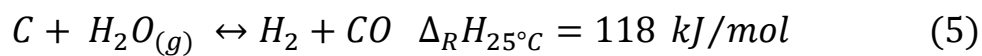
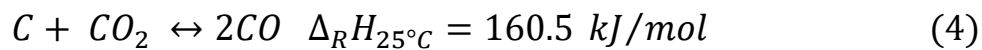
- Oxidation (exothermic stage),
- Drying (endothermic stage),
- Pyrolysis (endothermic stage), and
- Reduction (endothermic stage).

The oxidation stage is essential to get the thermal energy needed for the endothermic steps, to keep the working temperature at the required value. The combustion is performed in conditions of oxygen deficiency with respect to the stoichiometric ratio to oxidize only a portion of the fuel. Even though the incomplete oxidation involving all carbonaceous species, it is plausible to simplify the system considering that only char and the hydrogen contained in the syngas contribute in the incomplete combustion reactions. The most important reactions that happen throughout the combustion phase are the following²⁵.



Drying involves vaporization of the humidity included in the feed. The amount of energy needed in this step is correlated to the input humidity content. Normally, the energy needed for drying comes from other steps in the process.

The pyrolysis stage involves the thermo-chemical fractionalization of the matrix carbonaceous components; particularly, the cleavage of chemical bonds occurs with the generation of molecules with an inferior molecular weight. Depending on the conditions, pyrolysis yields different amounts of solids, liquids, and gaseous products. Finally, the reduction stage includes all the products coming from previous steps of pyrolysis and oxidation; the mixture of gases and char reacts generating the final synthesis gas. The main reactions occurring in this stage are^{25,27}:



Two points that have been addressed by scientists is the development of suitable reactors and operation conditions for the gasification process. The specific properties of scrap plastics, in particular the sticky behavior, low thermal conductivity, remarkable tar formation, and high volatile content, may constrain management of plastics waste in traditional gasification methodologies and presents a severe issue for the process execution. Therefore, an appropriate gasifier for managing plastic should be designed, considering the following characteristics:

- Be capable of supplying elevated heat transfer rates to give pass to a quick plastic waste depolymerization,

- Prevent operational issues associated to the gluey behavior of plastics,
- A proper residence time distribution is required to benefit tar cracking, and
- Permit using primary catalyst in situ providing a good contact with this catalyst.

Gasification process brings with it numerous benefits over conventional combustion of solid wastes. Gasification allows the possibility of playing with the type of starting waste desired, different operating conditions, and characteristics of the reactor to produce a syngas appropriated for use in diverse applications as a chemical feedstock, or a fuel gas that can be burned in gas reciprocating engines or gas turbines to generate electricity. Actually, this process can generate the electricity with an efficiency of around 34% which is higher than in the incineration^{18,28}.

Despite all benefits that plastic gasification might represent, this process continues to face several technical and economic issues. The gas coming from gasification might contain different pollutants like tars, particulates, halogens, heavy metals, and alkaline compounds depending on the fuel composition and the specific gasification method. This could cause accumulation in the gasification vessel, which might produce obstruction of fluidized beds and augmented tar generation.

1.1.3. Main components and impurities in syngas produced by gasification

The plastics gasification conducted with addition of air produces a syngas with heating values around 6.5–8.2 MJ m⁻³ range^{29,30}. The principal utilization of this nitrogen-containing syngas is combustion and energy generation. Steam gasification of plastics permits generation of nitrogen free syngas with a higher heating value above 15 MJ m⁻³, with its composition being appropriate for synthesis applications^{22,31}.

Table 1-1. Contaminants present after gasification of plastics and their maximum values for FT synthesis

Contaminant present	Amount after gasification (ppm)	Maximum allowed for FT process (ppb)
Particulates	13300	0
N (HCN + NH₃)	4700	20
S (H₂S)	1000	10
Alkalis	1000	10
Cl (HCl)	1000	10
Tars	2000	0

The syngas produced by gasification of plastics contains, besides the before mentioned gases (section 1.1.2), also several impurities, shown in **Table 1-1**, such as HCl, HCN, NH₃, H₂S, NO_x, alkali metals, and condensable tars³². If the final amount of these contaminants is not adjusted, their presence might negatively affect the activity in the FT synthesis because of catalyst poisoning. For example, sulfur is an irreversible poison for cobalt and iron catalysts (and to a smaller extent for the shift and reformer catalysts), because it could stick to the active sites.

The H₂/CO ratio of the syngas is another important issue. The temperature at which the reduction stage is performed has a critical role in defining the composition of the syngas, and consequently its characteristics. High temperatures reduce the formation of tar. Besides, they increase the risk of ash sintering and decrease the energy content of the syngas. Another way to perform the gas conditioning is using a water-gas shift reaction unit. However, this makes the gasification process more complicated and expensive^{33,34}.

1.1.4. Syngas purification

Some syngas composition could be particularly restrictive for being used in the catalytic conversion of syngas into value added products, such as FT synthesis (FTS). Due to this, it is imperative that the syngas produced could be cleaned up. Several

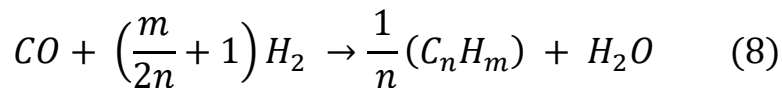
steps need to be followed in order to achieve the industrial standards required for syngas conversion to other products.

The cold gas clean-up has been the traditional way because of its demonstrated reliability and great effectiveness for the elimination of impurities. The cold syngas clean-up can be performed in either the “wet” or “dry” way. Among these two ways, the wet cold gas clean-up ways are more usually selected due to the easy simultaneous elimination of multiple contaminants. For example, HCl, NH₃, and H₂S are easily soluble in water. Consequently, wet towers, scrubbers, and cyclones working with aqueous solutions will take away all these impurities at changing removal efficiencies based on their solubility in water.

Another contaminant to be removed is tar. Typically, two types of strategies are considered to reduce the tar content in syngas³⁵. The first one involves the methods operating during the gasification stage, which limit the tars formation or convert tars in the gasification reactor. The second one is related to the post-treatment processes, which operate downstream of gasification with a variety of purification methods. These methods might involve physical (wet scrubbing, filtration, electrostatic precipitation), thermal and/or catalytic processes³⁶.

In addition to the previous presented techniques, warm and hot gas clean-up approaches are of great interest in contaminant removal from syngas. Warm and hot gas clean-up focus on the contaminant removal from syngas at high temperature (>300 °C). The benefit of hot gas clean-up is that it deals with the loss in efficiency obtained during cold gas cleanup. Furthermore, it decreases the waste streams with the possible conversion of different contaminants into ecologically kind or even valuable products^{37,38}.

Once syngas purification has been finalized, it is desired in the case of using iron-based catalysts for FTS, that the syngas has a H₂/CO ratio close to one. One of the key characteristics of iron catalysts is their activity towards water-gas-shift (WGS) reaction. The WGS process delivers extra hydrogen for Fischer-Tropsch synthesis, which is needed to produce hydrocarbons (eq. 8)^{39,40}.



1.2. CO hydrogenation and CO₂ hydrogenation

1.2.1. Thermodynamics

Thermodynamics allows predicting the spontaneity of a given reaction, based on the Gibbs free energy parameter (ΔG°). From the thermodynamic point of view, CO hydrogenation process is favored, since they present large changes in the Gibbs free energy in a wide temperature range, as can be seen in **Figure 1-5**. The positive slope of all the curves is consequence of the exothermic nature of all reactions.

From **Figure 1-5** the following generalizations can be inferred:

- Methane is the most thermodynamically favored hydrocarbon since it has the lower Gibbs free energy formation.
- The order of thermodynamic preference in the formation of hydrocarbons is generally: alkanes > alkenes > alcohols.

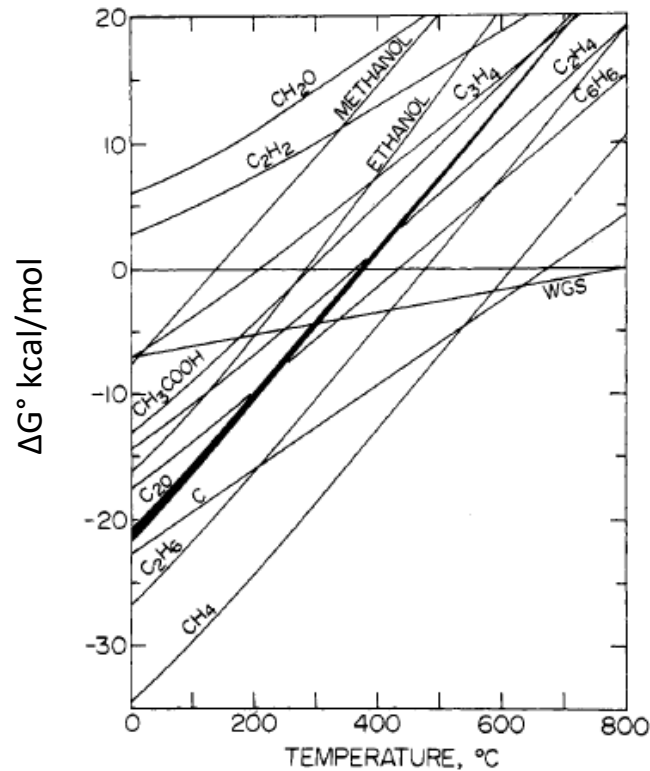
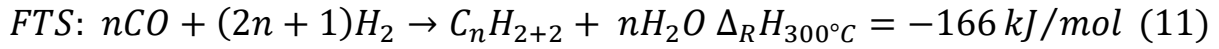


Figure 1-5. ΔG comparison for different products of CO hydrogenation⁴¹.

On the other hand, carbon dioxide is a highly oxidized, thermodynamically stable molecule ($\Delta G^\circ = -400$ kJ/mol) with two linear double bonds⁴², having low reactivity. This is the reason why CO_2 is one of the major products of the largest part of combustion reactions. This also makes clear why in many carbon dioxide valorization processes; the yield of target products is limited by the thermodynamic equilibrium. Consequently, an important challenge for chemical carbon dioxide conversion is thermodynamic limitations even if the reaction kinetics can be favorable⁴³.

Ideally, the direct conversion of CO_2 to hydrocarbons would be a more interesting process for industrial use. This requires the sequential reduction of CO_2 to CO via the reverse water-gas shift (RWGS) reaction followed by the Fisher-Tropsch synthesis (FTS)⁴⁴.



RWGS is an endothermic, equilibrium-limited process that displays increasing conversion at higher temperatures. **Figure 1-6** shows the constant decrease and eventual sign change in the Gibbs free energy for RWGS reaction as a function of temperature. Therefore, thermodynamically, the RWGS is favored at high temperature, low water, and high hydrogen concentration⁴⁵.

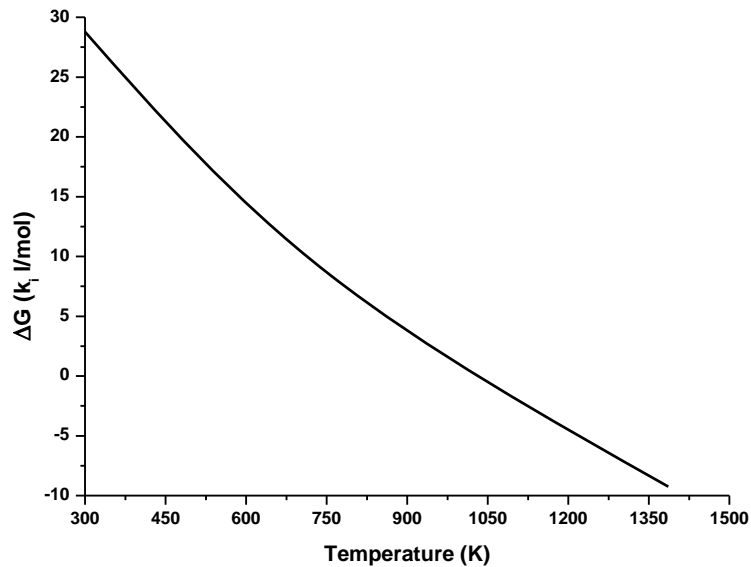


Figure 1-6. Variation of Gibbs free energy with reaction temperature⁴⁵.

1.2.2. Kinetics

The biggest problem with describing the kinetics of CO hydrogenation is the different pathways that the reaction could take (because of the complex mechanism) and the large number of species that are produced, making it difficult to obtain a general kinetic expression that explains the synthesis of all hydrocarbons.

Different kinetic models have been developed over the years and most of them operate within a narrow range of parameters. As an example, the following kinetic

equations are used for FT kinetics of iron-based catalysts⁴⁶:

$$-r = \frac{kP_{H_2}}{1 + ap_{H_2O}/P_{CO}} \quad (12)$$

This equation is mostly used when the WGS activity is low.

$$-r = \frac{kP_{H_2}}{1 + ap_{CO_2}/P_{CO}} \quad (13)$$

Equation 13 may be used at high WGS activity. The rate equation suggests that CO influence is rather more significant than that of H₂O under these conditions.

The work of Satterfield et al.⁴⁷ was centered on the fact that water constrains the FT synthesis rate more than CO₂ concentration does. So, the effect on the oxidation state produced by the H₂O amount present is more significant than the amount of CO₂. It was suggested that the inhibition attributed to CO₂ (shown in eq. 13), was actually produced by H₂O generated by the reverse WGS reaction. With this in mind, the rate equation 14 was favored⁴⁸:

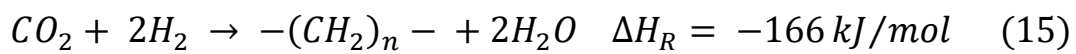
$$-r = \frac{KP_{H_2}}{1 + ap_{H_2O}/(P_{CO} * P_{H_2})} \quad (14)$$

Additionally, water gas shift (WGS) reaction has to be also taken into account (at least for iron-based catalysts) for kinetic models³⁹. WGS reaction can increase or decrease the FTS rate because these reactions share the same components, adsorption and desorption reactions, as well as, dissociation of H₂, H₂O, and CO₂.

In the case of CO₂ hydrogenation, CO intermediates can be produced through the reverse water gas shift (RWGS) reaction, followed by the FTS reaction. In the study presented by Willauer et al.⁴⁹, the RWGS reaction rate can reach 3.5 × 10⁵ s⁻¹ initially and decreases to 0.032 s⁻¹ within 2 s, while the FTS reaction rate is zero in the beginning and increases to 0.004 s⁻¹ at 18.7 s. So, the FT reaction is the rate

determining step caused by the considerable lower reaction rate. The major limiting of FT reaction while carrying out the CO₂ hydrogenation process is the reaction concerning the adsorbed CO and H₂ to form *HCO intermediates.

Lately the use of laser-generated Fe carbide catalysts proposed that the direct hydrogenation of carbon dioxide also contributed to hydrocarbon formation (eq. 15)⁵⁰. This reaction is recommended to progress via dissociative adsorption of CO₂ on the active catalyst phase by hydrogenation of the adsorbed carbon species.



Other study also evaluates the kinetics of the reverse water gas shift reaction⁵¹ (eq. 16). In contrast with the water gas shift process, this reaction is faster over different types of oxide and metallic catalysts with a lower activation energy¹³.

$$r_{SH_2} = K_{SH_2} \left(\frac{P_{CO_2} P_{H_2} - P_{CO} P_{H_2O} / K_{eq}}{P_{CO} + a_{SH_2, H_2O} + b_{SH_2, CO_2} P_{CO_2}} \right) \quad (16)$$

Despite several investigations addressed the study of CO₂ hydrogenation kinetics, there still existing major complications caused by the difficulty of the mechanism and the large amount of species involved.

1.2.3. Mechanism

1.2.3.1 Mechanism for CO hydrogenation

Catalytic conversion of synthesis gas (CO + H₂) into hydrocarbons, also known as Fischer-Tropsch Synthesis (FTS) is a complex reaction that can generate a wide variety of products such as paraffins, olefins, and oxygenates, including alcohols, ketones, aldehydes, and carboxylic acids. This is why most researchs are focused on controlling the selectivity of the reaction^{52,53,54,55}.

Since the actual mechanism of hydrocarbon formation is not fully understood, a

variety of mechanisms have been proposed during years of investigation. These mechanisms involve the following series of steps^{56,57}.

- a) Adsorption of reactants;
- b) Chain initiation;
- c) Chain growth;
- d) Chain termination;
- e) Desorption of products;
- f) Readsorption and secondary reactions.

Due to the complexity and wide range of FT products, it is generally assumed that several reaction pathways exist on the catalyst surface. Mechanisms among the most accepted are: surface carbide mechanism⁵⁸, hydrocarbene mechanism⁵⁹, and CO insertion mechanism⁶⁰.

Surface carbide mechanism: it is one of the most important mechanisms and the earliest proposed for the formation of hydrocarbons on Fe catalysts⁶¹. **Figure 1-7** displays a schematic representation of the initiation, growth, and termination of carbon chains. According to this mechanism, at the beginning, step 1 in **Figure 1-7**, CO and H₂ are adsorbed dissociatively. In a second step, the CH₂ species are formed from the dissociated reagents. Chain growth takes place by consecutive insertions of the monomer into the growing alkyl species, step 3. In the fourth step, the termination happens with α -elimination to form an α -olefin or with the addition of a CH₃⁺ or H⁺ species to form a paraffin⁵⁸.

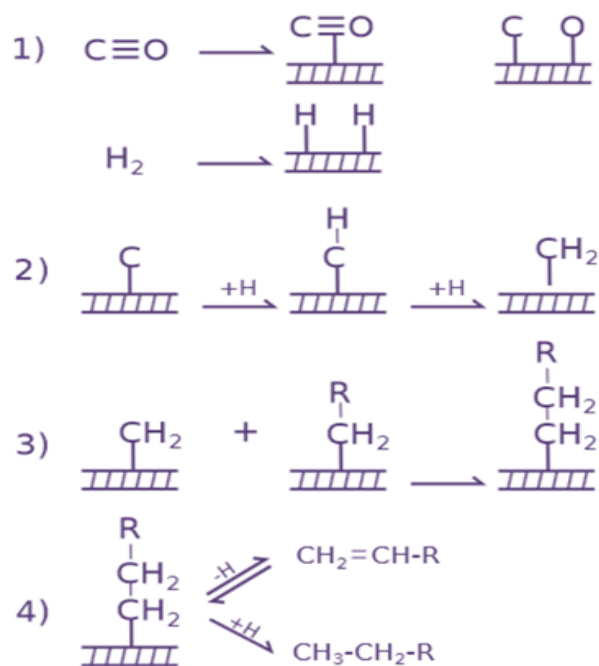


Figure 1-7. Carbide mechanism by insertion of methylene (CH_2)⁵⁸.

Reactions of the adsorbed oxygen and hydrogen give place to the elimination of water from the metal surface^{62,63}.

Hydrocarbene mechanism: this mechanism gained extensive acceptance during 1950s. This mechanism is based on the formation of H-CM-OH (hydrocarbene) intermediates (**Figure 1-8**) coming from CO reacting with adsorbed hydrogen. The condensation combined with water elimination allow the chain growth. The chain grows by the assistance of oxygenated surface intermediates^{64,48,65}. This mechanism was confirmed in the results published by Emmet et al⁶⁶.

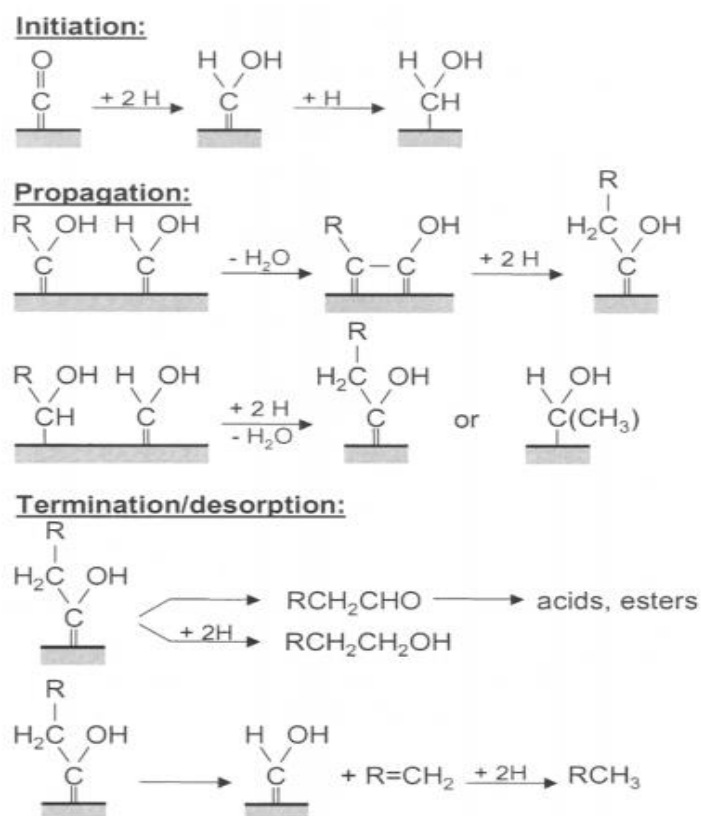


Figure 1-8. Mechanism of hydroxycarbene intermediates formation and chain growth pattern during FT synthesis⁶⁷.

CO insertion mechanism: Pichler and Schulz⁶⁸ proposed the CO insertion mechanism (**Figure 1-9**) to explain the formation of all typical FTS products (paraffins, olefins, and oxygenates). In this mechanism, chain growth takes place by CO coupling to an RCH₂ group, rather than by CH₂ coupling. Therefore, this mechanism does not need a high surface concentration of CH₂ groups to ensure fast chain growth relative to chain termination^{60,67}.

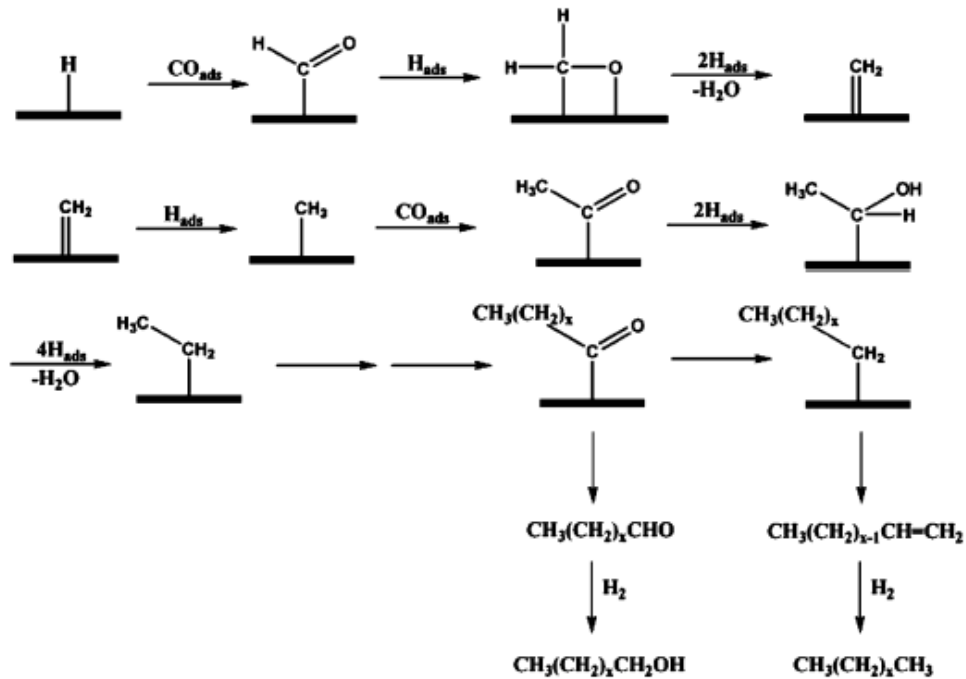


Figure 1-9. Mechanism of hydroxycarbene intermediates formation and chain growth pattern during FT synthesis⁶⁸.

Even though all mechanisms presented are able to explain some of the products obtained during FTS, opposing data exist for all of them⁵². Regardless the mechanism, it is known that the FT synthesis is a polymerization reaction which follows the Anderson, Schulz, and Flory (ASF) distribution^{69,70}. This is the most widely accepted and known model to describe the distribution of products by using the following equation:

$$W_n = n\alpha^{n-1}(1 - \alpha)^2 \quad (17)$$

Where W_n is the mass fraction by weight in the hydrocarbon product mixture with n carbon atoms, α is the probability of chain growth and $1 - \alpha$ is the probability of chain termination. This equation is represented graphically (**Figure 1-10**), where the variation of the percentage by weight of the different hydrocarbon fractions is plotted against the chain growth probability.

The desired chain growth probability (α) can, within limits, be changed by varying process parameters such as reaction temperature, H_2/CO ratio, and catalyst

composition. The strategies to break the ASF product distribution and to direct the reaction to a specific range of hydrocarbons remain a hot theme and one of the key challenges of CO hydrogenation¹

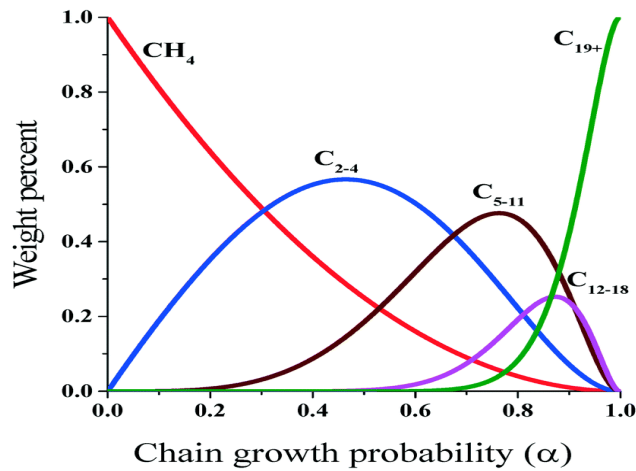


Figure 1-10. Hydrocarbon selectivity as function of the chain growth probability⁷¹.

1.2.3.2 Mechanism for CO₂ hydrogenation

It is suggested that the conversion of CO₂ takes place via a different reaction pathway compared to CO hydrogenation. In order to have a deeper understanding and clarify the difference in product distributions of CO and CO₂ hydrogenation, **Figure 1-11** shows a typical Anderson-Schulz-Flory (ASF) diagrams in terms of selectivity of total hydrocarbons for both processes⁷².

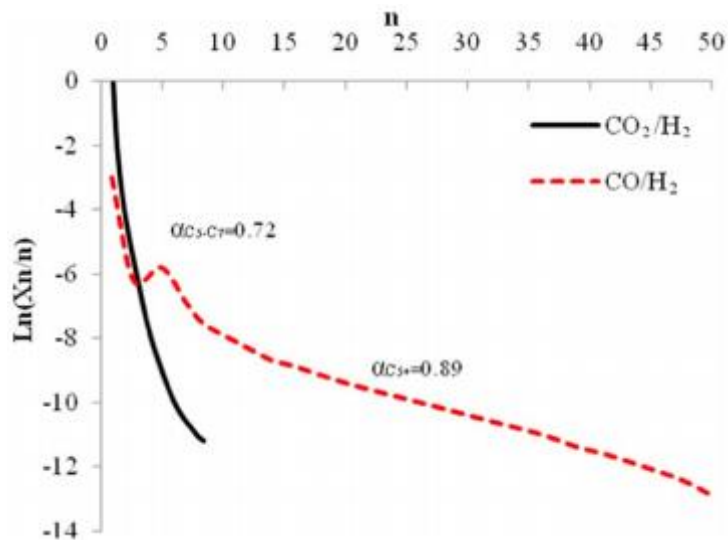


Figure 1-11. Hydrocarbons selectivity during CO and CO₂ hydrogenation⁷¹.

Clearly, CO₂ hydrogenation does not result in an ASF distribution comparable to classic FTS using CO and H₂. In general, it is known that the carbon to hydrogen ratio produced by hydrogenation of CO₂ is low because of the difficulty of adsorbing CO₂ on the surface of the catalyst mainly because of the high chemical and thermodynamic stability of CO₂. Enhancing the formation of methane with a decline in chain growth⁷³.

Investigations over the years have shown that carbon dioxide may be hydrogenated by direct or indirect routes (**Figure 1-12**). In the indirect route, CO₂ is transformed to methanol, which can be then converted into other more valuable hydrocarbons⁷⁴. Normally, the indirect routes are a combination of multi-stage process that can use separate reactors or single reactor employing multifunctional catalysts to perform the different conversions required⁷⁵. By contrast, in the direct route, CO₂ is converted to hydrocarbons throughout a modified FT process^{73,76,50}.

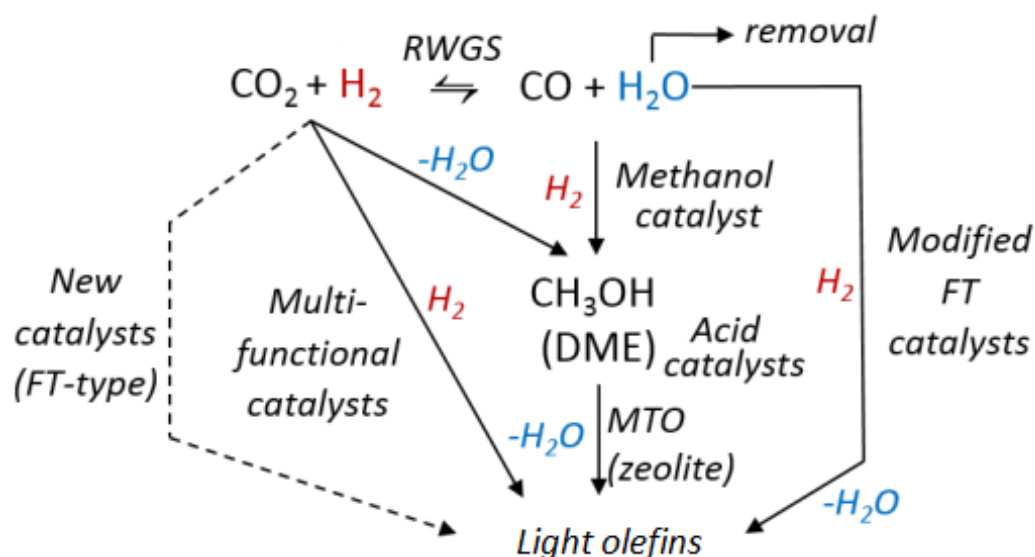
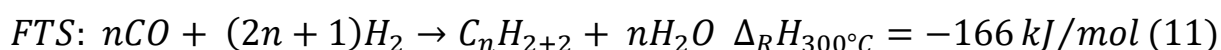


Figure 1-12. Possible routes for CO₂ hydrogenation⁷⁷.

So, in essence, catalytic hydrogenation of CO₂ process with the FTS route is the combination of two successive reactions taking place in the same reactor, reverse

water gas shift (eq. 9) reaction to generate CO, which subsequently reacts with hydrogen by FTS, producing mostly hydrocarbons, as described in the general FTS (eq. 11)⁴⁴.



1.2.4. Reaction conditions

FTS is usually carried out in two modes known as low temperature Fischer-Tropsch (LTFT) and high temperature Fischer-Tropsch (HTFT) synthesis (**Figure 1-13**). The former allows the syngas conversion using cobalt-based catalysts at temperatures of ~190-250 °C and pressures of 20–40 atm, correspondingly, with the goal of producing bigger carbon chains than those produced in HTFT, which normally comprises the use of iron-based catalysts at 350 °C and 10-20 atm^{78,79}.

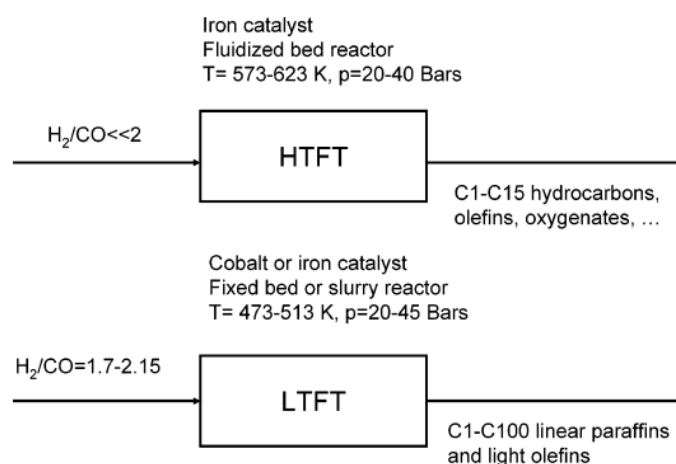


Figure 1-13. Hydrocarbons selectivity during CO and CO₂ hydrogenation⁷⁹.

For conducting the FTS with the different active metals (Fe, Co, Ni, and Ru) scientists rely on:

- The ability to adsorb carbon monoxide dissociatively at temperatures above 250 °C.

- Binding forces of the adsorbed species (M-C and M-O) are balanced in relation to the bond strength of carbon monoxide.
- Easy hydrogenation of surface species M-C and M-O.

1.2.5. Reactors

As CO hydrogenation is an exothermic process, the heat of reaction needs to be removed quickly so that avoiding a temperature increase which could result in undesired methane formation and catalyst deactivation, because of carbon deposition and sintering⁸⁰. In this order, there are three main types of reactors: fixed bed reactor, fluidized bed reactor, slurry phase reactor⁸¹ and microreactor.

Fixed bed reactors: the most common fixed bed reactor type is multi-tubular (**Figure 1-14**) with the catalyst placed inside the tubes and water flowing through the shell sides as cooling medium. These reactors are designed in a way that the catalyst be in close distance to the tube walls and at the same time that work at high gas space velocities, to assure turbulent flow, in these conditions the heat generated by the reaction is efficiently transferred to the cooling medium.

Multi-tubular reactors are usually not appropriate for high temperature operating conditions. In the case of iron based catalysts for example, at high temperature carbon deposition is almost inevitable⁸² and this can lead to catalyst swelling and obstruction of the reactor tubes. Large multi-tubular reactors may have thousands of tubes resulting in high priced building costs. Besides, the enormous weight of these reactors become a problem when thinking about their transportation, a reason why the size to which they can be scaled up is limited.

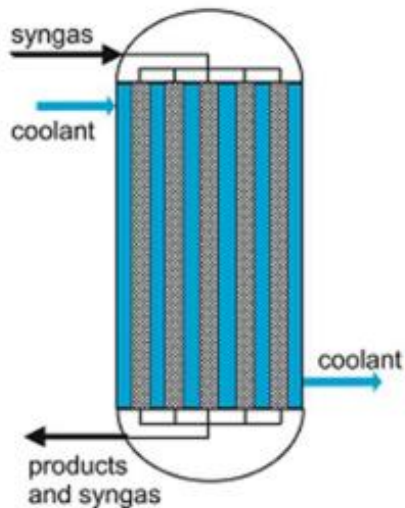


Figure 1-14. *Multi-tubular fixed bed reactor*⁸³.

However, not all are disadvantages, these reactors do present some features that makes them interesting for the industry. They can be easily operated. There is no need of extra equipment to separate the heavy hydrocarbons that could be produced since they just trickle down the bed and are recollected in a downstream knock-out pot^{84,85}.

Slurry bed reactor: in the past, the slurry reactor system (**Figure 1-15**) was believed the best way of producing heavy hydrocarbons using low temperature reaction conditions, since the catalyst would be suspended in the mixture of these generated hydrocarbons. Nevertheless, there was the necessity of separating the catalyst from the liquid product, problem that was not solved until 1990 by Sasol.

Derived from the research done in Sasolburg, the main benefits of the slurry phase reactor compare to the multi-tubular reactor are⁸⁶:

- The reactor cost is only one quarter of that of the alternative multi-tubular reactor with the identical capacity,
- Pressure drop in a slurry reactor is considerable less, normally 1 atm against 4 atm for a multi-tubular unit,

- Because of the insignificance of diffusion limitations, the catalyst loading per ton of product in slurry reactors is 25% of that used in fixed bed units,
- The slurry bed reactor can maintain a stable temperature better than a fixed-bed so it is possible to work at a higher average temperature resulting in enhanced reactant conversion, and
- The possibility of removing and adding catalyst on-line permits longer reactor runs at higher average conversions.

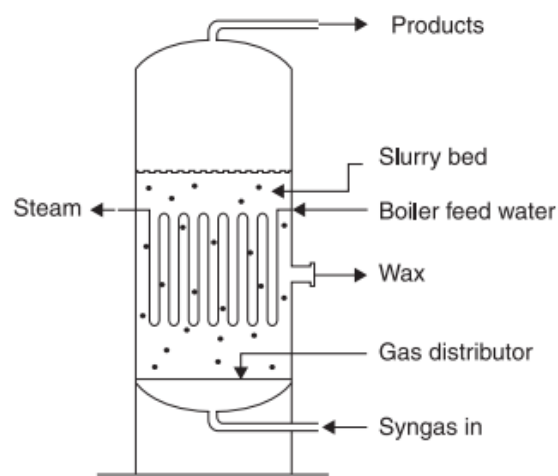


Figure 1-15. *Slurry phase reactor*⁸⁷.

Fluidized bed reactor: when light alkenes or gasoline production is desired using high temperature, fluidized bed reactors are normally the units selected. There are two types of fluidized bed reactors currently in commercial use (**Figure 1-16**), the turbulent or fixed fluidized bed (FFB) and the circulating fluidized bed (CFB)⁸⁸.

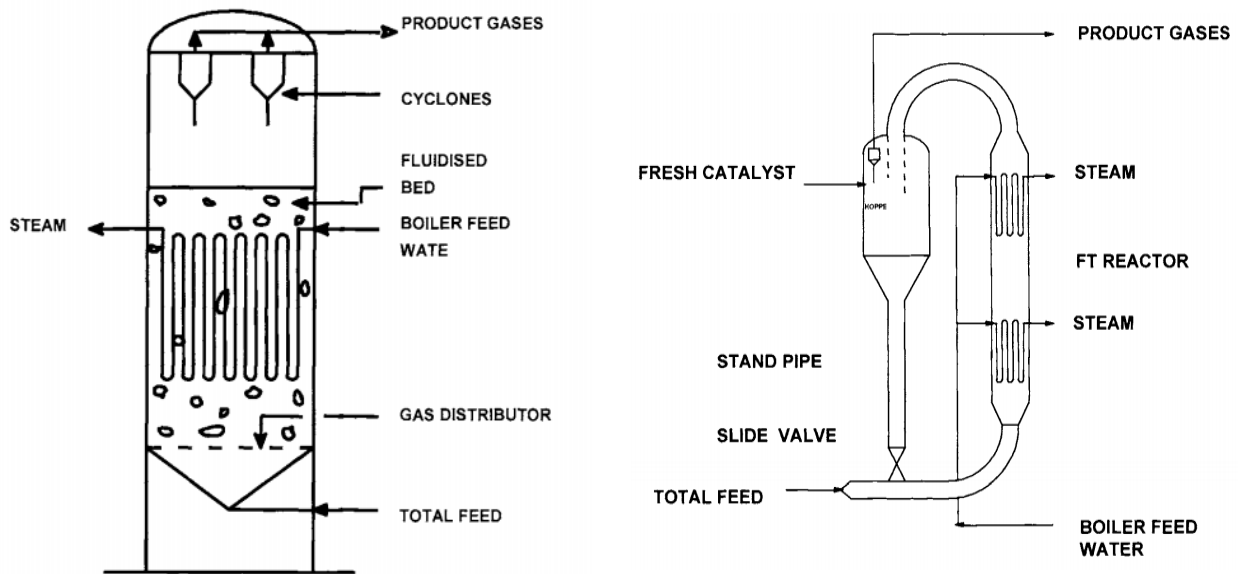


Figure 1-16. a) fixed fluidized bed (FFB) reactor and b) circulating fluidized bed (CFB) reactor⁸⁹.

The FFB type, also called, Sasol Advanced Synthol (SAS) reactors by the creators of this innovative technology. They present high heat exchange rates caused by the turbulence in fluidized beds. In other words, they can manage the big heat flow produced at high conversion levels with high feed gas throughputs that can be achieved at high operating temperatures. For this reason, there are only a few degrees of difference between the bottom and top temperature of the reactor. Also, these reactors permit to easily access to the catalyst since its particles are completely mixed with the gas or fluid, having the greatest possible surface area for reactions to occur. It is important, however, that process conditions are carefully controlled to limit the production of long chain hydrocarbons to avoid excessive liquid condensation in the pores of the catalyst. This condensation could generate de-fluidization of the catalyst bed and the unit would have to be stopped^{89,90}.

The main advantages of the SAS reactors versus the CFB reactors are:

- Building cost is 40% lower principally because the reactors are physically smaller,
- In CFB reactors only a portion of the catalyst charge participates in the reaction while in the SAS reactor all of the catalyst is involved. This results in higher conversions,
- The gas and catalyst linear velocities and the pressure drop across the reactor are much lower for the SAS reactors than the CFB's.

Another type of reactor that is gaining more consideration from both academic and industrial research community is **the microreactor**. This novel technology has brought new chances to intensify FTS processes. Microreactors consist of small parallel channels. The increment the specific surface area improves heat and mass transfers. This is why these reactors permit working at isothermal conditions in highly exothermic reactions. At a much lower cost, microreactors have better energy efficiency and reach an equal productivity compared with conventional reactors^{91,92}.

Several types of microreactors are available for FTS (**Figure 1-17**), including: reactors with microstructured catalyst (monolith), coated microchannel reactors, and micro- and mili-fixed bed reactors^{83,93}.

The main benefit of microreactors is their improved heat transfer capacity, which is frequently challenging in typical fixed bed centrimetric reactors. For other reactors, controlling the temperature becomes particularly difficult during the reactor start-up. Thanks to the improved heat transfer, catalysts with higher activity and better hydrocarbon productivities can be used in the microreactors⁸³.

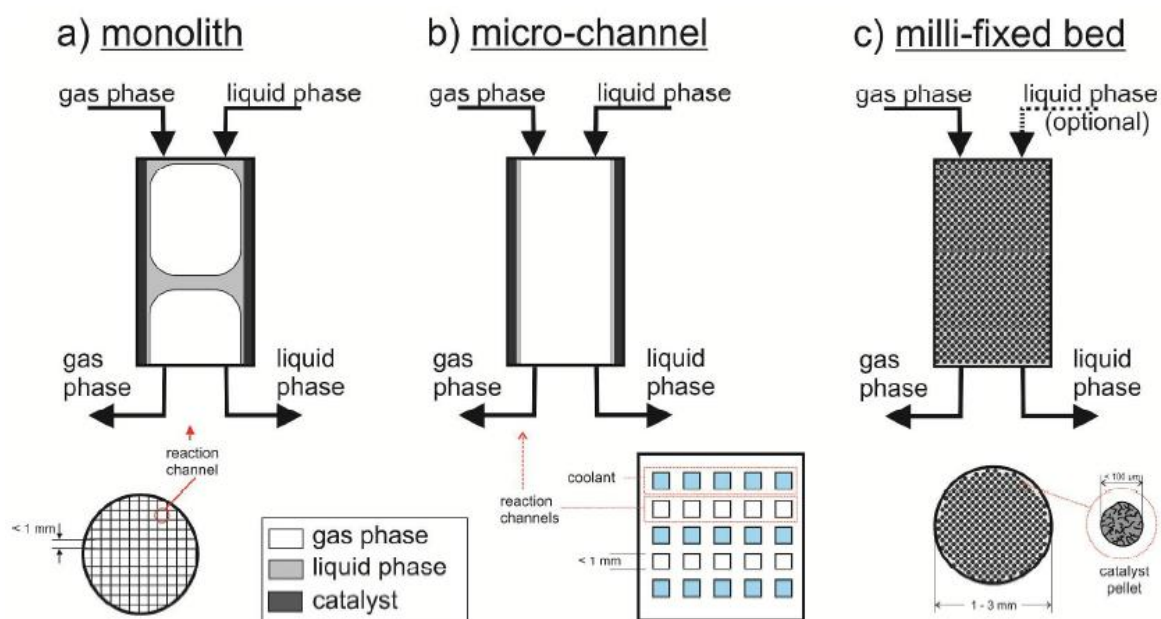


Figure 1-17. Microreactors for FTS: a) monolith microstructured catalyst reactor; b) microchannel reactor; c) milli-fixed bed reactor⁸³.

1.2.6. Catalysts for CO and CO₂ hydrogenation

Catalysts for FTS and CO₂ hydrogenation must be active, stable, and selective to the fraction of interest. Besides, they have to be highly available, resistant to mechanical stress, and low-priced. Therefore, the catalysts choice is one of the most important issues to take into account when designing new active catalysts.

Up to this time, the catalysts used for CO₂ hydrogenation to produce hydrocarbons are connected with those that are also employed for FTS such as Fe, Co, Ni, and Ru based-catalysts⁹⁴. Iron has been the most widely used metal as a catalyst because of its low cost compared to other active metals (**Table 1-2**). The activity of these metals towards both reactions is due to the fact that they can absorb CO, CO₂, and H₂ dissociatively. Nevertheless, numerous investigations have demonstrated that when supported Co, Ni, or Ru catalysts are used for CO₂ hydrogenation, methane is the major product while low or no C₂⁺ hydrocarbons are produced. Over iron catalyst

higher hydrocarbons can be obtained^{39,95,96,97}.

On the other hand, for CO hydrogenation, Fe-based catalysts show high selectivity towards oxygenates and branched hydrocarbons. Whereas, those promoted with alkali metals produce predominantly gasoline and α -olefins, in addition to presenting great hydrothermal stability when converting synthesis gas with high H₂/CO ratios^{98,99}.

Table 1-2. Relative cost of the catalysts⁷⁸

Metal	Price ratio
Fe	1 (base)
Ni	150
Co	500
Ru	144000

Cobalt catalysts offer better yields and stability for producing linear saturated hydrocarbons. The disadvantages of their use are the high price and high sensitivity to sulfur, which could easily contaminate them. However, the use of Co catalysts in FTS processes is viable for the production of high molecular weight and distillable products because their catalytic activity is not inhibited by the water resulting from the conversion of the synthesis gas at an industrial level¹⁰⁰.

Also, Ru is a very active metal for FTS, but its high cost compared to Co and Fe represents a great disadvantage. However, it is used in small amounts as a promoter to improve the performance of Co or Fe catalysts¹⁰¹. In general, in order to minimize the catalyst cost, different active metals mentioned above are dispersed over a porous support, such as: SiO₂, Al₂O₃, TiO₂, ZrO₂, etc⁹⁹.

Additionally, to these widely studied metals, molybdenum carbide and molybdenum sulfide base catalysts have been reported for conducting CO hydrogenation reactions. The former promoted with K₂CO₃ (Mo₂C/K₂CO₃) exhibits

selectivities of 50-70% to the C₂-C₅ olefins at CO conversions up to 70% at the same time that suppressed methane production, and show high activity to CO₂ production¹⁰². The latter, due to the high water-gas shift activity of the Mo₂S catalyst can convert carbon monoxide rich synthesis gas to mostly C₁-C₅ primary alcohols without installing a separate water-gas shift reactor. In addition, in sulfide form, the catalyst is naturally resistant to sulfur poisoning¹⁰³.

1.2.7 Light olefins synthesis

Light olefins (ethylene, propylene, and butylene), vital basic synthetic blocks in the chemical industry, are widely used to synthesize downstream products, such as paints, solvents, and polymers⁶¹. The traditional routes for producing light olefins by naphtha steam pyrolysis or fluid catalytic cracking of petroleum (FCC) involve low light olefins selectivity and high cost of raw feeds from petroleum¹⁰⁴.

In recent years great attention has been drawn to obtaining light olefins from one step conversion syngas¹⁰⁵. There are a number of possible routes for the conversion of syngas into lower olefins (**Figure 1-18**). Generally, these routes can be divided into two main groups: indirect and direct process.

Since selectivity is limited by Anderson–Schulz–Flory distribution, different indirect processes have been studied during the years¹⁰⁶. They include methanol synthesis, dimethyl ether or other intermediate products by using coal or biomass and then production of light olefins via C-C coupling or dehydration and cracking processes. These not direct processes have higher selectivity than the direct route. The challenges remain lower CO conversion and insufficient stability.

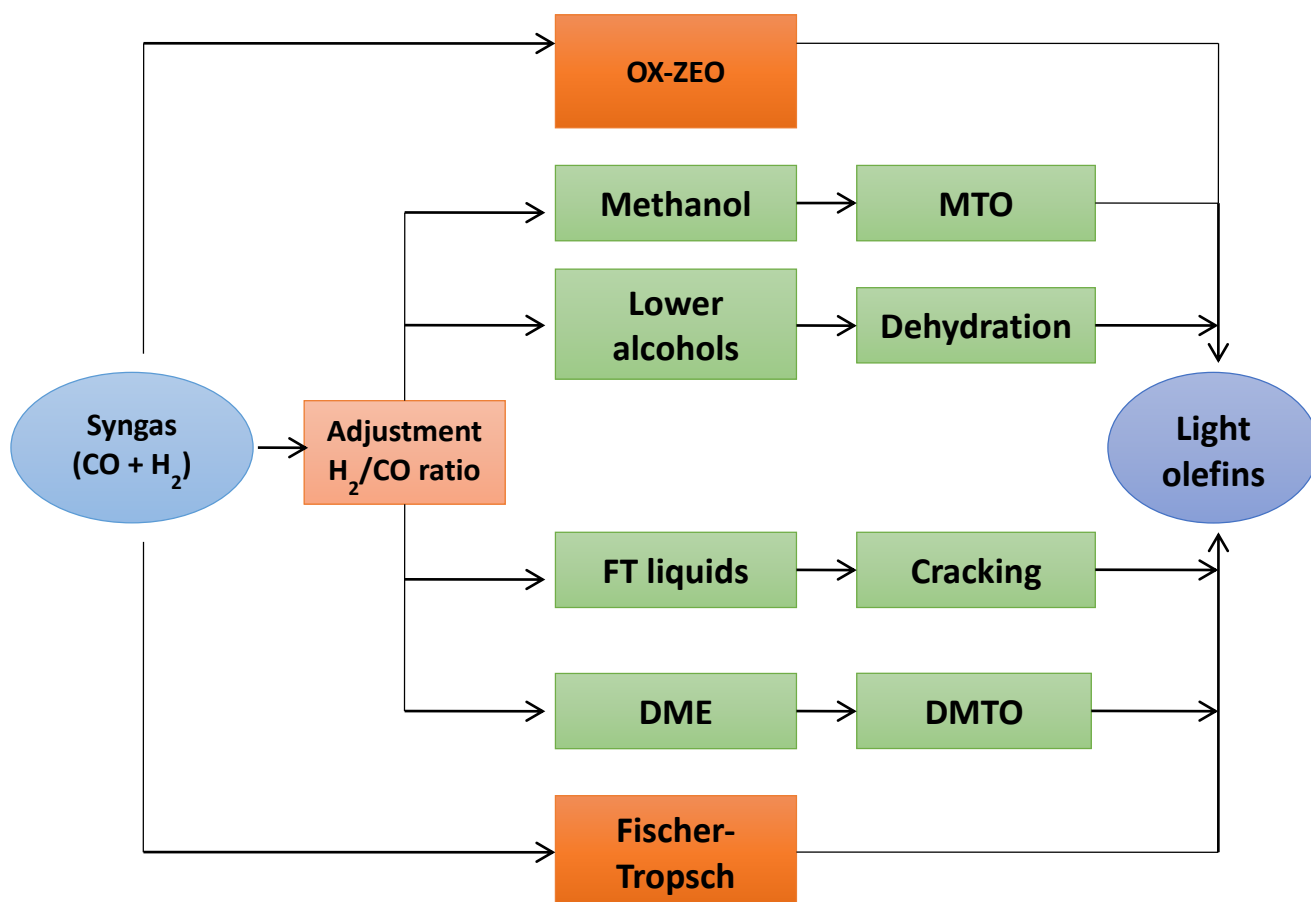


Figure 1-18. Processes for the transformation of synthesis gas into light olefins.⁶¹

In the direct process, light olefins can be generated directly from syngas via FTS and this route is known as FTO (Fischer-Tropsch to olefins). Industrial catalysts of Iron and cobalt are reasonably priced in such technology. Cobalt-based catalysts that have beneficial features like much activity and stability, low water–gas shift activity, and resistance to water are strongly studied due to these benefits^{61,78,79}. Even though, it is largely accepted that metallic Co generates mostly heavy hydrocarbons with high selectivity for C₅⁺ hydrocarbons^{79,107}. Zhong et al.¹⁰⁸ reported a Co-based FTO catalyst highly efficient for the selective conversion of syngas to lower olefins (~60%), with methane production about 5% at a CO conversion of ~32% at 250 °C over a Co₂C. Also, in several studies, the introduction of a promoter like Mn to Co catalyst

considerably increased the light olefins selectivity at the same time that methane selectivity decreased^{109,110}.

Qiao and co-workers studied the Fischer–Tropsch synthesis to lower olefins over a K modified Fe/rGO. They reported that selectivity to this fraction is, as high as, 68% attributing this performance to the favorable effect of potassium on the formation of Hägg carbide, one of the active phases for FTS (as discussed later). Another choice for syngas direct conversion to lower olefins is the use of bifunctional catalysts. Lately, different groups proposed the new OX-ZEO process, which is based on the combination of methanol synthesis and MTO on a single bifunctional catalyst constituted either by the Zn-Cr¹¹¹ or by Zr-Zn¹¹² and SAPO-34. They reported, C₂–C₄= selectivity up to 80% at carbon monoxide conversion of 17% and around 70% selectivity for C₂–C₄ olefins at about 10% CO conversion respectively. It is evident the selectivity of the OX-ZEO process towards lower olefins can be potentially higher than that of the conventional FT synthesis (around 60%). However, the challenges of this novel technology are related to achieve higher olefin yields (>10%) and improving catalyst stability at higher CO conversion levels.

Nowadays, in FTO, iron occupies an indispensable status not only due to its low cost and high water-gas shift activity but also for its high selectivity to lower olefins with low methane selectivity at the high reaction temperatures required by this process.

1.3. Iron catalysts for CO and CO₂ hydrogenation

1.3.1 Iron catalysts for CO hydrogenation

Iron has been for a long time the predominant FT catalyst for commercial use. From the early 1950s Sasol in South Africa uses it to produce fuel and commodity chemicals such as wax. The benefit of this technology is that the product spectrum can

be manipulated either via process conditions or choice of catalyst system to yield a range of high value products (olefins, waxes, liquid hydrocarbon fuels, etc.)¹¹³. Some general characteristics of iron-based catalysts are:

- The FT-regime with iron may be stable over a wide range of temperature⁸⁹,
- When reducing the CO partial pressure to very low values, the selectivity may be merely affected⁸⁹,
- With iron, H₂O inhibits the FT reaction and restricts the conversion⁴⁰,
- Alkali and copper are essential promoters for FT synthesis on iron giving positive effects on the reaction rate, selectivity, and catalyst stability¹¹⁴,
- The water–gas-shift and reverse reactions generally proceed rapidly on iron catalysts⁴⁰, and
- Processes of self-organization and restructuring of the catalyst occur. This concerns the reaction between the metal and carbon, which is formed by CO dissociation to produce iron carbide phases in addition to further compositional changes¹¹⁵.

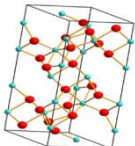
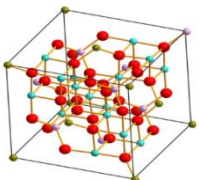
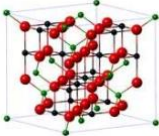
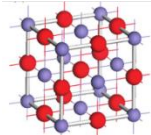
1.3.1.1 Active phases and promoters

During activation and FTS reaction using iron-based catalyst, the carburization process unavoidably results in the generation of metallic Fe, iron oxides, and iron carbides¹¹⁶. Metallic iron has been found in small amounts in the used iron catalysts and sometimes thought to be the active phase (as in similarity to the metallic cobalt, ruthenium, or nickel Fischer–Tropsch catalysts)^{46,86}.

Iron can be present in the form of several oxides, specifically hematite (α -Fe₂O₃), maghemite (γ -Fe₂O₃), magnetite (Fe₃O₄), and wüstite (FeO)¹¹⁷. Iron oxides have been

used as important precursors for the FT catalysts and during FTS itself. Some general characteristics are shown in **Table 1-3**.

Table 1-3. Iron oxide phases

<i>Formula</i>	<i>Name</i>	<i>Crystal system</i>	<i>Type of magnetism</i>
$\alpha\text{-Fe}_2\text{O}_3$	hematite	Trigonal 	Weakly ferromagnetic or antiferromagnetic
$\gamma\text{-Fe}_2\text{O}_3$	maghemite	Cubic or trigonal 	Ferrimagnetic
Fe_3O_4	magnetite	Cubic 	Ferrimagnetic
FeO	wüstite	Cubic 	antiferromagnetic

Iron oxide in the form of magnetite plays an important role. Given that magnetite co-exists with other iron phases during FTS, it can be decisive in the general activity and selectivity of the catalyst¹¹⁸. Besides of this, magnetite is also the phase responsible for the WGS activity of iron-based FT catalysts. This was demonstrated by Rhodes et al.¹¹⁹ using Mössbauer spectroscopy and isotopic labelling showing that the redox couple ($\text{Fe}^{2+}/\text{Fe}^{3+}$) in iron oxide is highly labile and capable of dissociating water

readily, possessing singular and well suited properties to operate as a WGS redox catalyst.

Regarding iron carbides, in spite of the disagreement concerning the actual nature of the active phases, a correlation between the carbide content and the Fischer–Tropsch activity has been extensively observed^{11,120,121}. Two models have been proposed to explain the role of the carbide phase. On the one hand, the carbide model¹²² suggests that FTS takes place in the surface of a bulk iron carbide phase; being the density of such sites dependent on the extent of the bulk carburization. On the other hand, the competition model¹²³ proposes that one or more carbon atoms together with metallic iron form the active site at which the carbon atoms are hydrogenated. It ought to be noted that on either model, Fe carbide generation is an essential step to yield the actual FTS catalyst.

In literature it is possible to find different carbide phases associated with FTS. Among them: ϵ -Fe₂C, ϵ -Fe_{2.2}C, Fe₇C₃, χ -Fe₅C₂, and θ -Fe₃C. Nevertheless, usually, the monoclinic Hägg carbide (χ -Fe₅C₂) and hexagonal closed packed carbide (ϵ -Fe_{2.2}C) are the principal carbide phases found¹¹⁵. However, despite all the available methods, such as magnetic measurements, X-ray diffraction, or Mössbauer spectroscopy the exact mechanism for the production of hydrocarbons over iron carbide phases is still a matter of study¹²⁰.

In order to improve the production of the wanted hydrocarbons, different elements can be used as promoters to adapt and optimize the product distribution. Electronic and structural promoters have been intensively employed to improve iron dispersion, degree of iron carbidization, FT reaction rates, and light olefin selectivity over Fe-based catalysts. Introduction of efficient promoting metals could affect iron

dispersion, iron carbidisation, electronic properties of the active species, inhibition of catalyst deactivation, and rate of primary and secondary elementary steps of FT synthesis¹²⁴.

In recent years, investigations around the world have been dedicated to study the promotion of iron catalysts with alkali metals^{125,126,127,128} and copper^{60,129,130}. The former group, leads to lower methane selectivity, higher activity, and a significant increase in the olefin-to-paraffin ratio and water-gas shift (WGS) activity. Justifications for this improved activity/selectivity are frequently given in terms of the basicity of the alkali promoter, which is suggested to cause an increase in the heat of CO adsorption on the catalytic surface, thus increasing the C/H ratio on the surface thanks to increased CO bond scission rates^{126,127,131}. The latter has been reported to decrease the temperature required for reduction of iron oxides while the product distributions do not change appreciably when copper is incorporated into an iron catalyst¹²⁵.

Recently, in our group, we have discovered^{132,133,134,135} a new kind of promoters (namely soldering metals). Our results show that the catalytic behavior of iron catalysts can be considerably improved by using bismuth or lead as promoters at the same time the reaction rate is increased several times. These results are attributed to the migration and close contact of the promoters to iron carbides that could help to facilitate CO dissociation via oxygen removal from iron carbide by scavenging (**Figure 1-19**), and by the enhancement of iron carbidisation and reducibility.

It is important to mention that a comparison between iron catalysts promoted with different elements is not easy since the use of different supports, promoter load, preparation methods, and activation procedures increase the complexity of the studies

together with the possibility that the rate of several FT elementary steps could be affected.

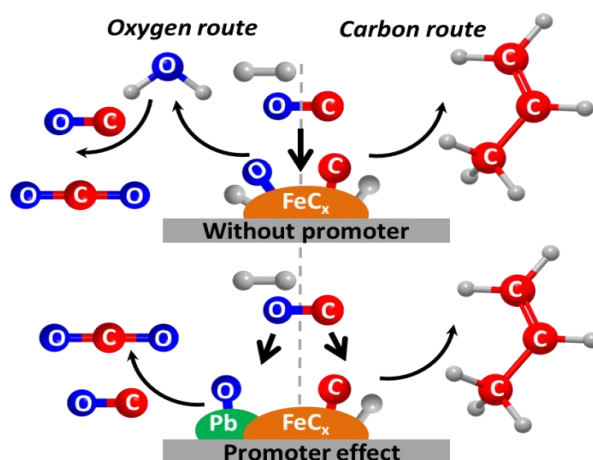


Figure 1-19. Effect of promotion with soldering atoms on FT synthesis¹³².

1.3.1.2 Bulk and Supported catalysts

Traditionally, bulk iron catalysts have been used for FT synthesis. Normally, these precipitated or fused catalysts are improved by adding promoters to enhance the selectivity to lower hydrocarbons (light olefins) and to reduce the amount of methane produced¹³⁶. Several studies have shown catalysts with high selectivity to C₂-C₄ olefins and to short-chain hydrocarbons. However, these catalysts are known to undergo attrition during exposure to synthesis gas at elevated temperatures¹³⁷.

It is well known that the bulk iron oxide is converted to carbides under typical FT reaction conditions. When Fe₂O₃ is used as a catalyst, it transforms into a complex mixture of iron oxide and iron carbides under reaction conditions^{47,138}, which are considered as a catalytic active phase.

During the last years, the research interests have shifted from bulk to supported iron FT catalysts. Currently, there is a growing attention in studying the structural, electronic, and chemical properties of supported catalyst systems that are of

significance in many industrial processes. The support texture and surface acidity have important influence on active metal dispersion, reducibility, catalytic performance, as well as, the interaction between metal and support. Conventionally, the oxide supports commonly employed in FTS are silica (SiO_2)¹³², alumina (Al_2O_3)¹³⁹ and titania (TiO_2)¹⁴⁰. Magnesia (MgO) and zinc oxide (ZnO) are also reported, but less frequently^{141,142}.

Bunches of investigation on iron-based catalysts dispersed on several supports have been conducted over the years and the product selectivities are deeply dependent on the supporting material. Supported iron catalysts show improved dispersion of the catalytically active phase and could resist the mechanical degradation that threatens bulk iron catalysts (**Figure 1-20**). Normally, what the employment of these supports seeks is to stabilize the active particles to avoid sintering during the reaction. Usually, alumina shows the best results in avoiding sintering, since it might impede sintering because of a stronger metal-support interaction, followed by silica and titania. In literature is possible to find that iron catalysts present a better activity when the particles are dispersed on alumina with low surface area than when they are dispersed on high surface area alumina. These results pointed out to a crucial feature of supported iron catalysts, that is to say, when there is a strong interaction iron oxide-support the formation of the active iron carbide is hindered^{121,143}.

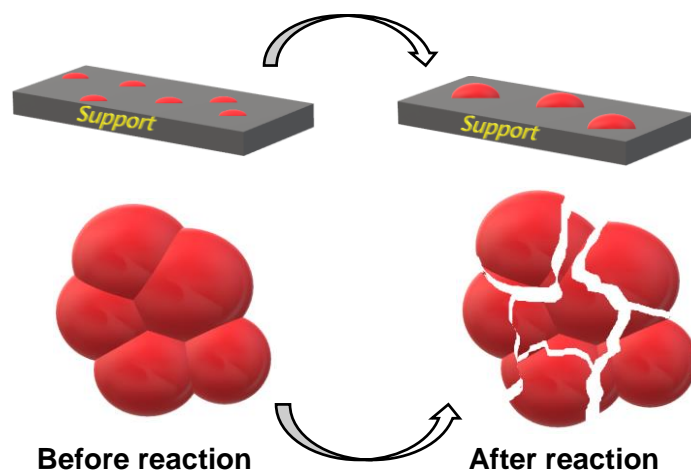


Figure 1-20. Stabilization of iron supported nanoparticles vs bulk iron catalyst.

Silica supported iron-based catalysts have been a matter of study in FTS process over the years. Such catalyst materials possess outstanding catalytic performances, for instance high attrition assistance and excellent stability. Nevertheless, the addition of silica also restrains the reducibility and catalyst activity caused by the variations in surface structure and interaction between iron and silica^{59,144}.

Zeolites have also attracted a lot of attention for FT synthesis. They present surface characteristics of pore structures and inner electric fields, giving place to different catalytic behaviors. The acidity of zeolites has allowed the development of efficient bifunctional or modified FT catalysts that could be useful in the production of iso-paraffins or aromatics in the gasoline range^{145,146}.

Lately, carbon nanotubes (CNT) have emerged as another type promising supports for FT synthesis. CNT utilization as possible catalytic support for iron FT catalysts brings some significant benefits. Carbon does not generate inactive mixed compounds between iron and support, like happens with SiO₂ or Al₂O₃, which, normally, are hard to reduce and to carbidize during the catalyst activation and reaction. In addition, the CNT-supported catalysts have been shown to be stable in FT reactions. Another attractive feature of these carbon materials is that a high dispersion of supported metal can be achieved. Thus, these catalysts usually exhibit higher CO conversion rates^{127,133,147}.

Generally, materials used as supports for FTS with a clearly defined structure have generated new opportunities for improving the catalytic properties (selectivity, stability, and activity).

1.3.1.3 Role of catalyst activation

The group VIII metals (Co, Ni, Ru, Fe) which are the most common FTS catalysts are usually synthesized in the form of a metal oxide. As a result, these catalysts have to be pre-treated in order to develop activity in FTS. Co, Ni, and Ru are generally activated in flowing H₂ at temperatures from 200 °C to 450 °C and remain as metals during the reaction process. Nonetheless, the activation procedure is not so evident in the case of iron catalysts¹²¹.

It is well-known that depending on the activation procedure employed for iron-based FTS catalysts, one could obtain an important effect on the catalyst activity and selectivity. Over the years, the influence of activation with different streams like H₂, CO, or syngas on surface species over iron-based catalysts has been investigated. These investigations demonstrated that mainly Hägg carbide species were generated when performing activation under CO resulting into greater FTS activity^{11,122}. Additionally, the nature of the different iron species generated during the activation hinges on the time on stream to the reactant feed, the composition of the feed, and the pretreatment conditions (temperature and pressure)¹⁴⁸. On the other hand, in hydrogen, the reduction of iron leads to the zero-valent state. These catalysts could lead to production of more gaseous hydrocarbons and less high molecular weight hydrocarbons¹⁴⁹. When syngas activation is performed, there is a correlation between the hydrogen partial pressure in the activation gas and the initial FTS activity. O'Brien et al.¹¹ discovered that when high partial pressures of hydrogen are present in the gas mixture used for activation, water hinders the catalyst reduction to active iron carbide phases and only fairly active magnetite (Fe₃O₄) is formed.

In addition, the temperature of the syngas pretreatment is vital to achieve high activity and selectivity. Normally, it has been claimed that excessively high a

temperature will generate extra carbonization while low temperatures will inhibit catalyst activation¹¹.

One major challenge of iron-based catalysts activation is the use of pure carbon monoxide as an activation gas. CO use is suitable for small laboratory reactors; nevertheless, it is high-priced for a pilot plant. As a consequence, it is easier operationally and economically affordable to be capable of activating the catalysts in situ using the identical syngas as employed during the reaction. This eliminates the need for a pure carbon monoxide stream.

1.3.1.4. Light olefin selectivity

Over the years, iron-based catalysts have widely been studied for FTO because of their low price and high water-gas-shift activity, which can adjust the H₂/CO ratio in syngas produced from gasification of plastics, biomass, or coal. Additionally, compared to other FT catalysts, (Co and Ru catalysts), it is known that Fe has a better resistance to the contaminants that could be present in syngas (sulfur, nitrogen, and chlorine compounds)¹⁵⁰.

Cheng et al. synthesized Fe nanoparticles confined in pod-like carbon nanotubes (Pod-Fe). Results suggest that the Pod-Fe catalysts have good selectivity towards light olefins (up to 45%) and excellent anti-sintering performance, particularly at high temperature. In addition, this performance was superior to a supported Fe-based catalyst because the Fe particles in Pod-Fe were well protected by the carbon shells providing a rational way to enhance the activity and stability of Fe-based catalysts.

In recent times, the team of de Jong^{151,136,152} and Sasol researchers¹¹³ claimed that simultaneous impregnation of sodium and sulfur can change the hydrocarbon

selectivity. These investigations have demonstrated that for Fe-based catalysts impregnated over α -Al₂O₃, low loads of sulfur and sodium enhance activity of these catalysts, reduce selectivity towards methane, increase the chain growth probability, and improve olefin selectivity (being close to 60%), at the same time that reduction, and carbidization of iron species are enhanced. Also, they showed that the impact of these elements is related to promoter concentration, pretreatment, and conditions employed.

Bang et al.¹³⁴ prepared nanoconfined iron catalysts using carbon nanotubes as support and promoted them with Bi and Pb. The results show an extraordinary selectivity to the light olefins fraction (~60%) at high CO conversion levels (around 40%). They noted that nanoconfinement helped controlling the migration of the different promoters by containing the promoters inside the CNT and consequently facilitating their interaction with iron particles, which is critical for achieving enhanced catalytic performance in high temperature FT synthesis.

Even though important advances have been achieved for the FTO route, the selectivity to C₂–C₄ hydrocarbons is still limited to ~60% because of the intrinsic mechanism of FT synthesis that follows the ASF distribution¹⁵³. Nowadays, this limitation represents one of the biggest challenges that FTO process faces with.

1.3.2 Iron catalysts for CO₂ hydrogenation

Hydrocarbons production using CO₂ hydrogenation reaction is basically a variation of the classical Fischer–Tropsch synthesis, where the starting gas is CO₂ instead of CO. Because of this, the catalyst formulation for this reaction is similar to that for CO hydrogenation nonetheless this formulation needs to be adjusted to take full advantage of the catalyst during the hydrocarbons production. In literature is stated

that CO₂ can be successfully hydrogenated to hydrocarbons using direct or indirect routes. On one hand, the direct CO₂ hydrogenation (also called CO₂-Fischer-Tropsch) comprises the combination of two processes: a) reduction of carbon dioxide to carbon monoxide by means of the reverse water-gas shift (RWGS) reaction, b) hydrogenation of CO to hydrocarbons via FTS.

1.3.2.1 Active phases, promoters, selectivity, and supports

As mention previously, due to their remarkable capacity to catalyze both RWGS and FTS reactions (**Figure 1-21**), iron-based catalysts continue as the chosen catalysts for successfully conduct CO₂-FT process¹⁵⁴.

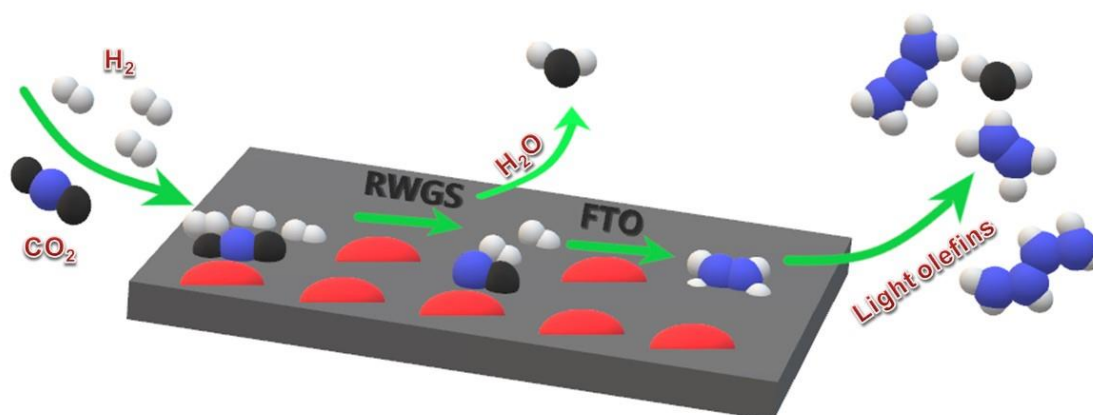
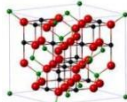
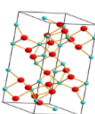
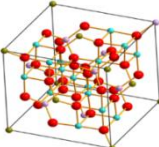


Figure 1-21. Representation of CO₂ hydrogenation to lower olefins.

Riedel et al.¹²⁰ claimed that the iron phases (**Table 1-4**) in the non-reduced catalyst comprise mostly α -Fe and Fe₃O₄. During time, magnetite and hematite phases are consumed and a new, most probable oxidic, iron phase is generated, which seems to be the responsible for the activity in the RWGS reaction. Finally, they claimed that FT activity starts by the formation of Hägg carbide (χ -Fe₅C₂) by the reaction of iron with carbon coming from CO dissociation.

Table 1-4. Iron oxide phases involved during CO₂ hydrogenation process

Formula	Name	Crystal system	Type of magnetism
$\alpha\text{-Fe}$	Ferrite	Cubic 	Ferrimagnetic
Fe_3O_4	Magnetite	Cubic 	Ferrimagnetic
$\alpha\text{-Fe}_2\text{O}_3$	Hematite	Trigonal 	Weakly ferromagnetic or antiferromagnetic
$\gamma\text{-Fe}_2\text{O}_3$	Maghemite	Cubic or trigonal 	Ferrimagnetic

In order to activate the CO₂ molecules, it is crucial to modify the surface basicity to enhance the adsorption ability towards CO₂. In this point, the impact of impregnating several rare earth and transition metals on catalytic properties in CO₂ hydrogenation has been widely studied in the last years.

Wang et al.¹⁵⁵ added alkali metal ions to Fe/ZrO₂ catalysts. They found that these metals (except Li) considerably reduced the selectivities to methane and lower paraffins at the same time that improved the selectivity to light olefins and C₅⁺ hydrocarbons, predominantly C₅⁺ olefins. Additionally, they established that the impregnation with Na, K, or Cs enhanced the CO₂ conversion as well. Additionally, the most promising results for lower olefin synthesis was achieved over the K-modified Fe/ZrO₂ catalyst. This better performance of potassium promoted catalysts was explained suggesting that K speeds up the Hägg carbide formation.

Other studied metal is manganese. Mn can act as both electronic modifier for iron-based catalysts and structural promoter. It is claimed that addition of Mn increases the ratio of olefin/paraffin in CO₂ hydrogenation at the same time that restrains the formation of CH₄^{44,156}. In addition, investigations have shown that manganese benefits the carburization, dispersion, and reduction of iron oxides, at the same time that significantly improves surface basicity of the catalyst¹⁵⁷. Nevertheless, a load excess of Mn reduces the promotional effect⁴⁴.

In previous works different approaches have been used to enhance the yield of higher hydrocarbons. One of these viable strategies is the application of bimetallic synergy. Satthawong and coworkers¹⁵⁸ performed screening experiments over Fe-M/Al₂O₃ (M = Co, Ni, Cu, and Pd) catalysts. The mixture of Fe with Co, Cu, or Pd generate a significant enhancement of chain-growth probability and interesting bimetallic promoting result on C₂⁺ hydrocarbon formation, while the Fe–Ni catalysts, on the contrary, selectively produced CH₄. Fascinatingly, the combination of Fe and Co, Cu, or Pd produced a strong synergetic effect and close proximity that could be seen by the improvement of the catalyst activity in comparison with their monometallic counterparts.

Supporting a metal catalyst over a porous support can enhance metal dispersion. Wang et al.¹⁵⁵ performed a numerous amount of experiments on catalysts synthesized using a wide variety of supports, including SiO₂, Al₂O₃, TiO₂, ZrO₂, mesoporous carbon, and carbon nanotubes, obtaining the best light olefins selectivity on ZrO₂ and TiO₂ supported catalysts (46% and 43% respectively).

Chew et al¹⁶³. synthesized iron-based catalysts using N-doped CNTs as support, for comparison O-doped CNT- and SiO₂-supported catalysts were also

prepared. As a result of a proper metal–support interaction The use of NCNTs considerably improved the iron dispersion and reducibility. In contrast, the O-doped SiO₂ support resulted in extremely strong interaction iron-support, the reason why the reducibility of Fe species was negatively affected.

Another studied support in CO₂ hydrogenation is ceria (CeO₂). Murciano et al. prepared Fe catalysts by using ceria with different morphological properties. Results showed that the addition of promoters is not the only factor that can alter Fe-based catalysts, it is also having an effect the features on the structure of the ceria support. Among the different ceria materials used, the one presenting cubic morphology facilitated the reducibility of Fe species. This result was supported by the shift the initial reduction temperature towards lower temperatures, giving place to a highest olefin/paraffin ratio compared to rod-type and nanoparticle-type ceria.

Zeolites is another example showing that the product distributions are deeply dependent on supporting materials¹⁵⁹. Zeolites are highly active in the oligomerization, aromatization, and isomerization of hydrocarbons. The use of an Fe-based CO₂-FT catalyst together with a zeolite into a multifunctional catalyst can change the product selectivity towards high-octane gasoline-range, isoparaffins, and aromatics¹⁵⁴. For instance, a study focused on zeolite effect on catalytic activity to obtain isoalkanes from CO₂ hydrogenation was performed using Fe–Zn–Zr/zeolite catalysts¹⁶⁰. They found that zeolite is an interesting support for synthesis of this fraction because of medium and strong acid sites present in zeolite.

Iron based-catalysts has not only provided an efficient methodology for syngas conversion to different products but also stimulated the hydrogenation of CO₂ to high-value chemicals, which has now become a hot research field. Obtaining high

selectivity of C₂₊ products involving C-C bond formation is still a challenging task in the CO₂ hydrogenation. Some suitable catalysts for hydrogenation of CO₂ are shown in

Table 1-5.

Table 1-5. Some suitable catalysts for hydrogenation of CO₂

Catalyst	Reaction conditions			CO ₂ conv (%)	CO select. (%)	Product selectivity (%)				Ref
	H ₂ /CO ₂	T (°C)	P (bar)			CH ₄	C ⁰ ₂₋₄	C ⁼ ₂₋₄	C ₅₊	
Fe/ZrO ₂	3	340	20	32	25	70	0.1	29	0.9	155
FeNa/ZrO ₂	3	340	20	39	21	21	8.8	49	15	155
FeK/ZrO ₂	3	340	20	43	15	18	9.2	44	19	155
FeRb/ZrO ₂	3	340	20	31	15	19	8.0	43	19	155
FeCs/ZrO ₂	3	340	20	39	16	26	9.6	43	14	155
FeCo/K/Al ₂ O ₃	3	300	11	31	18	13	NR	69*	NR	158
20%Fe/SiO ₂	1	220	1	6	NR	57	NR	32	13	116
K-Fe15	3	300	5	45	12	17	6	37	33	161
Fe-Zn-K	3	320	5	51	6	35	8	54	4	162

NR= not reported; *Including alcohols

1.3.2.2 Catalyst activation for CO₂ Hydrogenation

Since CO₂ hydrogenation using iron catalysts is similar to FT synthesis, activation of these catalysts for CO₂ hydrogenation have not been specially studied in literature. On the one hand, Visconti et al.¹⁶¹ synthesized a high surface area K-promoted iron-based catalyst. It was found that activation treatment using CO/H₂ mixtures at 350 °C allowed to obtain highly active catalysts in the CO₂ hydrogenation to lower olefins (about 37%) at mild process conditions (300 °C and 5 barg). On the other hand, Wang et al.¹⁵⁵ activated Fe/ZrO₂ catalysts promoted with different alkali metals using an H₂ flow rate of 50 mL min⁻¹ at 400 °C for 5 h. They reported high CO₂ conversions (up to 43%) with high selectivity to light olefins (about 44%), while methane selectivity was limited to less than 20%.

In another study, Shafer et al.¹⁶³ activated iron catalysts promoted with K, Rb, and Cs using CO at 270 °C for 24 h and evaluated the performance of these catalysts

for carbon dioxide hydrogenation. They reported a CO₂ conversion around 20% with the high selectivity to C₂-C₄ fraction (50% olefins and paraffins). However, they also reported a high selectivity to methane (40%).

1.4. Catalyst deactivation

In catalytic processes, the continuous deactivation of catalysts is one of the principal financial problems, and understanding how stability could be improved is as important as controlling their activity and selectivity. Since the main portion of the production at Sasol has been carried out with the high temperature catalysis and because of important early operating problems due to catalyst deactivation, much of the current understanding of this subject has been developed from the high temperature studies.

1.4.1 Catalyst deactivation during CO hydrogenation

Catalysts deactivation causes an important impact on the economic benefits that certain catalysts could generate. This is why researchers are paying more attention to the main causes of the loss of catalytic activity for iron-based FTS catalysts. Four central mechanisms of deactivation are addressed by the researchers:

- The first one proposes that active iron phases are converted to less active or completely inactive phases. For example, investigations reported that the active iron carbide phase is progressively oxidized to magnetite (Fe₃O₄), which has no activity in FTS^{82,149,164}. Other studies have claimed that there exists transformation of one type of iron carbide species to another less active in FTS. For this case, the intrinsic activity of iron carbide phases is supposed to be essentially different^{165,166}.

- The second mechanism suggests that deactivation is originated by coke formation on the catalyst surface, in that way restraining the contact between reactant gases and the catalytically active phase^{118,123,167}.
- Sintering is one of the major reasons for the Fe-based catalyst deactivation in FT reaction. It causes important decline of the performance of a catalytic system due to: (a) the reduction in specific surface area and therefore the number of active sites; (b) the reduction in contribution from low-coordination atoms at edges and corners; and (c) the variation of electronic structure, which can give place to different adsorption and/or desorption energy barriers for the reaction intermediates and thus different reaction pathways^{82,166,168}. Generally, the sintering of a catalyst can take place through two different pathways (shown in **Figure 1-22**): coalescence and Ostwald ripening¹⁶⁹.

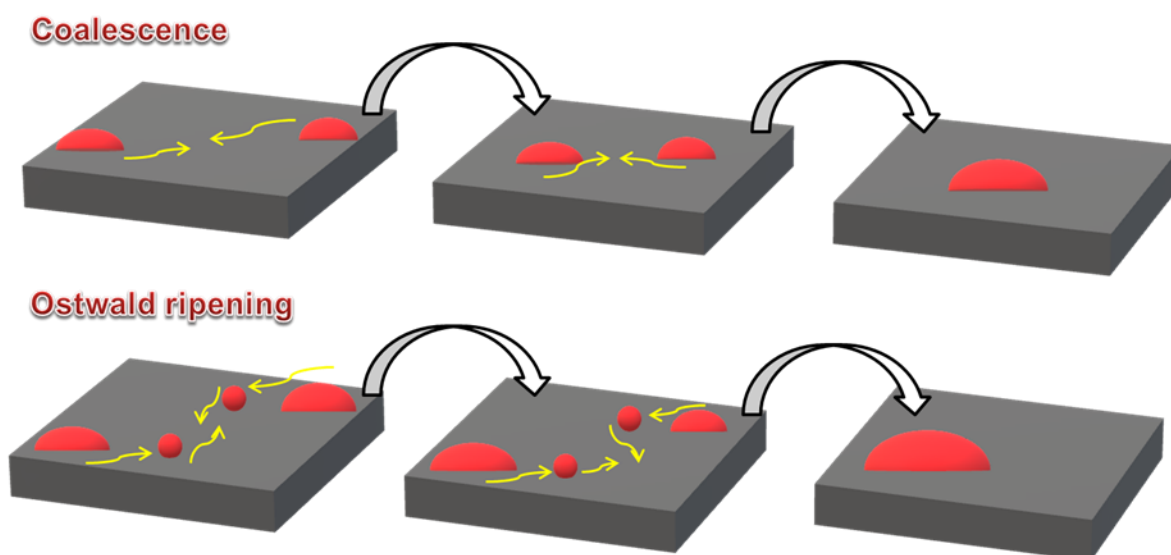


Figure 1-22. Schematic illustrations of the two principal sintering mechanisms.

- Lastly, iron-based catalysts are stated to be poisoned and deactivated by sulfur or nitrogen containing compounds, present in most industrial syngas feeds.

Indeed, the presence of a few ppm H₂S or NH₃ in the feed gas could limit catalysts life to a few hours or days. Therefore, it is indispensable to purify syngas mixture of sulfur and nitrogen compounds to the lowest practical levels possible. It is also important to be able to model the deactivation process at low H₂S levels in order to predict catalyst life^{82,96,168}.

Even though most groups suggest that the catalysts deactivate because of the contributions of several mechanisms, the main mechanisms related to the catalysts deactivation are carbon deposition and sintering. Studying deeply the catalyst deactivation mechanism might help us to design efficient and stable FT catalysts¹⁷⁰.

1.4.2. Catalyst deactivation during CO₂ hydrogenation

As in the case of CO hydrogenation, one of the principal causes of iron catalyst deactivation is the transformation of active surface carbon species and/or active iron carbide phases to inactive carbon or carbide forms that poison the surface. Lee et al.¹⁷¹ studied the reasons for deactivation of FeK/γ-Al₂O₃ for CO₂ hydrogenation to hydrocarbons using several techniques such as HR-TEM, HR-TEM, XPS, TPO, and Mössbauer spectroscopy. The results showed that deactivation is different depending on the location in the reactor. With time on stream, the hematite phase was reduced to active Hägg carbide phase (χ-Fe₅C₂) and lastly this was converted into θ-FeC₃, which have been reported as not active specie for CO₂ hydrogenation. For this reason, in the inlet reactor region, the deactivation took place due to phase transformation. On the other hand, they claimed that carbon deposition was the principal reason of deactivation at the outlet part of the reactor.

In other study Li et al.¹⁷² obtained a notable metal sintering for supported FeCo/ZrO₂ catalysts which generated a fast deactivation. On the contrary, with the

employment of Fe-Co-Zr polymetallic fibers, in which Fe and Co were impregnated close to zirconia but separated between them, resulted in a stable activity over the reaction period due to the less extent of sintering.

1.4.3. Catalyst regeneration

In hydrogenation processes, the used catalyst progressively gets contaminated by carbon deposits. These deposits generate a coating around the surface of the catalyst and consequently inhibit the diffusion of produced hydrocarbons into the catalyst pores. Partial elimination of these deposits is a vital step towards regeneration and reuse of the used catalyst. Due to the high cost of some catalysts, the techniques to effectively regenerate the spent catalysts have been more studied over the last years.

The undesirable results of this mechanism could be delayed and/or reversed by regeneration of the spent catalysts¹⁷³. Investigations have shown that control catalyst deactivation by coal deposits can be performed by adapting the catalyst surface composition, for instance the employment of polymetallic catalysts and/or manipulating the reaction conditions¹⁷⁴. In the moment that the catalyst activity drops to unpleasant limits, renewal by the oxidative burning off of carbon deposits, in the presence of a medium containing oxygen gas, is typically performed. Nevertheless, it has been shown that this oxidative process should be prudently controlled to prevent overheating, which could cause the catalyst sintering. Consequently, dilution of the oxygen with inert gases such as nitrogen or argon might be more appropriate¹⁷⁵.

Among the processes reported in literature,¹⁷⁶ it is shown that in situ oxidative methods for regeneration of FT catalysts could be applied for such purpose. Although this technique may not have been optimum, most of the carbon was removed from the

catalyst after the oxidative treatment. However, as determined by X-ray diffraction analysis, sintering of the active component of the catalyst occurred with each successive oxidative regeneration, and this originated a decline in the catalyst activity and possibly a change in the hydrogenation activity.

Also, the active sites of a catalyst can be poisoned by sulfur or nitrogen compounds coming from with the syngas generation process. The catalysts may be regenerated by flushing in H₂ at a suitable temperature in order to avoid sintering.

In short, to extend the catalyst life, it is important to be able to regenerate a deactivated iron catalyst and use it again in the CO and CO₂ hydrogenation process. The choice to dispose or regenerate the catalyst hinges on the cost of the catalyst, viability of recuperating appreciated components like noble metals, facilities for external regeneration of the catalyst, the time needed to renew and reload the catalyst, and the consequence of shutting down a plant on downstream or upstream processes. Although regeneration has been applied previously, the mechanism of regeneration is not completely clear and continues to be challenging.

1.5. High throughput experimentation for catalysts screening

High throughput experimentation (HTE) is a technique that permits a huge amount of experiments that can be carried out in parallel with the benefit of requiring not as much effort per experiment in comparison with the traditional ways of experimentation. When used in chemical research, HTE is commonly employed to evaluate a varied selection of reaction conditions to rapidly decide the “best” catalyst, reagents, and solvents to use for specified processes^{177,178}. These groups of reactions are logically planned to give a response on precise chemical interrogations and to reach specific process chemistry objectives¹⁷⁹.

Traditional reactions such as substitutions, condensations, and cyclo-additions follow reasonably well understood mechanisms and intuitive relationships between the different parameters. On the other hand, most catalytic reactions happen by the cautious interplay of several elementary stages that must all be carried out surrounded by the same chemical environment. Besides, these catalytic processes take place in competition with side reactions and catalyst decomposition or deactivation pathways¹⁸⁰.

HTE speeds up experimental effort in numerous critical dimensions. Grouping similar processes saves time by reducing the number of operations to be executed. High throughput approaches are characterized not only by its productiveness capability but also by the ability to generate exceptionally large data sets in an incredible short time that it would be unimaginable by the traditional ways. For heterogeneous catalysis field, the supplementary difficulty of measuring reaction temperatures, different gas space velocities, catalytic activity, yield, and quantification of the products that frequently enclose mixtures of related species, HTE represents a well-proven tool for determining valuable transformations¹⁷⁷.

One main limitation is that even a powerful tool like HTE only explores a quite minor region of chemical space. Here is where the knowledge of a researcher in a particular reaction helps to narrow the number of possible catalyst combinations for synthesis and experimentation^{179,181}.

There are much more advantages than drawbacks when conducting HTE chemical research. First, new synthetic methods for generating highly valuable products, such as light olefins, certainly need important amounts of experimentation in order to accomplish innovative discoveries. This device permits researchers try more

varied catalysts and conditions in shorter time than it has been conventionally possible. Second, catalytic reactions need parameters screening (different catalysts composition, pressure, GHSV, temperature, etc.) in order to determine conditions that are satisfactory.

1.6. Challenges and objectives of the thesis

Literature review allowed identification of major challenges regarding CO and CO₂ hydrogenation reactions. Studies pursue the developing of new, active, stable, and selective catalysts for the production of useful base chemicals. Even though FT synthesis is a widely studied reaction, there still space for continue improving and designing new catalysts that could aim problems of unsatisfactory selectivity to specific hydrocarbon fractions and catalyst activity. Literature shows high olefin selectivities in CO hydrogenation reaction. However, catalyst stability and higher CO conversions levels are still challenging.

On the other hand, important advance has been done during last years in the catalytic hydrogenation of CO₂ in order to generate different value-added products that can be easily monetized like dimethyl ether¹⁸², olefins¹⁸³, liquid fuels¹⁵⁴, and higher alcohols¹⁸⁴. However, the state of the art development of catalysts for the hydrogenation of CO₂ to useful C₂₊ hydrocarbons is far from satisfactory. C₂₊ product synthesis is extremely puzzling caused by the high stability of CO₂ and the high C-C coupling barrier, as well as, numerous opposite reactions conducting to the generation of C₁ products.

In the framework of the Interreg Psyche Project we aim the development of new efficient catalysts, that are commercially easy to use and synthesize, for both CO and CO₂ hydrogenation reactions to selectively produce light olefins (C₂-C₄) maintaining a

good activity and stability. At the same time, we try to give details on how the promoters improve catalysts behavior and the main active phases taking part in both processes. All this backed by a series of simple and complex characterization techniques.

In this work we try to use some of the most representative promoters according to their properties (some of them known, other we little or no information in literature). we took alkali metals which bring basicity improvement, several transition metals which can have multiple oxidation states and “soldering” metals which their low melting point could give them higher mobility on the catalysts surface like Bi, Sn, Sb etc.

1.7. Outline of the thesis

This thesis is divided in 6 chapters as follows:

Chapter 1 presents a literature review on the production of syngas from plastic waste. In addition, it gives insights on the different mechanisms proposed for CO and CO₂ hydrogenation and ways of improving light olefin production. It also addresses the most suitable catalysts for those reactions and the possible deactivation mechanisms. Finally, it is noted that there are challenges that need to be addressed for both reactions: activity, selectivity and stability of the catalyst remain the most important points to be addressed.

Chapter 2 describes the procedures for synthesis of the catalysts, their catalytic evaluation and characterization techniques used.

Chapter 3 addresses the identification of new efficient promoters and selectivity trends in FT synthesis by using a simple preparation method. For this, High Throughput Experimentation unit allowed the identification of suitable promoters within a large variety of possible candidates all of them tested under exactly the same conditions.

Chapter 4 develops the results obtained in chapter 3. We try to explain the reasons of the activity and stability improvement of the selected catalysts by using a wide variety of characterization techniques including: XRD, TPR, TEM, Mössbauer Spectroscopy, XPS, TGA and XAS.

Chapter 5 focuses on the evaluation of different promoters for CO₂ hydrogenation reaction. Iron-based catalysts supported on zirconia were synthesized for this study. We discuss on the structure-performance correlations and reaction paths for light olefins production from CO₂.

Finally, chapter 6 gives general conclusion and draws perspectives of this work.

1.8. References

1. Zhang, Q., Deng, W. & Wang, Y. Recent advances in understanding the key catalyst factors for Fischer-Tropsch synthesis. *J. Energy Chem.* **22**, 27–38 (2013).
2. Centi, G. & Perathoner, S. Heterogeneous catalytic reactions with CO₂: Status and perspectives. *Stud. Surf. Sci. Catal.* **153**, 1–8 (2004).
3. Richard, A. R. & Fan, M. Low-Pressure Hydrogenation of CO₂ to CH₃OH Using Ni-In-Al/SiO₂ Catalyst Synthesized via a Phyllosilicate Precursor. *ACS Catal.* **7**, 5679–5692 (2017).
4. Ou, M. *et al.* Amino-Assisted Anchoring of CsPbBr₃ Perovskite Quantum Dots on Porous g-C₃N₄ for Enhanced Photocatalytic CO₂ Reduction. *Angew. Chemie* **130**, 13758–13762 (2018).
5. Lin, S. *et al.* Covalent Organic Frameworks Comprising Cobalt Porphyrins for Catalytic CO₂ Reduction in Water. *Contemp. Psychol. A J. Rev.* **1**, 1–6 (2015).
6. Matsubu, J. C., Yang, V. N. & Christopher, P. Isolated metal active site concentration and stability control catalytic CO₂ reduction selectivity. *J. Am. Chem. Soc.* **137**, 3076–3084 (2015).
7. Al-Salem, S. M., Lettieri, P. & Baeyens, J. Recycling and recovery routes of plastic solid waste (PSW): A review. *Waste Manag.* **29**, 2625–2643 (2009).
8. Bion, N., Duprez, D. & Epron, F. Design of nanocatalysts for green hydrogen production from bioethanol. *ChemSusChem* **5**, 76–84 (2012).
9. Dincer, I. Green methods for hydrogen production. *Int. J. Hydrogen Energy* **37**, 1954–1971 (2012).
10. Levin, D. B. & Chahine, R. Challenges for renewable hydrogen production from biomass. *Int. J. Hydrogen Energy* **35**, 4962–4969 (2010).
11. O'Brien, R. J., Xu, L., Spicer, R. L. & Davis, B. H. Activation study of precipitated iron fischer-tropsch catalysts. *Energy and Fuels* **10**, 921–926 (1996).
12. Jin, Y. & Datye, A. K. Phase transformations in iron Fischer-Tropsch catalysts during temperature-programmed reduction. *J. Catal.* **196**, 8–17 (2000).
13. Riedel, T., Schaub, G., Jun, K. W. & Lee, K. W. Kinetics of CO₂ hydrogenation on a K-promoted Fe catalyst. *Ind. Eng. Chem. Res.* **40**, 1355–1363 (2001).
14. Chiche, D. *et al.* Synthesis Gas Purification. *Oil Gas Sci. Technol.* **68**, 707–723 (2013).
15. Subramanian, P. M. Plastics recycling and waste management in the US. *Resour. Conserv. Recycl.* **28**, 253–263 (2000).
16. Moore, C. Synthetic polymers in the marine environment: A rapidly increasing. *Environmental Res.* **108**, 131–139 (2008).
17. Aznar, M. P., Caballero, M. A., Sancho, J. A. & Francés, E. Plastic waste elimination by co-gasification with coal and biomass in fluidized bed with air in pilot plant. *Fuel Process. Technol.* **87**, 409–420 (2006).
18. Murphy, J. D. & McKeogh, E. Technical, economic and environmental analysis of energy production from municipal solid waste. *Renew. Energy* **29**, 1043–1057 (2004).
19. Katami, T., Yasuhara, A., Okuda, T. & Shibamoto, T. Formation of PCDDs, PCDFs, and Coplanar PCBs from Polyvinyl Chloride during Combustion in an Incinerator. *Energy Environ. Sci.* **36**, 1320–1324 (2002).
20. Siddique, R., Khatib, J. & Kaur, I. Use of recycled plastic in concrete: A review. *Waste Manag.* **28**, 1835–1852 (2008).
21. Lopez, G. *et al.* Recent advances in the gasification of waste plastics. A critical overview. *Renew. Sustain. Energy Rev.* **82**, 576–596 (2018).
22. Erkiaga, A., Lopez, G., Amutio, M., Bilbao, J. & Olazar, M. Syngas from steam gasification of polyethylene in a conical spouted bed reactor. *Fuel* **109**, 461–469 (2013).
23. Baeyens, J., Brems, A. & Dewil, R. Recovery and recycling of post-consumer waste materials. Part 2. Target wastes (glass beverage bottles, plastics, scrap metal and steel cans, end-of-life tyres, batteries and household hazardous waste). *Int. J. Sustain. Eng.* **3**, 232–245 (2010).
24. Richardson, Y., Blin, J. & Julbe, A. A short overview on purification and conditioning of syngas produced by biomass gasification: Catalytic strategies, process intensification and new concepts. *Prog. Energy Combust. Sci.* **38**, 765–781 (2012).
25. Kim, J. W., Mun, T. Y., Kim, J. O. & Kim, J. S. Air gasification of mixed plastic wastes using a two-stage gasifier for the production of producer gas with low tar and a high caloric value. *Fuel* **90**, 2266–2272 (2011).
26. Ragaert, K., Delva, L. & Van Geem, K. Mechanical and chemical recycling of solid plastic waste. *Waste Manag.* **69**, 24–58 (2017).
27. Donaj, P. J., Kaminsky, W., Buzeto, F. & Yang, W. Pyrolysis of polyolefins for increasing the yield of monomers' recovery. *Waste Manag.* **32**, 840–846 (2012).

28. Arena, U. Gasification: An alternative solution for waste treatment with energy recovery. *Waste Manag.* **31**, 405–406 (2011).
29. Xiao, R., Jin, B., Zhou, H., Zhong, Z. & Zhang, M. Air gasification of polypropylene plastic waste in fluidized bed gasifier. *Energy Convers. Manag.* **48**, 778–786 (2007).
30. Sancho, J., Toledo, J. & Aznar, P. Catalytic Air Gasification of Plastic Waste (Polypropylene) in Fluidized Bed. Part I: Use of in-Gasifier Bed Additives. *Ind. Eng. Chem. Res.* **47**, 1005–1010 (2008).
31. Wilk, V. & Hofbauer, H. Conversion of mixed plastic wastes in a dual fluidized bed steam gasifier. *Fuel* **107**, 787–799 (2013).
32. Dudynski, M., Dyk, J. C. Van, Kwiatkowski, K. & Sosnowska, M. Biomass gasification: Influence of torrefaction on syngas production and tar formation. *Fuel Process. Technol.* **131**, 203–212 (2015).
33. Zeng, J. *et al.* High H₂/CO Ratio Syngas Production from Chemical Looping Gasification of Sawdust in a Dual Fluidized Bed Gasifier. *Energy and Fuels* **30**, 1764–1770 (2016).
34. Wender, I. Reactions of synthesis gas. *Fuel Process. Technol.* **48**, 189–297 (1996).
35. Devi, L., Ptasinski, K. J. & Janssen, F. J. J. G. A review of the primary measures for tar elimination in biomass gasification processes. **24**, 125–140 (2003).
36. Chen, H., Namioka, T. & Yoshikawa, K. Characteristics of tar , NO_x precursors and their absorption performance with different scrubbing solvents during the pyrolysis of sewage sludge. *Appl. Energy* **88**, 5032–5041 (2011).
37. Liu, Z. & Karimi, I. A. Simulating combined cycle gas turbine power plants in Aspen HYSYS. *Energy Convers. Manag.* **171**, 1213–1225 (2018).
38. Tijmensen, M. J. A., Faaij, A. P. C., Hamelinck, C. N. & Van Hardeveld, M. R. M. Exploration of the possibilities for production of Fischer Tropsch liquids and power via biomass gasification. *Biomass and Bioenergy* **23**, 129–152 (2002).
39. Riedel, T. *et al.* Comparative study of Fischer – Tropsch synthesis with H₂/CO and H₂/CO₂ syngas using Fe- and Co-based catalysts. *Appl. Catal. A Gen.* **186**, 201–213 (1999).
40. Prakash, A. On the effects of syngas composition and water-gas-shift reaction rate on ft synthesis over iron based catalyst in a slurry reactor. *Chem. Eng. Commun.* **128**, 143–158 (1994).
41. Anderson, R. B. Thermodynamics of the hydrogenation of oxides of carbon. *J. Phys. Chem.* **90**, 4806–4810 (1986).
42. Zhao, G., Huang, X., Wang, X. & Wang, X. Progress in catalyst exploration for heterogeneous CO₂ reduction and utilization: A critical review. *J. Mater. Chem. A* **5**, 21625–21649 (2017).
43. Ordonsky, V. V., D., A.-B., Schwiedernoch, R. & A., K. Challenges and Role of Catalysis in CO₂ Conversion to Chemicals and Fuels. in *Nanotechnology in Catalysis: Applications in the Chemical Industry, Energy Development, and Environment protection* (eds. Sels, B. & Van de Voorde, M.) 805–848 (2017).
44. Dorner, R. W., Hardy, D. R., Williams, F. W. & Willauer, H. D. Heterogeneous catalytic CO₂ conversion to value-added hydrocarbons. *Energy Environ. Sci.* **3**, 884–890 (2010).
45. Demirel, E. & Azcan, N. Thermodynamic modeling of water-gas shift reaction in supercritical water. *Lect. Notes Eng. Comput. Sci.* **2**, 804–807 (2012).
46. Dry, M. E. Practical and theoretical aspects of the catalytic Fischer-Tropsch process. *Appl. Catal. A Gen.* **138**, 319–344 (1996).
47. Satterfield, C. N., Hanlon, R. T., Tung, S. E., Zou, Z. *mln* & Papaefthymiou, G. C. Effect of Water on the Iron-Catalyzed Fischer-Tropsch Synthesis. *Ind. Eng. Chem. Prod. Res. Dev.* **25**, 407–414 (1986).
48. Huff, G. A. & Satterfield, C. N. Intrinsic kinetics of the Fischer-Tropsch synthesis on a Reduced Fused-Magnetite Catalyst. *Ind. Eng. Chem. Process Des. Dev.* **23**, 696–705 (1984).
49. Willauer, H. D. *et al.* Modeling and kinetic analysis of CO₂ hydrogenation using a Mn and K-promoted Fe catalyst in a fixed-bed reactor. *J. CO₂ Util.* **3–4**, 56–64 (2013).
50. Fiato, R. A., Iglesia, E., Rice, G. W. & Soled, S. L. Iron catalyzed CO₂ hydrogenation to liquid hydrocarbons. *Stud. Surf. Sci. Catal.* **114**, 339–344 (1998).
51. Pekridis, G. *et al.* Study of the reverse water gas shift (RWGS) reaction over Pt in a solid oxide fuel cell (SOFC) operating under open and closed-circuit conditions. *Catal. Today* **127**, 337–346 (2007).
52. ROFER-DePOORTER, C. K. A Comprehensive Mechanism for the Fischer-Tropsch Synthesis. *Chem. Rev.* **81**, 447–474 (1981).
53. Van Santen, R. A., Markvoort, A. J., Filot, I. A. W., Ghouri, M. M. & Hensen, E. J. M. Mechanism and microkinetics of the Fischer-Tropsch reaction. *Phys. Chem. Chem. Phys.* **15**,

- 17038–17063 (2013).
54. Rausch, A. K. *et al.* Enhanced olefin production in Fischer–Tropsch synthesis using ammonia containing synthesis gas feeds. *Catal. Today* **275**, 94–99 (2016).
 55. Iqbal, S. *et al.* Fischer Tropsch synthesis using cobalt based carbon catalysts. *Catal. Today* **275**, 35–39 (2016).
 56. De Smit, E. & Weckhuysen, B. M. The renaissance of iron-based Fischer-Tropsch synthesis: On the multifaceted catalyst deactivation behaviour. *Chem. Soc. Rev.* **37**, 2758–2781 (2008).
 57. Adesina, A. A. Hydrocarbon synthesis via Fischer-Tropsch reaction: Travails and triumphs. *Appl. Catal. A Gen.* **138**, 345–367 (1996).
 58. Van Der Laan, G. P. & Beenackers, A. A. C. M. Kinetics and Selectivity of the Fischer-Tropsch Synthesis: A Literature Review. *Catal. Rev. - Sci. Eng.* **41**, 255–318 (1999).
 59. Mahmoudi, H. *et al.* A review of Fischer Tropsch synthesis process, mechanism, surface chemistry and catalyst formulation. *Biofuels Eng.* **2**, 11–31 (2018).
 60. Todic, B., Ma, W., Jacobs, G., Davis, B. H. & Bukur, D. B. CO-insertion mechanism based kinetic model of the Fischer-Tropsch synthesis reaction over Re-promoted Co catalyst. *Catal. Today* **228**, 32–39 (2014).
 61. Torres Galvis, H. M. & De Jong, K. P. Catalysts for production of lower olefins from synthesis gas: A review. *ACS Catal.* **3**, 2130–2149 (2013).
 62. Henrici-Olivé, G. & Olivé, S. The Fischer-Tropsch Synthesis: Molecular Weight Distribution of Primary Products and Reaction Mechanism. *Angew. Chemie Int. Ed. English* **15**, 136–141 (1976).
 63. Brady, R. C. & Pettit, R. On the Mechanism of the Fischer-Tropsch Reaction. The Chain Propagation Step. *J. Am. Chem. Soc.* **103**, 1287–1289 (1981).
 64. Yang, J., Ma, W., Chen, D., Holmen, A. & Davis, B. H. Fischer-Tropsch synthesis: A review of the effect of CO conversion on methane selectivity. *Appl. Catal. A Gen.* **470**, 250–260 (2014).
 65. Kummer, J. T. & Emmet, P. . Fischer-Tropsch Synthesis Mechanism Studies. The Addition of Radioactive Alcohols to the Synthesis Gas. *J. Am. Chem. Soc.* **75**, 5177–5183 (1953).
 66. Podgurski, H. H., Kummer, J. T., DeWitt, T. W. & Emmett, P. H. Preparation, Stability and Adsorptive Properties of the Carbides of Iron. *J. Am. Chem. Soc.* **72**, 5382–5388 (1950).
 67. Claeys, M. & Van Steen, E. *Basic studies. Studies in Surface Science and Catalysis* vol. 152 (Elsevier B.V., 2004).
 68. Pichler, H. & Schulz, H. Neuere Erkenntnisse auf dem Gebiet der Synthese von Kohlenwasserstoffen aus CO und H₂. *Chemie Ing. Tech.* **42**, 1162–1174 (1970).
 69. Hindermann, J. P., Hutchings, G. J. & Kiennemann, A. Mechanistic Aspects of the Formation of Hydrocarbons and Alcohols from CO Hydrogenation. *Catal. Rev. - Sci. Eng.* **1**, 1–127 (1993).
 70. Gu, B., Khodakov, A. Y. & Ordonsky, V. V. Selectivity shift from paraffins to α -olefins in low temperature Fischer-Tropsch synthesis in the presence of carboxylic acids. *Chem. Commun.* **54**, 2345–2348 (2018).
 71. Wang, Q., Chen, Y. & Li, Z. Research Progress of Catalysis for Low-Carbon Olefins Synthesis Through Hydrogenation of CO₂. *J. Nanosci. Nanotechnol.* **19**, 3162–3172 (2019).
 72. Visconti, C. G. *et al.* Fischer-Tropsch synthesis on a Co/Al₂O₃ catalyst with CO₂ containing syngas. *Appl. Catal. A Gen.* **355**, 61–68 (2009).
 73. Wang, W., Wang, S., Ma, X. & Gong, J. Recent advances in catalytic hydrogenation of carbon dioxide. *Chem. Soc. Rev.* **40**, 3703–3727 (2011).
 74. Kaiser, P., Unde, R. B., Kern, C. & Jess, A. Production of liquid hydrocarbons with CO₂ as carbon source based on reverse water-gas shift and fischer-tropsch synthesis. *Chemie-Ingenieur-Technik* **85**, 489–499 (2013).
 75. Saeidi, S. *et al.* Mechanisms and kinetics of CO₂ hydrogenation to value-added products: A detailed review on current status and future trends. *Renew. Sustain. Energy Rev.* **80**, 1292–1311 (2017).
 76. Cubeiro, M. L. *et al.* Hydrogenation of carbon oxides over Fe/Al₂O₃ catalysts. *Appl. Catal. A Gen.* **189**, 87–97 (1999).
 77. Centi, G., Quadrelli, E. & Perathoner, S. Catalysis for CO₂ conversion: a key technology for rapid introduction of renewable energy in the value chain of chemical industries. *Energy Environ. Sci.* **6**, 1711–1729 (2013).
 78. Dry, M. E. The Fischer-Tropsch process: 1950-2000. *Catal. Today* **71**, 227–241 (2002).
 79. Khodakov, A. Y., Chu, W. & Fongarland, P. Advances in the development of novel cobalt Fischer-Tropsch catalysts for synthesis of long-chain hydrocarbons and clean fuels. *Chemical Reviews* (2007) doi:10.1021/cr050972v.
 80. Sie, S. T. & Krishna, R. Fundamentals and selection of advanced Fischer-Tropsch reactors.

- Appl. Catal. A Gen.* **186**, 55–70 (1999).
81. Steynberg, A. P., Dry, M. E., Davis, B. H. & Breman, B. B. Fischer-Tropsch reactors. in *Studies in Surface Science and Catalysis* vol. 152 64–195 (Elsevier B.V., 2004).
 82. Dry, M. E. Fischer-Tropsch synthesis over iron catalysts. *Catal. Letters* **7**, 241–251 (1990).
 83. Todić, B., Ordonsky, V. V., Nikačević, N. M., Khodakov, A. Y. & Bukur, D. B. Opportunities for intensification of Fischer-Tropsch synthesis through reduced formation of methane over cobalt catalysts in microreactors. *Catal. Sci. Technol.* **5**, 1400–1411 (2015).
 84. Guettel, R. & Turek, T. Comparison of different reactor types for low temperature Fischer-Tropsch synthesis: A simulation study. *Chem. Eng. Sci.* **64**, 955–964 (2009).
 85. De Swart, J., Krishna, R. & Sie, S. Selection, Design and Scale Up of the Fischer-Tropsch Reactor. in *Studies in Surface Science and Catalysis* vol. 107 213–218 (1997).
 86. Espinoza, R. L., Steynberg, A. P., Jager, B. & Vosloo, A. C. Low temperature Fischer-Tropsch synthesis from a Sasol perspective. *Appl. Catal. A Gen.* **186**, 13–26 (1999).
 87. Botes, F. G. *et al.* *Middle distillate fuel production from synthesis gas via the Fischer-Tropsch process. Advances in Clean Hydrocarbon Fuel Processing: Science and Technology* (Woodhead Publishing Limited, 2011). doi:10.1533/9780857093783.4.329.
 88. Moutsoglou, A. & Sunkara, P. P. Fischer-Tropsch synthesis in a fixed bed reactor. *Energy and Fuels* **25**, 2242–2257 (2011).
 89. Steynberg, A. P., Espinoza, R. L., Jager, B. & Vosloo, A. C. High temperature Fischer-Tropsch synthesis in commercial practice. *Appl. Catal. A Gen.* **186**, 41–54 (1999).
 90. Jager, B., Dry, M. E., Shingles, T. & Steynberg, a. P. Experience with a New Type of Reactor for Fischer-Tropsch Synthesis. *Catal. Letters* **7**, 293–302 (1990).
 91. Lerou, J. J., Tonkovich, A. L., Silva, L., Perry, S. & McDaniel, J. Microchannel reactor architecture enables greener processes. *Chem. Eng. Sci.* **65**, 380–385 (2010).
 92. Myrstad, R., Eri, S., Pfeifer, P., Rytter, E. & Holmen, A. Fischer-Tropsch synthesis in a microstructured reactor. *Catal. Today* **147**, 3–6 (2009).
 93. Ying, X. *et al.* Efficient Fischer-Tropsch microreactor with innovative aluminizing pretreatment on stainless steel substrate for Co/Al₂O₃ catalyst coating. *Fuel Process. Technol.* **143**, 51–59 (2016).
 94. Krishnamoorthy, S., Li, A. & Iglesia, E. Pathways for CO₂ formation and conversion during Fischer-Tropsch synthesis on iron-based catalysts. *Catal. Letters* **80**, 77–86 (2002).
 95. Sathawong, R., Koizumi, N., Song, C. & Prasassarakich, P. Comparative Study on CO₂ Hydrogenation to Higher Hydrocarbons over Fe-Based Bimetallic Catalysts. *top Catal.* **57**, 588–594 (2014).
 96. Weatherbeeand, G. D. & Bartholomew, C. H. Hydrogenation of CO₂ on Group VIII Metals. *J. Catal.* **87**, 352–362 (1984).
 97. Sheintuch, M. & Yesgar, P. Nickel-Catalyzed Methanation Reactions Studied with an in Situ Magnetic Induction Method: Experiments and Modeling. *J. Catal.* **127**, 576–594 (1991).
 98. Kölbel, H. & Ralek, M. Catalysis Reviews : Science and Engineering The Fischer-Tropsch Synthesis in the Liquid Phase. *Catal. Rev. - Sci. Eng.* **21**, 225–274 (1980).
 99. Iglesia, E. Design, synthesis, and use of cobalt-based Fischer-Tropsch synthesis catalysts. *Appl. Catal. A Gen.* **161**, 59–78 (1997).
 100. Visconti, C. G., Tronconi, E., Lietti, L., Zennaro, R. & Forzatti, P. Development of a complete kinetic model for the Fischer-Tropsch synthesis over Co/Al₂O₃ catalysts. *Chem. Eng. Sci.* **62**, 5338–5343 (2007).
 101. Li, J., Xu, L., Keogh, R. & Davis, B. Fischer-Tropsch synthesis. Effect of CO pretreatment on a ruthenium promoted Co/TiO₂. *Catal. Letters* **70**, 127–130 (2000).
 102. Park, K. Y., Seo, W. K. & Lee, J. S. Selective synthesis of light olefins from syngas over potassium-promoted molybdenum carbide catalysts. *Catal. Letters* **11**, 349–356 (1991).
 103. Woo, H. C., Park, K. Y., Kim, Y. G., NamauJong ShikChung, I. S. & Lee, J. S. Mixed alcohol synthesis from carbon monoxide and dihydrogen over potassium-promoted molybdenum carbide catalysts. *Appl. Catal.* **75**, 267–280 (1991).
 104. Corma, A., Melo, F. V., Sauvanaud, L. & Ortega, F. Light cracked naphtha processing: Controlling chemistry for maximum propylene production. *Catal. Today* **107–108**, 699–706 (2005).
 105. Zafari, R., Abdouss, M. & Zamani, Y. Application of response surface methodology for the optimization of light olefins production from CO hydrogenation using an efficient catalyst. *Fuel* **237**, 1262–1273 (2019).
 106. Janardanarao, M. Direct Conversion of Synthesis Gas to Lower Olefins. *Ind. Eng. Chem. Res.* **29**, 1735–1753 (1990).

107. Diehl, F. & Khodakov, A. Y. Promotion of Cobalt Fischer-Tropsch Catalysts with Noble Metals: a Review. *Oil Gas Sci. Technol.* **64**, 11–24 (2009).
108. Zhong, L. *et al.* Cobalt carbide nanoprisms for direct production of lower olefins from syngas. *Nature* **538**, 84–87 (2016).
109. Mirzaei, A. A., Faizi, M. & Habibpour, R. Effect of preparation conditions on the catalytic performance of cobalt manganese oxide catalysts for conversion of synthesis gas to light olefins. *Appl. Catal. A Gen.* **306**, 98–107 (2006).
110. Khodaei, M. M., Feyzi, M., Shahmoradi, J. & Joshaghani, M. The sol-gel derived Co-Mn/TiO₂ catalysts for light olefins production. *Ranliao Huaxue Xuebao/Journal Fuel Chem. Technol.* **42**, 212–218 (2014).
111. Jiao, F. *et al.* Selective conversion of syngas to light olefins. *Science (80-.)*. **351**, 1065–1068 (2016).
112. Cheng, K. *et al.* Direct and Highly Selective Conversion of Synthesis Gas into Lower Olefins: Design of a Bifunctional Catalyst Combining Methanol Synthesis and Carbon-Carbon Coupling. *Angew. Chemie - Int. Ed.* **55**, 4725–4728 (2016).
113. Botes, G. F. *et al.* Development of a chemical selective iron Fischer Tropsch catalyst. *Catal. Today* **275**, 40–48 (2016).
114. Luo, M. & Davis, B. H. Deactivation and regeneration of alkali metal promoted iron Fischer-Tropsch synthesis catalysts. *Stud. Surf. Sci. Catal.* **139**, 133–140 (2001).
115. Wezendonk, T. A. *et al.* Controlled formation of iron carbides and their performance in Fischer-Tropsch synthesis. *J. Catal.* **362**, 106–117 (2018).
116. Sirikulbodee, P., Ratana, T., Sornchamni, T., Phongaksorn, M. & Tungkamani, S. Catalytic performance of Iron-based catalyst in Fischer-Tropsch synthesis using CO₂ containing syngas. *Energy Procedia* **138**, 998–1003 (2017).
117. Khan, A. & Smirniotis, P. G. Relationship between temperature-programmed reduction profile and activity of modified ferrite-based catalysts for WGS reaction. *J. Mol. Catal. A Chem.* **280**, 43–51 (2008).
118. Butt, J. B. Carbide phases on iron-based Fischer-Tropsch synthesis catalysts part I: Characterization studies. *Catal. Letters* **7**, 61–81 (1990).
119. Rhodes, C., Hutchings, G. J. & Ward, A. M. Water-gas shift reaction: finding the mechanistic boundary. *Catal. Today* **23**, 43–58 (1995).
120. Riedel, T. *et al.* Fischer-Tropsch on iron with H₂/CO and H₂/CO₂ as synthesis gases: The episodes of formation of the Fischer-Tropsch regime and construction of the catalyst. *Top. Catal.* **26**, 41–54 (2003).
121. Shroff, M. D. *et al.* Activation of Precipitated Iron Fischer-Tropsch Synthesis Catalysts. *J. Catal.* **156**, 185–207 (1995).
122. Raupp, G. B. & Delgass, W. N. Mössbauer investigation of supported Fe catalysts. III. In situ kinetics and spectroscopy during Fischer-Tropsch synthesis. *J. Catal.* **58**, 361–369 (1979).
123. Niemantsverdriet, J. W., Van Der Kraan, A. M., Van Dijk, W. L. & Van Der Baan, H. S. Behavior of metallic iron catalysts during Fischer-Tropsch synthesis studied with Mössbauer spectroscopy, X-ray diffraction, carbon content determination, and reaction kinetic measurements. *J. Phys. Chem.* **84**, 3363–3370 (1980).
124. Brodén, G., Gafner, G. & Bonzel, H. P. Co adsorption on potassium promoted Fe(110). *Surf. Sci.* **84**, 295–314 (1979).
125. Bukur, D. B., Mukesh, D. & Patel, S. A. Promoter Effects on Precipitated Iron Catalysts for Fischer-Tropsch Synthesis. *Ind. Eng. Chem. Res.* **29**, 194–204 (1990).
126. Ribeiro, M. C. *et al.* Fischer-tropsch synthesis: An in-situ TPR-EXAFS/XANES investigation of the influence of group I alkali promoters on the local atomic and electronic structure of carburized iron/silica catalysts. *J. Phys. Chem. C* **114**, 7895–7903 (2010).
127. Cheng, K. *et al.* Sodium-promoted iron catalysts prepared on different supports for high temperature Fischer-Tropsch synthesis. *Appl. Catal. A Gen.* **502**, 204–214 (2015).
128. Li, J. *et al.* Alkalis in iron-based Fischer-Tropsch synthesis catalysts: distribution, migration and promotion. *J. Chem. Technol. Biotechnol.* **28**, 1472–1480 (2017).
129. Chernavskii, P. A. *et al.* Influence of copper and potassium on the structure and carbidisation of supported iron catalysts for Fischer-Tropsch synthesis. *Catal. Sci. Technol.* **7**, 2325–2334 (2017).
130. Peña, D. *et al.* The Effect of Copper Loading on Iron Carbide Formation and Surface Species in Iron-Based Fischer-Tropsch Synthesis Catalysts. *ChemCatChem* **10**, 1300–1312 (2018).
131. Dry, M. E., Shingles, T., Boshoff, L. J. & Oosthuizen, G. J. Heats of chemisorption on promoted iron surfaces and the role of alkali in Fischer-Tropsch synthesis. *J. Catal.* **15**, 190–199 (1969).

132. Ordonsky, V. V. *et al.* Soldering of iron catalysts for direct synthesis of light olefins from syngas under mild reaction conditions. *ACS Catal.* **7**, 6445–6452 (2017).
133. Gu, B. *et al.* Effects of the promotion with bismuth and lead on direct synthesis of light olefins from syngas over carbon nanotube supported iron catalysts. *Appl. Catal. B Environ.* **234**, 153–166 (2018).
134. Gu, B. *et al.* Synergy of nanoconfinement and promotion in the design of efficient supported iron catalysts for direct olefin synthesis from syngas. *J. Catal.* **376**, 1–16 (2019).
135. Gu, B. *et al.* Size and promoter effects on iron nanoparticles confined in carbon nanotubes and their catalytic performance in light olefin synthesis from syngas. *Catal. Today* 0–1 (2019) doi:10.1016/j.cattod.2019.05.054.
136. Torres Galvis, H. M. *et al.* Effects of sodium and sulfur on catalytic performance of supported iron catalysts for the Fischer-Tropsch synthesis of lower olefins. *J. Catal.* **303**, 22–30 (2013).
137. Bukur, D. B., Patel, S. A., Dalai, A. & Jayanthi, G. *Development of Improved Iron Fischer-Tropsch Catalysts. Quarterly Technical Progress Report for the Period I January 1990 - 31 March 1990* (1990).
138. Niemantsverdriet, J. W. & van der Kraan, A. M. On the time-dependent behavior of iron catalysts in Fischer-Tropsch synthesis. *J. Catal.* **72**, 385–388 (1981).
139. Fratallocchi, L., Visconti, C. G., Lietti, L., Fischer, N. & Claeys, M. A promising preparation method for highly active cobalt based Fischer-Tropsch catalysts supported on stabilized Al₂O₃. *Appl. Catal. A Gen.* **556**, 92–103 (2018).
140. Eschemann, T. O., Oenema, J. & De Jong, K. P. Effects of noble metal promotion for Co/TiO₂ Fischer-Tropsch catalysts. *Catal. Today* **261**, 60–66 (2016).
141. Al-Dossary, M., Fierro, J. L. G. & Spivey, J. J. Cu-promoted Fe₂O₃/MgO-based Fischer-Tropsch catalysts of biomass-derived syngas. *Ind. Eng. Chem. Res.* **54**, 911–921 (2015).
142. Ali, A., Henda, R., Aluha, J. & Abatzoglou, N. Co-doped ZnO thin films grown by pulsed electron beam ablation as model nano-catalysts in fischer-tropsch synthesis. *AIChE J.* **64**, 3332–3340 (2018).
143. Barrault, J., Forquy, C. (Laboratoire de Catalyse Organique), ERA CNRS 371, U. de P., Menezo, J. & Maurel, R. HYDROCONDENSATION OF CO₂ (CO). OVER SUPPORTED IRON CATALYSTS. *Catal. Letters* **17**, 373–378 (1981).
144. Raje, A., Inga, J. R. & Davis, B. H. Fischer-Tropsch synthesis: Process considerations based on performance of iron-based catalysts. *Fuel* **76**, 273–280 (1997).
145. de la Osa, A. R., Romero, A., Díez-Ramírez, J., Valverde, J. L. & Sánchez, P. Influence of a Zeolite-Based Cascade Layer on Fischer-Tropsch Fuels Production over Silicon Carbide Supported Cobalt Catalyst. *Top. Catal.* **60**, 1082–1093 (2017).
146. Lee, S. C. *et al.* The effect of binders on structure and chemical properties of Fe-K/γ-Al₂O₃ catalysts for CO₂ hydrogenation. *Appl. Catal. A Gen.* **253**, 293–304 (2003).
147. Chen, X., Deng, D., Pan, X. & Bao, X. Iron catalyst encapsulated in carbon nanotubes for CO hydrogenation to light olefins. *Chinese J. Catal.* **36**, 1631–1637 (2015).
148. Wang, D., Chen, B., Duan, X., Chen, D. & Zhou, X. Iron-based Fischer-Tropsch synthesis of lower olefins: The nature of χ-Fe₅C₂ catalyst and why and how to introduce promoters. *J. Energy Chem.* **25**, 911–916 (2016).
149. Bukur, D. B., Koranne, M., Lang, X., Rao, K. R. P. M. & Huffman, G. P. Pretreatment effect studies with a precipitated iron Fischer-Tropsch catalyst. *Appl. Catal. A, Gen.* **126**, 85–113 (1995).
150. Gu, B. *et al.* Polyaniline-supported iron catalyst for selective synthesis of lower olefins from syngas. *J. Energy Chem.* **26**, 608–615 (2017).
151. Torres Galvis, H. M. *et al.* Supported iron nanoparticles as catalysts for sustainable production of lower olefins. *Science (80-.)*. **335**, 835–838 (2012).
152. Xie, J. *et al.* Size and Promoter Effects in Supported Iron Fischer-Tropsch Catalysts: Insights from Experiment and Theory. *ACS Catal.* **6**, 3147–3157 (2016).
153. Zhou, W. *et al.* New horizon in C1 chemistry: Breaking the selectivity limitation in transformation of syngas and hydrogenation of CO₂ into hydrocarbon chemicals and fuels. *Chem. Soc. Rev.* **48**, 3193–3228 (2019).
154. Wei, J. *et al.* Directly converting CO₂ into a gasoline fuel. *Nat. Commun.* **8**, 1–8 (2017).
155. Wang, J., You, Z., Zhang, Q., Deng, W. & Wang, Y. Synthesis of lower olefins by hydrogenation of carbon dioxide over supported iron catalysts. *Catal. Today* **215**, 186–193 (2013).
156. Xu, L. *et al.* The promotions of MnO and K₂O to Fe/silicalite-2 catalyst for the production of light alkenes from CO₂ hydrogenation. *Appl. Catal. A Gen.* **173**, 19–25 (1998).

157. Herranz, T. *et al.* Hydrogenation of carbon oxides over promoted Fe-Mn catalysts prepared by the microemulsion methodology. *Appl. Catal. A Gen.* **311**, 66–75 (2006).
158. Sathawong, R., Koizumi, N., Song, C. & Prasassarakich, P. Light olefin synthesis from CO₂ hydrogenation over K-promoted Fe-Co bimetallic catalysts. *Catal. Today* **251**, 34–40 (2015).
159. Sai Prasad, P. S., Bae, J. W., Jun, K. W. & Lee, K. W. Fischer-Tropsch synthesis by carbon dioxide hydrogenation on Fe-based catalysts. *Catal. Surv. from Asia* **12**, 170–183 (2008).
160. Rongxian, B., Yisheng, T. & Yizhuo, H. Study on the carbon dioxide hydrogenation to iso-alkanes over Fe-Zn-M/zeolite composite catalysts. *Fuel Process. Technol.* **86**, 293–301 (2004).
161. Visconti, C. G. *et al.* CO₂ hydrogenation to lower olefins on a high surface area K-promoted bulk Fe-catalyst. *Appl. Catal. B Environ.* **200**, 530–542 (2017).
162. Zhang, J. *et al.* Selective formation of light olefins from CO₂ hydrogenation over Fe-Zn-K catalysts. *J. CO₂ Util.* **12**, 95–100 (2015).
163. Shafer, W. D., Jacobs, G., Graham, U. M., Hamdeh, H. H. & Davis, B. H. Increased CO₂ hydrogenation to liquid products using promoted iron catalysts. *J. Catal.* **369**, 239–248 (2019).
164. Raymond, J. P. & Pommier, B. Deactivation of iron catalysts in the hydrogenation of carbon monoxide. *Stud. Surf. Sci. Catal.* **126**, 299–306 (1999).
165. Bartholomewa, C. H., Stoker, M. v., Manskerb, L. & Datyeb, A. Effects of pretreatment, reaction, and promoter on microphase structure and fischer-tropsch activity of precipitated iron catalysts. *Stud. Surf. Sci. Catal.* **126**, 265–272 (1999).
166. Mansker, L. D., Jin, Y., Bukur, D. B. & Datye, A. K. Characterization of slurry phase iron catalysts for Fischer-Tropsch synthesis. *Appl. Catal. A Gen.* **186**, 277–296 (1999).
167. Torres Galvis, H. M. *et al.* Iron particle size effects for direct production of lower olefins from synthesis gas. *J. Am. Chem. Soc.* **134**, 16207–16215 (2012).
168. Duvenhage, D. J. & Coville, N. J. Deactivation of a precipitated iron Fischer-Tropsch catalyst - A pilot plant study. *Appl. Catal. A Gen.* **298**, 211–216 (2006).
169. Campbell, C. T. The energetics of supported metal nanoparticles: Relationships to sintering rates and catalytic activity. *Acc. Chem. Res.* **46**, 1712–1719 (2013).
170. Bartholomew, C. H. & Bowman, R. M. Sulfur poisoning of cobalt and iron fischer-tropsch catalysts. *Appl. Catal.* **15**, 59–67 (1985).
171. Lee, S. C., Kim, J. S., Shin, W. C., Choi, M. J. & Choung, S. J. Catalyst deactivation during hydrogenation of carbon dioxide: Effect of catalyst position in the packed bed reactor. *J. Mol. Catal. A Chem.* **301**, 98–105 (2009).
172. Li, W. *et al.* The anti-sintering catalysts: Fe-Co-Zr polymetallic fibers for CO₂ hydrogenation to C₂ = -C₄ = -rich hydrocarbons. *J. CO₂ Util.* **23**, 219–225 (2018).
173. Gosselink, J. V. V. & Van Veen, J. A. R. Coping with Catalyst Deactivation in Hydrocarbon Processing. *Stud. Surf. Sci. Catal.* **126**, 3–16 (1999).
174. Jiménez-García, G., Quintana-Solórzano, R., Aguilar-López, R. & Maya-Yescas, R. Modelling catalyst deactivation by external coke deposition during fluid catalytic cracking. *Int. J. Chem. React. Eng.* **8**, (2010).
175. Katzer, J. & Windawi, H. Process for the Regeneration of Metallica Catalysts. 2–6 (1981).
176. Pennline, H. W. & Pollack, S. S. Deactivation and Regeneration of a Promoted Transition-Metal-Zeolite Catalyst. *Ind. Eng. Chem. Prod. Res. Dev.* **25**, 11–14 (1986).
177. Collins, K. D., Gensch, T. & Glorius, F. Contemporary screening approaches to reaction discovery and development. *Nat. Chem.* **6**, 859–871 (2014).
178. Schmink, J. R., Bellomo, A. & Berritt, S. Scientist-led High-Throughput Experimentation (HTE) and its utility in academia and industry. *Aldrichimica Acta* **46**, 71–80 (2013).
179. Mennen, S. M. *et al.* The Evolution of High-Throughput Experimentation in Pharmaceutical Development and Perspectives on the Future. *Org. Process Res. Dev.* **23**, 1213–1242 (2019).
180. Crabtree, R. H. Deactivation in Homogeneous Transition Metal Catalysis: Causes, Avoidance, and Cure. *Chem. Rev.* **115**, 127–150 (2015).
181. Isbrandt, E. S., Sullivan, R. J. & Newman, S. G. High Throughput Strategies for the Discovery and Optimization of Catalytic Reactions. *Angew. Chemie - Int. Ed.* **58**, 7180–7191 (2019).
182. Saravanan, K., Ham, H., Tsubaki, N. & Bae, J. W. Recent progress for direct synthesis of dimethyl ether from syngas on the heterogeneous bifunctional hybrid catalysts. *Appl. Catal. B Environ.* **217**, 494–522 (2017).
183. Li, Z. *et al.* Highly Selective Conversion of Carbon Dioxide to Lower Olefins. *ACS Catal.* **7**, 8544–8548 (2017).
184. Yang, C. *et al.* Hydroxyl-mediated ethanol selectivity of CO₂ hydrogenation. *Chem. Sci.* **10**, 3161–3167 (2019).

Chapter 2 Catalysts and experiments

2.1. Catalyst preparation

2.1.1. Silica supported catalysts

Commercial amorphous silica (CARIACT Q-10, Fuji Silesia) was used as the catalytic support. Generally, distilled water is served as solvent. In the case of Nb, Sn and Sb, ethanol (Verbiese) is applied as to the insolubility of these precursor salts in water. The following precursors were used for the promotion of silica supported iron catalysts: LiNO_3 (Fluka), KNO_3 (Sigma-Aldrich), CsNO_3 (Aldrich), $\text{Mg}(\text{NO}_3)_2 \cdot 6\text{H}_2\text{O}$ (Sigma-Aldrich), $\text{Ca}(\text{NO}_3)_2 \cdot 4\text{H}_2\text{O}$ (Sigma-Aldrich), $\text{Sr}(\text{NO}_3)_2$ (Sigma-Aldrich), $\text{Ba}(\text{NO}_3)_2$ (Sigma-Aldrich), $\text{La}(\text{NO}_3)_3 \cdot 6\text{H}_2\text{O}$ (Fluka), $\text{Ce}(\text{NO}_3)_3 \cdot 6\text{H}_2\text{O}$ (Fluka), $\text{ZrO}(\text{NO}_3)_2 \cdot x\text{H}_2\text{O}$ (Fluka), NbCl_5 (Alfa Aesar), $\text{Cr}(\text{NO}_3)_3 \cdot 9\text{H}_2\text{O}$ (Sigma-Aldrich), $(\text{NH}_4)_6\text{Mo}_7\text{O}_{24} \cdot 4\text{H}_2\text{O}$ (Fluka), $(\text{NH}_4)_{10}(\text{H}_2\text{W}_{12}\text{O}_{42}) \cdot x\text{H}_2\text{O}$ (Aldrich), $\text{Mn}(\text{NO}_3)_2 \cdot 4\text{H}_2\text{O}$ (Alfa Aesar), $\text{Co}(\text{NO}_3)_2 \cdot 6\text{H}_2\text{O}$ (Sigma-Aldrich), $\text{Ni}(\text{NO}_3)_2 \cdot 6\text{H}_2\text{O}$ (Sigma-Aldrich), $\text{Pd}(\text{NO}_3)_2 \cdot x\text{H}_2\text{O}$ (Aldrich), $\text{Cu}(\text{NO}_3)_2 \cdot 3\text{H}_2\text{O}$ (Acros Organics), AgNO_3 (Sigma-Aldrich), HAuCl_4 (Aldrich), $\text{Zn}(\text{NO}_3)_2 \cdot 6\text{H}_2\text{O}$ (Sigma-Aldrich), $\text{Ga}(\text{NO}_3)_3 \cdot x\text{H}_2\text{O}$ (Sigma-Aldrich), $\text{In}(\text{NO}_3)_3 \cdot x\text{H}_2\text{O}$ (Sigma-Aldrich), $\text{SnCl}_2 \cdot 2\text{H}_2\text{O}$ (Sigma-Aldrich), $\text{Pb}(\text{NO}_3)_2$ (Sigma-Aldrich), $(\text{NH}_4)_2\text{HPO}_4$ (Sigma-Aldrich), SbCl_3 (Sigma-Aldrich), $\text{Bi}(\text{NO}_3)_3 \cdot 5\text{H}_2\text{O}$ (Sigma-Aldrich), ammonium thiosulfate (Alfa Aesar).

Except for the Sb-promoted iron catalysts, all other promoted catalysts were prepared by single-step co-incipient wetness impregnation. The Fe catalysts promoted with Sb were synthesized twice via alternating the impregnation sequence. In first case, silica was impregnated first with the Fe precursor and then with Sb. It gave the SbFe/SiO_2 sample. In the second case, silica was impregnated first with Sb and then with Fe. The FeSb/SiO_2 catalyst was obtained. The concentrations of the impregnating solutions were calculated in order to obtain about 10 wt. % iron in the final catalysts,

the ratio of Fe to promoter (M) was 100:2. After the impregnation, the catalysts were dried overnight in an oven at 100 °C. Then they were calcined in air at 400 °C for 6 h with the 1 °C/min temperature ramping.

2.1.2. Silica supported catalysts prepared by mechanical mixing

The non-promoted Fe(20%)/SiO₂ catalyst prepared by impregnation with iron nitrate was used for mechanical mixing. After the impregnation, the samples were dried in oven at 100 °C for 12 h followed by calcination in air at 400 °C for 6 h with the heating ramp of 1 °C/min. The FeSb/SiO₂ (M) and FeSn/SiO₂ (M) samples were prepared by mechanical mixing of Fe(20%)/SiO₂ and Sb/SiO₂, Fe(20%)/SiO₂ and Sn/SiO₂ catalysts, respectively. The Fe content in the final catalysts prepared by impregnation and mechanical mixing was fixed at 10 wt. %, while the molar ratios of Fe/Sb and Fe/Sn were 100:2.

2.1.3. Zirconia supported catalysts

Commercial zirconia (Alfa Aesar) was used as the catalytic support. Normally, distilled water is served as solvent. As in previous case Nb, Sn and Sb salts were dissolved using ethanol. The following precursors were used for the promotion of zirconia supported iron catalysts: KNO₃ (Sigma-Aldrich), CsNO₃ (Aldrich), Mg(NO₃)₂·6H₂O (Sigma-Aldrich), Ba(NO₃)₂ (Sigma-Aldrich), Ce(NO₃)₃·6H₂O (Fluka), NbCl₅ (Alfa Aesar), (NH₄)₆Mo₇O₂₄·4H₂O (Fluka), Mn(NO₃)₂·4H₂O (Alfa Aesar), Cu(NO₃)₂·3H₂O (Acros Organics), Zn(NO₃)₂·6H₂O (Sigma-Aldrich), Ga(NO₃)₃·xH₂O (Sigma-Aldrich), In(NO₃)₃·xH₂O (Sigma-Aldrich), SnCl₂·2H₂O (Sigma-Aldrich), Pb(NO₃)₂ (Sigma-Aldrich), SbCl₃ (Sigma-Aldrich), Bi(NO₃)₃·5H₂O (Sigma-Aldrich), NH₄VO₃ (Sigma-Aldrich).

Except for the Sb-promoted iron catalyst, all the other promoted catalysts were prepared by single-step co-impregnation method. For this, a 0.2 M solution of $\text{Fe}(\text{NO}_3)_3 \cdot 9\text{H}_2\text{O}$ along with the promoter salt was added drop by drop to the zirconia support. After the impregnation, the mixture was stirred for 8 h at room temperature. Next, the mixture was evaporated to dryness at 80 °C, then the catalysts were dried overnight in an oven at 120 °C. Finally, they were calcined in air at 500 °C for 5 h with the 1 °C/min temperature ramping. The concentrations of the impregnating solutions were calculated in order to obtain about 10 wt. % iron in the final catalysts, the ratio of Fe to promoter (M) was 100:2. The nominal concentration of the K containing catalysts was 1%.

2.2. Evaluation of catalytic performance

2.2.1. Evaluation of Fe-based catalysts in fixed-bed reactors

The catalytic performance of SiO_2 and ZrO_2 -supported iron catalysts for FT synthesis and CO_2 hydrogenation reaction was measured using reactors with the internal diameter of 2 mm (**Figure 2-1**). Typically, 100 mg of fresh catalyst have been loaded into the reactor. The catalyst was activated with a heating ramp of 2 °C/min until reaching the temperature of 350 °C and dwelling at that temperature for 10 h under CO flow (10 mL/min) at atmospheric pressure. After cooling down to 180 °C, syngas (for SiO_2 -supported iron catalysts) with $\text{H}_2/\text{CO} = 1/1$ or $\text{CO}_2:\text{H}_2$ 3:1 (for ZrO_2 -supported iron catalysts) was introduced into the reactor. Nitrogen with flow of 1 mL/min was used as internal standard for the calculation of conversion. After the flow rates and pressure have been stabilized, the temperature was increased up to 350 °C to start the reaction.

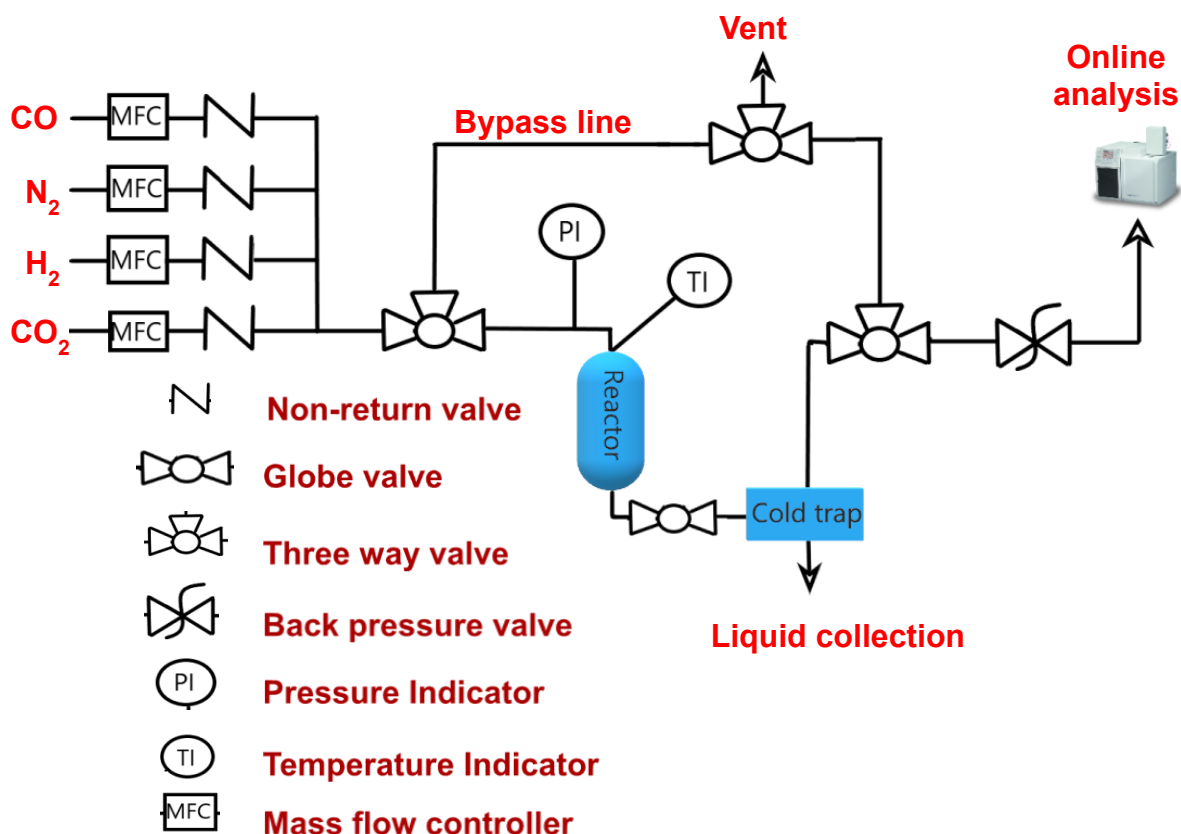


Figure 2-1. High pressure catalytic set-up for CO and CO₂ hydrogenation.

The TOF values were obtained as proposed by de Jong¹ et al. using the density of Hägg iron carbide Fe₅C₂ ($\rho = 7.57 \text{ g/cm}^3$) and assuming 14 Fe atoms/nm². Also, it has been assumed that the spherical iron-containing particles consist completely of iron carbide at their surfaces. The particle size used for TOF calculation shown in chapters 3 and 4 was determined after catalyst activation. Indeed, the catalysts can change when they are exposed to air. However, for our calculation and following previous works in our group^{2,3} we assumed that all the Fe present in the catalyst will be active and in the form of Fe₅C₂. Finally, we are aware that these assumptions can lead to overestimation of TOF values. However, it allows us to have a comparison of the tested catalysts.

2.2.2. Avantium high throughput equipment for determination of suitable promoters

The catalytic tests were carried out in the high throughput experimentation unit (HTE, Flowrence, Avantium, **Figure 2-2**) and in a laboratory fixed-bed reactor. In the HTE unit, the feed gas is homogeneously split by calibrated high pressure-drop capillaries into 16 reactors. Each four reactors formed one independent block, where the temperature can be separately controlled. High boiling point product (liquid phase) is constantly collected at 60 °C, before the rest gas phase flows through GC for analysis. Catalyst loading was completed in a stainless-steel tube with inner diameter of 2.0 mm, length of 15 cm. Both ends (height of 3.5 cm) of the reactor tube were filled with inert SiC (size of 0.105 mm and 0.210mm), where the catalyst (size: 50 – 150 μm) was loaded in between. Prior to FT synthesis, all catalysts were treated in the CO atmosphere (10 mL/min) at 350 °C for 10 h and cooled to 180 °C. The activation procedure for silica supported iron catalysts was optimized in our earlier report⁴. After pressurized in H₂/CO (1:1) to 10 bar, temperature was stepwise (1 °C/min) increased to 350 °C. The catalytic performance was measured under five different WHSV: 3.4 L/g.h → 4.5 L/g.h → 6.75 L/g.h → 2.25 L/g.h → 1.5 L/g.h. No liquid phase was collected within all the HTE tests over iron catalysts. The gaseous products were analyzed online using a gas chromatograph (GC). Permanent gases (He, H₂, O₂, N₂, CH₄, and CO) were separated by a Hayesep Q/molsieve column and determined by a TCD; CO₂ and C₂-C₃ hydrocarbons by a PPQ/PPQ column and TCD; C₅-C₁₂ hydrocarbons by a CP-Sil5/CP-Sil5 column and FID, respectively.

In the case of zirconia-supported catalysts, the activation procedure was performed at 350 °C for 10 h with a heating ramp 2 °C/min. After pressurized in H₂/CO₂ (3:1) to 10 bar, temperature was stepwise (1 °C/min) increased to 350 °C. The catalytic

performance was measured under different WHSV (4.67-18.19 L/g.h) staying at least 12 h at each gas space velocity. No liquid phase was collected within all the HTE tests over iron catalysts.

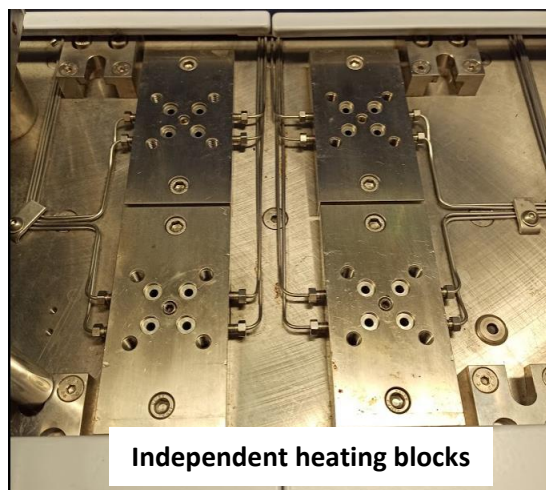
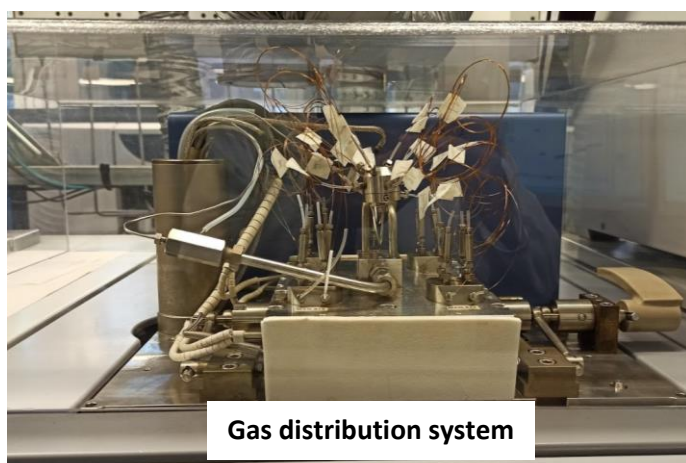
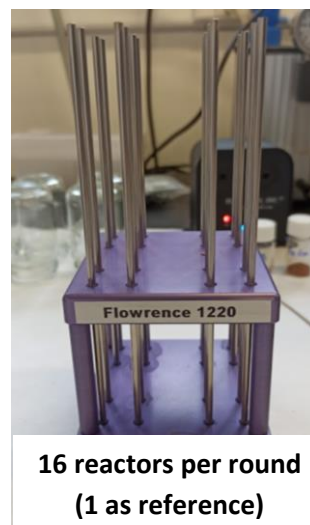


Figure 2-2. Flowrence Avantium High Through put Experiment unit.

2.3. Analysis method

The FT and CO₂ hydrogenation reaction products were analyzed on-line and by gas chromatography (GC). The periodical analysis of unreacted N₂ and CO or CO₂, and produced CH₄ and CO or CO₂ were performed using a packed CTR-1 column and a thermal conductivity detector (TCD) in order to determine CO/CO₂ conversion and CO/CO₂ and CH₄ selectivity. Uncondensed light hydrocarbons were analyzed also on-line using a capillary Rt-Q-PLOT column by a flame-ionization detector (FID).

The CO/CO₂ conversions are calculated as follows:

$$X_{CO} = \left[1 - \left(\frac{A_{initial\ N_2}/A_{reaction\ N_2}}{A_{initial\ CO}/A_{reaction\ CO}} \right) \right] * 100 \quad (17)$$

$$X_{CO_2} = \left[1 - \left(\frac{A_{initial\ N_2}/A_{reaction\ N_2}}{A_{initial\ CO_2}/A_{reaction\ CO_2}} \right) \right] * 100 \quad (18)$$

The feed gas of the internal standard gas (N₂) is controlled by a mass flow controller. The inlet molars of CO and N₂ (n_{CO} and n_{N₂}) can be calculated from the ideal gas equation (eq. 19). So, the generation rate of CH₄ and CO₂ can be calculated by equation 20 and 21, respectively, and the selectivity can be also calculated by equation 22 and equation 23, respectively.

$$PV = nRT \quad (19)$$

$$n_{CH_4} = \frac{A_{CH_4}/f_{CH_4}}{A_{N_2}/f_{N_2}} * n_{N_2} \quad (20)$$

$$n_{CO_2} = \frac{A_{CO_2}/f_{CO_2}}{A_{N_2}/f_{N_2}} * n_{N_2} \quad (21)$$

$$S_{CH_4} = \frac{n_{CH_4}}{n_{CO} * CO_{conv\%} - n_{CO_2}} * 100\% \quad (22)$$

$$S_{CO_2} = \frac{n_{CO_2}}{n_{CO} * CO_{conv\%}} * 100\% \quad (23)$$

Hydrocarbons selectivity were calculated from FID data as follows:

$$S = n \left(\frac{A_i}{A_{CH_4}} \right) \left(\frac{f_i}{f_{CH_4}} \right) \left(\frac{M_{CH_4}}{M_i} \right) * S_{CH_4} \quad (24)$$

Where: n = carbon atoms, A_i = Area of component "i", A_{CH₄} = Area of methane in FID. f_i/f_{CH₄} = Detector response factor for component "i" relative to methane, M_{CH₄} = Methane molecular weight. M_i = Molecular weight for component "i" and S_{CH₄} = Selectivity of methane in TCD.

The absence of intraparticle transport limitations was checked by calculating the Weisz-Prater criterion was way below 0.3 indicating no internal diffusion limitations.

$$N_{w-p} = \frac{r \cdot L^2}{D_{eff} \cdot C} \leq 0.3 \quad (25)$$

External diffusion limitations were evaluated using the Carberry number:

$$Ca = \frac{r \cdot L}{K_D \cdot C} \leq 0.05 \quad (26)$$

The isothermal regime in milli-fixed bed and centimetric fixed bed reactors was verified using the Mears criterion for neglecting radial temperature gradient:

$$(1 - \varepsilon) |\Delta H r| \frac{T_A d_t^2}{4 \lambda_{er}^{sf} T_p^2} \left(1 + \frac{8 \lambda_{er}^{sf} T_p^2}{U d_t} \right) < 0.4 \quad (27)$$

2.4. Catalysts characterization

2.4.1. X-Ray diffraction



Figure 2-3. Bruker AXS D8 diffractometer.

The ex situ X-ray powder diffraction (XRD) experiments were conducted using a Bruker AXS D8 diffractometer (**Figure 2-3**) with CuK α radiation ($\lambda = 0.1538$ nm). The

XRD patterns were collected in the 5–90° (2θ) range, with the 0.02° step size and 0.5 s step time. The crystalline phases were identified by comparing the diffraction patterns with this of the standard powder XRD files (JCPDS). The average crystallite size was calculated using the diffraction peaks according to the Scherrer equation.

2.4.2. X-Ray fluorescence

Relative content of oxide was determined with the use of an energy dispersive micro-X-ray Fluorescence spectrometer M4 TORNADO (**Figure 2-4**). This instrument is equipped with 2 anodes: a Rhodium X-ray tube 50 kV/600 mA (30 W) and a Tungsten X-Ray tube 50 kV/700 mA (35 W). For sample characterization, the X-rays Rhodium with a polycapillary lens enabling excitation of an area of 200 μm was used. The detector used was a Silicon-Drift-Detector Si (Li) with <145 eV resolution at 100000 cps (Mn $K\alpha$) and cooled with a Peltier cooling (253°K). The measurement was done under vacuum (20 mbar). The elements, that can be measured by this instrument unit range from sodium (Na) to uranium (U). Quantitative analysis was done using fundamental parameter (FP) (standard less). The quantification was made based on the identified element.



Figure 2-4. *Micro-X-ray Fluorescence spectrometer M4 TORNADO (Bruker).*

2.4.3. Surface area and porosity

The N₂ physisorption measurements were performed on a Micromeritics Tristar II PLUS Surface Area and Porosimetry analyser (**Figure 2-5**). The samples were degassed under vacuum at 250 °C for 2 h. The nitrogen adsorption-desorption isotherms were measured at -196 °C. The specific surface area of the samples was calculated by the BET method.

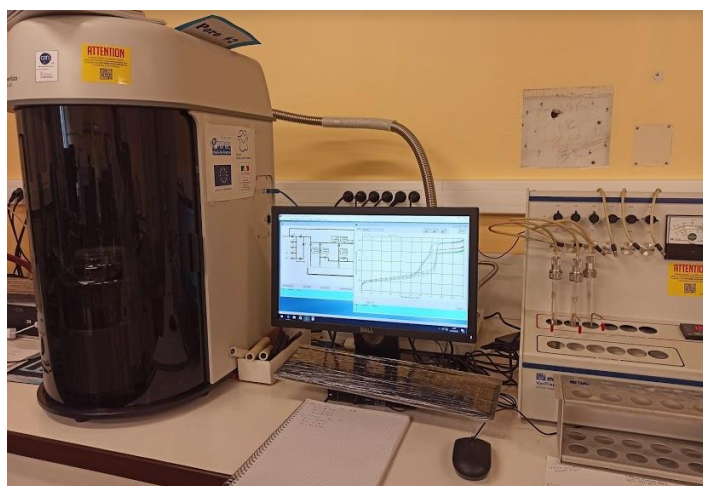


Figure 2-5. *Micromeritics Tristar II PLUS Surface Area and Porosimetry analyzer.*

2.4.4. Transmission electron microscopy

Fresh sample and catalysts activated in a flow of CO at 350 °C and then passivated in a flow of nitrogen at room temperature were characterized using Scanning Transmission Electron Microscopy (STEM), under the High-Angle Annular Dark- Field imaging (STEM-HAADF) and Energy-Dispersive X-ray Spectroscopy (STEM-EDS) modes. The powder specimens were dispersed in ethanol by ultrasounds and corresponding to each sample, a drop of solution was deposited on a holey carbon film previously deposited on a 300 mesh TEM Cu grid. The catalysts were analysed using STEM with a high energy beam of 200 kV and a beam size of <math><1 \text{ \AA}</math> for the imaging purposes, whereas the chemical maps were carried out by a probe with a diameter of about 1 Å. STEM-HAADF with Z-contrast enabled the identification of atoms and atoms agglomerations of species associated with heavy elements, more specific, the heavier

the element the higher the contrast is. The STEM-EDS mapping allowed the analysis of elemental composition within the samples. The Analytical TEM Jeol-ARM200 Cold FEG microscope with Objective and Probe correctors was used for these investigations. The microscope was operated at 200 kV under STEM using a 1 Å diameter of the beam achieved by using the diaphragms of 150 μm and 50 μm. The STEM-EDS maps were acquired on a Jeol Centurio 100 mm² detector mounted on the TEM. A scanning speed of 20 μsec/px was employed for imaging within the Digital Micrograph software and 0.05 μs/px for STEM-EDS elemental mapping using the Analysis Station software, respectively. The maps size was fixed at 256x256 px with a spatial drift correction every 60 s. In order to gather maps with high signal to noise ratios, long duration chemical mapping were carried out for durations between 80 and 180 minutes. The elemental maps were used in a first approach to assess qualitatively the presence, distribution and location of the elements of interest and to quantitatively estimate the size of the Fe NPs, in a second time. The size distribution histogram of each sample was conducted based on more than 100 nanoparticles taken from different micrographs acquired in the Digital Micrograph software, whilst the elemental maps acquired in the Analysis Station were employed to assess for the size of Fe particles (measured in the longer direction). The Scanning Transmission Electron Microscopy (STEM) analyses were carried on a double corrected analytical TEM 200 CF operating at 200 kV. Elemental mapping of the elements of interest (256 × 256 px) was carried out using the Energy Dispersive X-ray Spectrometer (EDX) Centurio 100 detector with a scanning speed of 0.05 msec/px, whilst applying a drift correction every 60 s. STEM micrographs were acquired using a High Angular Annular Dark Field (HAADF) detector and a camera length of 8 cm, with a spot diameter of 0.1 nm.

2.4.5. Temperature programmed reduction

The reduction behavior of the catalysts was examined by hydrogen temperature-programmed reduction (TPR) using an AutoChem II 2920 apparatus (Figure 2-6). The samples (0.05 g) were reduced in a flow of 5% H₂/Ar flow (30 mL/min) and heated up to 1100 °C with the temperature ramp rate of 10 °C/min.

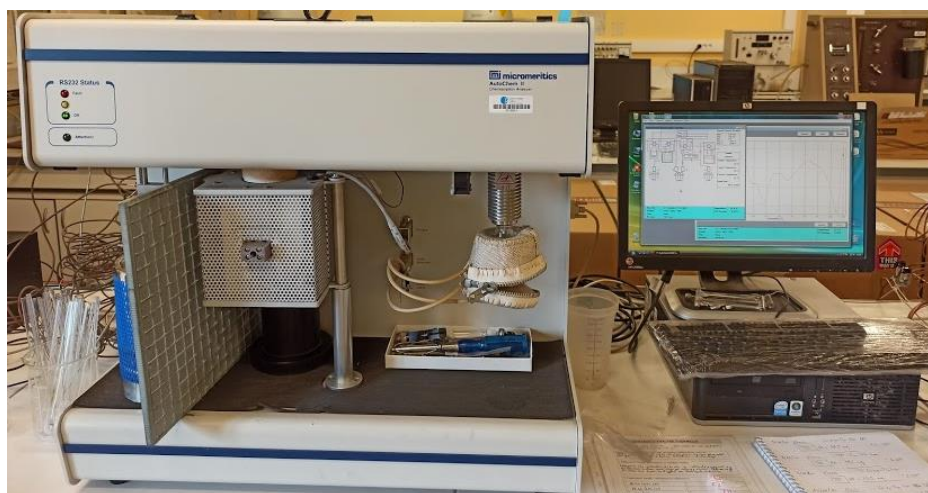


Figure 2-6. *Micrometrics Auto Chem II 2920 equipment.*

2.4.6 Thermogravimetric analysis

To determine the carbon deposition in the catalysts, the thermogravimetric analysis was performed using a SDT Q600 V20.9 Build 20 Thermogravimetric Analyzer (TGA) & Differential Scanning Calorimeter (DSC) shown in Figure 2-7 with the 10 mg sample, submitted to a temperature ramp of 5 °C/min until 600 °C under air.



Figure 2-7. *SDT Q600 V20.9 Build 20 Thermogravimetric Analyzer.*

2.4.7 Temperature programme desorption

For the CO₂ temperature programmed desorption (TPD) experiments, the samples were pretreated at 500°C in He for 1 h, cooled down to 40°C, and exposed to CO₂ for 30 min. Then, the samples were heated up with the ramping rate of 10°C/min to reach 700°C in He flow. The CO₂ desorption was measured by a TCD detector.

2.4.8. X-Ray photoelectron spectra

The X-Ray Photoelectron Spectra (XPS) were obtained using a Kratos AXIS UltraDLD spectrometer working with Al K α X-rays at 1486.7 eV (**Figure 2-8**). The instrument work function was calibrated to give an Au 4f_{7/2} metallic gold binding energy (BE) of 83.96 eV. The spectrometer calibration was adjusted to give a binding energy (BE) of 932.62 eV for metallic Cu 2p_{3/2}. As the sample holder and spectrometer are in electrical contact, the Fermi level of the spectrometer and conductive samples are aligned; so we can use the spectrometer work function instead. For non-conductive samples (as our case), due to charging effect, we adjusted them to the binding energies with respect to a known energy reference. We used Si 2p (103.3 eV) as energy reference. The charge neutralizer for this spectrometer is a low energy electron emitting filament together with a charge balance plate localized above the sample.

The XPS spectra of the fresh catalyst were first measured and then the catalyst was placed into the in-situ reaction cell heated under a flow of CO (50 mL/min, 1 bar) from room temperature up to 250 °C and after 350 °C at a heating rate of 5 °C/min and kept for 1 h at each temperature. The treated sample was then transferred under vacuum (without exposure to air) to the analysis chamber where the XPS spectra of the sample was recorded. The (NAP) XPS spectra were analyzed by fitting the Shirley-type function and a combination of Gaussian and Lorentzian functions to fit the data with the Casa XPS software.



Figure 2-8. *X-Ray Photoelectron Spectra (XPS) Kratos AXIS UltraDL D spectrometer.*

2.4.9. Near Ambient Pressure – X-Ray photoelectron spectra

The freshly calcined samples were first loaded into the NAP-XPS spectrometer (**Figure 2-9**) and exposed to CO at 50°C. Then, the temperature was increased subsequently from room to 250 °C and to 350 °C. After the exposure to 350 °C in CO, the sample was cooled down to 50 °C. After the subsequent temperature increase to 350 °C, CO was switched to syngas ($H_2/CO=1$) at 350 °C. The sample was maintained in syngas at this temperature and then cooled back again to 50 °C. At different steps of the in-situ catalyst treatment under about 1 mbar of CO or syngas, the position, shape and intensity of Fe 2p, C 1s, and Bi 4f peaks were thoroughly analyzed by XPS. Since the catalysts were supported on CNT, we interpret the data based on the binding energies corrected to C 1s peak (284.5 eV).



Figure 2-9. *Near Ambient Pressure X-Ray Photoelectron Spectroscopy at Charles University.*

2.4.10. In-situ magnetic characterization

The magnetic characterization was performed using a Föner vibrating-sample magnetometer^{5,6,7} equipped with an in-situ cell. 10 mg of the sample was placed in the in-situ cell and heated to 350 °C under the flow of pure CO (0.3°C/min, $V_{CO}=30$ ml/min). After reaching 350 °C, the samples were kept in the flow of CO until reaching a constant value of magnetisation. After the activation, the sample was cooled to the room temperature in the flow of CO. The pre-treatment with syngas ($H_2/CO = 1$, $V_{syngas} = 30$ ml/min) was performed with the samples already activated in CO and using similar procedure as pre-treatment in CO. The thermomagnetic curves (magnetisation versus temperature) were measured during cooling down the catalyst in syngas from 350 °C to room temperature.

2.4.11. Mössbauer spectroscopy

The transmission ^{57}Fe Mössbauer spectra were collected at -153 °C or room temperature with a sinusoidal velocity spectrometer using a $^{57}Co(Rh)$ source. The

velocity calibration was carried out using an α -Fe foil at room temperature. The source and absorbing samples were kept at the same temperature during the measurements. The Mössbauer spectra were fitted using the Mosswinn 4.0 program⁸. The in-situ experiments were performed at the pressures up to 10 bar, in a state-of-the-art high-pressure Mössbauer in-situ cell – recently developed at the Reactor Institute in Delft⁹. The high-pressure beryllium windows used in this cell contain 0.08% Fe impurity whose spectral contribution was fitted and removed from the final spectra.

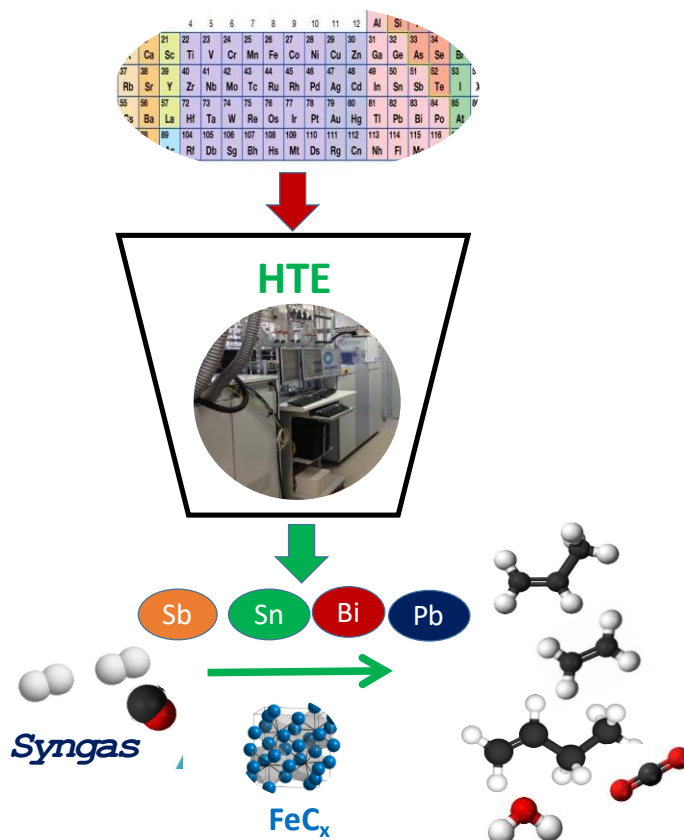
2.4.12. In-situ X-ray absorption spectroscopy

The in-situ Sb K-edge and Sn K-edge X-ray absorption spectroscopy (XAS) spectra were measured at Beamline CLÆSS of the ALBA synchrotron (Barcelona, Spain). The X-ray energy range 2.4–63.2 keV can be covered, using pairs of Si (111) and Si (311) crystals. The current signals from the ionization chambers were collected, amplified and converted to output voltage by the ALBA Electrometer. For the in-situ XANES and EXAFS measurements, the sample was pressed into a pellet with a 5 mm diameter and added in a reactor ITQ-ALBA Multipurpose Cell. The measurements were performed in presence of CO ($P = 1$ bar) for cabidization and syngas ($H_2/CO = 1$, $P = 7$ bar) for the FT reaction at temperature ranging from ambient to 350 °C. The data were collected in transmission mode and analyzed with the Athena software¹⁰.

2.5. References

1. Torres Galvis, H. M. *et al.* Iron particle size effects for direct production of lower olefins from synthesis gas. *J. Am. Chem. Soc.* **134**, 16207–16215 (2012).
2. Gu, B. *et al.* Synergy of nanoconfinement and promotion in the design of efficient supported iron catalysts for direct olefin synthesis from syngas. *J. Catal.* **376**, 1–16 (2019).
3. Gu, B. *et al.* Size and promoter effects on iron nanoparticles confined in carbon nanotubes and their catalytic performance in light olefin synthesis from syngas. *Catal. Today* 0–1 (2019) doi:10.1016/j.cattod.2019.05.054.
4. Cheng, K. *et al.* Pore size effects in higher temperature Fischer-Tropsch synthesis over supported iron catalysts. *J. Catal.* **328**, (2015).
5. Chernavskii, P. A., Lunin, B. S., Zakharyan, R. A., Pankina, G. V. & Perov, N. S. Experimental setup for investigating topochemical transformations of ferromagnetic nanoparticles. *Instruments Exp. Tech.* **57**, 78–81 (2014).
6. Chernavskii, P. A., Dalmon, J.-A., Perov, N. S. & Khodakov, A. Y. Magnetic characterization of Fischer-Tropsch catalysts. *Oil Gas Sci. Technol.* **64**, 25–48 (2009).
7. Chernavskii, P. A., Khodakov, A. Y., Pankina, G. V., Girardon, J.-S. & Quinet, E. In situ characterization of the genesis of cobalt metal particles in silica-supported Fischer-Tropsch catalysts using Foner magnetic method. *Appl. Catal. A Gen.* **306**, 108–119 (2006).
8. Klencsár, Z. Mössbauer spectrum analysis by Evolution Algorithm. *Nucl. Instruments Methods Phys. Res. Sect. B Beam Interact. with Mater. Atoms* **129**, 527–533 (1997).
9. Wezendonk, T. A. *et al.* Elucidating the Nature of Fe Species during Pyrolysis of the Fe-BTC MOF into Highly Active and Stable Fischer-Tropsch Catalysts. *ACS Catal.* **6**, 3236–3247 (2016).
10. Ravel, B. & Newville, M. ATHENA, ARTEMIS, HEPHAESTUS: Data analysis for X-ray absorption spectroscopy using IFEFFIT. *J. Synchrotron Radiat.* **12**, 537–541 (2005).

Chapter 3 Identification of efficient promoters and selectivity trends in high temperature Fischer-Tropsch synthesis over supported iron catalysts



Abstract: In this work, 29 elements were evaluated as promoters for silica supported iron catalysts for high temperature Fischer-Tropsch synthesis using a high-throughput experimentation unit. The selected promoters include alkali/alkaline metals, transition metals, precious metals and lanthanides. Several general selectivity trends were observed and discussed. The selectivity enhancement to light olefins requires maintaining low selectivity to methane and light paraffins and at the same time, slowing the chain growth to the C₅₊ hydrocarbons. A major increase in FT rate principally due to higher intrinsic site activity, was observed over the catalysts promoted with metals with low melting points such as tin, antimony, bismuth and lead. These promoted catalysts also exhibited better stability. The effect of the promotion with tin and antimony on the olefin selectivity was not noticeable, while the presence of bismuth and lead results in the major enhancement of the selectivity to light olefins, lower methane and C₂-C₄ paraffin selectivities.

Paper published in Applied Catalysis B: Environmental, Volume 273, 15 September 2020

3.1. Introduction

The interest in high temperature FT synthesis has been growing in the last decades, because this reaction provides an opportunity for conversion of alternative and renewal feedstocks^{1,2}, such as biomass, organic and plastic waste, into value-added chemicals such as light olefins. In addition, FT synthesis produces ultra clean and environmentally friendly chemicals, which are essentially free from sulfur, nitrogen and undesirable aromatics. Iron catalysts have shown the highest activity and olefin selectivity in FT synthesis^{3,4,5,6}. In recent years, the research interests have shifted from bulk to supported iron FT catalysts. Indeed, supported iron catalysts provide higher surface area and iron dispersion, more efficient use of active phase and promoters, better mechanical resistance and potentially enhanced activity, selectivity and stability. The catalytic performance of supported iron catalysts can be further improved by several strategies such as promotion^{7,8}, nanoconfinement^{9,10,11} of active phase and by optimization of the interaction of iron species with the support¹².

The FT reaction involves iron carbide species^{13,14,15,16,17}, which form in-situ in the iron catalysts during activation in carbon monoxide or syngas. FT synthesis is a complex catalytic reaction; in addition to iron carbide, the presence of different iron oxide species and metallic iron can affect the overall catalytic performance^{18,19}. Electronic and structural promoters have been intensively used in order to increase iron dispersion, extent of iron carbidization, FT reaction rates and light olefin selectivity over Fe-based catalysts. Addition of promoters can affect iron dispersion, iron carbidization, electronic properties of the active species and rate of primary and secondary elementary steps of FT synthesis. Most of earlier publications have been focused on the promotion of iron catalysts with alkali metals^{6,20,21,22,23,24,25,26} and copper^{7,25,27,28}. More recently, the group of de Jong^{3,29,30} and Sasol researchers³¹

reported that simultaneous addition of sodium and sulfur improved the selectivity to olefins. They suggested³² that sulfur could shift the selectivity toward the short-chain C₂–C₄ hydrocarbons without a simultaneous increase in the selectivity to methane, while the presence of alkali ions increased the olefin to paraffin ratio.

Note however, that promoter effect on the FT reaction selectivity over iron catalysts is rather complex, since the rate of several FT elementary steps could be affected. In many cases, direct comparison of iron catalysts promoted with different elements is not obvious, because of different supports, promoter content, catalyst preparation and activation procedures. Very few information is available in the literature about influence of the promoters on the catalytic performance of iron catalysts on the same support, prepared using the same method, at the same concentration level and tested under exactly the same reaction conditions. Recently, we have discovered^{10,11,33,34} that the catalytic performance of iron catalysts can be significantly improved by using bismuth or lead as promoters; the reaction rate was increased several times over the promoted catalysts.

High throughput experimentation (HTE)^{35,36,37} represents nowadays a powerful tool for the design of new efficient heterogeneous catalysts. The goal of this chapter is to explore the potential of HTE for identification of efficient promoters and selectivity trends in FT synthesis. The conducted experiments cover numerous promoters from 1A-5A and 1B-8B groups of the Periodic Table, which include alkali/alkaline metals, transition metals, precious metals and lanthanides for iron FT catalysts. 29 elements (Li, K, Cs, Mg, Ca, Sr, Ba, La, Ce, Zr, Nb, Cr, Mo, W, Mn, Co, Ni, Pd, Cu, Ag, Au, Zn, Ga, In, Sn, Pb, P, Sb, Bi) at the same molar concentration in the catalyst were evaluated in high temperature FT synthesis. Silica is a common support for many heterogeneous catalysts and has been widely used in numerous industrial

applications. The supported iron catalysts were prepared by incipient wetness impregnation of silica with aqueous solutions of hydrous iron nitrate. The catalytic results and in particular those relevant to the selectivity and stability were measured as a function of carbon monoxide conversion. They are compared and discussed with those obtained for the reference non-promoted iron catalyst.

3.2. Results and discussion

3.2.1. Silica supported iron catalysts promoted with 29 elements

3.2.1.1. Conversion and reaction rate

All the catalysts were tested in high temperature FT synthesis under identical conditions ($H_2/CO = 1$, $P = 10$ bar, $T = 350$ °C) in HTE. The carbon monoxide conversion was negligible over the Cr-, Nb-, Ga-, Pd-, Co-, In-, Mo-, Zn-promoted catalysts. All other examined catalysts presented measurable CO conversions within the tested WHSV ranges. High temperature FT synthesis over all catalytic leads to light C_2 - C_4 olefins, light C_2 - C_4 paraffins, methane, CO_2 and C_{5+} longer chain hydrocarbons. The carbon monoxide conversions measured at iso-WHSV= 3.4 L/g.h in the HTE unit over different promoted iron catalysts are shown in **Figure 3-1**. Most of the promoted Fe catalysts exhibit a CO conversion in the range of 10% - 30%, which is similar or slightly higher than the non-promoted Fe/SiO₂ counterpart (**Figure 3-1**). Interestingly, the Bi-, Pb-, Sn- and Sb-promoted catalysts exhibit an enhanced catalytic activity. Under the same conditions, the carbon monoxide conversion on these catalysts was much higher (30-85%). The catalytic tests in the HTE setup clearly identify Bi-, Pb-, Sn-, and Sb as the most promising promoters in order to obtain iron catalysts with higher activity in FT synthesis.

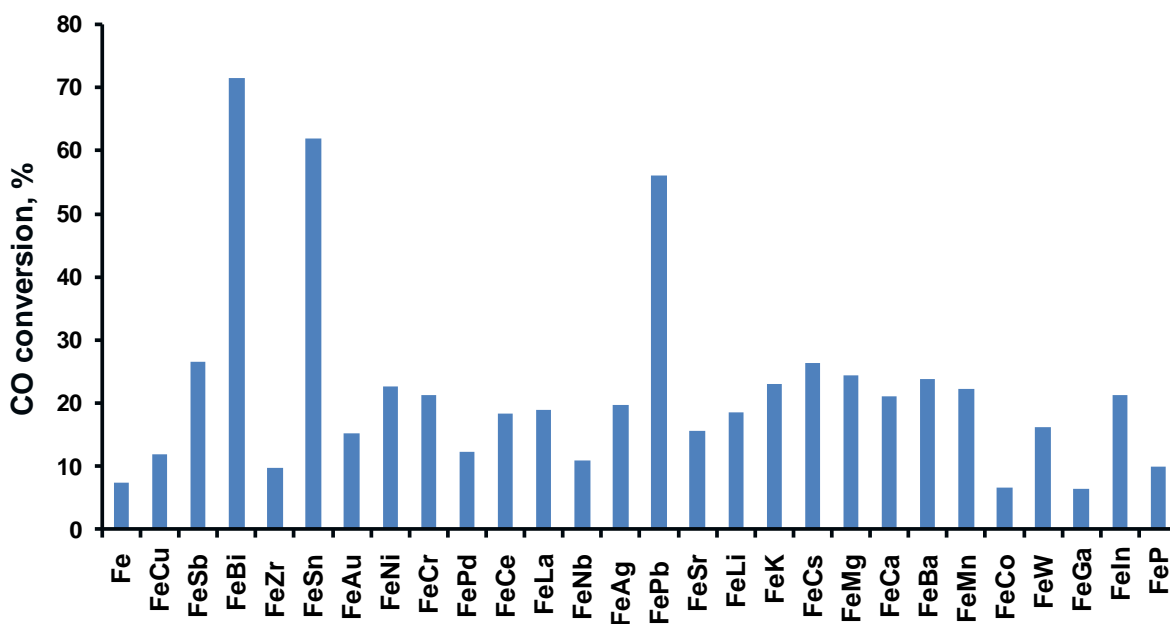


Figure 3-1. Carbon monoxide conversion measured over the promoted silica supported iron catalysts at iso-WHSV: $T=350^{\circ}\text{C}$, $\text{H}_2/\text{CO}=1$, $P=10$ bar, $\text{WHSV}=3.4$ L/g.h.

3.2.1.2 Selectivity trends in high temperature FT synthesis

The selectivities to CO_2 , methane, $\text{C}_2\text{-C}_4$ light olefins, light paraffins and C_{5+} hydrocarbons for all investigated catalysts measured at different WHSV are displayed in **Figure 3-2** and **Figure 3-3**, and plotted as functions of carbon monoxide conversion. The selectivity to carbon dioxide (**Figure 3-3a**) displays scattered points at low conversion. The CO_2 selectivity increases as function of conversion over all catalysts and reaches the stoichiometric value of 50% at CO conversion exceeding 30%. Carbon dioxide in FT synthesis over iron catalysts is principally produced via water gas-shift (WGS) reaction: $\text{CO} + \text{H}_2\text{O} = \text{CO}_2 + \text{H}_2$. Thus, some variation of the activity of the promoted catalysts can be assigned to their different activities in WGS and FT synthesis. The CO_2 selectivity close to 50% at high CO conversion suggests that FT synthesis over iron catalysts occurs simultaneously with the WGS reaction with almost complete conversion of water by its reaction with CO:

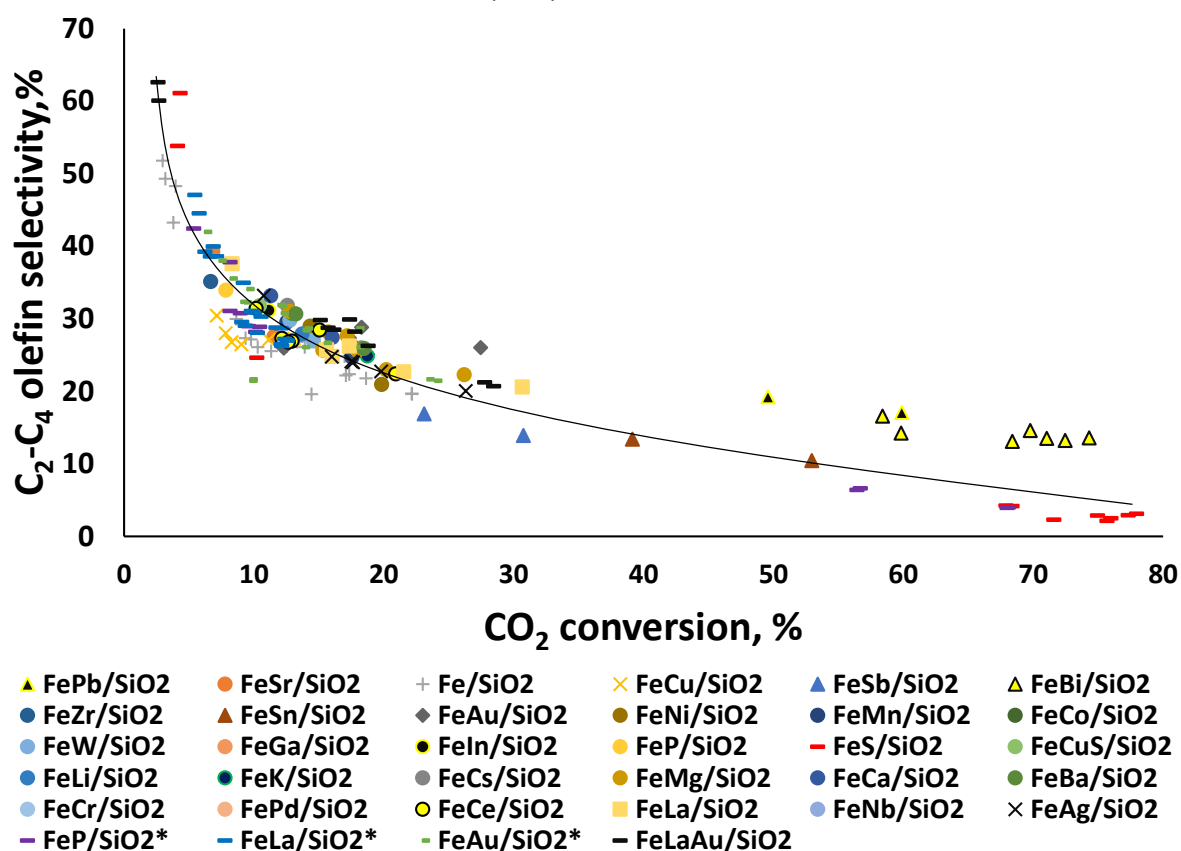
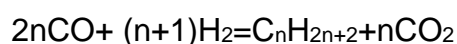
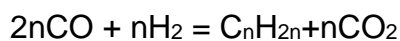


Figure 3-2. Light olefin selectivity versus carbon monoxide conversion. Promoted Fe/SiO_2 , catalysts. $\text{Fe}/\text{P}=100:2$, $\text{H}_2/\text{CO}=1$, $\text{WHSV}=2.25\text{-}6.75 \text{ L/g.h}$, $P=10 \text{ bar}$. *These catalysts have different amount of promoter

Figure 3-3b displays methane selectivity observed on the promoted iron catalysts as a function of conversion. Higher methane selectivities were observed at rather low carbon monoxide conversion (<10%). The methane selectivity decreases with increase in conversion and at higher conversion scatters between 5 and 15% as a function of catalysts. The lowest methane selectivity was observed over the Pb and Bi-promoted catalysts and the highest over the Sn- and Zr-promoted counterparts.

The selectivity to light olefins (**Figure 3-2**) also decreases as a function of carbon monoxide conversion. The maximum light olefin selectivity close to 60 % is observed at the relatively low CO conversion (< 2-3 %). Indeed, the selectivity to a specific hydrocarbon range in FT synthesis is limited by the Anderson–Schulz–Flory (ASF)

statistics, which predicts the maximum selectivity of ~58% for the C₂-C₄ hydrocarbons. In this work, we observed the maximum C₂-C₄ light olefin selectivity up to 60%. Again, the bismuth and lead promoted catalysts do not follow the general trend; the light olefin selectivities higher at the same conversion level on the Bi and Pb-containing iron catalysts than on any other counterparts. The decrease in both methane and light olefin selectivities with the carbon monoxide conversion suggests that all these compounds could be primary products of FT synthesis over iron catalysts.

Interestingly, only very slight effect of carbon monoxide conversion on the selectivity to the C₂-C₄ paraffinic hydrocarbons was observed over various promoted iron catalysts (**Figure 3-3c**). The selectivity data scatter between 5 and 20%. Interestingly, the C₂-C₄ paraffin selectivity only slightly increases as a function of carbon monoxide conversion. Taking into account that the selectivity to light olefins decreases with the CO conversion, while the selectivity to light paraffins is only slightly affected by the conversion, one can suggest that secondary olefin hydrogenation could be only one of the main reasons responsible for the decrease in the light olefin selectivity with conversion.

Carbon monoxide conversion affects to a greater extent the C₅₊ hydrocarbon selectivity (**Figure 3-3d**). The C₅₊ selectivity is close to zero at the CO conversion slower than 10%. It steadily increases with the CO conversion and reaches 25-30% at the CO conversion higher than 20%. The C₅₊ selectivity remains nearly constant, when the CO conversion higher than 30%. It worth noting that the decrease in the C₂-C₄ light olefin selectivity clearly coincides with the increase in the C₅₊ selectivity.

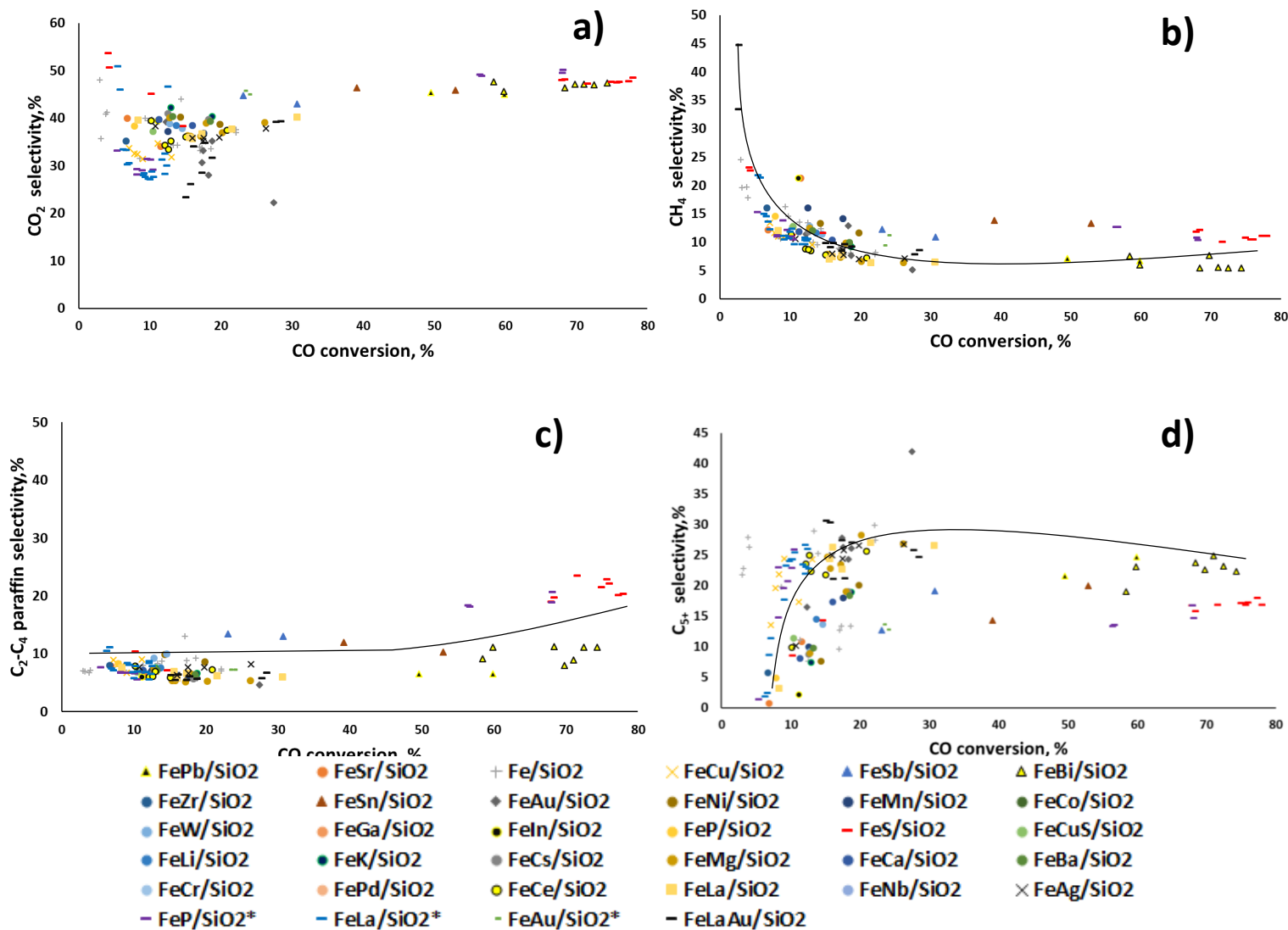


Figure 3-3. Selectivity versus carbon monoxide conversion: a) CO₂ selectivity, b) methane selectivity, c) light paraffin selectivity, d) C₅₊ hydrocarbon selectivity. Promoted Fe/SiO₂ catalysts. Fe/P=100:2, H₂/CO=1, WHSV=2.25-6.75 L/gh, P=10 bar.

According to Schulz³⁸, FT synthesis is a “non-trivial surface polymerization reaction”. Carbon monoxide adsorption over surface sites of iron catalyst results in the formation of the C₁ surface monomers, which can be produced either by direct or hydrogen-assisted CO dissociation^{39,40}. The shape of the methane selectivity versus conversion curve (**Figure 3-3b**) suggests that methane, which is produced with high selectivity at low conversion, could form directly from the hydrogenation of the C₁ surface monomers. The shape of the selectivity versus conversion curves can also be explained from the polymerization mechanism of FT synthesis. Indeed, at very low

conversions, the concentrations of adsorbed C_1 monomer is potentially insufficient for noticeable polymerization to form longer chain surface fragments and respectively longer chain hydrocarbons. This could explain lower selectivity to long chain C_{5+} hydrocarbons at lower CO conversion levels.

Oligomerization of the surface C_1 monomers results in the C_2 - C_4 fragments on the catalyst surface. The C_2 - C_4 surface fragments can then undergo the following reaction pathways (**Figure 3-4**). First, they can desorb with possible partial hydrogenation yielding light olefins. Second, they can be fully hydrogenated to yield paraffins. Finally, they can react with another C_1 surface monomer, producing longer chain fragments and hydrocarbons. In addition, the experimental results (**Figure 3-2**) indicate that the increase in CO conversion results in decrease in the selectivity to the C_2 - C_4 light olefins, increase in the selectivity to longer C_{5+} hydrocarbons, while the selectivity to the C_2 - C_4 hydrocarbons is much less affected by the conversion. The scheme shown in **Figure 3-4** suggests that higher selectivity to light olefins requires lower selectivity to the C_{5+} hydrocarbons. Indeed, on all studied iron promoted catalysts higher carbon monoxide conversion results in the increase in the C_{5+} hydrocarbon selectivity at the expense of the light olefin selectivity. Interestingly, the light paraffin selectivities much less affected by the conversion. This suggests that full hydrogenation of adsorbed C_2 - C_4 species and olefins does not become significant with the conversion. To keep high light olefin selectivity, the selectivities to long chain C_{5+} hydrocarbons and light paraffins should be reduced in particular at high carbon monoxide conversion.

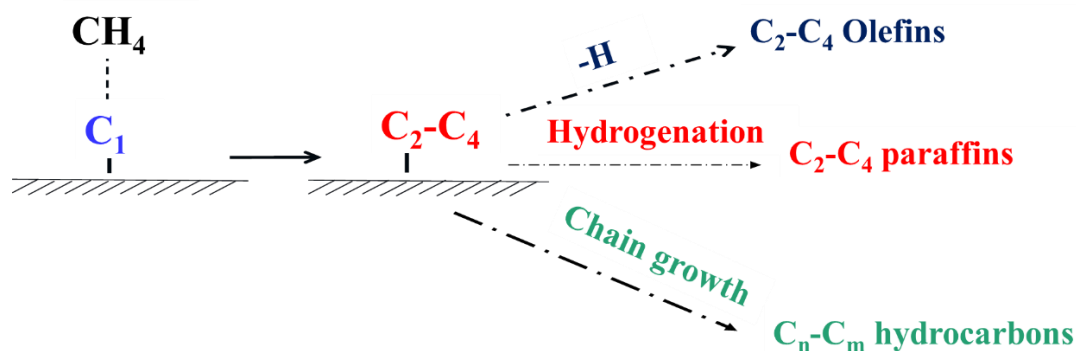


Figure 3-4. Surface polymerization paths in high temperature FT synthesis over iron catalysts.

Figure 3-1 indicates a major increase in FT reaction rate over the iron catalyst promoted with Sn, Sb, Bi, and Pb compared to any other promoters investigated in this work. In order to provide further insights into the enhancement of the catalytic activity on the promotion, the structure of the tin and antimony promoted catalysts was studied in detail by a combination of characterization techniques. The characterization data for tin and antimony promoted catalysts are compared with those for the bismuth and lead promoted counterparts.

3.3.1. Characterization of the promoted catalysts

The XRF elemental analysis data for the Sn, Sb, Bi and Pb promoted catalysts are displayed in **Table 3-1**. All catalysts present similar iron content (around 10 wt. %), while the Sn, Sb, Pb, and Bi promoters contents were close to 0.8 wt.%. **Figure 3-5 a** shows the XRD profiles of reference iron catalyst and those co-impregnated with the Sn, Sb, Pb, and Bi promoters. All the studied calcined catalysts exhibit the characteristic diffraction peaks of hematite phase (Fe_2O_3 , JCPDS13-0534). No XRD patterns attributed to the crystalline phases of the promoters were observed. The Scherrer equation has provided information about the iron oxide particle size (**Table 3-1**). The addition of promoters Bi, Pb, and Sb (impregnated in second position) to the silica supported iron catalyst results in hematite crystallites with the sizes between

15-17 nm, which are comparable to the reference catalyst (17 nm). On the other side, the Sn promoted catalyst has the smallest crystallite size (11 nm). Consequently, with exception for Sn, these promoters seem have very slight effect on iron oxide dispersion.

Table 3-1. Physical properties of supported Fe catalysts

Sample	Fe content ^a (wt%)	Promoter content ^a (wt%)	Doxide ^b (nm)	Total H ₂ consum ^c (mmol/g)
Fe/SiO ₂	11.2	-	17	2.76
FeBi/SiO ₂	10.8	0.75	15	2.81
FePb/SiO ₂	11.9	0.79	17	2.68
FeSn/SiO ₂	10.9	0.69	11	2.77
FeSb/SiO ₂	9.4	0.72	22	2.70
SbFe/SiO ₂	11.0	0.78	16	2.62

^aThe Fe and promoter content from XRF.

^bAverage particle size of iron oxide by XRD.

^cThe total H₂ consumption and iron reducibility degree from TPR analysis.

We also carried out XRD measurements (**Figure 3-5 b**) for non-promoted and promoted iron catalysts after FT reaction. The diffraction peaks around 2θ angle 44° for all catalysts are attributed to the iron carbide phase. In this case, the width of the iron carbide XRD peak clearly depends on the promoters. The apparent sizes of iron carbide nanoparticles calculated from XRD peak for promoted catalysts were between 4 and 6 nm, while for non-promoted reference catalysts the iron particle size amounted to 12 nm. The results can be interpreted in terms of the better stability of the iron particles promoted with Sn, Sb, Bi and Pb versus sintering in the presence of carbon monoxide and reaction mixture. Recently, we found that promotion of iron catalysts with mobile promoters such as Bi and Pb results in less significant iron sintering and better catalyst stability^{10,33}. In this work, similar improvement of the stability of iron carbide nanoparticles towards sintering was also observed for the Sn- and Sb-promoted samples.

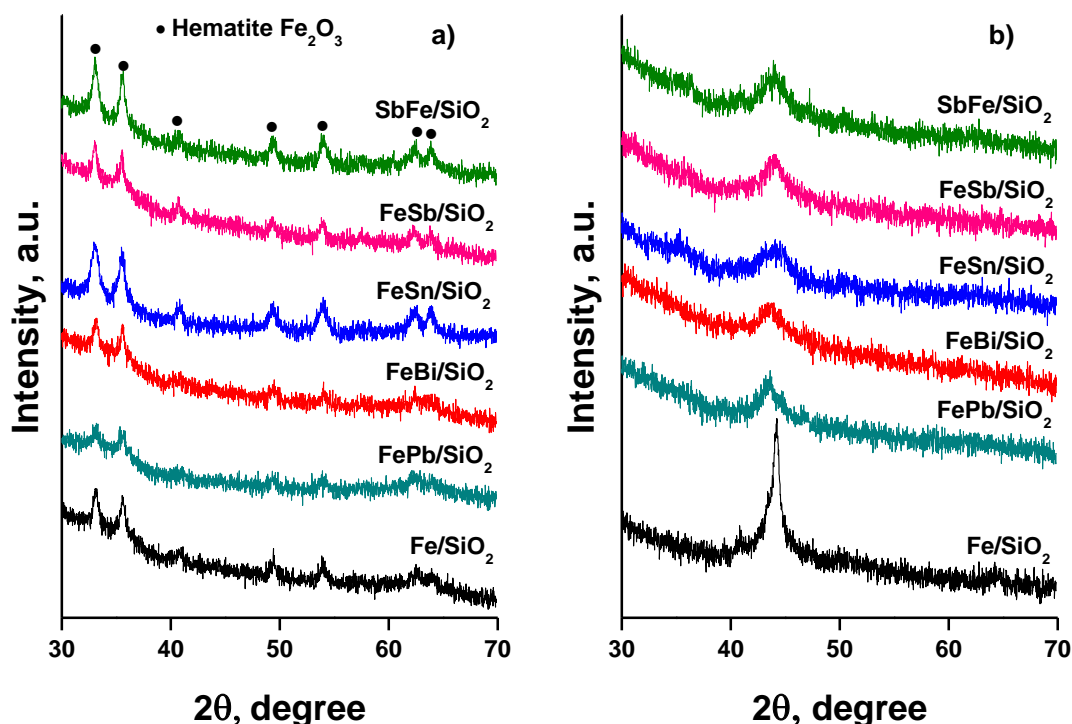


Figure 3-5. XRD patterns of the catalysts after calcination (a) and after FT reaction (b).

Figure 3-6 shows the H₂-TPR profiles measured for iron catalysts promoted with Sn, Sb, Pb, and Bi. As the promoted catalysts were prepared with a ratio of Fe:promoter 100:2, the hydrogen consumption amounts measured by TPR principally provide information about iron reduction. The amount of promoter was too small to noticeably contribute to the TPR peaks. The TPR profiles display several hydrogen consumption peaks, which are attributed to the multi-step iron reduction from Fe₂O₃ hematite to metallic iron.



In agreement with previous reports^{10,41,42,43}, the first peak at 350-420°C can be associated to the reduction of hematite (Fe₂O₃) to magnetite(Fe₃O₄), the second peak can be correlated to the reduction of magnetite (Fe₃O₄) to wüstite (FeO), whereas the third peak at 650-700°C can be attributed to the reduction of wüstite (FeO) to metallic iron (Fe). The TPR peaks observed at T>1000°C can be related to barely reducible iron silicate species⁴⁴. Interestingly, the promotion with mobile promoters only relatively

slightly affects the positions of TPR peaks for iron catalysts. In general, all the promoted catalysts present a better reducibility than the reference non-promoted iron catalyst. Fascinatingly, for Sb promoted catalysts the impregnation order has a significant effect on iron reducibility. A lower fraction of iron silicate species was observed in SbFe/SiO₂ compared to the FeSb/SiO₂. Introduction of Sb to silica before iron slows down interaction of iron with the support, which may result in iron silicates. It seems that the Sb impregnation after impregnation with iron favors iron reducibility and formation of iron metallic species. The characterization data suggests that the promotion of iron catalysts with Bi and Pb only slightly affects iron dispersion and iron reducibility. Iron dispersion is enhanced over the Sn-promoted catalyst, while iron reducibility is modified in the Sb-containing counterpart.

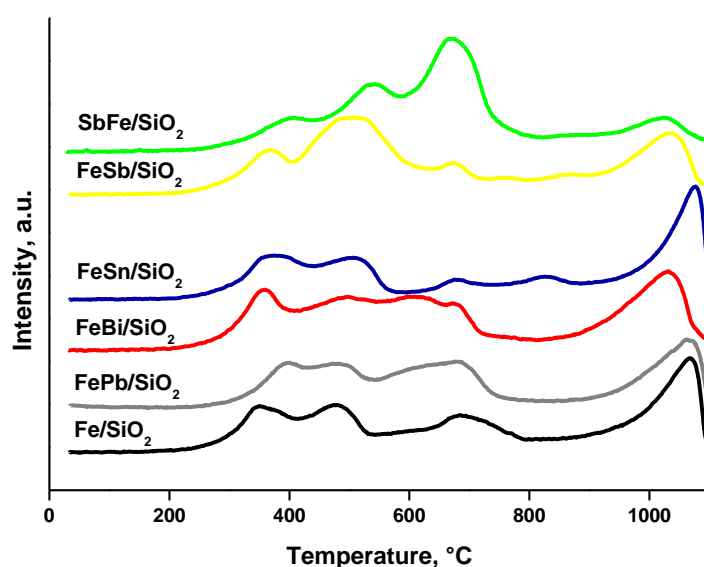
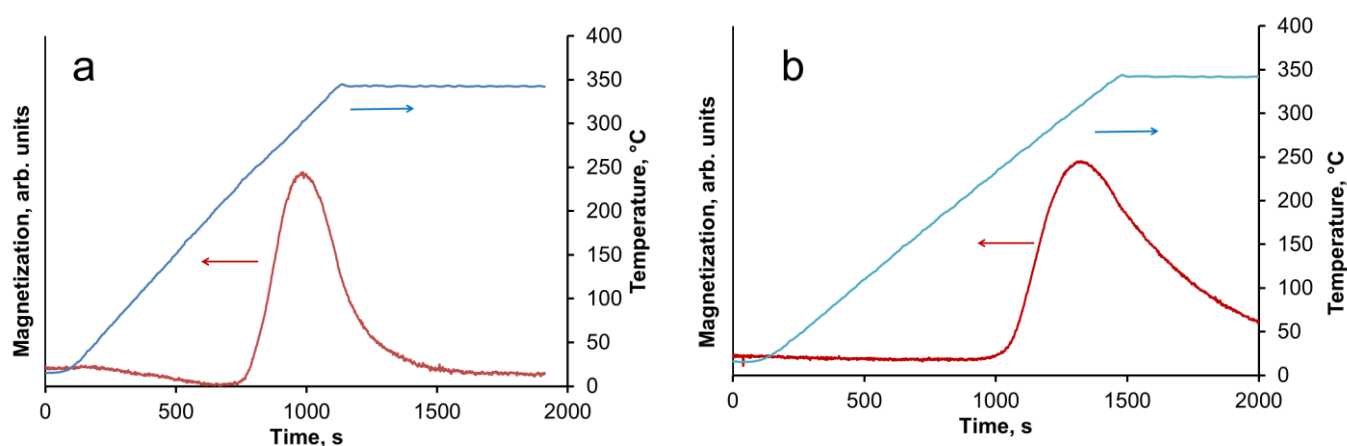


Figure 3-6. *H₂-TPR profiles of reference and promoted catalysts with Sn, Sb, Bi and Pb.*

3.3.2. *In-situ catalyst characterization*

Further information about the genesis of active phases in non-promoted iron catalyst and catalysts promoted with tin and antimony was obtained using the *in-situ* magnetic method^{45,46,47} and NAP-XPS. The Pb and Bi promoted silica supported iron catalysts were previously³⁴ characterized by the *in-situ* magnetic method. The dependence of

magnetization on the temperature during exposure of non-promoted Fe/SiO₂ and tin- and antimony-promoted iron catalysts to CO is shown in Figure 3-7 the catalysts exhibit some low magnetization at room temperature. The magnetization of freshly calcined catalysts at room temperature can be due to the presence of ferromagnetic magnetite (Fe₃O₄) phase, which forms together with the hematite (Fe₂O₃) phase after the catalyst calcination. Heating of the catalysts in CO results in the increase in magnetization, which can be possibly due to the reduction of hematite into magnetite and formation of ferromagnetic iron carbide. Indeed, previously we showed⁴⁸ that carbidization of hematite proceeds via intermediate formation of magnetite. The magnetization drops at higher temperature for Fe/SiO₂ and FeSn/SiO₂ (Figure 3-7 a and b), while the magnetization remains high for the catalyst promoted with antimony (Figure 3-7 c and d). The decrease in the magnetization for the Fe/SiO₂ and FeSn/SiO₂ samples seems to be due to the formation of ferromagnetic phase with the Curie temperature lower than 250°C, which can be Hägg iron carbide ($T_{\text{Curie}} = 205\text{-}256\text{ °C}$) or cementite ($T_{\text{Curie}} = 208\text{ °C}$)¹². Higher magnetization observed for FeSb/SiO₂ and SbFe/SiO₂ samples seems to be due to the presence of the ferromagnetic phase with higher Curie temperature, possibly magnetite ($T_{\text{Curie}} = 585\text{ °C}$)¹².



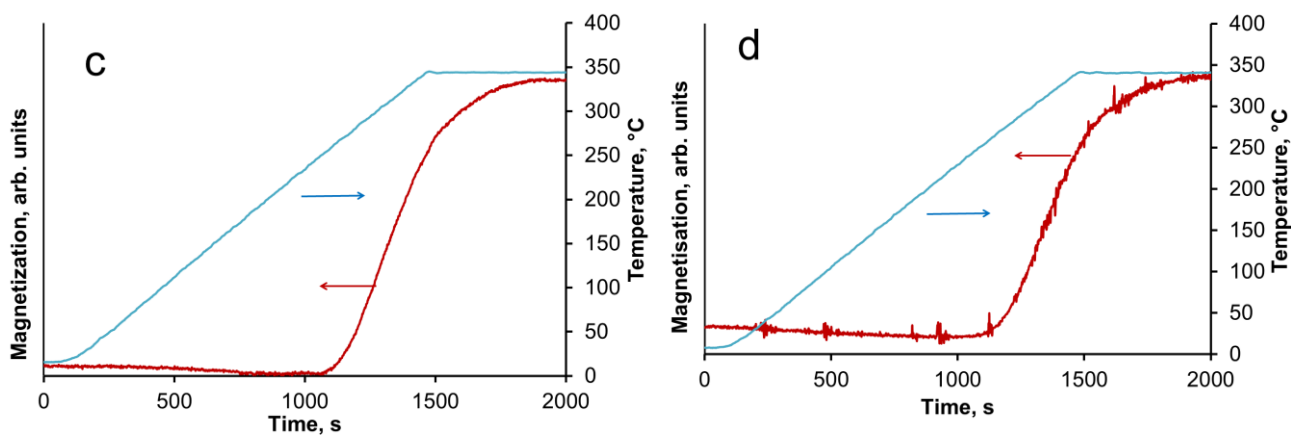


Figure 3-7. Variation of magnetization during exposure of silica supported iron catalysts to CO as a function of temperature (a- Fe/SiO₂, b- FeSn/SiO₂; c- FeSb/SiO₂, d- SbFe/SiO₂)

The variation of magnetization during subsequent treatment of iron catalysts in syngas (H₂/CO=1) after their activation in CO is shown in **Figure 3-8**. All the samples display some magnetization at room temperature, which can be due to the presence of iron carbide or magnetite, which formed during the exposure to pure CO. Heating in syngas results in initial increase in the magnetization for Fe/SiO₂ and FeSn/SiO₂ samples (**Figure 3-8 a and b**) due to further formation of iron carbide. The magnetization then drops at the temperatures higher than 250 °C, which indicates the presence of iron carbides with Curie temperature lower than 250 °C. Interestingly, for the FeSb/SiO₂ and SbFe/SiO₂ samples (**Figure 3-8 c and d**), the magnetization drops during the temperature ramp in syngas without any initial increase. Magnetite has been formed in these samples during their pretreatment in CO. The decrease in magnetization during the subsequent exposure of FeSb/SiO₂ and SbFe/SiO₂ to syngas can be attributed to the carbidization of magnetite and formation of iron carbides. This suggests that the non-promoted iron catalyst and catalysts promoted with tin can be carbidized in CO, while the presence of syngas is required for carbidization of the catalysts promoted with antimony. It should be also noted that the non-promoted Fe/SiO₂ catalyst did not show any noticeable magnetization at 350 °C. This indicates that almost all magnetite has been converted to iron carbides, while the catalysts

promoted with tin or antimony exhibited residual magnetization even at high temperature. Thus, the presence of some amounts of residual magnetite in the Sn- and Sb-promoted catalysts is expected after activation in CO and syngas.

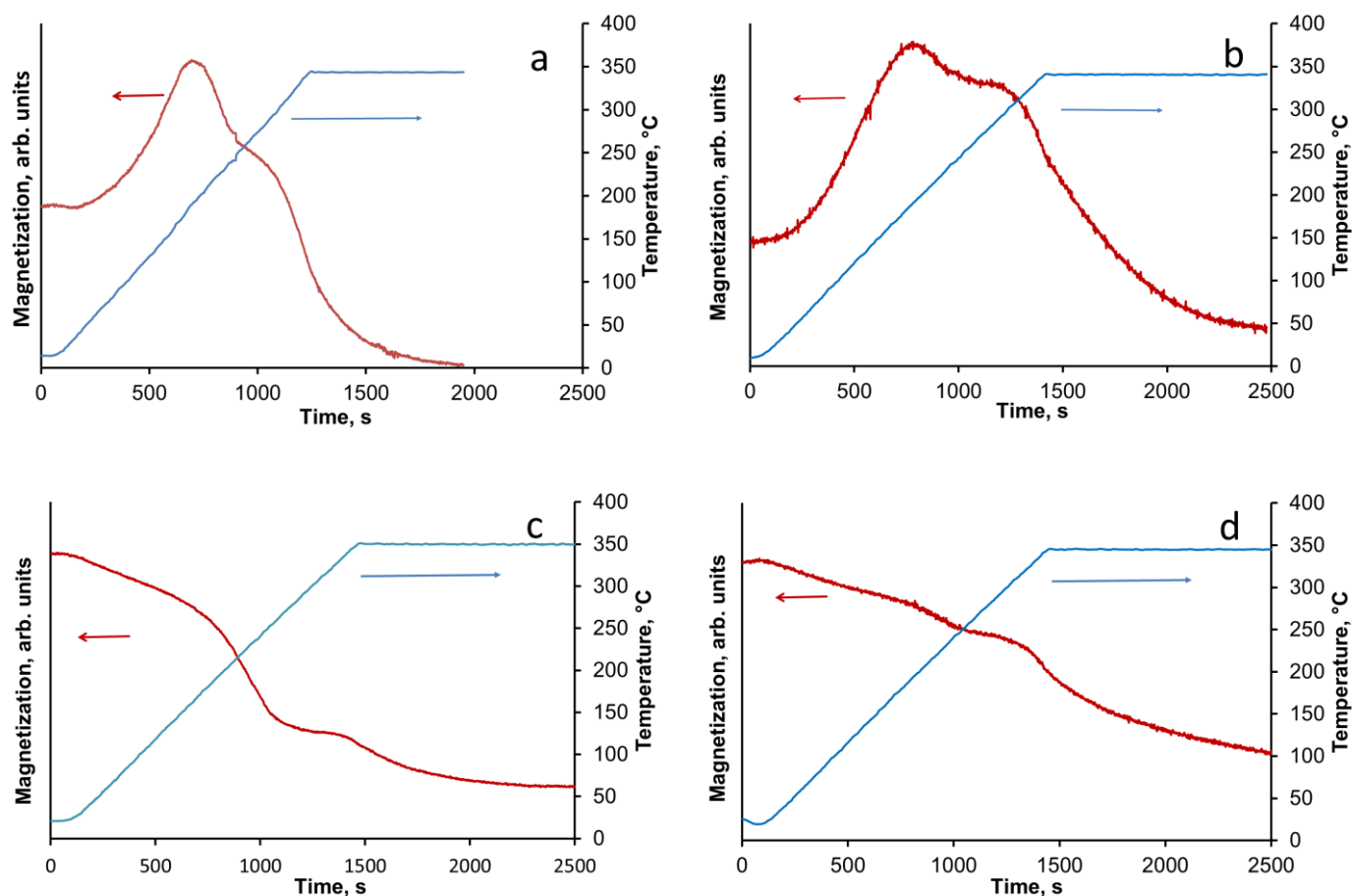


Figure 3-8. Variation of magnetization during exposure of silica supported iron catalysts activated in pure CO to syngas ($H_2/CO=1$) as a function of temperature (a- Fe/SiO_2 , b- $FeSn/SiO_2$; c- $FeSb/SiO_2$, d- $SbFe/SiO_2$).

After the catalyst activation in CO and subsequently in syngas, the catalyst temperature was decreased from 350 °C to ambient. All the catalysts showed an increase in magnetization during this temperature decrease. This suggests the presence of iron carbides with the Curie temperature between 200 and 250 °C. Note that the magnetization increases in somewhat lower temperature for the non-promoted Fe/SiO_2 than for the promoted samples. This could be indicative of the cementite type

carbide with lower Curie temperature ($T_{\text{Curie}} = 208 \text{ }^{\circ}\text{C}$) in Fe/SiO₂. In the promoted catalysts, the major iron carbide phase could be the Hagg Fe₅C₂ carbide.

In order to have deeper information about promoters, a model catalyst supported on CNT was studied. CNT has the advantage of being conductive like this we can overcome signal-noise problems arising from SiO₂ (insulating material). In addition, these model catalysts were also tested for FT synthesis obtaining similar tendencies to those of SiO₂-supported catalysts. The surface of the catalyst usually is more sensitive to the conditions of catalyst activation and catalytic reaction than the catalyst bulk structure. Information about evolution of the surface and sub-surface layer in the monometallic and bismuth promoted catalysts in CO or syngas at the activation and reaction temperatures was extracted from the NAP-XPS data.

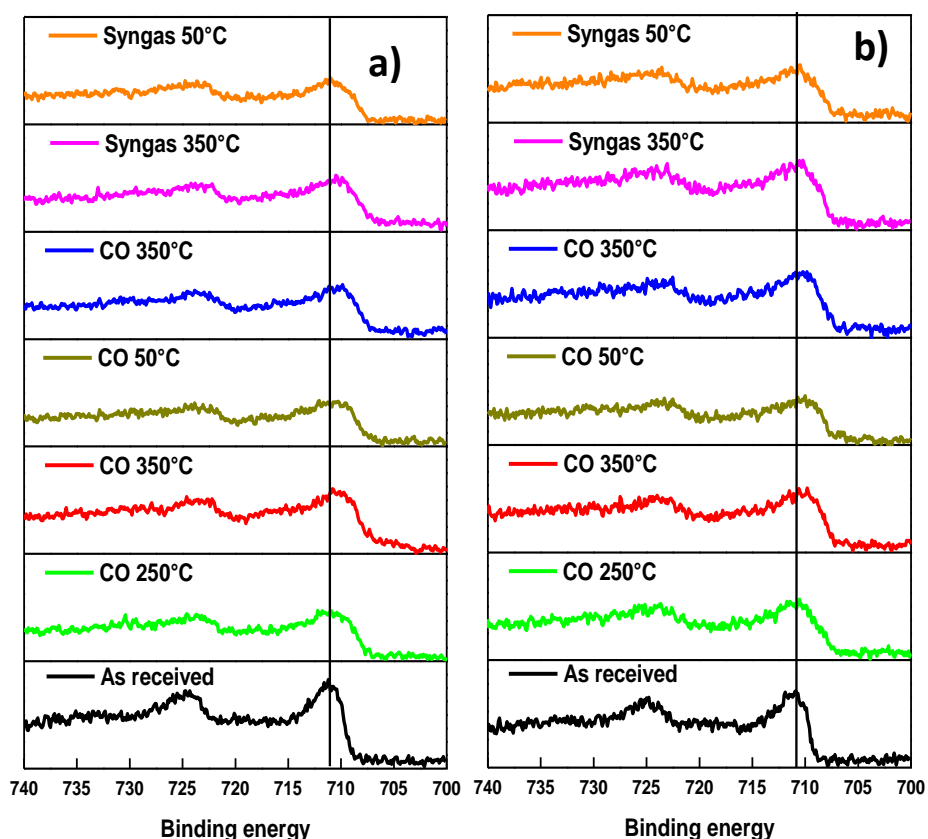


Figure 3-9. Fe 2p NAP-XPS spectra measured in CO and syngas at different temperatures: a) FeBi/CNT; b) Fe/CNT+Bi/CNT

The freshly calcined samples were first loaded into the NAP-XPS spectrometer and exposed to CO at 50 °C. Then, the temperature was increased subsequently from room to 250 °C and to 350 °C. After the exposure to 350 °C in CO, the sample was cooled down to 50 °C. After the subsequent temperature increase to 350 °C, CO was switched to syngas (H₂/CO=1) at 350 °C. The sample was maintained in syngas at this temperature and then cooled back again to 50 °C. At different steps of the in-situ catalyst treatment under about 1 mbar of CO or syngas, the position, shape and intensity of Fe 2p, C 1s, and Bi 4f peaks were thoroughly analyzed by XPS.

The Fe 2p NAP-XPS spectra of the FeBi/CNT and Fe/CNT+Bi/CNT catalysts are presented in **Figure 3-9**. The spectra of the calcined catalysts exhibit the Fe 2p peaks at ~711.2 eV (Fe2p_{3/2}) and ~724.6 eV (Fe 2p_{1/2}) with a shakeup satellite peak at ~719.2 eV. The spectra and binding energies distinctly indicate the presence of Fe³⁺ species⁴⁹.

Table 3-2. Relative intensities of NAP-XPS peaks measured in the presence of carbon monoxide and syngas

Catalyst	Gas	Temperature, °C	I _{Fe} /I _C	I _{Bi} /I _{Fe}
FeBi/CNT	CO	50	3.70	0.167
		250	3.32	0.088
		350	3.71	0.040
		50	2.40	0.026
		350	3.02	0.025
	H ₂ /CO=1	350	3.44	0.042
Fe/CNT+Bi/CNT	CO	50	2.75	0.118
		250	2.27	0.074
		350	2.44	0.023
		50	1.99	0.039
		350	2.07	0.011
	H ₂ /CO=1	350	2.22	0.031
		50	2.13	0.031

This observation is consistent with the results of other techniques and indicates the presence of iron oxides in the fresh samples. After the temperature increase in CO

to 250 °C and then to 350 °C, a broad shoulder with the binding energy of 707.3 eV could be indicative of the presence of iron carbides⁵⁰ or metallic iron. However, the XRD analysis, magnetization in syngas and Mössbauer analysis (discussed in chapter 4) of spent catalysts showed that the main phase obtained is iron carbide, specifically the Hägg carbide (Fe_5C_2) letting us think that the shift observed can be attributed to iron carbide formation under the CO treatment. Higher intensity of this feature and correspondingly higher amount of iron carbide were observed in syngas ($\text{H}_2/\text{CO} = 1$) compared to pure CO. The NAP-XPS results in the Fe 2p region are consistent with our previous ex-situ XPS data for iron catalysts^{10,51}. Since the catalysts were supported on CNT, we consider that the intensity of C 1s peak does not change during the experiments. The C 1s intensity was used therefore, as a reference in order to evaluate variation of the relative intensity of Fe 2p XPS peaks during the treatments in CO and syngas at high temperatures. The relative intensities ($I_{\text{Fe}}/I_{\text{C}}$) are shown in **Table 3-2**. No noticeable modification of the intensity of the Fe 2p XPS peaks was observed after exposure of both FeBi/CNT and Fe/CNT + Bi/CNT to carbon monoxide or syngas at 250 °C and 350 °C. Indeed, **Table 3-2** displays only relatively small variation of the relative iron intensity in the activated and spent catalysts.

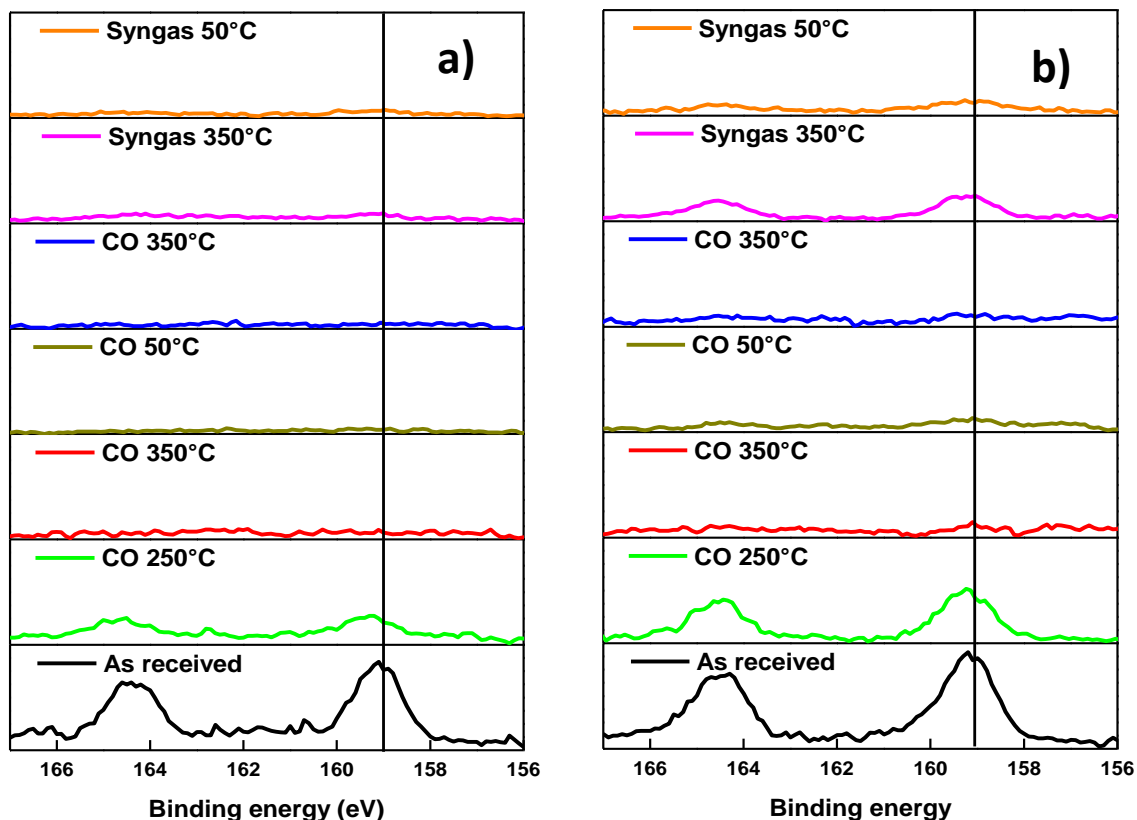


Figure 3-10. *Bi 4f* NAP-XPS spectra measured in CO and syngas at different temperatures: a) FeBi/CNT; b) Fe/CNT+Bi/CNT

The Bi 4f XPS spectra of the bismuth promoted iron catalysts are shown in **Figure 3-10**. The calcined catalysts exhibit XPS peaks with binding energies of 158.6 and 165 eV assigned to Bi 4f_{7/2} and Bi 4f_{5/2} bands in Bi₂O₃⁵², respectively. Catalyst activation in carbon monoxide at 250 °C leads to the Bi signal reduction.

Interestingly, a further temperature increase to 350 °C in the NAP-XPS experiments results in a major decrease in the intensity of the Bi 4f_{7/2} and Bi 4f_{5/2} doublet peaks in both FeBi/CNT and Fe/CNT+Bi/CNT (**Table 3-2**). This could be indicative of a major decrease in the bismuth surface and sub-surface concentrations in both catalysts prepared by co-impregnation and mechanical mixing, probably because of bismuth sintering. Remarkably, different relative localization of iron carbide and bismuth in the catalysts prepared by co-impregnation and mechanical mixing does not affect bismuth sintering. Minimization of surface area is a major thermodynamic driving force for sintering of bismuth nanoparticles, while higher diffusivity of liquid

bismuth at temperature higher or comparable to the Bi melting point significantly decreases the kinetic barrier for the migration.

Higher diffusivity and mobility of liquid bismuth at the conditions of catalyst activation in CO and FT reaction could also result in the bismuth infiltration inside CNT. Indeed, migration of Bi from outer surface to inside CNT would result in lower intensity of the Bi XPS signal. In order to provide further insights into migration of bismuth under activation in CO, we measured ex-situ TEM images of the Bi/CNT sample after exposure to CO at 250 and 350 °C (**Figure 3-11**). Small bismuth nanoparticles of 5-10 nm were detected in the fresh Bi/CNT calcined in nitrogen (**Figure 3-11 a**). Slightly larger Bi nanoparticles were observed in the same sample after exposure to CO to 250°C (**Figure 3-11 b**). Further increase in the temperature during the pretreatment in CO results in a spectacular growth of Bi nanoparticles (**Figure 3-11 c**). The TEM images show the presence of very large spherical Bi particles (>50 nm) in Bi/CNT exposed to CO at 350 °C (which can generate lower Bi signal). Exposure of Bi/CNT to CO at 350 °C results in formation of liquid Bi, which has very high diffusivity over the CNT support. No bismuth infiltration inside CNT was observed. Other possible explanation is that the sample is not homogeneous due to the migration of Bi particles on the catalyst surface under temperature and gas treatment and we analyzed a spot where there was no Bi anymore.

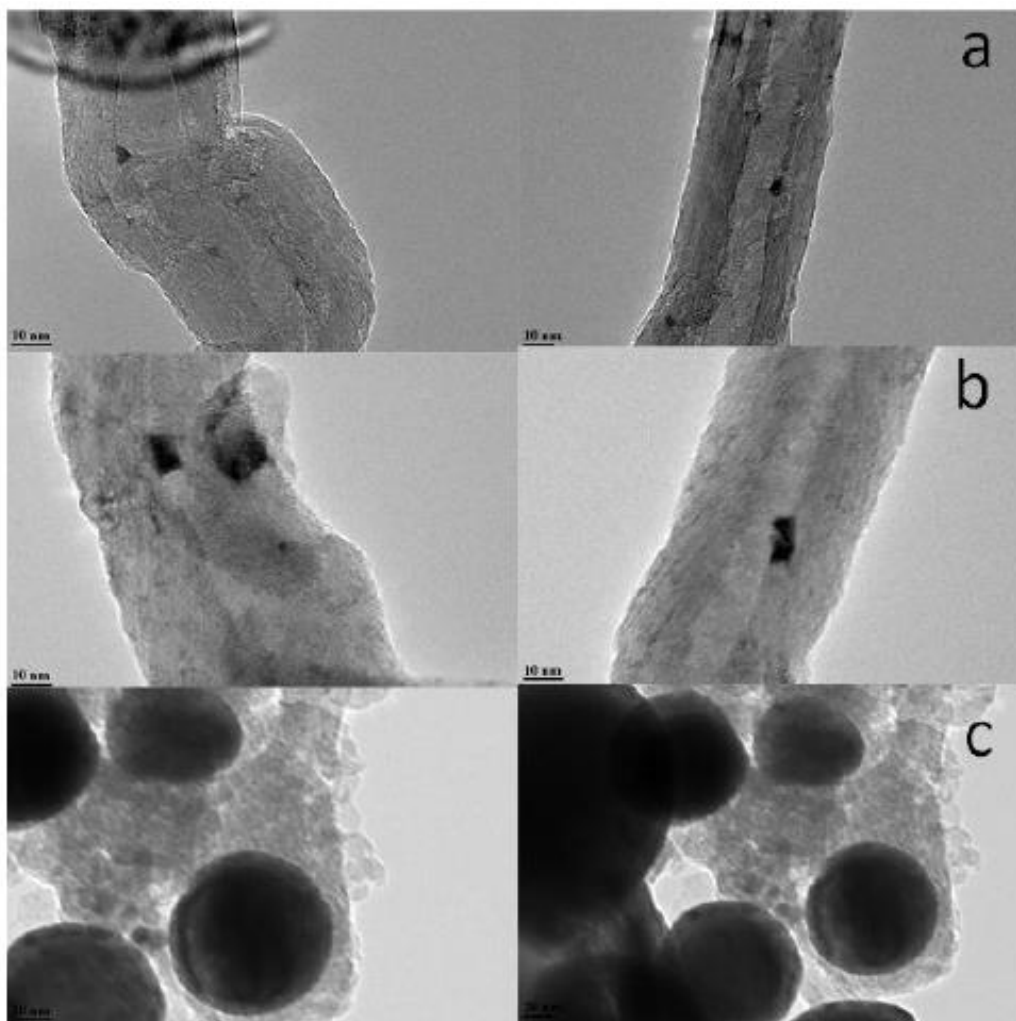


Figure 3-11. TEM images of Bi/CNT (2 wt.%) after calcination in nitrogen (a), after the pretreatments in CO at 250°C (b) and at 350°C (c)

3.3.3. Catalytic performance of the Sn-, Sb-, Bi and Pb-promoted catalysts.

The results of HTE catalytic tests have clearly indicated unusually high FT reaction rates of Sn-, Sb-, Bi and Pb-promoted iron catalysts compared to other counterparts (**Figure 3-1** and **Table 3-3**). All these four metals have relatively low melting points, i.e. Sn 232 °C, Sb 630 °C, Bi 271 °C, and Pb 328 °C, compared to most of other metals. They possibly exist either in the liquid state or are highly mobile under FT reaction conditions. The reasons for the increase in FT reaction rate over the bismuth and lead promoted catalysts have been already discussed in our previous reports^{10,11,33,34}. During the activation, bismuth and lead form the core-shell structures

with iron species. The conducted kinetic and isotopic tracing experiments³⁴ indicated that the Bi and Pb promoters facilitated carbon monoxide dissociation by scavenging O atoms from the surface of iron carbide. One possible explanation could be that the promoting effect of Bi and Pb results in a stronger Fe-C interaction consequently reducing the amount of hydrogen adsorbed on the surface and, hence, limiting the hydrogenation ability of the catalyst. At the same time could Iron time yield (FTY) in the catalysts promoted with Bi, Pb, Sn and Sb increased 3-5 times (**Table 3-3**). The observed strong enhancement of FT reaction rate over the Bi and Pb-promoted iron catalysts obtained in this work is in agreement with previous reports^{10,33,34}.

Table 3-3. Catalytic performance of iron catalysts promoted with soldering metals in FT synthesis measured in a conventional fixed bed reactor at iso-GHSV (10 bar, 350 °C, H₂/CO= 1/1, WHSV = 3.6 L/g.h, TOS = 48h)

Catalysts	FTY 10 ⁻⁴ mol _{CO} g _{Fe} ⁻¹ s ⁻¹	TOF, s ⁻¹	CO conv. (%)	CO ₂ sel. (%)	Hydrocarbon selectivity (%)				C ₂₋₄ ⁻ /C ₂₋₄ ⁰
					CH ₄	C ₂₋₄ ⁻	C ₂₋₄ ⁰	C ₅ ⁺	
Fe/SiO ₂	0.20	0.09	11	15	24	31	5	40	6.20
FeBi/SiO ₂	1.11	-	60	49	15	25	10	50	2.50
FePb/SiO ₂	0.82	-	44	46	16	34	7	43	4.86
FeSn/SiO ₂	0.98	0.84	53	49	23	17	13	47	1.31
FeSb/SiO ₂	0.87	0.69	47	47	14	17	10	59	1.70
SbFe/SiO ₂	0.61	-	33	43	21	20	12	47	1.67

Interestingly, the Sb- and Sn-promoted catalysts also achieved remarkable reaction rate, which is much higher than for any other promoted iron catalysts (**Figure 3-1**). The elements such as Sn and Sb are also (as Bi and Pb) located in groups IV and V of the Periodic Table and have similar properties. They exhibit several oxidation states. Their melting points are respectively situated at 232 and 630 °C. High temperature FT synthesis proceeds in the temperature range between 300 and 350 °C. This is higher than the Tamman temperature of all these metals (~0.5 of the melting point temperature measured in K). This suggests noticeable bulk mobility of Sb and Sn under the reaction conditions. Importantly, the carbon monoxide conversions and

reaction rates for all non-promoted, Bi-, Pb-, Sn- and Sb-promoted catalysts observed either in the HTE or in laboratory fixed bed reactors are respectively rather similar (**Figure 3-1** and **Table 3-3**).

Catalyst deactivation remains one of the main challenges of FT synthesis. Deactivation results in the loss of catalytic activity with time on steam, low productivity and necessity to replace or to regenerate the catalysts. **Figure 3-12** shows variation of the carbon monoxide conversion with time on stream over the Sn-, Sb-, Bi- and Pb-promoted catalysts during the first 48 h of reaction. In agreement with previous reports⁵⁴, the reference non-promoted catalyst showed continuous decrease in the activity occurring until it reached a stable conversion of around 11%. On the other hand, the iron catalysts promoted with Sn, Sb, Bi and Pb reached stable conversions after 10 h of reaction and they did not show appreciable deactivation during 48 h on stream. Better stability of iron catalyst with the Sb, Bi and Pb promoters can be therefore, attributed to less significant iron sintering. Definitely, XRD suggests (**Figure 3-5 b**) highly dispersed iron carbides species in the spent promoted catalysts, while major iron sintering was observed during FT reaction in the non-promoted Fe/SiO₂. Indeed, formation of protective layer of quasi-liquid metal can slow down iron carbide sintering.

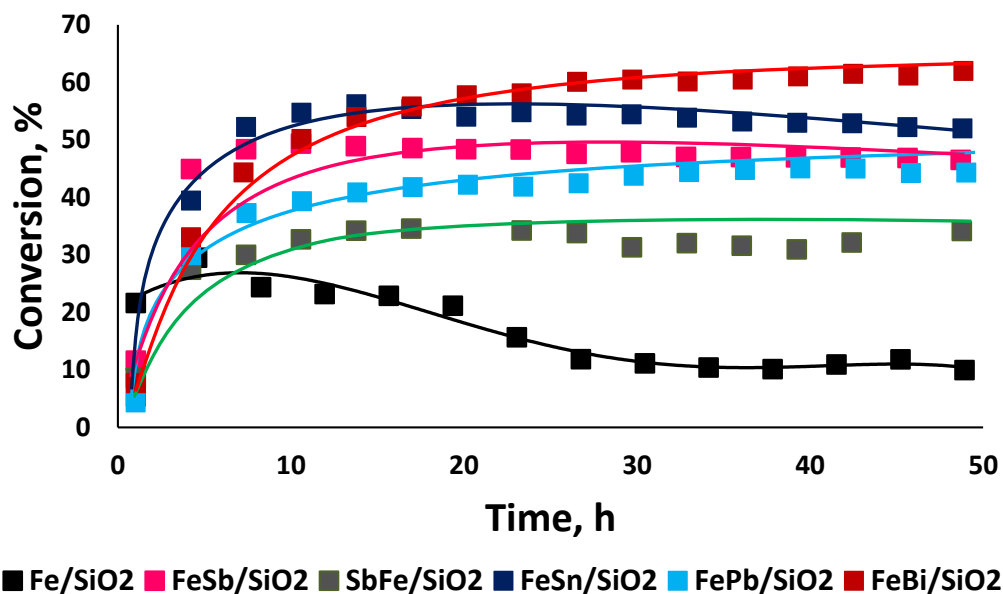


Figure 3-12. CO conversion as a function of time for iron catalysts promoted with Sn, Sn, Bi and Pb. Reaction conditions: $P = 10$ bar, $H_2/CO = 1$, $WHSV = 3.6$ L/g.h.

The catalytic tests show strong effect of the promotion with bismuth, tin, antimony, and lead, on the FT reaction rate (**Figure 3-12, Table 3-3**). High selectivity to light olefins is an extremely important reaction parameter and a major challenge of FT synthesis. In order to obtain more information about the effect of the promotion with Bi, Sb, Sn and Pb on the reaction selectivities, the selectivity to different products was measured at a wide range of CO conversion. The selectivity conversion curves (**Figure 3-13**) clearly emphasize the unique nature of bismuth and lead as the promoters, which at the same time, increase both overall reaction rate and light olefin selectivity. The data points for the light olefin selectivity plotted as a function of conversion over the catalyst promoted with bismuth and lead are clearly above the values observed for the Sn and Sb promoted counter parts and non-promoted iron catalysts (**Figure 3-13 a**). The methane selectivity curves indicate lower values over the Bi- and Pb-promoted catalysts observed at the same CO conversion compared with the Sb-promoted and in particular Sn-Promoted samples (**Figure 3-13 b**). Simultaneously, the Bi and Pb-promoted catalysts exhibit lower selectivity to the C_2 - C_4 paraffins compared with the

Sn and Sb promoted counterparts (**Figure 3-13 c**) The C_{5+} selectivity conversion curves measured for all four promoted catalysts do not indicate any major differences. **Figure 3-13 d** show general increase in the C_{5+} selectivity with the CO conversion. This suggests that the gain in the selectivity over the Bi and Pb promoted catalysts can be principally attributed to the decrease in the selectivity to methane and light paraffins. Indeed, the promotion of silica supported iron catalysts with Bi and Pb leads to a major increase in both FT reaction rate and light olefins selectivity while tin and antimony when added to the silica supported iron catalysts have a major impact in the FT reaction rate, but at the same time they do not increase the light olefin selectivity.

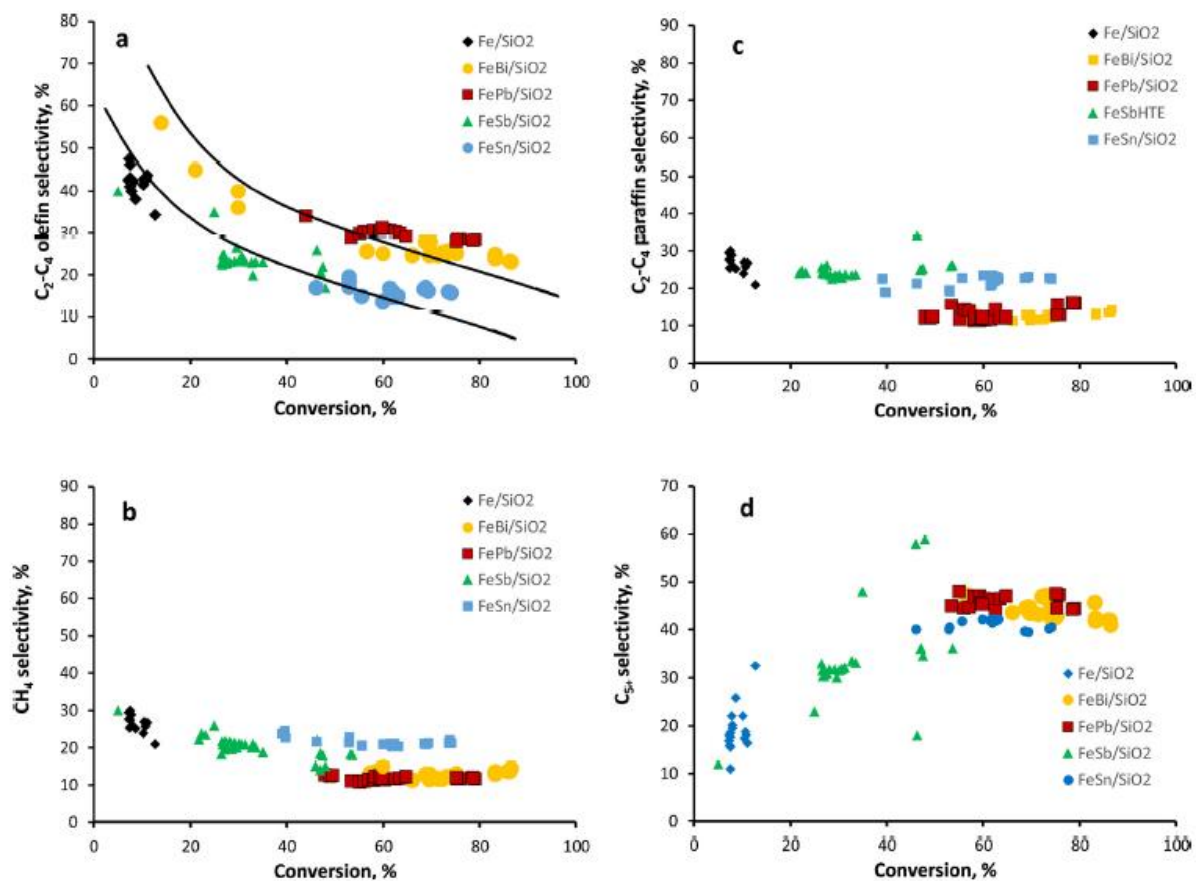


Figure 3-13. Selectivity conversion curves for silica supported iron catalysts promoted with Bi, Pb, Sn, Sb and reference iron catalysts. The data were obtained in HTE unit, millimetric and centimetric reactors.

The activation procedure was different for those catalysts tested in HTE unit. This could be the main fact why we observe slightly different activities for the catalysts tested in HTE and single fixed-bed reactor. **Figure 3-13** is a compilation of all the results obtained for these catalysts in different systems (HTE, milireactor and centimetric reactor).

3.4. Conclusions

HTE approach allows identification of new efficient promoters and selectivity trends over iron catalysts for high temperature FT synthesis within a short time frame. The catalytic tests suggest that the selectivity of FT synthesis over silica supported iron catalysts a function several parameters relevant to the presence of promoters and reaction operating conditions. The light olefin selectivity close to 60% over iron catalysts is observed at low carbon monoxide conversion and then decreases with conversion. The methane and light paraffin selectivities follow similar trend. The selectivity to carbon dioxide increases with carbon monoxide conversion and reaches the stoichiometric values of 50% at carbon monoxide conversion higher than 30%. The selectivity to the C₅₊ long chain hydrocarbons increases with carbon monoxide conversion.

The evolution of the catalyst structure during activation and reaction has been elucidated using a combination of the cutting-edge characterization techniques such as in-situ magnetic method and NAP-XPS. In the promoted catalysts, the major iron phase was the Hägg carbide (Fe₅C₂). Under the conditions of catalyst activation and reaction, bismuth migrates over the catalyst surface forming larger spherical bismuth droplet and strongly interacts with iron carbide species.

Promotion of iron catalysts with metals with low melting points such as Bi, Pb, Sn and Sb resulted in a major increase (several fold) in FT reaction rate. This promotion also results in higher intrinsic activity of surface sites. Two types of the promotion were observed. The promotion with Sn and Sb results only in the enhancement of the FT reaction rate, while the light olefin selectivity is not much affected. The promotion with Bi and Pb leads to the increase in both the FT reaction rate and selectivity to light olefins.

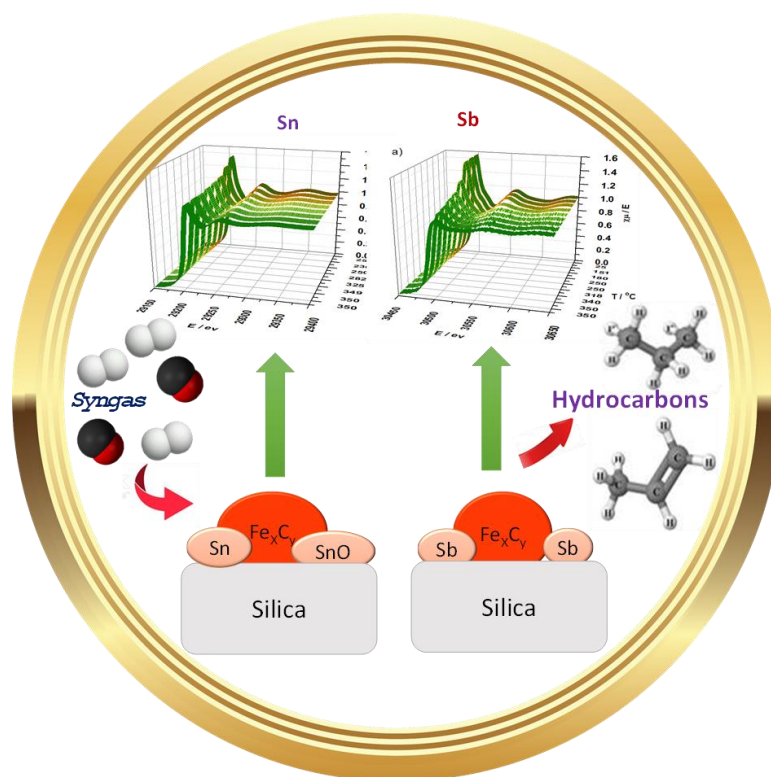
3.5 References

1. van Steen, E. & Claeys, M. Fischer-Tropsch catalysts for the biomass-to-liquid process. *Chem. Eng. Technol.* **31**, 655–666 (2008).
2. Zhang, Q., Kang, J. & Wang, Y. Development of Novel Catalysts for Fischer-Tropsch Synthesis: Tuning the Product Selectivity. *ChemCatChem* **2**, 1030–1058 (2010).
3. Torres Galvis, H. M. *et al.* Supported iron nanoparticles as catalysts for sustainable production of lower olefins. *Science (80-.)*. **335**, 835–838 (2012).
4. Dry, M. E. The Fischer–Tropsch process: 1950–2000. *Catal. Today* **71**, 227–241 (2002).
5. Torres Galvis, H. M. & De Jong, K. P. Catalysts for production of lower olefins from synthesis gas: A review. *ACS Catal.* **3**, 2130–2149 (2013).
6. De Smit, E. & Weckhuysen, B. M. The renaissance of iron-based Fischer-Tropsch synthesis: On the multifaceted catalyst deactivation behaviour. *Chem. Soc. Rev.* **37**, 2758–2781 (2008).
7. Bukur, D. B., Mukesh, D. & Patel, S. A. Promoter Effects on Precipitated Iron Catalysts for Fischer-Tropsch Synthesis. *Ind. Eng. Chem. Res.* **29**, 194–204 (1990).
8. Lohitharn, N., Goodwin Jr., J. G. & Lotero, E. Fe-based Fischer–Tropsch synthesis catalysts containing carbide-forming transition metal promoters. *J. Catal.* **255**, 104–113 (2008).
9. Chen, W., Fan, Z., Pan, X. & Bao, X. Effect of Confinement in Carbon Nanotubes on the Activity of Fischer–Tropsch Iron Catalyst. *J. Am. Chem. Soc.* **130**, 9414–9419 (2008).
10. Gu, B. *et al.* Synergy of nanoconfinement and promotion in the design of efficient supported iron catalysts for direct olefin synthesis from syngas. *J. Catal.* **376**, 1–16 (2019).
11. Gu, B. *et al.* Size and promoter effects on iron nanoparticles confined in carbon nanotubes and their catalytic performance in light olefin synthesis from syngas. *Catal. Today* 0–1 (2019) doi:10.1016/j.cattod.2019.05.054.
12. Cheng, K. *et al.* Support effects in high temperature Fischer-Tropsch synthesis on iron catalysts. *Appl. Catal. A Gen.* **488**, (2014).
13. Dictor, R. A. & Bell, A. T. Fischer-Tropsch synthesis over reduced and unreduced iron oxide catalysts. *J. Catal.* **97**, 121–136 (1986).
14. Li, S., Meitzner, G. D. & Iglesia, E. Structure and Site Evolution of Iron Oxide Catalyst Precursors during the Fischer–Tropsch Synthesis. *J. Phys. Chem. B* **105**, 5743–5750 (2001).
15. Ordonsky, V. V., Legras, B., Cheng, K., Paul, S. & Khodakov, A. Y. The role of carbon atoms of supported iron carbides in Fischer-Tropsch synthesis. *Catal. Sci. Technol.* **5**, 1433–1437 (2015).
16. HERRANZ, T. *et al.* Genesis of iron carbides and their role in the synthesis of hydrocarbons from synthesis gas. *J. Catal.* **243**, 199–211 (2006).
17. Yang, C., Zhao, H., Hou, Y. & Ma, D. Fe₅C₂ Nanoparticles: A Facile Bromide-Induced Synthesis and as an Active Phase for Fischer–Tropsch Synthesis. *J. Am. Chem. Soc.* **134**, 15814–15821 (2012).
18. Davis, B. H. Fischer–Tropsch Synthesis: Comparison of Performances of Iron and Cobalt Catalysts. *Ind. Eng. Chem. Res.* **46**, 8938–8945 (2007).
19. Davis, B. H. Fischer–Tropsch Synthesis: Reaction mechanisms for iron catalysts. *Catal. Today* **141**, 25–33 (2009).
20. Ribeiro, M. C. *et al.* Fischer-tropsch synthesis: An in-situ TPR-EXAFS/XANES investigation of the influence of group I alkali promoters on the local atomic and electronic structure of carburized iron/silica catalysts. *J. Phys. Chem. C* **114**, 7895–7903 (2010).
21. Li, J. *et al.* Alkalis in iron-based Fischer-Tropsch synthesis catalysts: distribution, migration and promotion. *J. Chem. Technol. Biotechnol.* **28**, 1472–1480 (2017).
22. Lohitharn, N. & Goodwin, J. G. Effect of K promotion of Fe and FeMn Fischer–Tropsch synthesis catalysts: Analysis at the site level using SSITKA. *J. Catal.* **260**, 7–16 (2008).
23. Arakawa, H. & Bell, A. T. Effects of potassium promotion on the activity and selectivity of iron Fischer-Tropsch catalysts. *Ind. Eng. Chem. Process Des. Dev.* **22**, 97–103 (1983).
24. Ngantsoue-Hoc, W., Zhang, Y., O'Brien, R. J., Luo, M. & Davis, B. H. Fischer–Tropsch synthesis: activity and selectivity for Group I alkali promoted iron-based catalysts. *Appl. Catal. A Gen.* **236**, 77–89 (2002).
25. Chernavskii, P. A. *et al.* Influence of copper and potassium on the structure and carbidisation of supported iron catalysts for Fischer-Tropsch synthesis. *Catal. Sci. Technol.* **7**, 2325–2334 (2017).
26. Cheng, K. *et al.* Sodium-promoted iron catalysts prepared on different supports for high temperature Fischer-Tropsch synthesis. *Appl. Catal. A Gen.* **502**, 204–214 (2015).
27. Pendyala, V. R. R. *et al.* Selectivity control of Cu promoted iron-based Fischer-Tropsch catalyst by tuning the oxidation state of Cu to mimic K. *Appl. Catal. A Gen.* **495**, 45–53 (2015).

28. Peña, D. *et al.* The Effect of Copper Loading on Iron Carbide Formation and Surface Species in Iron-Based Fischer–Tropsch Synthesis Catalysts. *ChemCatChem* **10**, 1300–1312 (2018).
29. Torres Galvis, H. M. *et al.* Effects of sodium and sulfur on catalytic performance of supported iron catalysts for the Fischer-Tropsch synthesis of lower olefins. *J. Catal.* **303**, 22–30 (2013).
30. Xie, J. *et al.* Size and Promoter Effects in Supported Iron Fischer-Tropsch Catalysts: Insights from Experiment and Theory. *ACS Catal.* **6**, 3147–3157 (2016).
31. Botes, G. F. *et al.* Development of a chemical selective iron Fischer Tropsch catalyst. *Catal. Today* **275**, 40–48 (2016).
32. Jiang, F., Zhang, M., Liu, B., Xu, Y. & Liu, X. Insights into the influence of support and potassium or sulfur promoter on iron-based Fischer-Tropsch synthesis: Understanding the control of catalytic activity, selectivity to lower olefins, and catalyst deactivation. *Catal. Sci. Technol.* **7**, 1245–1265 (2017).
33. Gu, B. *et al.* Effects of the promotion with bismuth and lead on direct synthesis of light olefins from syngas over carbon nanotube supported iron catalysts. *Appl. Catal. B Environ.* **234**, 153–166 (2018).
34. Ordonsky, V. V. *et al.* Soldering of iron catalysts for direct synthesis of light olefins from syngas under mild reaction conditions. *ACS Catal.* **7**, 6445–6452 (2017).
35. Allen, C. L., Leitch, D. C., Anson, M. S. & Zajac, M. A. The power and accessibility of high-throughput methods for catalysis research. *Nat. Catal.* **2**, 2–4 (2019).
36. Isbrandt, E. S., Sullivan, R. J. & Newman, S. G. High Throughput Strategies for the Discovery and Optimization of Catalytic Reactions. *Angew. Chemie - Int. Ed.* **58**, 7180–7191 (2019).
37. Maier, W. F. Early Years of High-Throughput Experimentation and Combinatorial Approaches in Catalysis and Materials Science. *ACS Comb. Sci.* **21**, 437–444 (2019).
38. Schulz, H. Selforganization in Fischer–Tropsch synthesis with iron- and cobalt catalysts. *Catal. Today* **228**, 113–122 (2014).
39. Ojeda, M. *et al.* CO activation pathways and the mechanism of Fischer–Tropsch synthesis. *J. Catal.* **272**, 287–297 (2010).
40. Pham, T. H., Duan, X., Qian, G., Zhou, X. & Chen, D. CO Activation Pathways of Fischer–Tropsch Synthesis on χ -Fe 5 C 2 (510): Direct versus Hydrogen-Assisted CO Dissociation. *J. Phys. Chem. C* **118**, 10170–10176 (2014).
41. Subramanian, V. *et al.* Design of iron catalysts supported on carbon-silica composites with enhanced catalytic performance in high-temperature Fischer-Tropsch synthesis. *Catal. Sci. Technol.* **6**, 4953–4961 (2016).
42. Romero, M. D., de Lucas, A., Calles, J. A. & Rodríguez, A. Bifunctional catalyst NiHZSM-5: effects of the nickel incorporation method. *Appl. Catal. A Gen.* **146**, 425–441 (1996).
43. Mai, K., Elder, T., Groom, L. H. & Spivey, J. J. Fe-based Fischer Tropsch synthesis of biomass-derived syngas: Effect of synthesis method. *Catal. Commun.* **65**, 76–80 (2015).
44. Yogo, K., Tanaka, S., Ono, T., Mikami, T. & Kikuchi, E. Characterization of Fe-silicates and their catalytic properties for the selective reduction of nitric oxide by hydrocarbons. *Microporous Mater.* **3**, 39–46 (1994).
45. Chernavskii, P. A., Lunin, B. S., Zakharyan, R. A., Pankina, G. V. & Perov, N. S. Experimental setup for investigating topochemical transformations of ferromagnetic nanoparticles. *Instruments Exp. Tech.* **57**, 78–81 (2014).
46. Chernavskii, P. A., Dalmon, J.-A., Perov, N. S. & Khodakov, A. Y. Magnetic characterization of Fischer-Tropsch catalysts. *Oil Gas Sci. Technol.* **64**, 25–48 (2009).
47. Chernavskii, P. A., Khodakov, A. Y., Pankina, G. V., Girardon, J.-S. & Quinet, E. In situ characterization of the genesis of cobalt metal particles in silica-supported Fischer-Tropsch catalysts using Foner magnetic method. *Appl. Catal. A Gen.* **306**, 108–119 (2006).
48. Chernavskii, P. A., Kazak, V. O., Pankina, G. V., Ordonsky, V. V. & Khodakov, A. Y. Mechanistic aspects of the activation of silica-supported iron catalysts for Fischer-Tropsch synthesis in carbon monoxide and syngas. *ChemCatChem* **8**, 390–395 (2016).
49. Shroff, M. D. *et al.* Activation of Precipitated Iron Fischer-Tropsch Synthesis Catalysts. *J. Catal.* **156**, 185–207 (1995).
50. Butt, J. B. Carbide phases on iron-based Fischer-Tropsch synthesis catalysts part I: Characterization studies. *Catal. Letters* **7**, 61–81 (1990).
51. Gu, B. *et al.* Effects of the promotion with bismuth and lead on direct synthesis of light olefins from syngas over carbon nanotube supported iron catalysts. *Appl. Catal. B Environ.* **234**, 153–166 (2018).
52. Wang, C., Shao, C., Liu, Y. & Zhang, L. Photocatalytic properties BiOCl and Bi₂O₃ nanofibers prepared by electrospinning. *Scr. Mater.* **59**, 332–335 (2008).

53. Chang, C., Zhu, L., Fu, Y. & Chu, X. Highly active Bi/BiOI composite synthesized by one-step reaction and its capacity to degrade bisphenol A under simulated solar light irradiation. *Chem. Eng. J.* **233**, 305–314 (2013).
54. Ordonsky, V. V. *et al.* Soldering of iron catalysts for direct synthesis of light olefins from syngas under mild reaction conditions. *ACS Catal.* **7**, 6445–6452 (2017).

Chapter 4 Active phases for high temperature Fischer-Tropsch synthesis in the silica supported iron catalysts promoted with antimony and tin



Abstract: Fischer-Tropsch synthesis provides an important opportunity for utilization of biomass and plastic waste. Iron catalysts are the catalysts of choice for light olefin synthesis using Fischer-Tropsch reaction. In this chapter, we investigate strong promoting effects of antimony and tin on the catalytic performance of silica supported iron FT catalysts using a combination of advanced and in-situ techniques. The catalyst doping with these elements added via impregnation results in a major increase in the reaction rate and much better catalyst stability. No enhancement of iron dispersion was observed after the promotion, while somewhat higher extent of iron carbidization was observed in the antimony promoted catalysts. Iron antimony bimetallic nanoparticles are detected by several techniques. In the working catalysts, the promoters are located in close proximity to the iron nanoparticles. The promotion leads to the 7–10 times increase in the intrinsic activity of iron surface sites due to their interaction with the promoters.

Paper published in Applied Catalysis B: Environmental, Volume 292, 5 September 2021

4.1. Introduction

Fischer-Tropsch synthesis is an attractive way to convert syngas generated from non-petroleum and renewable feedstocks such as biomass, plastic and organic waste into fuels and chemicals. Iron catalysts are the catalysts of choice^{1,2} for high temperature FT synthesis, which can produce a larger fraction of olefins. Activity, selectivity to light olefins and catalyst stability are major challenges of FT synthesis over iron catalysts. FT synthesis is a complex reaction. The reaction rate and selectivity to the target hydrocarbons depend on the rate of different elementary steps. The selectivity of FT synthesis is usually following a rather broad Anderson-Schulz-Flory distribution.

As stated before, the presence of iron carbide species is crucial to the catalytic activity. Preparation of iron catalysts for FT synthesis is a complex process³ intended to result in the materials with desirable chemical, physical, catalytic and mechanical properties. The supported iron catalysts are usually prepared by impregnation followed by drying, calcination and activation in carbon monoxide or syngas.

Promotion is one of the common approaches to improve the performance of iron catalysts. Two types of promoters⁴: electronic promoters and structural promoters, are usually considered for enhancement of the FT catalytic performance. The electronic promoters⁵ enhance the intrinsic activity of the active sites. They can affect the intrinsic rate of the reaction elementary steps and shift the reaction selectivity to the target products, while the structural promoters⁶ increase the dispersion of active phase, stabilize the catalyst surface and improve the mechanical strength. The overall enhancement of the catalytic performance on the promotion is often an interplay⁴ of the electronic and structural promoters, their concentration, coverage and interaction with the active phase.

For example, alkali promoters affect the electronic state of iron and support. They usually decrease the methane selectivity and shift the hydrocarbon distribution to long chain hydrocarbons, while copper enhances iron reducibility and carbidization. Much higher reaction rates have been often observed⁷ on copper-promoted catalysts than on the potassium-promoted and non-promoted counterparts, while the promotion with potassium had a stronger impact on the selectivity.

In chapter three we addressed screening of 29 elements, as promoters for silica supported iron FT catalysts using the high throughput experimentation approach. We found that the performance of iron catalysts could be enhanced by promotion with soldering metals. The promotion of iron catalysts with bismuth and lead resulted in a remarkable increase in the carbon monoxide hydrogenation rate, light olefin selectivity and productivity with a possibility to conduct Fischer–Tropsch synthesis at low reaction pressure. In previous reports^{8,9,10,11}, we showed that bismuth and lead showed the properties of both electronic and structural promoters. The bismuth and lead promoted catalysts exhibited 2-3 times higher intrinsic activity¹⁰ (TOF) relative to the non-promoted iron catalyst with the 60% increase in the selectivity to light olefins. At the same time, the catalyst stability against sintering and carbon deposition was enhanced in the presence of bismuth. A detailed in-situ characterization study¹¹ uncovered a remarkable mobility and versatility of bismuth under the reaction conditions. Bismuth metallic species, which transform into larger spherical bismuth liquid droplets under the reaction temperatures readily migrate over the catalyst surface, with the formation of iron-bismuth core–shell structures. In the working FT catalysts, metallic bismuth located at the interface of iron species undergoes continuous oxidation and reduction cycles¹¹, which facilitate carbon monoxide dissociation.

HTE experiments also showed that the promotion of iron catalysts with tin and antimony also led to a major increase in the FT reaction rate. Both tin and antimony also have relatively low melting temperatures. Their Tammann and Hüttig temperatures¹², corresponding respectively to bulk and surface mobility are well below the reaction temperature of high temperature FT synthesis. This suggests that these promoters can be also mobile under the reaction conditions. At the same time, very few information is available about the active species, which form on addition of tin and antimony to iron catalysts and their role in FT synthesis.

The goal of this chapter is to elucidate the genesis and evolution of active phases in the silica supported iron catalysts promoted with antimony and tin during their activation and catalytic reaction using a combination of in-situ and advanced characterization techniques. The characterization results are discussed alongside with the catalytic results obtained in a high-pressure catalytic reactor.

4.2. Results

4.2.1. Ex-situ characterization

The XRF elemental analysis data for the Sn and Sb promoted catalysts (prepared by co-impregnation and mechanical mixture) are displayed in **Table 4-1**. All the catalysts have similar iron contents to the inventory (around 10 wt.%) in most of samples and 21 wt.% in Fe(20%)/SiO₂. The Sn and Sb promoter contents were close to 0.7 - 0.8 wt.%. The XRD profiles of the Fe/SiO₂ reference iron catalyst and those co-impregnated with the Sn and Sb promoters are available in previous chapter. **Figure 4-1 a** shows the XRD profiles of the Fe/SiO₂ (20%) catalyst and those prepared by mechanical mixture of Fe(20%)/SiO₂ and Sn/SiO₂ or Sb/SiO₂. The calcined catalysts display distinguished diffraction peaks of the hematite phase (Fe₂O₃, JCPDS13-0534). No diffraction peaks attributed to the crystalline phases of the

antimony and tin promoters were observed. The Scherrer equation has supplied additional information about the iron oxide crystallite size (**Table 4-1**). Note that Fe/SiO₂(20%) has slightly larger iron oxide crystallites compared to Fe/SiO₂ with the iron content of about 10 wt.%. As expected, the addition of Sn and Sb promoters by mechanical mixing to the Fe/SiO₂(20%) catalyst seems to have no effect on the iron oxide dispersion, the hematite crystallites sizes measured by XRD were around 20 nm, which is essentially the same as on relevant silica supported iron catalyst. In the FeSn/SiO₂ catalysts prepared by co-impregnation, the hematite crystallite sizes were slightly smaller compared to the reference Fe/SiO₂ catalyst.

Table 4-1. Physical properties of supported Fe catalysts

Sample	Fe content ^a (wt%)	Promoter content ^a (wt%)	D_{oxide} ^b (nm)	Total H ₂ consum ^c (mmol/g)	S_{BET} ^d (m ² /g)	V_{tot} ^e (cm ³ /g)
Fe/SiO ₂	11.2	-	17	2.76	268.5	1.045
FeSn/SiO ₂	10.9	0.69	11	2.77	263.0	1.041
FeSb/SiO ₂	9.4	0.72	22	2.70	274.6	1.060
Fe(20%)/SiO ₂	21.3	-	21	4.68	203.4	1.021
FeSn/SiO ₂ (M)	9.2	0.71	20	2.75	229.4	1.035
FeSb/SiO ₂ (M)	9.2	0.74	21	2.74	228.0	1.032

^aFe and promoter content from XRF.

^bAverage particle size of iron oxide by XRD, estimated error 10 %.

^cThe total H₂ consumption and iron reducibility degree from TPR analysis.

^dBET surface area.

^eSingle point desorption total pore volume of pores, $P/P_0=0.975$.

We also performed XRD measurements (**Figure 4-1 b**) for the non-promoted and promoted iron catalysts (prepared by mechanical mixing) after FT reaction. The diffraction peaks around 2θ angle of 44° for all the catalysts are attributed to the iron carbide phases. For this study, the width of the iron carbide XRD peak was not much affected by the promoters. Our previous magnetization data¹³ suggest that χ -Fe₅C₂ or ϵ -Fe₂C can contribute to the intensity and width of the XRD peak at 2θ angle of 44° . This suggests that the unambiguous identification of specific iron carbide phases could

be difficult from the XRD patterns. The apparent sizes of iron carbide nanoparticles calculated from the XRD peak for these catalysts using the Scherrer equation were around 5 nm. These sizes are underestimated due to the possible overlapping of several XRD peaks of iron carbide phases.

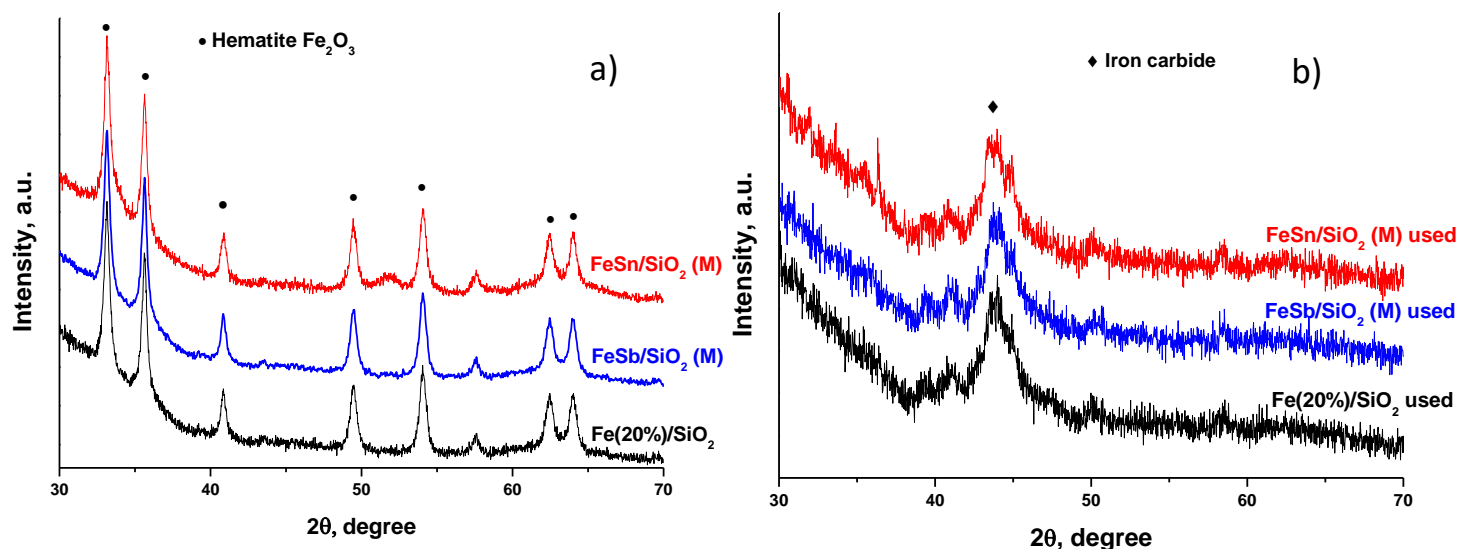


Figure 4-1. XRD patterns of the catalysts after calcination (a) and after FT reaction (b).

Figures 4-2 to 4-4 show the STEM-HAADF (High Angle Annular Dark Field) micrographs and STEM-EDX (Energy Dispersive X-ray Spectroscopy) elemental maps for the fresh Fe/SiO₂, FeSn/SiO₂ and FeSb/SiO₂ co-impregnated catalysts and those after activation in CO. Two types of support morphologies are identified in Fe/SiO₂ (**Figure 4-2 a**): porous support constituted by small grains with sizes <20 nm and heterogeneous support formed by the co-existence of large grains (sizes >50nm) with small grains disposed in a porous non-regular matrix. Owing to the Z contrast achieved in the STEM-HAADF imaging mode, the presence of high Z elements such as Fe, is unambiguously determined (**Figure 4-2 a**). The Fe particles are uniformly distributed on/within the porous support (white features in the STEM-HAADF micrograph). The Fe particle sizes range from 10 nm to 100 nm. In the calcined FeSn/SiO₂ catalyst (**Figure 4-3 a**), the Fe nanoparticles are also uniformly dispersed on the SiO₂ porous support

with the size slightly larger than for Fe/SiO₂. The STEM-EDX confirms the presence of Sn homogeneously distributed within the specimen. In calcined FeSb/SiO₂ (Figure 4-4 a) catalyst, we also detected a homogenous distribution of Fe nanoparticles with the sizes <100 nm on the porous support constituted by the SiO₂ grains. Antimony was also homogeneously distributed over SiO₂. The Sb quantification was not possible however, from EDX, because the Sb peak is superimposed with the Si K line.

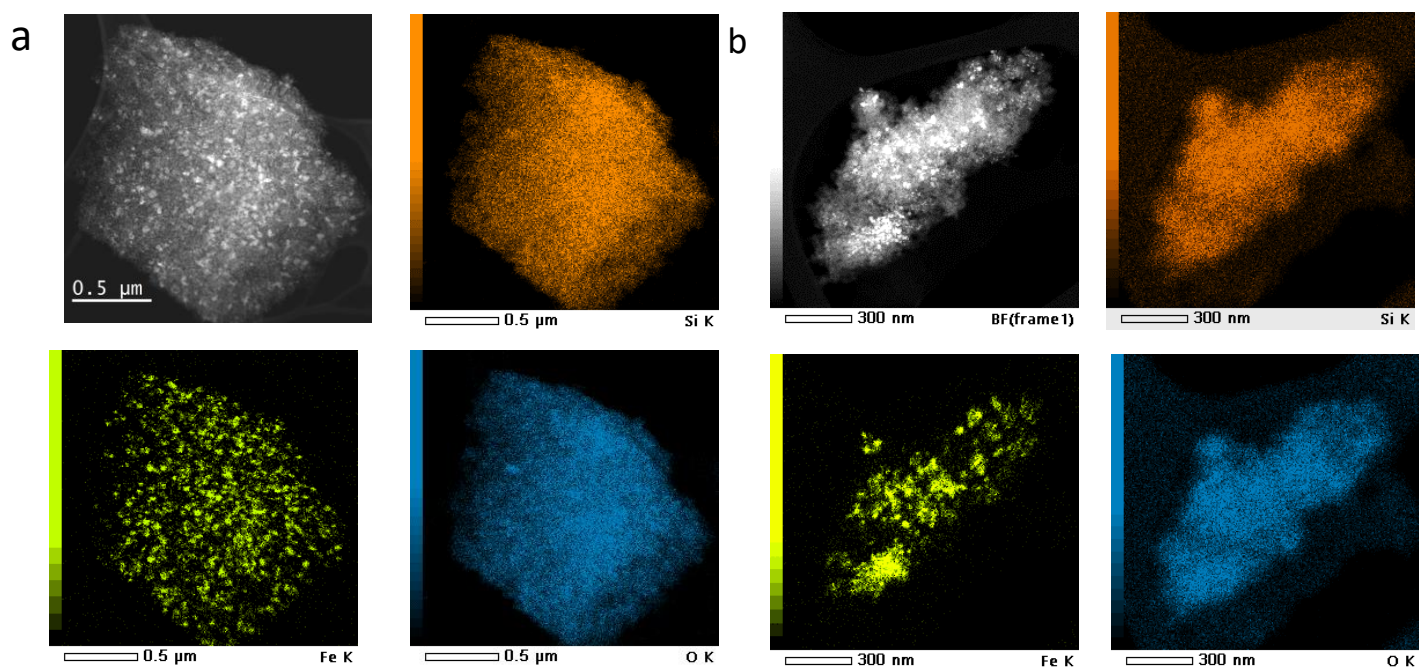
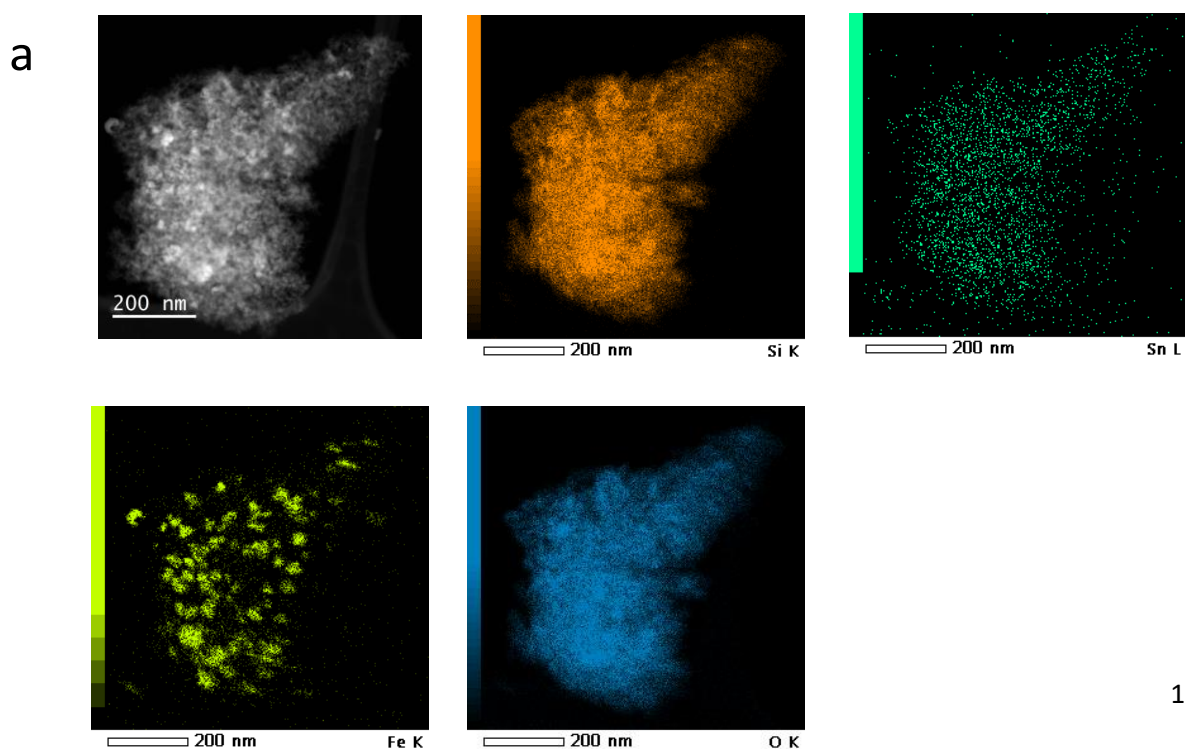


Figure 4-2. STEM-HAADF and SEM-EDX mapping of the Fe/SiO₂ catalyst: (a) after calcination; (b) after activation in CO.



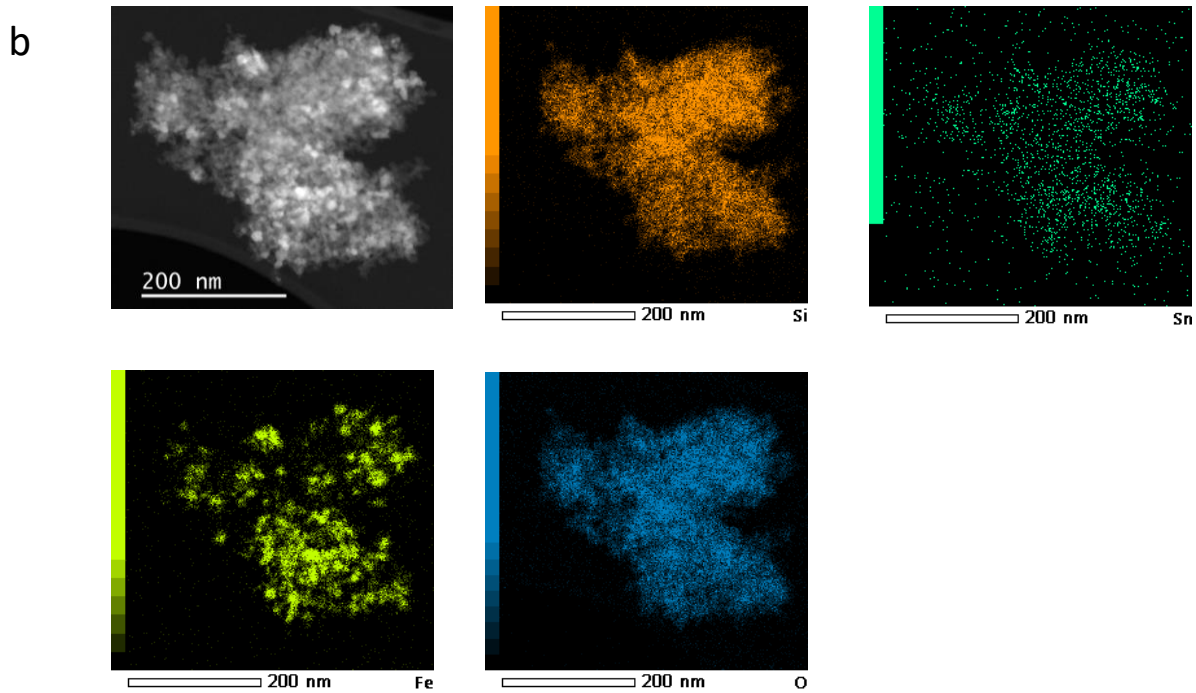
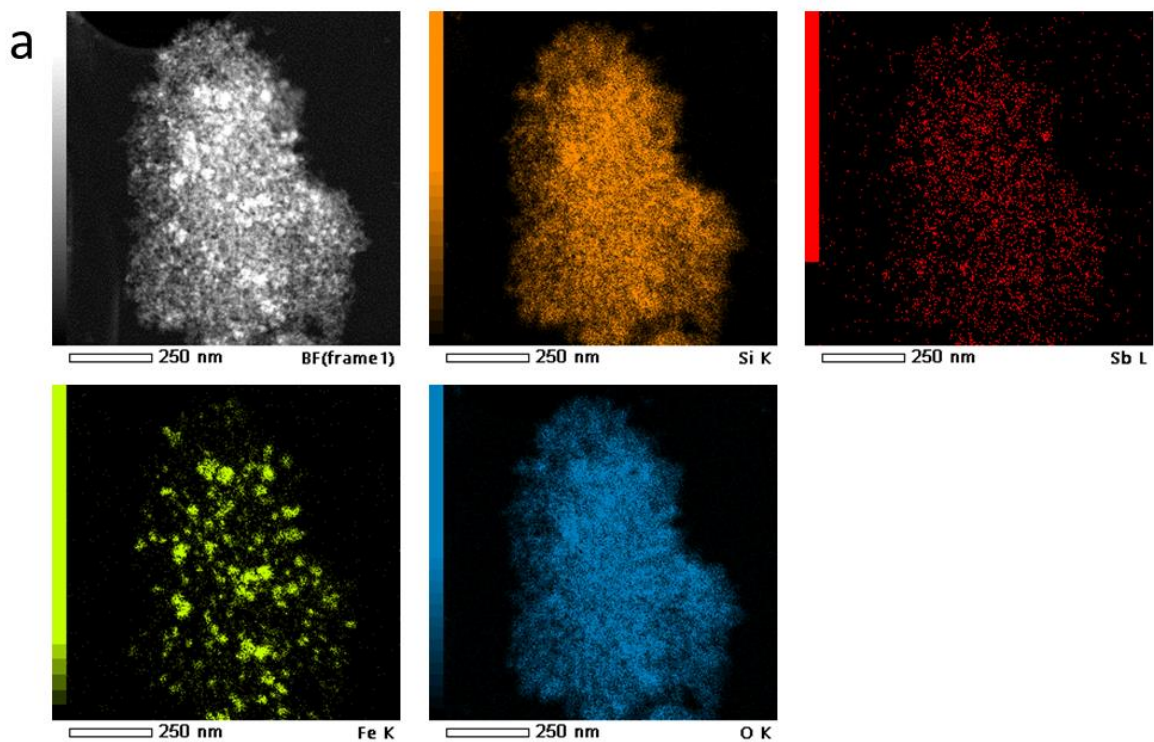


Figure 4-3. STEM-HAADF and SEM-EDX mapping of the FeSn/SiO₂ catalyst: (a) after calcination; (b) after activation in CO.



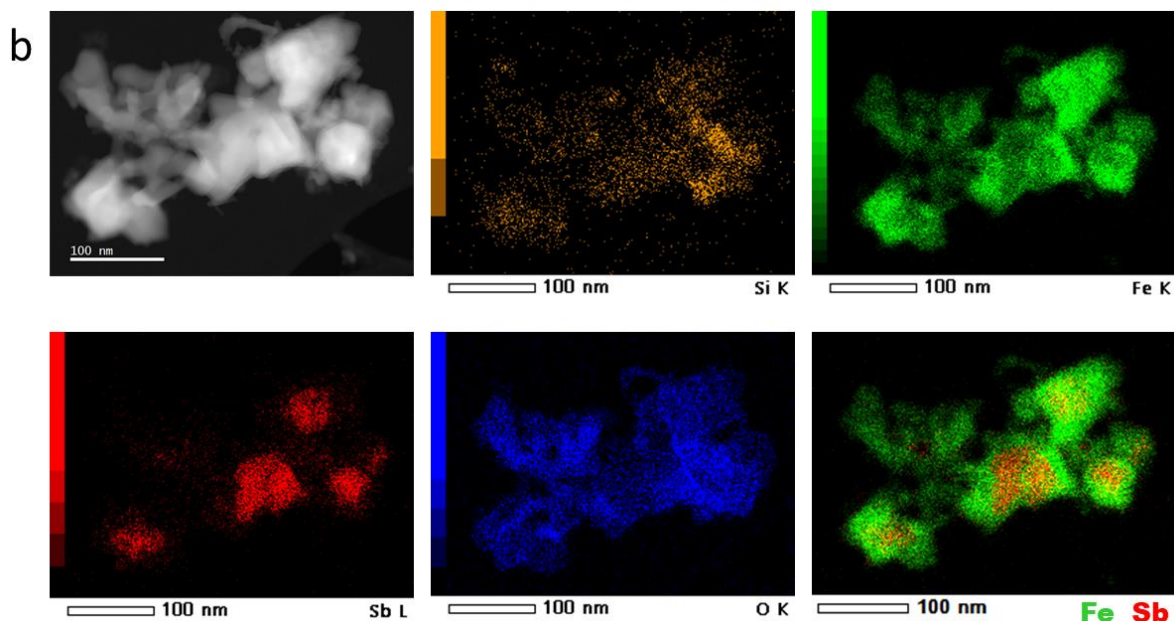
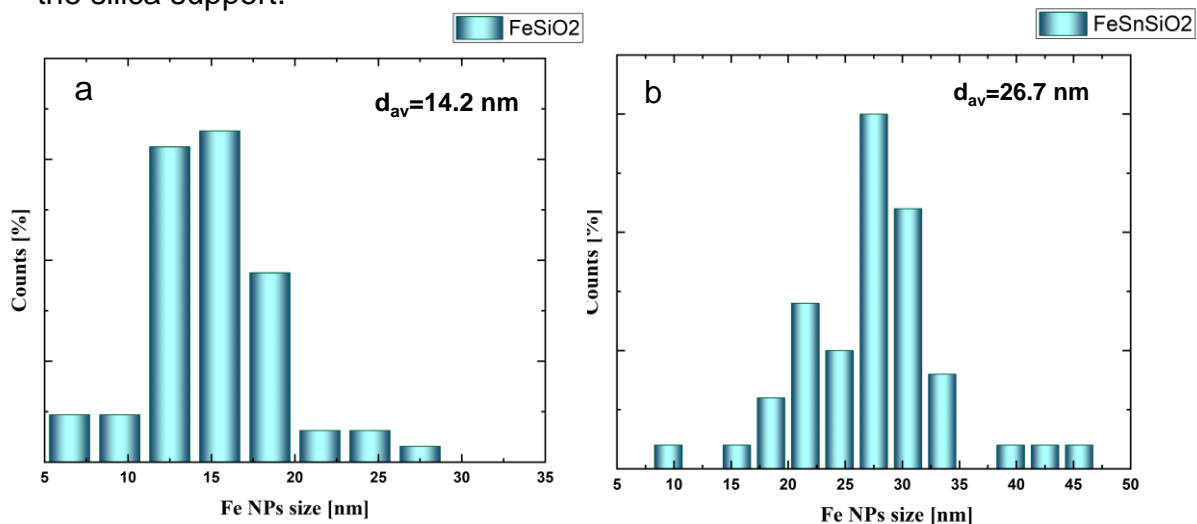


Figure 4-4. STEM-HAADF and SEM-EDX mapping of the FeSb/SiO₂ catalyst: (a) after calcination; (b) after activation in CO showing the formation of Fe-Sb core-shell structures.

In order to get deeper understanding on the catalyst's evolution prior to the reaction, the STEM-EDX analysis was also conducted for the activated iron catalysts. In the activated Fe/SiO₂ catalyst (**Figure 4-2 b**), both individual small Fe nanoparticles and larger agglomerates of about 100 nm were detected. The activated FeSn/SiO₂ catalyst (**Figure 4-3 b**) shows the regions of the specimens with different sizes, shapes and morphologies of the support and/or the nanoparticles. The size of Fe nanoparticles varies between 20 and 100 nm and their shapes varies from rounded to platelets. No Sn-containing nanoparticles area is observed and the Sn seems highly dispersed on the silica support.



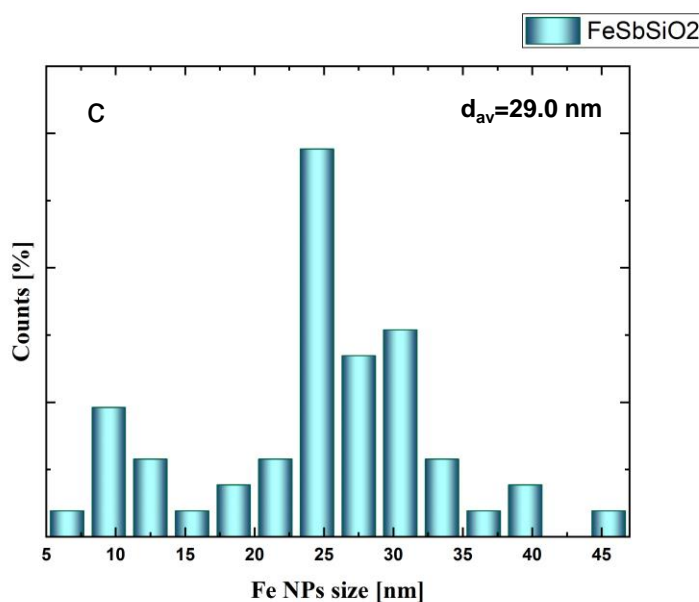
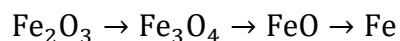


Figure 4-5. Histograms of iron nanoparticles distribution in silica supported catalysts activated in CO at 350 °C: a) Fe/SiO₂, b) FeSn/SiO₂, c) FeSb/SiO₂.

The activated FeSb/SiO₂ catalyst (**Figure 4-5 b**) displays iron nanoparticles with sizes comprised between 10 and 50 nm and larger nanoparticle agglomerates. The nanoparticles show a core-shell morphology, with the core rich in Sb and the shell constituted mainly by iron. The Fe shell appears to be oxidized probably due to the exposure of the activated nanoparticle to air and catalyst surface passivation. **Figure 4-5** displays the histogram of iron nanoparticle distribution calculated from the STEM images of the activated catalysts using at least 50 iron nanoparticles. The average iron nanoparticle size is of 14.2 nm in the activated Fe/SiO₂ catalyst (**Figure 4-5 a**), while the promotion results in the increase in the iron nanoparticle size to 26.7 nm for FeSn/SiO₂ (**Figure 4-5 b**) and 29.0 nm for FeSb/SiO₂ (**Figure 4-5 c**).

Reducibility is an important feature of iron catalysts. **Figure 4-6** shows the H₂-TPR profiles for iron catalysts promoted with Sn and Sb via mechanical mixing. The H₂-TPR profiles of the catalyst prepared by co-impregnation are available in the previous chapter. Since the amount of promoter is too small, no noticeable contribution of the promoters to the area of TPR peaks can be expected. The hydrogen

consumption amounts measured by TPR principally provide therefore, useful information about the iron reduction. The TPR profiles display three main hydrogen consumption peaks, which are attributed to the step-wise iron reduction from hematite to metallic iron:



The TPR profiles are consistent with previous works^{14,15,16,17}, the first peak at 340-420°C is generally related to the reduction of hematite (Fe_2O_3) to magnetite (Fe_3O_4), the second peak can be associated with the reduction of magnetite (Fe_3O_4) to wüstite (FeO), while the third peak at 650-700°C can be attributed to the last step of iron reduction from wüstite (FeO) to metallic iron (Fe). Also, we observe an intense peak at temperatures exceeding 1000°C that can be linked to hardly reducible iron silicate species. The promotion with Sb and Sn slightly affects the position of TPR peaks for iron catalysts. Almost all TPR peaks slightly shift to lower temperatures on the promotion with antimony and tin (**Figure 4-6**), while the first peak referring to the reduction of hematite to magnetite slightly shifts to higher temperature (from 365 °C to 390 °C). At the same time, the overall hydrogen consumptions are similar on the non-promoted iron catalyst and the counterparts promoted with Sb or Sn (**Table 4-1**).

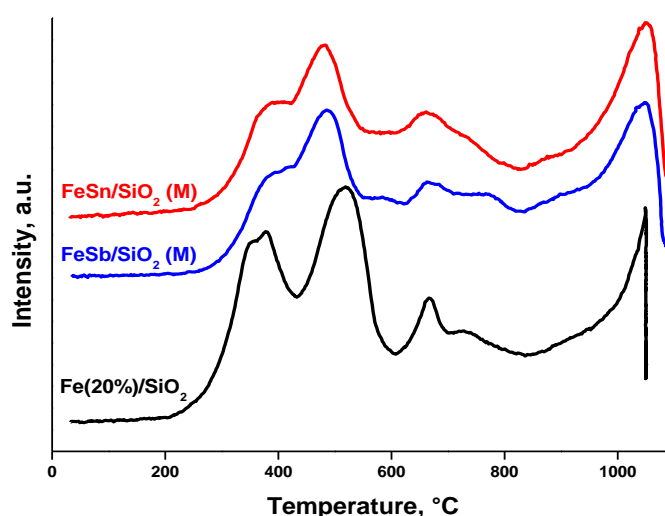


Figure 4-6. H_2 -TPR profiles of $\text{Fe}(20\%)/\text{SiO}_2$, FeSb/SiO_2 (m) and FeSn/SiO_2 (m) prepared by mechanical mixing.

Figure 4-7 shows the thermogravimetric analysis (TGA) results of activated and spent catalysts prepared respectively by co-impregnation, under an air atmosphere. The thermograms show a first weight loss between 80 °C to 150 °C, that can be associated to physisorbed water removal and dehydration of iron oxyhydroxide (FeOOH) generated by ambient moisture. Furthermore, the significant weight losses within 350-550 °C can be assigned to the combustion of carbonaceous deposits. This loss is smaller for the catalysts activated in CO (**Figure 4-7 a**). It corresponds to the combustion of iron carbides in the activated samples.

The weight loss is more significant for the catalysts, which were exposed to FT reaction (**Figure 4-7 b**). For the spent catalysts, this loss corresponds to the oxidation of carbon species, which may have been deposited on the catalysts during the FT reaction. It can be clearly seen that the Sn and Sb promoters inhibit carbon deposition on catalyst surface. The spent Sn- and Sb-promoted catalysts prepared by co-impregnation show ~60% and 30% less deposition respectively compared to the reference non-promoted Fe/SiO₂ catalyst. This smaller amount of carbon deposition seems to contribute to better stability of the Sn- and Sb-promoted catalysts in FT reaction. In our previous work¹⁸, the carbon deposition was reduced in the iron catalysts promoted by bismuth. The observed phenomenon was explained by the continuous carbon removal from the surface by mobile promoter. Similar mechanism can possibly operate for antimony.

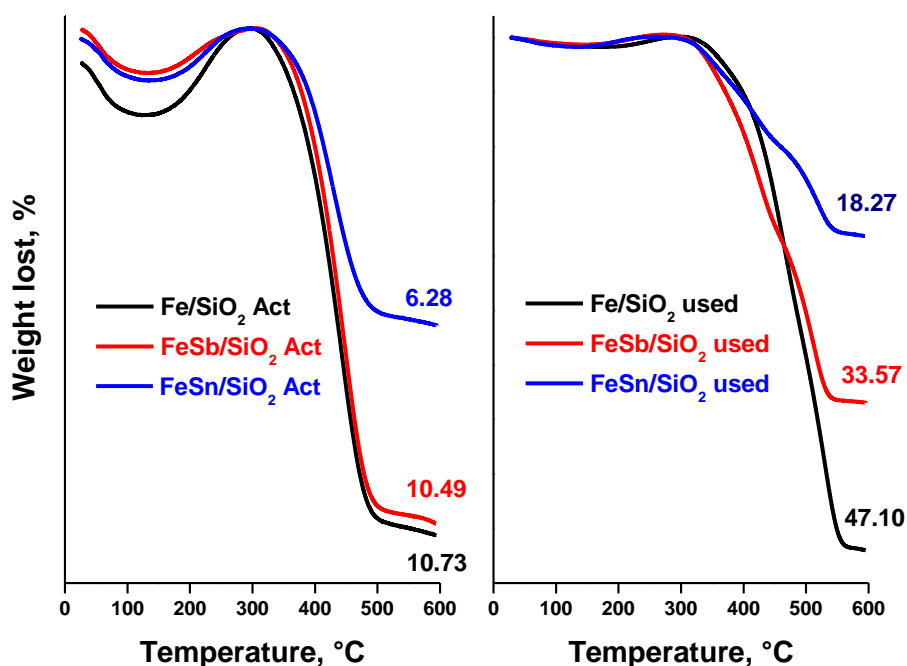
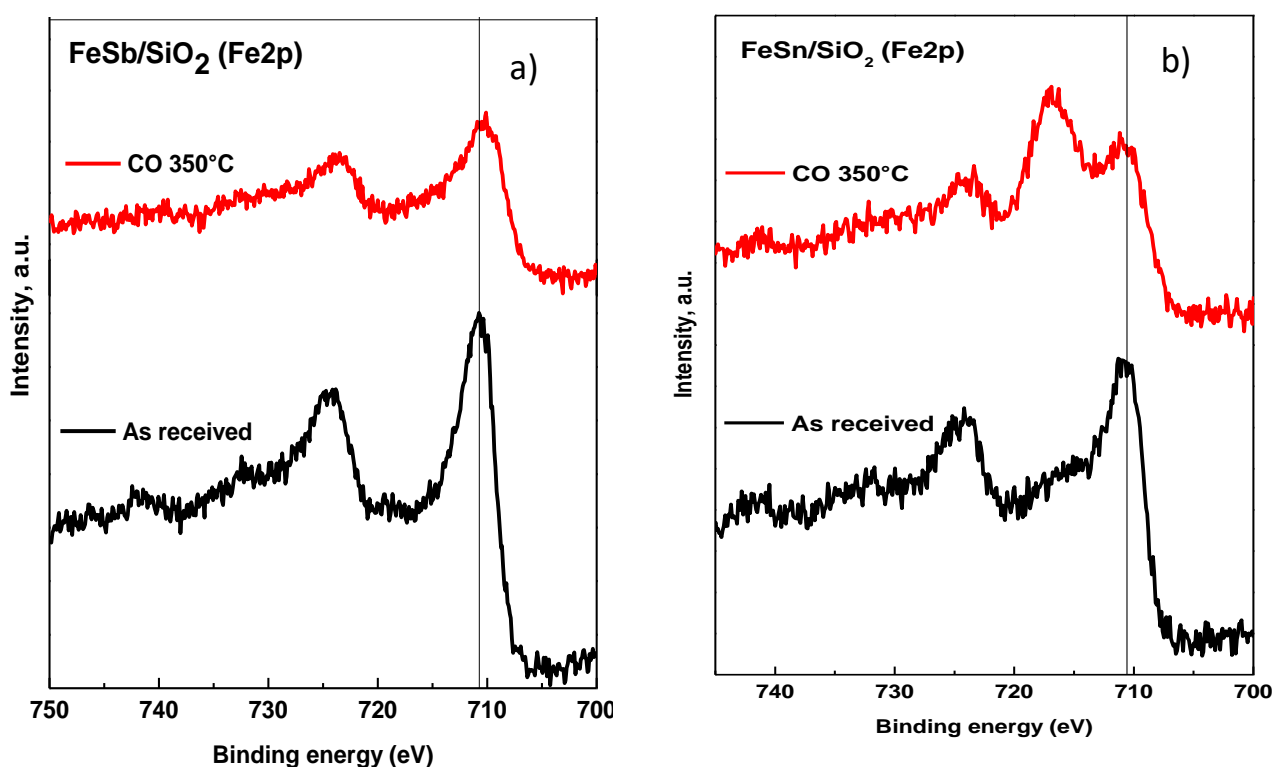


Figure 4-7. Thermogravimetric analysis (TGA) curves for activated (a) and spent catalysts (b).

Since the catalytic processes occur on the surface, the surface structure of iron catalysts was studied by XPS (**Figure 4-8**). The Fe 2p XPS spectra (**Figure 4-8 a and b**) for calcined catalysts display peaks at ~711.2 eV (Fe 2p_{3/2}) and ~724.3 eV (Fe 2p_{1/2}) with a shakeup satellite structure at ~719.2 eV. The shape of the peaks combined with the binding energies clearly indicate the presence of Fe³⁺ species. The XPS data are consistent with XRD that showed the presence of (Fe₂O₃) hematite phase in the calcined catalysts. After treatment with CO at 350 °C, the XPS spectra present noticeable changes. First, the peaks assigned to Fe³⁺ in FeSb/SiO₂ considerably decrease in intensity. The ratio of the I_{Fe}/I_{Si} XPS signals decreases from 3.44 to 2.31, which can be attributed to iron sintering (**Table 4-2**). We see a subtle Fe 2p peak broadening after activation, identification of the exact binding energy and attribution of this peak to iron carbide or metallic iron is difficult because of its low intensity. It appears as a shoulder. However, like in previous case, as we observe by Mössbauer

analysis after activation a high iron carbide content we could suggest that this broadening is generated by formation of carbide species. This confirms the presence of iron oxide and iron carbide in the activated catalysts. In addition, after the CO treatment, another peak appears at ~ 716.5 eV in the XPS spectrum of activated FeSn/SiO_2 , that can be assigned to the Sn $3p_{3/2}$ level. The Sn $3p_{3/2}$ peaks at 716.5 eV can be attributed either to the Sn^{4+} or Sn^{2+} species. The major increase in the intensity of this peak after the treatment with CO suggests an increase in the surface Sn concentration and tin redispersion on the catalyst surface.



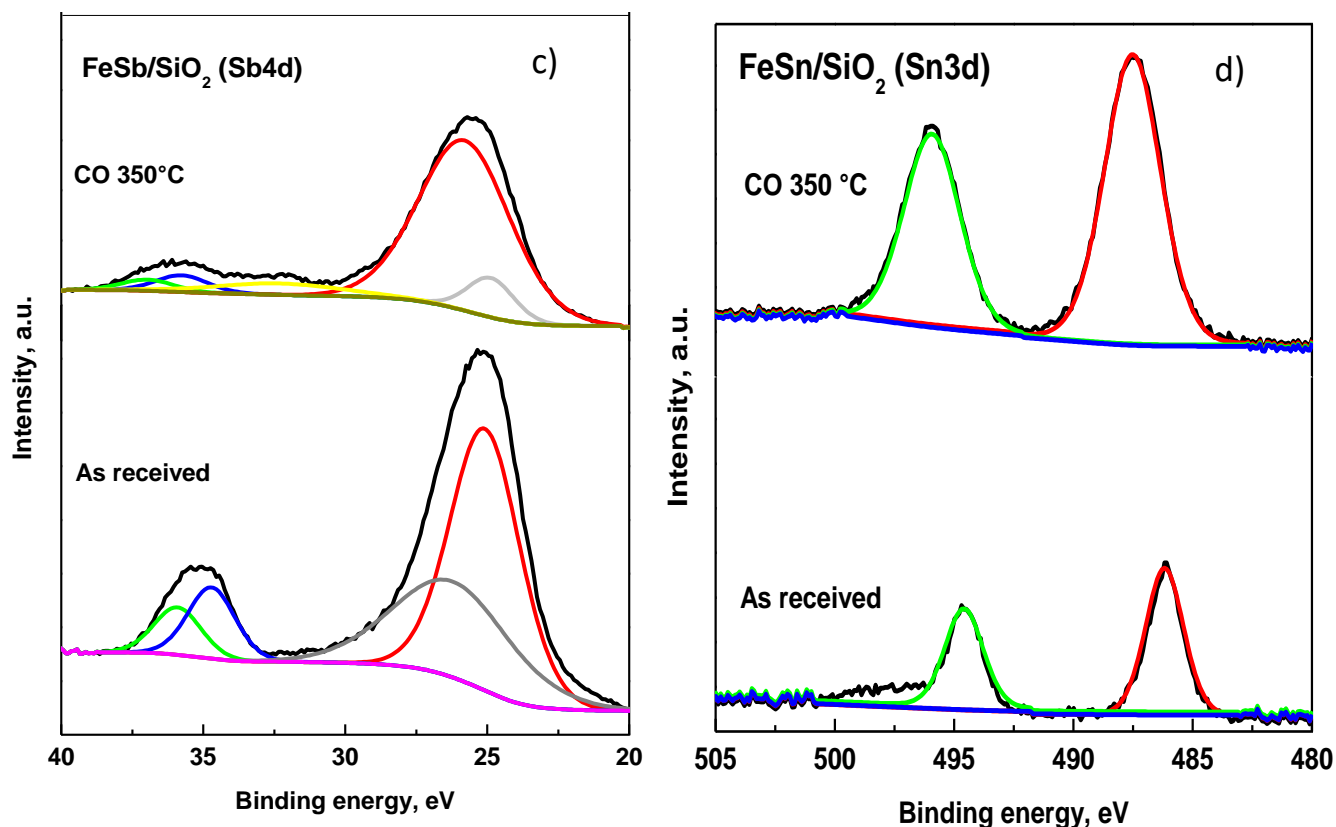


Figure 4-8. XPS spectra after calcinations and exposure to carbon monoxide: (a) Fe 2p XPS spectra of the FeSb/SiO₂ catalyst, (b) Fe 2p XPS spectra of the FeSn/SiO₂ catalyst, (c) Sb 4d XPS spectra of the FeSb/SiO₂ catalyst, (d) Sn 3d XPS spectra of the FeSn/SiO₂ catalyst.

Table 4-2. XPS ratio before and after activation

	FeSb/SiO ₂		FeSn/SiO ₂	
	I _{Fe} /I _{Si}	I _{Sb} /I _{Si}	I _{Fe} /I _{Si}	I _{Sn} /I _{Si}
As received	3.44	1.32	2.68	0.29
After activation in CO 350 °C	2.31	1.36	-*	1.18

*The value obtained for I_{Fe}/I_{Si} after CO treatment for FeSn/SiO₂ is not reliable because of the contribution of Sn peak.

The Sb 4d XPS spectra are shown in **Figure 4-8 c**. The presence of a broad peak ~35 eV demonstrates the presence of oxidized Sb. The deconvolution of this peak generates two peaks at ~35.9 eV and ~34.7 that can be assigned respectively to the Sb 4d_{5/2} and 4d_{3/2} components in the Sb₂O₃. Note that XPS did not detect any noticeable concentration of Sb₂O₅ in the calcined FeSb/SiO₂ catalyst (Sb 4d binding energies 36.70 and 35.50 eV in Sb₂O₅). The broad low-intense feature at 25 eV can be assigned to the O 2s peak. The treatment in CO leads to partial Sb reduction to

metallic state with a characteristic XPS peak at ~ 32.3 eV. The Sb/Si XPS ratio does not change after the catalyst activation in CO (**Table 4-2**). This suggests that no visible changes in the Sb dispersion, which might occur during the activation. These data are further corroborated with the XAS experiments presented below. The Sn 3d XPS spectra are shown in **Figure 4-8 d**. The calcined catalyst exhibits XPS peaks with binding energies of 486.2 and 494.6 eV that are assignable²⁰ to Sn 3d_{5/2} and Sn 3d_{3/2} and that are characteristics of the Sn²⁺ species. After the CO treatment, a displacement of the Sn 3d XPS signal to higher binding energies is observed. The peak at 487.5 eV can be related to the framework Sn⁴⁺ species in the materials, in which Sn⁴⁺ substituted Si⁴⁺ atoms as previously stated by Pachamuthu²¹ et al. Also, the increase in the I_{Sn}/I_{Si} XPS ratio from 0.29 to 1.18 (**Table 4-2**) confirms tin redispersion on the catalyst surface at high temperature in CO. This suggestion is consistent with the increase in the intensity of the Sn 3p_{3/2} peak at 716.5 eV (**Figure 4-8 b**) observed after the exposure to CO.

4.2.2. In-situ Mossbauer measurements

To identify different Fe species and correlate them with the catalytic performance, we performed in-situ Mössbauer spectrometric investigation of the non-promoted Fe/SiO₂, Sb- and Sn-promoted catalysts prepared by impregnation and mixing under CO and syngas. The Mössbauer spectra were measured at -153 °C (**Figure 4-9 and 4-10**). **Table 4-4** displays the Mössbauer fit parameters of fresh catalysts and catalysts exposed to syngas in-situ under the conditions similar to those in the catalytic tests. Analysis of all fresh catalysts reveals the presence of hematite species (Fe₂O₃). This observation agrees well with the XRD and XPS data. Then, the catalysts were in-situ activated in CO at 350 °C at 1 bar and then exposed to syngas under the FT reaction conditions (H₂/CO=1, P=10 bar). The Mossbauer spectra of the

spent catalysts were measured at $-153\text{ }^{\circ}\text{C}$ without exposure of the catalysts to air (Figure 4-10).

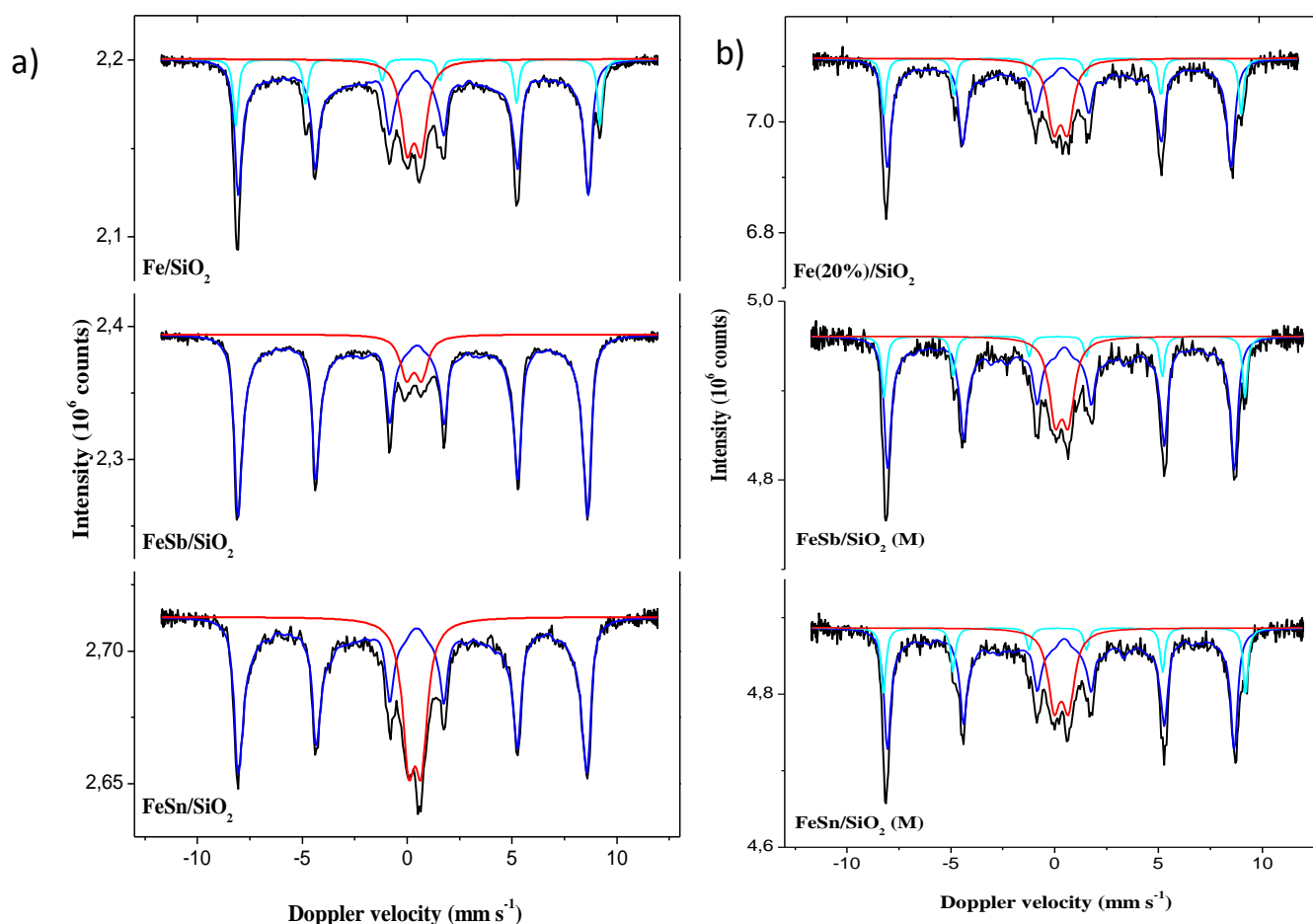


Figure 4-9. Mössbauer spectra obtained for fresh (a) impregnated and (b) mixed catalysts at $-153\text{ }^{\circ}\text{C}$.

The Mössbauer spectra of the activated and spent catalysts are rather different from the fresh ones. Iron species are present in the spent Fe/SiO₂ catalyst as 70% Hägg carbide and 30% wüstite (Table 4-4). An obvious promoting effect is observed for the FeSb/SiO₂ sample, in which the fraction of Hägg carbide increases to ~90%. The promotion with Sb seems to enhance iron carbidization. In the FeSn/SiO₂ sample, the extent of carbidization is lower and the fraction of wüstite is higher ~57%. The fraction of the Hägg carbide formed after the FT reaction with the Fe(20%)/SiO₂ sample is ~76%, which is higher than in the non-promoted Fe(10%)/SiO₂ catalyst (70%), but lower than in the Sb-promoted catalyst (78-80%). Higher extent of carbidization in

Fe(20%)/SiO₂ compared to Fe/SiO₂ can be due to large iron particle sizes (Table 4-1). Indeed, previously it was shown²² that larger iron oxide particles are easier to carburize than smaller ones.

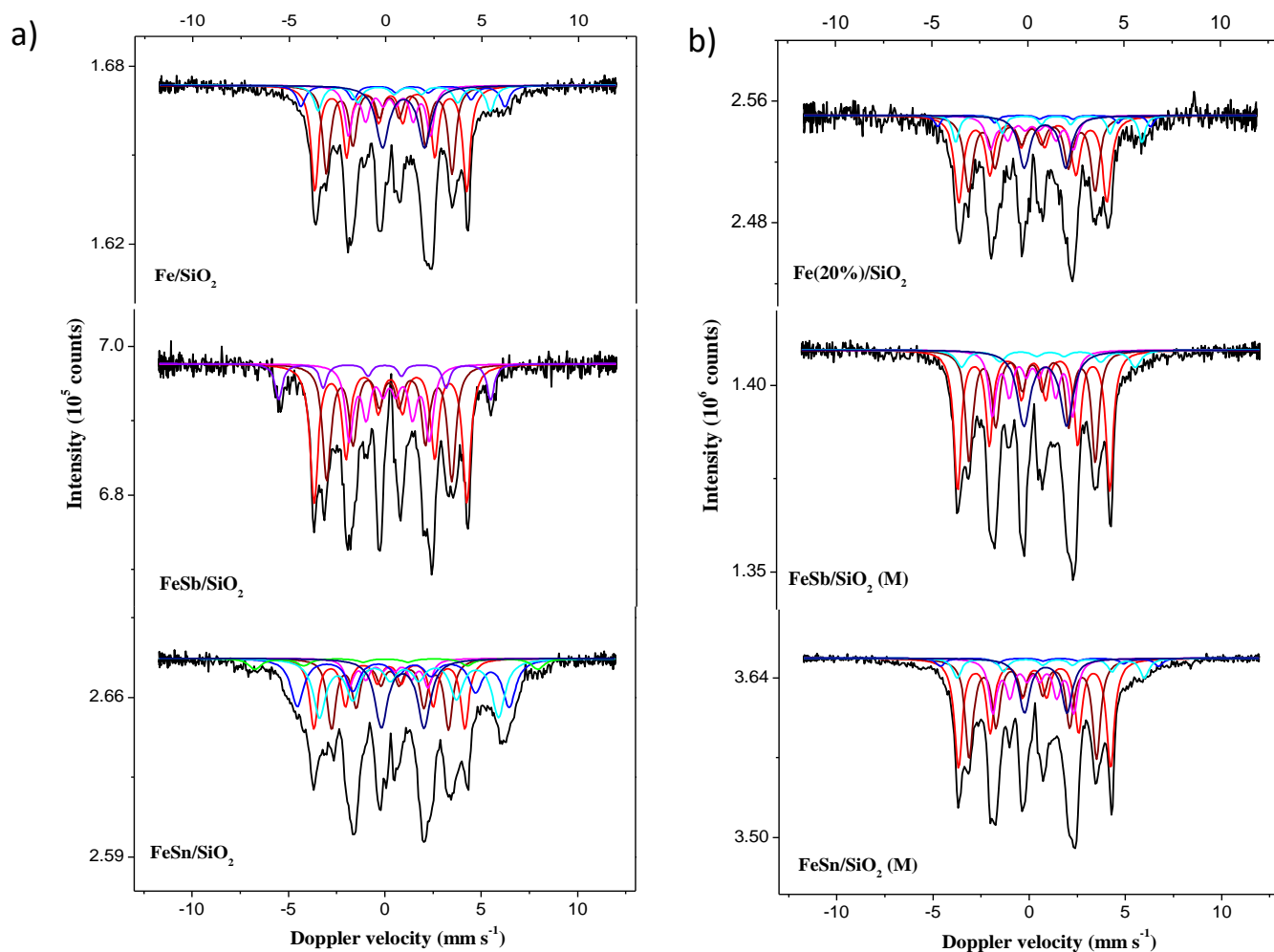


Figure 4-10. Mössbauer spectra after reaction for impregnated and mixed catalysts at -153 °C.

Table 4-3. The Mössbauer fitted parameters of fresh and spent catalysts, obtained at -153 °C

Sample/ Treatment	IS (mm·s ⁻¹)	QS (mm·s ⁻¹)	Hyperfine field (T)	Γ (mm·s ⁻¹)	Phase	Spectral contribution (%)
Fe/SiO ₂	0.37	-0.15	51.4*	0.40	α-Fe ₂ O ₃	70
	0.35	0.33	54.0	0.28	α-Fe ₂ O ₃ (Morin ^b)	12
	0.33	0.67	-	0.70	Fe ³⁺ (SPM)	18
Fe/SiO ₂ H ₂ /CO=1 350 °C, 10 bar	0.26	-	24.5	0.47	χ-Fe ₅ C ₂ (I)	30
	0.19	-	20.2	0.47	χ-Fe ₅ C ₂ (II)	26
	0.20	-	13.2	0.47	χ-Fe ₅ C ₂ (III)	14
	1.13	-0.47	32.9	0.54	Fe _{1-x} O (I- Fe ²⁺)	7
	1.06	-0.18	27.8	0.54	Fe _{1-x} O (II- Fe ²⁺)	8
	0.93	2.19	-	0.79	Fe _{1-x} O (SPM)	15
Fe(20)/SiO ₂ Fresh sample	0.37	-0.15	51.8*	0.43	α-Fe ₂ O ₃	69
	0.32	0.32	53.9	0.28	α-Fe ₂ O ₃ (Morin)	13
	0.35	0.67	-	0.70	Fe ³⁺ (SPM)	18

Fe(20)/SiO₂ H₂/CO=1 350 °C, 10 bar	0.26	-	23.9	0.54	χ -Fe ₅ C ₂ (I)	33
	0.20	-	20.5	0.54	χ -Fe ₅ C ₂ (II)	29
	0.19	-	13.4	0.54	χ -Fe ₅ C ₂ (III)	14
	1.16	-0.65	34.4	0.40	Fe _{1-x} O (I- Fe ²⁺)	3
	1.27	-0.37	30.1	0.40	Fe _{1-x} O (II- Fe ²⁺)	8
	0.89	2.16	-	0.70	Fe _{1-x} O (SPM)	13
FeSb/SiO₂	0.36	-0.20	51.5*	0.40	α -Fe ₂ O ₃	89
	0.33	0.73	-	0.70	Fe ³⁺ (SPM)	11
FeSb/SiO₂ H₂/CO=1 350 °C, 10 bar	0.26	-	24.6	0.51	χ -Fe ₅ C ₂ (I)	38
	0.20	-	20.1	0.51	χ -Fe ₅ C ₂ (II)	32
	0.21	-	12.9	0.51	χ -Fe ₅ C ₂ (III)	21
	0.00	-	34.1	0.45	Fe ⁰	9
FeSn/SiO₂	0.36	-0.20	51.3*	0.40	α -Fe ₂ O ₃	74
	0.37	0.60	-	0.70	Fe ³⁺ (SPM)	26
FeSn/SiO₂ H₂/CO=1 350 °C, 10 bar	0.27	-	24.3	0.51	χ -Fe ₅ C ₂ (I)	18
	0.24	-	19.0	0.51	χ -Fe ₅ C ₂ (II)	17
	0.20	-	12.7	0.51	χ -Fe ₅ C ₂ (III)	8
	0.31	0.36	45.7	0.80	Fe _{1-x} O (I- Fe ³⁺)	4
	1.24	-0.57	34.2	0.80	Fe _{1-x} O (II- Fe ²⁺)	18
	1.14	-0.14	29.7	0.80	Fe _{1-x} O (III- Fe ²⁺)	22
FeSb/SiO₂ (M)	0.37	-0.15	51.8*	0.40	α -Fe ₂ O ₃	70
	0.32	0.33	54.0	0.28	α -Fe ₂ O ₃ (Morin)	12
	0.34	0.64	-	0.70	Fe ³⁺ (SPM)	18
FeSb/SiO₂ (M) H₂/CO=1 350 °C, 10 bar	0.27	-	24.4	0.45	χ -Fe ₅ C ₂ (I)	34
	0.21	-	20.2	0.45	χ -Fe ₅ C ₂ (II)	28
	0.22	-	12.9	0.45	χ -Fe ₅ C ₂ (III)	16
	1.08	-0.10	27.9	0.67	Fe _{1-x} O (Fe ²⁺)	6
	0.88	2.21	-	0.81	Fe _{1-x} O (SPM)	16
FeSn/SiO₂ (M)	0.37	-0.16	51.8*	0.40	α -Fe ₂ O ₃	69
	0.32	0.33	54.1	0.28	α -Fe ₂ O ₃ (Morin)	13
	0.33	0.69	-	0.70	Fe ³⁺ (SPM)	18
FeSn/SiO₂ (M) H₂/CO=1 350 °C, 10 bar	0.27	-	24.6	0.49	χ -Fe ₅ C ₂ (I)	33
	0.20	-	20.5	0.49	χ -Fe ₅ C ₂ (II)	31
	0.22	-	13.0	0.49	χ -Fe ₅ C ₂ (III)	16
	1.34	-0.57	35.2	0.54	Fe _{1-x} O (I- Fe ²⁺)	3
	1.30	-0.36	30.3	0.54	Fe _{1-x} O (II- Fe ²⁺)	6
	0.86	2.21	-	0.68	Fe _{1-x} O (SPM ^a)	11

4.2.3. In-situ XAS characterization of the Sn and Sb promoters

The in-situ XANES spectra at the Sb K- and Sn K-absorption edges in the iron catalysts prepared by impregnation and mechanical mixing and their evolution during the catalyst activation in CO are shown in **Figure 4-11**. The comparison with the reference spectra²³ suggests that in the calcined FeSb/SiO₂ catalyst, antimony is present as Sb₂O₅. The FeSb/SiO₂ (M) catalyst prepared by mechanical mixing in addition to Sb₂O₅ also contains about 20% of Sb₂O₃. Exposure of the antimony-promoted catalysts to CO during temperature ramping results in gradual evolution of

the XANES spectra (**Figure 4-11 a and b**). Analysis of the XANES data suggests that the reduction of Sb_2O_5 species to metallic state in the CO flow proceeds via intermediate formation of Sb_2O_3 . In order to provide quantitative information about the fraction of different antimony phases during the catalyst activation and FT reaction, the XANES data were analyzed using fitting with a linear combination of XANES spectra of the reference compounds (Sb_2O_5 , Sb_2O_3 , antimony foil and Fe-Sb antimony-iron alloy). The evolution of the antimony phase composition under the conditions of catalyst activation and catalytic reaction is shown in **Figure 4-12 a and b**. The reduction of Sb^{5+} species to Sb^{3+} and then to metallic antimony occurs at relatively low temperatures. Starting from 100°C , metallic Sb species are detected in both the catalysts prepared by co-impregnation and mechanical mixing. Interestingly, low intensity of the Sb white line after the reduction at 350°C suggests a higher fraction of the antimony metallic phase in the FeSb/ SiO_2 sample prepared by impregnation, while somewhat lower extent of antimony reduction was observed in the FeSb/ SiO_2 (M). The XANES fitting is indicative of the presence of FeSb alloy, which appears in both catalysts starting from 150°C (**Figure 4-12 a and b**). As expected, a higher fraction of the FeSb alloy has been detected in the FeSb/ SiO_2 catalyst prepared by co-impregnation. Indeed, the STEM-EDX analysis suggests the presence of Fe-Sb core-shell structures (**Figure 4-4**) in FeSb/ SiO_2 . Important, a noticeable concentration of oxide can be observed in the mechanically mixed FeSb/ SiO_2 (M) sample (**Figure 4-12 b**), while antimony is only present as the Sb and FeSb metallic species in the catalyst prepared by impregnation after conducting FT reaction (**Figure 4-12 a**).

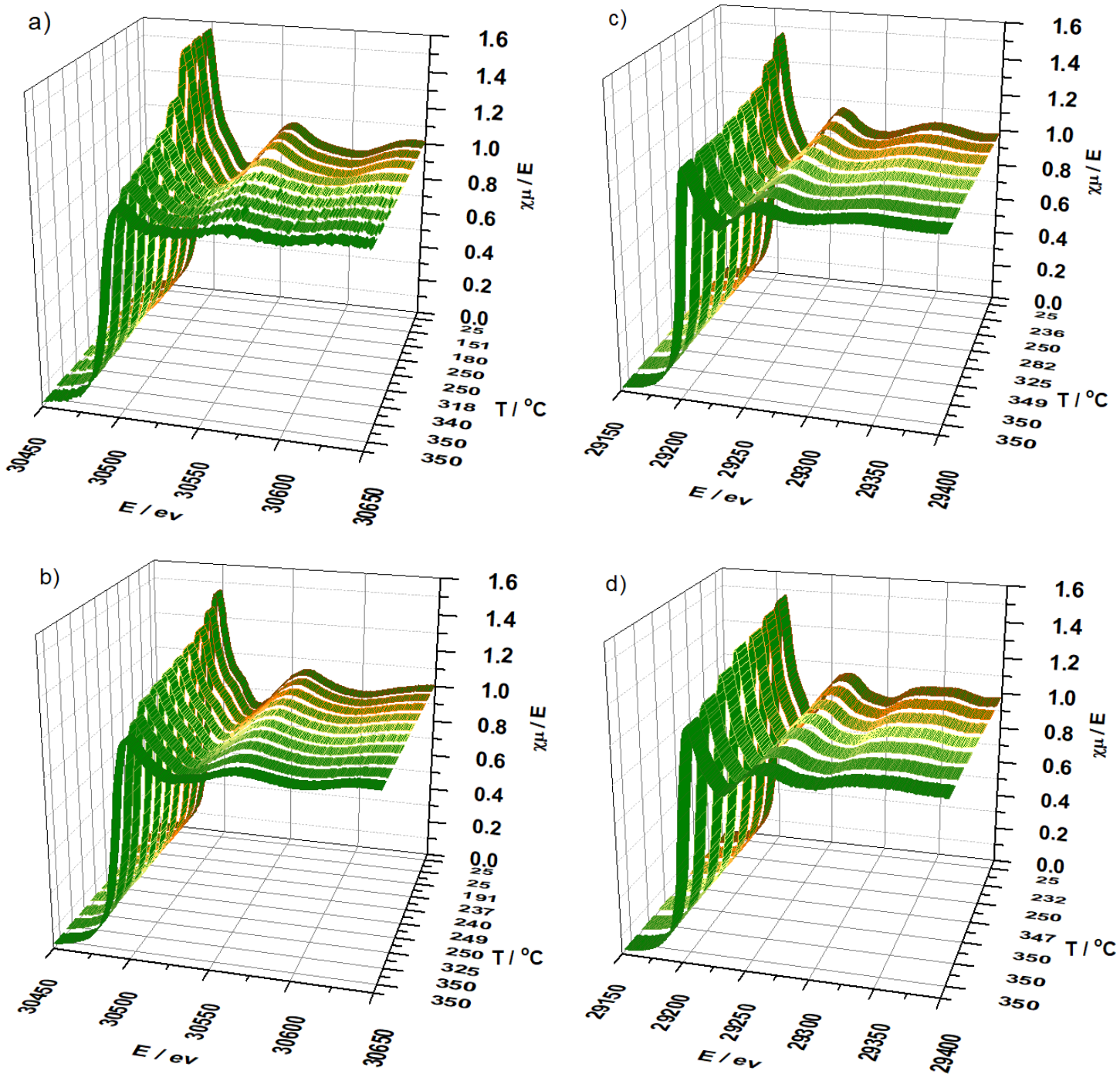


Figure 4-11. Evolution of the Sb K and Sn absorption edges during the heating in carbon monoxide: a) FeSb/SiO₂; b) FeSb/SiO₂ (m), c) FeSn/SiO₂; d) FeSn/SiO₂ (m).

The XANES data for the catalysts promoted with Sb are consistent with EXAFS results measured for the catalysts cooled down to room temperature in CO after activation and exposure to syngas at 350 °C. Interestingly, the EXAFS Fourier

transform moduli of the FeSb/SiO₂ and FeSb/SiO₂ (M) samples are different from that of the antimony foil (**Figure 4-13 a and b**) as they show an additional peak at 2.2 Å. The intensity of this peak is particularly high in the FeSb/SiO₂ catalyst prepared by impregnation. Note that XANES shows almost complete reduction of antimony in the FeSb/SiO₂ sample to metallic state. The additional peaks at 2.2 Å seems to be attributable to Sb-Fe coordination in the bimetallic Sb-Fe nanoparticles²⁴. The EXAFS results agree with the XANES data (**Figure 4-12 a and b**), which are also indicative of a higher fraction of FeSb alloy in the used FeSb/SiO₂ catalysts prepared by impregnation and with the STEM-EDX data, showing the Fe-Sb core shell nanoparticles (**Figure 4-4**).

The situation is different with the tin-promoted catalysts (**Figure 4-11 c and d**). Both calcined FeSn/SiO₂ and FeSn/SiO₂ (M) catalysts contain mostly SnO₂ species with a small fraction of SnO. The intensity of the Sn white line decreases during heating of the tin -promoted catalysts in CO, suggesting gradual tin reduction. The evolution of the tin phase composition in FeSn/SiO₂ and FeSn/SiO₂ (M) calculated from linear decomposition of the catalyst XANES spectra during heating in CO and syngas is shown in **Figure 4-12 c and d**. Note that the tin reduction proceeds much easier for the impregnated catalyst. The tin metallic phase can be already detected at 50-100 °C during the exposure of FeSn/SiO₂ in CO, while in the FeSn/SiO₂ (M) catalyst prepared by mechanical mixing, metallic Sn was observed at much high temperatures (T>175 °C) (**Figure 4-12 d**). Different to the antimony-promoted catalysts a significant amount of the tin oxide species was still observed after the catalyst activation in CO and exposure to syngas at 350 °C. Similar to the antimony-promoted catalysts, the FeSn/SiO₂ sample prepared by co-impregnation exhibits a higher fraction of metallic Sn phase and a higher extent of tin reduction, while the FeSn/SiO₂ (M) mechanically

mixed sample still contains a large fraction of the Sn oxides species (SnO and SnO₂). For the FeSn/SiO₂ and FeSn/SiO₂ (M) catalysts after exposure to syngas, these differences increase to 22.4 and 16.4%, respectively. Higher uncertainty of the catalyst analysis after the syngas treatment can be tentatively attributed to the formation of small tin metal nanoparticles or tin carbide species in the presence of CO.

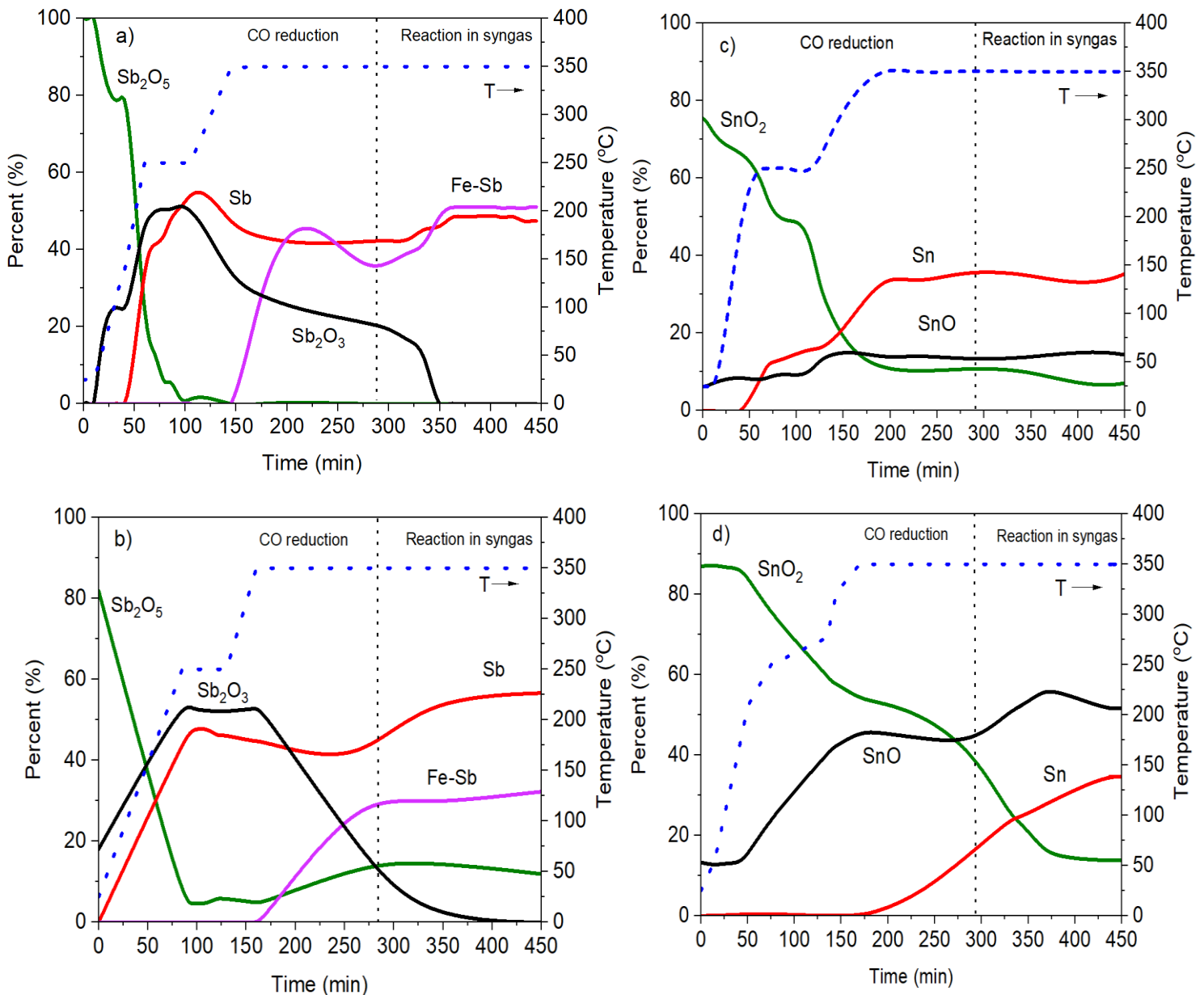


Figure 4-12. Evolution of the Sb and Sn phase compositions during heating in CO and exposure to syngas at 350 °C: a) FeSb/SiO₂; b) FeSb/SiO₂ (M), c) FeSn/SiO₂; d) FeSn/SiO₂ (M).

The EXAFS Fourier transform moduli of the calcined tin-promoted FeSn/SiO₂ and FeSn/SiO₂ (M) catalysts and those after the exposure to syngas at 350 °C and cooling down to room temperature in nitrogen are shown in **Figure 4-13 c and d**. The Fourier transform modulus of the tin foil is also shown for comparison. The Fourier transform moduli of the fresh calcined samples display an intense peak at 1.6 Å, which can be attributed to Sn-O coordination. The EXAFS data agrees with a large fraction of tin oxide in the calcined iron catalysts promoted with tin, which was also detected by XANES (**Figure 4-12 c and d**). The Fourier transform modulus evolves significantly after the catalyst activation in CO and exposure to the FT reaction. The Fourier transforms of the catalysts activated in CO, exposed to syngas and cooled down to room temperature show (**Figure 4-12 c and d**) the presence of Sn-O coordination shells with a possible small contribution of tin-tin metallic coordination, which was identified by the peak at 2.8 Å. The EXAFS data for the spent catalysts are consistent with XANES, which shows partially reduced tin species in FeSn/SiO₂ and FeSn/SiO₂ (M) after their activation in CO and reaction. The low intensity of the peaks at 2.8 Å attributed to the Sn-Sn coordination relative to the Sn foil in the promoted iron catalysts suggests the presence of extremely small tin nanoparticles in the used FT catalysts. Indeed, the characterization of the activated FeSn/SiO₂ catalysts by STEM (**Figure 4-3**) and XPS showed extremely high tin dispersion. Extremely small Sn nanoparticles were discovered in the activated FeSn/SiO₂ by STEM, while XPS showed an increase in the I_{Sn}/I_{Si} ratio in FeSn/SiO₂ after the activation in CO (**Table 4-2**). Note that we did not detect FeSn alloy in the activated and working FeSn/SiO₂ catalysts.

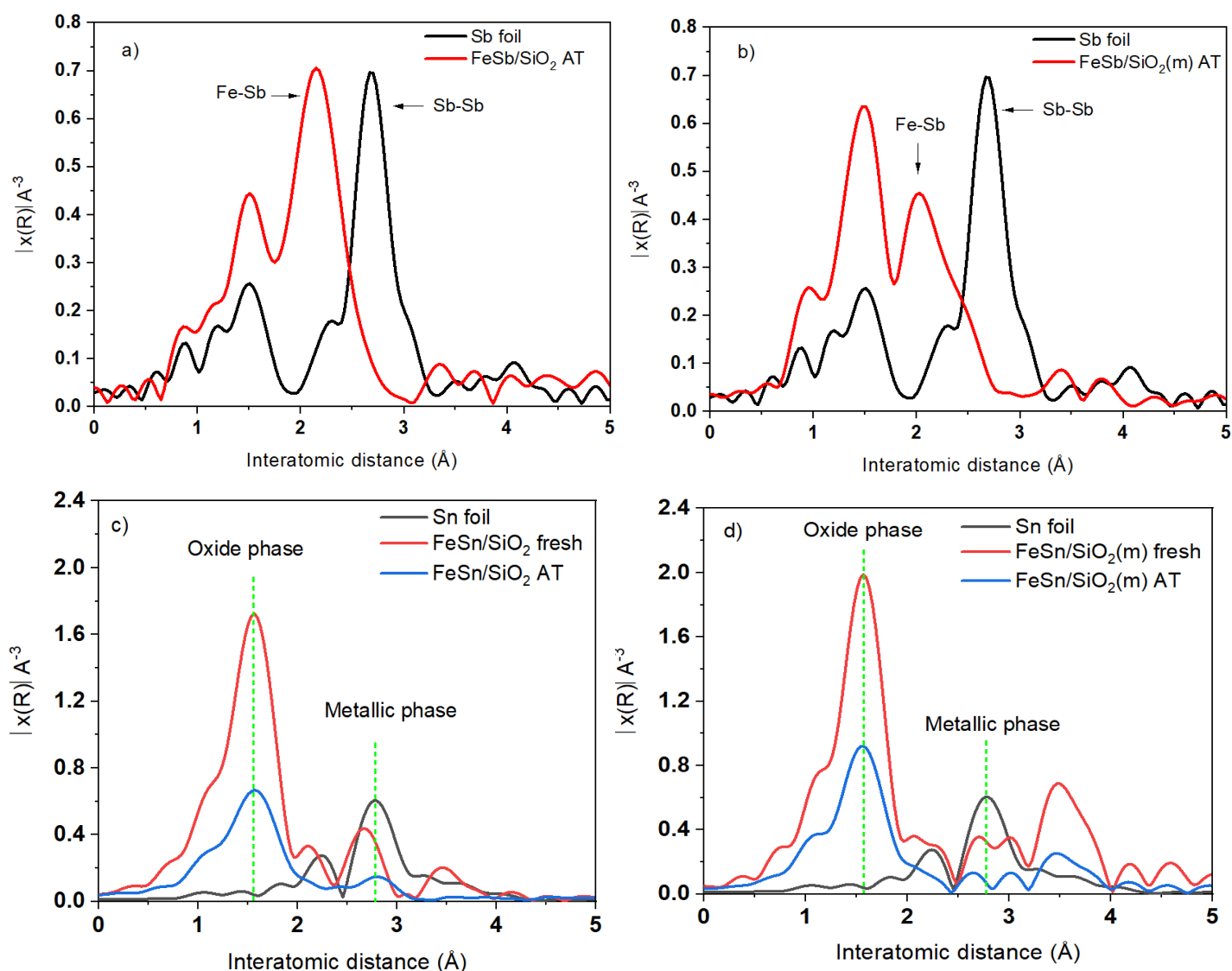


Figure 4-13. EXAFS Fourier transform moduli of iron catalysts: a) FeSb/SiO_2 , b) FeSb/SiO_2 (M), c) FeSn/SiO_2 and d) FeSn/SiO_2 (M) after activation in CO, FT reaction and cooling down to ambient temperature.

4.3. Catalytic performance

Carbon monoxide conversion over iron catalysts under the conditions of high temperature FT synthesis results in production of methane, C_2 - C_4 olefins, paraffins and higher C_{5+} hydrocarbons. CO_2 and water are also present as reaction products. The catalytic results are summarized in **Figures 4-14, 4-15** and **Table 4-4**. **Figure 4-14** displays evolution of carbon monoxide conversion at iso-WHSV (WHSV = 3.6 L/g.h) with time on stream over co-impregnated and mixed Sn- and Sb- promoted iron

catalysts during the first 24 h of reaction. Both non-promoted iron catalysts with 10 and 20 wt.% iron (Fe/SiO_2 and $\text{Fe}/\text{SiO}_2(20\%)$) showed a gradual decrease in the CO conversion with the reaction time. Note that the iron catalysts promoted with antimony and tin prepared by mechanical mixing exhibit CO conversion similar to the non-promoted iron catalysts. They also showed gradual deactivation similar to the non-promoted counterparts. The promotion with Sb of the FeSb/SiO_2 (M) catalyst did not increase FTY, which remained between $0.14\text{-}0.26 \times 10^{-4}$ molCO/gFe.s with similar selectivities to methane, light olefins and C_{5+} hydrocarbons (Table 4-4). Thus, the catalytic performance and deactivation behavior of the antimony and tin promoted iron catalysts prepared by mechanical mixing is similar to non-promoted iron Fe/SiO_2 catalyst. $\text{Fe}/\text{SiO}_2(20\%)$ displays a lower FTY (Table 4-4) compared to the Fe/SiO_2 catalyst containing about 10 wt.% Fe. The lower iron-based activity (FTY) of the $\text{Fe}/\text{SiO}_2(20\%)$ can be attributed to larger iron particle size (Table 4-1) and lower concentration of FT active sites.

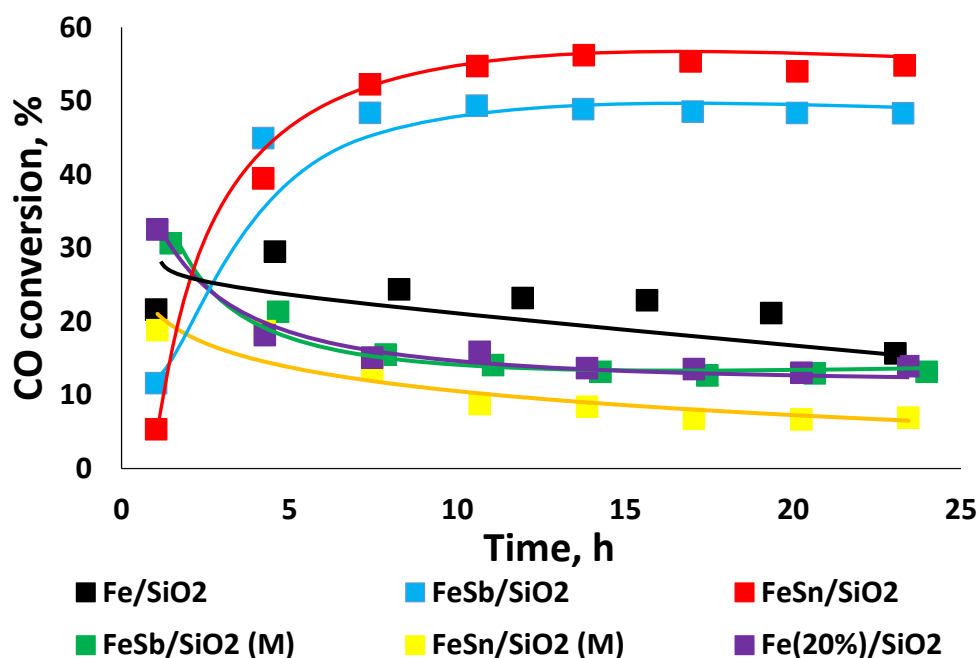


Figure 4-14. CO conversion as a function of time for iron catalysts promoted with Sn and Sb prepared by co-impregnation and mechanical mixture. Reaction conditions: $T = 350$ °C, $P = 10$ bar, $\text{H}_2/\text{CO} = 1$, $\text{WHSV} = 3.6$ L/g.h.

Note that the FeSb/SiO₂ and FeSn/SiO₂ catalysts promoted with antimony and tin and prepared by co-impregnation showed higher FT reaction rate. More specifically, FTY increased 4-5 times after the promotion (Table 4-4). The increase in FTY can be either attributed to better dispersion to the active phase or to the increase in the intrinsic activity of each active site, i.e. increase in the turnover frequent (TOF). The STEM measurements suggest an increase in the iron particle size in the promoted catalysts activated in CO (Figure 4-5). This suggests somewhat lower iron dispersion in the promoted catalysts. Therefore, the FT rate increase cannot be assigned to the modification of iron dispersion or extent of carbidization but to the increase in TOF (Table 4-4).

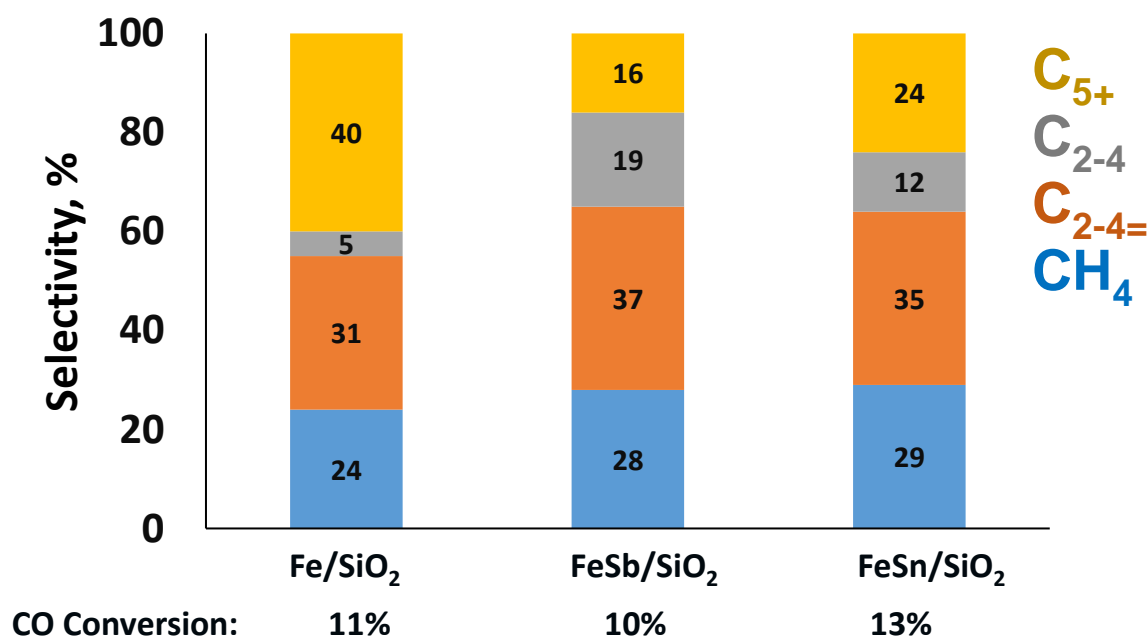


Figure 4-15. Selectivity patterns over Fe/SiO₂, FeSb/SiO₂ and FeSn/SiO₂ measured at the CO conversion of 10 - 13 %.

The Sb and Sn promoted catalysts, prepared by impregnation reached the stable performance after ~10 h of reaction and did not show any noticeable deactivation during 24 h on stream. Previously, we showed (chapter 3) that this better

stability of iron catalyst with the Sn and Sb promoters could be attributed to less significant iron sintering. Note that the most significant promotion phenomena were only observed for the Sb- and Sn-promoted catalyst prepared by impregnation. This suggests that an intimate contact between the promoter and iron active phase is indispensable for attaining higher reaction rate and better stability in FT synthesis. **Figure 4-15** displays selectivity measured over Fe/SiO₂, FeSn/SiO₂, FeSb/SiO₂ at iso-conversion (between 10-13%). The promotion results in a slight increase in the methane selectivity (from 24% for Fe/SiO₂ catalyst to 28 and 29% for Sb- and Sn-promoted catalysts, respectively) and of a slight increase in the selectivity to light olefins (37 and 35% for Sb- and Sn- promoted catalysts, respectively). These observations are consistent with the data previously presented, which showed only very small variation of light olefin selectivity over silica supported iron catalysts promoted with Sn and Sb. Note that the influence of the promotion with antimony and tin was much more significant on the reaction rate (**Table 4-4**).

Table 4-4. Catalytic performance of iron catalysts promoted with Sn and Sb in FT synthesis measured in a conventional fixed bed reactor at iso-WHSV (10 bar, 350oC, H₂/CO = 1/1, WHSV = 3.6 L/g.h, TOS = 24h)

Catalysts	FTY 10 ⁻⁴ mol _{CO} g _{Fe} ⁻¹ s ⁻¹	TOF ^a , s ⁻¹	CO conv. (%)	CO ₂ select. (%)	Hydrocarbon selectivity (%)				C ₂₋₄ ⁻ /C ₂₋₄ ⁰
					CH ₄	C ₂₋₄ ⁼	C ₂₋₄ ⁰	C ₅ ⁺	
Fe/SiO ₂	0.20	0.09	11	15	24	31	5	40	6.20
FeSn/SiO ₂	0.98	0.84	53	49	23	17	13	47	1.31
FeSb/SiO ₂	0.87	0.69	47	47	14	17	10	59	1.70
Fe(20%)/SiO ₂	0.13	-	14	47	24	34	6	36	5.67
FeSn/SiO ₂ (M)	0.14	-	8	26	28	33	6	33	5.50
FeSb/SiO ₂ (M)	0.26	-	14	24	18	24	5	53	4.8

^aTOF calculated using the average iron carbide particle size from TEM for the activated catalysts

4.4. Discussion

The promotion of iron catalysts is an efficient strategy² to enhance their performance in the synthesis of light olefins from syngas using FT reaction. Our

catalytic results show that the FT reaction rate increases 4-5 times after addition of small amounts of antimony or tin to the silica supported iron catalysts. Besides of this major increase in the FT reaction rate, the promoted iron catalysts exhibit much better stability compared to the non-promoted counterparts (**Table 4-4**), while the selectivity to light olefins and methane only very slightly increases after the promotion (**Figure 4-15**). Both metallic antimony and tin have relatively low melting points. It can be considered that under FT reaction conditions, these elements can migrate over the catalyst surface and modify the activity, localization and dispersion of iron species. The diffusion of mobile phase into crystalline lattice will be appreciable at half way to melting point on Kelvin scale. At this temperature, known as Toman temperature, a solid has 70 % of its vibrational freedom and its diffusion becomes possible. Metallic antimony and tin have melting points of 631 °C and 232 °C respectively. At the activation and reaction temperature (350 °C), their migration could consequently take place.

However, the migration phenomena seem to be less important compared to the previously studied bismuth and lead catalysts^{8,9,25}. Indeed, the enhancement effects in catalysis were only observed in the FeSb/SiO₂ and FeSn/SiO₂ catalysts prepared by impregnation, while the catalytic performance and stability of the mechanical mixed catalysts were rather similar to non-promoted Fe/SiO₂ (**Table 4-4, Figure 4-14**)

Let us discuss the effect of the promotion with antimony and tin on the characteristics of iron catalysts such as dispersion of active phase and extent of carburization. There is a general consensus in the literature that the activity of iron catalysis in FT synthesis can be principally attributed to iron carbides, though iron oxides can contribute in a lesser extent by affecting to some extent the intrinsic activity of iron carbide species, enhancing water gas shift and secondary reactions^{26,27,28}.

Iron dispersion and extent of iron carbidization are therefore, important parameters, which should be considered in the interpretation of the catalytic data. The characterization performed in this chapter suggests, that the promotion with antimony and tin does not result in any positive effect on the iron dispersion. Moreover, the average iron particle size in the activated catalysts increases from 14.2 to 26.7 and 29 nm after the promotion (**Figure 4-5**). Thus, the enhancement of FT reaction rate in the catalysts promoted with antimony and tin cannot be assigned to better iron dispersion.

Let us now evaluate possible contribution of the promoters on iron carbidization. The in-situ Mossbauer spectrometry is indicative of better iron carbidization in the presence of the Sb promoter. Almost complete carbidization of iron was observed in FeSb/SiO₂ under FT reaction conditions, while some concentrations of the residual iron oxide species were detected in the non-promoted and tin-promoted catalysts (**Table 4-3**). Higher extent of iron carbonization was observed in the FeSb/SiO₂ catalyst prepared by impregnation compared to the FeSb/SiO₂ (M) catalyst prepared by mechanical mixing. This suggests that a close interaction between iron and promoter is indispensable for transformation of iron oxide into iron carbide. At the same time, both the Sn-promoted catalysts FeSn/SiO₂ and FeSn/SiO₂ (M) showed much lower extent of iron carbidization and noticeable concentrations of iron oxide species even under FT reaction conditions. Despite somewhat lower iron carbidization, the FT reaction rate increased several times on the promotion of silica supported iron catalysts with tin (**Table 4-4**). This suggests that the effect of the tin and antimony promoters on the FT catalytic performance cannot be solely attributed to better iron carbidization.

More information about the type of the promotion with antimony and tin was extracted from the TOF values. **Table 4-4** shows the 7-10 times increase in TOF in the

iron catalysts promoted with either antimony or tin, while we did not identify any positive influence of antimony and tin on the iron dispersion. No clear effect of Sb and Sn was either uncovered on iron carbidization. Antimony and tin can be therefore considered as electronic promoters, which mostly affect the intrinsic activity of the iron carbide active sites without noticeable positive effect on iron dispersion and carbidization.

The promoters also improve the stability of silica supported iron nanoparticles in the catalysts prepared by co-impregnation. Previously, we observed²⁵ sintering of iron nanoparticles in the non-promoted silica supported catalysts, while the iron carbide particle size remains stable during the FT reaction in the promoted catalysts. The promotion with antimony and tin also increases the stability of iron particle against coke deposition. The TG analysis (**Figure 4-7**) shows the smaller carbon deposition obtained with the promoted catalysts.

A wide range of characterization techniques employed in this work have provided detailed information about interaction of the active iron phase and promoters. The observed strong effect of the Sb- and Sn-promoters on the catalytic performance of iron catalysts might be therefore due to the intimate contact observed between Fe and the promoter. This contact is more visible in the antimony promoted catalysts. STEM-EDX showed the formation of iron antimony core-shell bimetallic particles in the activated FeSb/SiO₂ catalyst (**Figure 4-4**). In-situ XANES showed the presence of Fe-Sb alloy species in the activated and working antimony-promoted iron catalysts under the typical conditions of FT synthesis (**Figure 4-12 a and b**). The FeSb alloy was also confirmed by EXAFS. The EXAFS Fourier transform moduli of FeSb/SiO₂ and FeSb/SiO₂ (M) (**Figure 4-13 a and b**) showed the peaks attributed to Fe-Sb coordination in the alloy. As expected, the fraction of the Fe-Sb alloy is less significant in the FeSb/SiO₂ (M) catalyst prepared by mechanical mixing. This is consistent with

the enhancement of the FT reaction rate observed only for the FeSb/SiO₂ catalyst prepared by impregnation (**Table 4-4**), where the fraction of Fe-Sb bimetallic particles is much higher.

The FT tests also showed a strong promoting effect of tin on the catalytic performance of iron catalysts. Differently to antimony, tin is highly dispersed on silica. In addition, tin cannot be completely reduced to the metallic state as antimony, during the catalyst activation and FT reaction. In situ XANES data showed that more than 30-60% of tin is still in the oxide form after several hours of the FT reaction (**Figure 4-4 c and d**). Higher extent of tin reduction was observed in the iron catalyst prepared by impregnation. We did not detect from XANES and EXAFS any distinct Sn-Fe alloy species or alloys. Tin is known to modulate the hydrogenation activity of metal catalysts and is often used as a promoter for a number of selective hydrogenation reactions. Previously, it was shown²⁹ that the promotion cobalt catalysts with tin modifies the CO adsorption on cobalt catalysts. Sn preferentially blocks the sites of multiple multi-bonded CO, likely located in hollow sites. The promotion with tin also reduces production of methanol during FT synthesis over alumina supported cobalt catalysts³⁰. The active sites containing metallic cobalt in interaction with tin oxides SnO_x favor the selective hydrogenolysis of methyl esters to unsaturated alcohols^{31,32}.

An interaction of tin with silica support and possible reinsertion of tin cationic species in the silica structure after the catalyst activation in CO was observed by several techniques. XPS, which is a surface sensitive technique, showed a major increase in the ISn/ISi ratio in FeSn/SiO₂ (**Table 4-2**) after the catalyst activation in CO. In the subsurface layer of silica, tin maintains the Sn⁴⁺ oxidation state. The XPS data are also consistent with the STEM analysis of the activated FeSn/SiO₂ sample. Extremely highly dispersed tin species were discovered (**Figure 4-3**). Interestingly,

STEM also shows higher concentration of tin species in a close proximity to iron carbide nanoparticles (**Figure 4-16**). This suggests that the mechanism of the promotion of silica supported iron catalysts with tin can be different from that with antimony. The enhancement of FT reaction rate and catalyst stability in the catalyst promoted with antimony can be assigned to the formation of antimony-iron carbide nanoparticles, which were identified using STEM-EDX and XANES/EXAFS. The promotion effect of tin seems to be more relevant to the localization of tin mostly as high dispersed cationic species in the silica and possible very small Sn metallic species in close proximity to the iron carbide nanoparticles. Both antimony and tin species strongly affect the electronic structure of supported iron carbide nanoparticles. A major increase in the TOF in FT synthesis is observed on the promotion of iron catalysts with these elements. Tentatively, the electronic effect for catalysts promoted by antimony can be explained by the formation of a metallic alloy between Fe-Sb, which modifies the Fermi level. For the catalyst promoted by tin, we did not observe formation of bimetallic particles at the reaction temperature. Indeed, the formation of tin and iron alloy can only start, when the temperature exceeds 350 °C³³. In this case, the electronic effect could be related to the effect of electron charge transfer and polarization, which can occur, because of localization of mostly tin oxide species in the proximity to iron carbide nanoparticles.

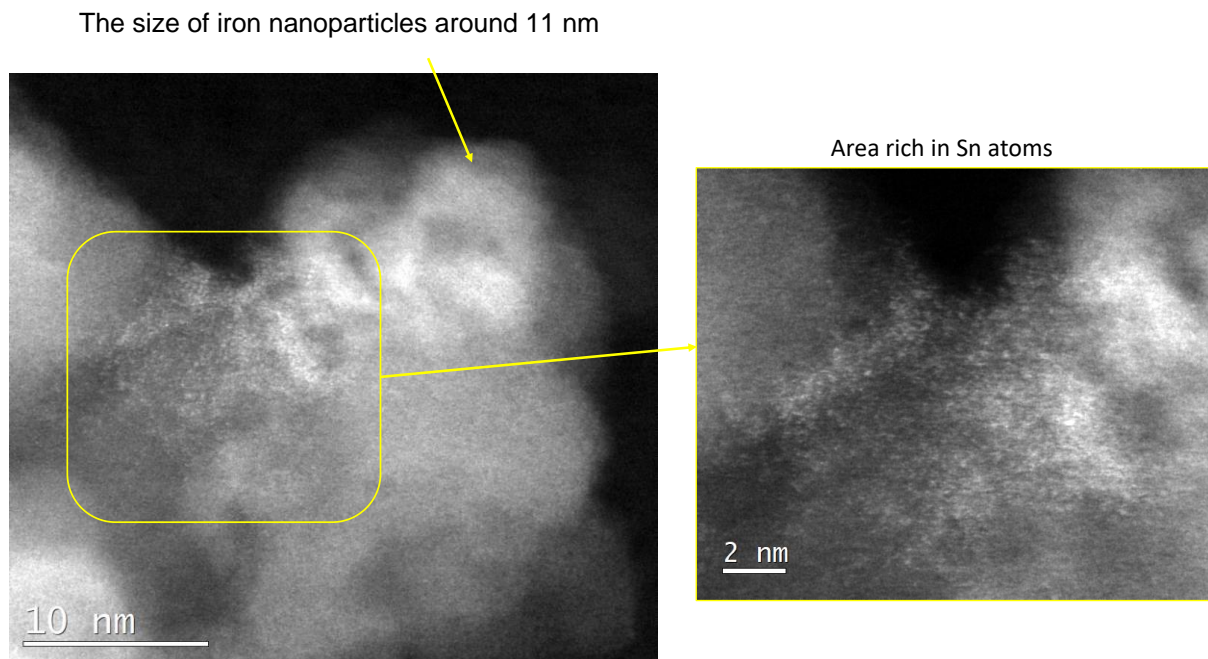


Figure 4-16. Tin-enriched areas in the close proximity of iron nanoparticles in the activated FeSn/SiO_2 catalyst.

4.5. Conclusions

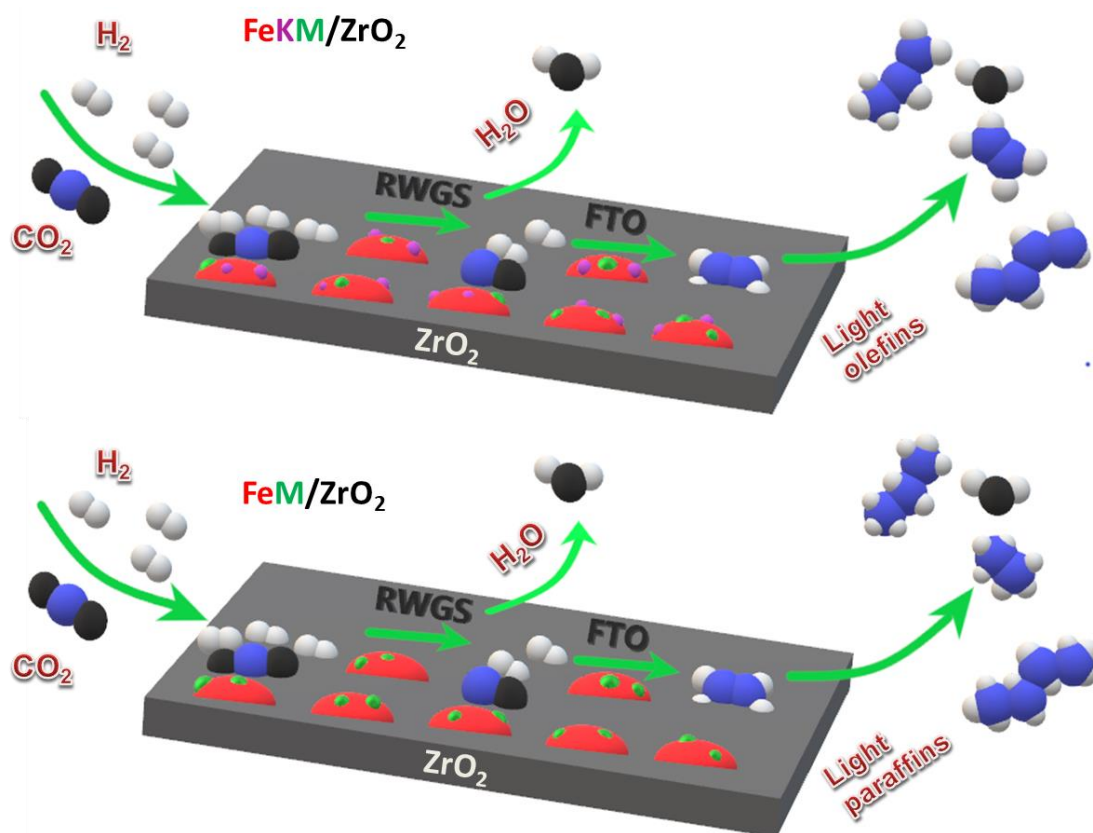
The promotion of silica supported iron catalysts with tin and antimony results in a major increase in FT reaction rate. The effect is much more pronounced, when the promoted catalysts were prepared by co-impregnation compared to the mechanically mixed samples. The promotion with antimony results in some enhancement in iron carbidization, while no visible influence of tin on iron carbidization was observed. Antimony is completely reduced to the metallic state and forms iron-antimony bimetallic nanoparticles under the reaction conditions, while a significant fraction of tin oxide is present in the iron catalysts in FT synthesis. The enhancement of the reaction rate over silica supported iron catalysts promoted with antimony and tin was attributed to the electronic effects arising from the promoters localized in close proximity to the iron carbide nanoparticles. The turnover frequency increases 7-10 times due to the interaction of iron carbide species with antimony and tin

4.6 References

1. De Smit, E. & Weckhuysen, B. M. The renaissance of iron-based Fischer-Tropsch synthesis: On the multifaceted catalyst deactivation behaviour. *Chem. Soc. Rev.* **37**, 2758–2781 (2008).
2. Torres Galvis, H. M. & De Jong, K. P. Catalysts for production of lower olefins from synthesis gas: A review. *ACS Catal.* **3**, 2130–2149 (2013).
3. Brunner, K. M. *et al.* Preparation of an Unsupported Iron Fischer–Tropsch Catalyst by a Simple, Novel, Solvent-Deficient Precipitation (SDP) Method. *Energy & Fuels* **29**, 1972–1977 (2015).
4. Hutchings, G. J. Promotion in heterogeneous catalysis: A topic requiring a new approach? *Catal. Letters* **75**, 1–12 (2001).
5. Dahl, S., Logadottir, A., Jacobsen, C. J. H. & Norskov, J. K. Electronic factors in catalysis: The volcano curve and the effect of promotion in catalytic ammonia synthesis. *Appl. Catal. A Gen.* **222**, 19–29 (2001).
6. Sharma, P., Elder, T., Groom, L. H. & Spivey, J. J. Effect of structural promoters on Fe-based fischer-tropsch synthesis of biomass derived syngas. *Top. Catal.* **57**, 526–537 (2014).
7. Chernavskii, P. A. *et al.* Influence of copper and potassium on the structure and carbidisation of supported iron catalysts for Fischer-Tropsch synthesis. *Catal. Sci. Technol.* **7**, 2325–2334 (2017).
8. Gu, B. *et al.* Effects of the promotion with bismuth and lead on direct synthesis of light olefins from syngas over carbon nanotube supported iron catalysts. *Appl. Catal. B Environ.* **234**, 153–166 (2018).
9. Ordonsky, V. V. *et al.* Soldering of iron catalysts for direct synthesis of light olefins from syngas under mild reaction conditions. *ACS Catal.* **7**, 6445–6452 (2017).
10. Gu, B. *et al.* Synergy of nanoconfinement and promotion in the design of efficient supported iron catalysts for direct olefin synthesis from syngas. *J. Catal.* **376**, 1–16 (2019).
11. Gu, B. *et al.* Mobility and versatility of the liquid bismuth promoter in the working iron catalysts for light olefin synthesis from syngas. *Chem. Sci.* (2020) doi:10.1039/D0SC01600D.
12. Moulijn, J. A., van Diepen, A. E. & Kapteijn, F. ChemInform Abstract: Catalyst Deactivation: Is It Predictable? What to Do? *ChemInform* **32**, no-no (2010).
13. Torres Galvis, H. M. *et al.* Iron particle size effects for direct production of lower olefins from synthesis gas. *J. Am. Chem. Soc.* **134**, 16207–16215 (2012).
14. Yu, G. *et al.* Fe x O y @C Spheres as an Excellent Catalyst for Fischer–Tropsch Synthesis. *J. Am. Chem. Soc.* **132**, 935–937 (2010).
15. Subramanian, V. *et al.* Design of iron catalysts supported on carbon-silica composites with enhanced catalytic performance in high-temperature Fischer-Tropsch synthesis. *Catal. Sci. Technol.* **6**, 4953–4961 (2016).
16. Romero, M. D., de Lucas, A., Calles, J. A. & Rodríguez, A. Bifunctional catalyst NiHZSM-5: effects of the nickel incorporation method. *Appl. Catal. A Gen.* **146**, 425–441 (1996).
17. Mai, K., Elder, T., Groom, L. H. & Spivey, J. J. Fe-based Fischer Tropsch synthesis of biomass-derived syngas: Effect of synthesis method. *Catal. Commun.* **65**, 76–80 (2015).
18. Gu, B., Bahri, M., Ersen, O., Khodakov, A. & Ordonsky, V. V. Self-Regeneration of Cobalt and Nickel Catalysts Promoted with Bismuth for Non-deactivating Performance in Carbon Monoxide Hydrogenation. *ACS Catal.* **9**, 991–1000 (2019).
19. Butt, J. B. Carbide phases on iron-based Fischer-Tropsch synthesis catalysts part I: Characterization studies. *Catal. Letters* **7**, 61–81 (1990).
20. Shukla, A. K. *et al.* An X-ray photoelectron spectroscopic study on the effect of Ru and Sn additions to platinised carbons. *Appl. Surf. Sci.* **137**, 20–29 (1999).
21. Pachamuthu, M. P., Shanthi, K., Luque, R. & Ramanathan, A. SnTUD-1: A solid acid catalyst for three component coupling reactions at room temperature. *Green Chem.* **15**, 2158–2166 (2013).
22. Cheng, K. *et al.* Pore size effects in higher temperature Fischer-Tropsch synthesis over supported iron catalysts. *J. Catal.* **328**, (2015).
23. Takaoka, M. *et al.* Determination of chemical form of antimony in contaminated soil around a smelter using X-ray absorption fine structure. *Anal. Sci.* **21**, 769–773 (2005).
24. Fehse, M. *et al.* The Electrochemical Sodiation of FeSb 2 : New Insights from Operando 57 Fe Synchrotron Mössbauer and X-Ray Absorption Spectroscopy . *Batter. Supercaps* **2**, 66–73 (2019).
25. Barrios, A. J. *et al.* Identification of efficient promoters and selectivity trends in high temperature Fischer-Tropsch synthesis over supported iron catalysts. *Appl. Catal. B Environ.* **273**, (2020).

26. Li, S., Ding, W., Meitzner, G. D. & Iglesia, E. Spectroscopic and Transient Kinetic Studies of Site Requirements in Iron-Catalyzed Fischer–Tropsch Synthesis. *J. Phys. Chem. B* **106**, 85–91 (2002).
27. Cano, L. A., Cagnoli, M. V., Bengoa, J. F., Alvarez, A. M. & Marchetti, S. G. Effect of the activation atmosphere on the activity of Fe catalysts supported on SBA-15 in the Fischer–Tropsch Synthesis. *J. Catal.* **278**, 310–320 (2011).
28. Ma, W. *et al.* Fischer–Tropsch synthesis and water gas shift kinetics for a precipitated iron catalyst. *Catal. Today* **275**, 49–58 (2016).
29. Paredes-Nunez, A. *et al.* CO Hydrogenation on Cobalt-Based Catalysts: Tin Poisoning Unravels CO in Hollow Sites as a Main Surface Intermediate. *Angew. Chemie - Int. Ed.* **57**, 547–550 (2018).
30. Paredes-Nunez, A., Lorito, D., Guilhaume, N., Schuurman, Y. & Meunier, F. C. Effect of Sn on the production of methanol during syngas conversion over Co/alumina. *Catal. Today* **336**, 84–89 (2019).
31. Pouilloux, Y., Autin, F. & Barrault, J. Selective hydrogenation of methyl oleate into unsaturated alcohols. *Catal. Today* **63**, 87–100 (2000).
32. De Oliveira, K., Pouilloux, Y. & Barrault, J. Selective hydrogenation of methyl oleate into unsaturated alcohols in the presence of cobalt-tin supported over zinc oxide catalysts. *J. Catal.* **204**, 230–237 (2001).
33. Crichton, T. J. & Farr, J. P. G. The effect of heat treatment on the Fe-Sn alloy system. *Trans. Inst. Met. Finish.* **82**, 169–173 (2004).

Chapter 5 Efficient promoters and reaction paths in the CO₂ hydrogenation to light olefins over zirconia supported iron catalysts



Abstract: Hydrogenation into light olefins is an attractive strategy for CO₂ fixation into chemicals. The goals of this chapter are to identify the most efficient promoters for zirconia supported iron catalysts and to elucidate the reaction paths using high throughput experimentation. K, Cs, Ba, Ce, Nb, Mo, Mn, Cu, Zn, Ga, In, Sn, Sb, Bi, and V were added in the same concentrations (Fe/promoter=50) to iron catalyst and the promoted catalysts were tested under the same conditions. The strongest promoting effect is reported for alkaline metals. A further increase in the light olefin selectivity is observed after simultaneous addition of potassium with copper, molybdenum, gallium or cerium.

A relatively low selectivity to light olefins over the promoted catalysts, without potassium, is not much affected by the CO₂ conversion. Over the iron catalysts with alkaline and second promoters, higher selectivity to light olefins shows a significant decrease with the CO₂ conversion.

Paper submitted in Applied Catalysis B: Environmental, 13 September 2021

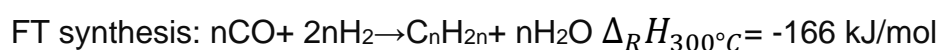
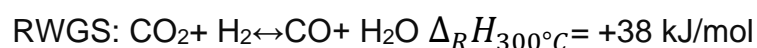
5.1. Introduction

The growing concentration of CO₂ in the atmosphere is the major reason of the climate change. There are currently two strategies for dealing with the ever-increasing levels of CO₂ in the atmosphere: Carbon Capture and Storage (CCS)¹ and Carbon Capture and Utilization (CCU)². CCS is based on the capture of CO₂ from power plants and industrial facilities including its separation, compression and transport, for permanent storage in a geological layer. The CCU strategy involves either direct technological use of CO₂ or its chemical and biological conversion into high value-added products^{2,3,4}. The direct use of carbon dioxide involves several industrial applications: enhanced oil or natural gas recovery, beverage additives, antibacterial and antifungal agents, refrigeration, solvents, food packaging, fire extinguishers, welding, molding, rustproofing, water treatment.

Another important strategy is CO₂ fixation into chemicals through biological or chemical routes. In this strategy, CO₂ can be considered not only the major pollutant but also a feedstock for the synthesis of valuable chemicals and fuels^{5,6}. Nevertheless, CO₂ chemical utilization is challenging, because of its thermodynamic stability, resulting in low conversions⁷. Using sustainable hydrogen as co-reagent, CO₂ can be hydrogenated to methanol^{8,9,10}, dimethyl ether^{11,12}, formic acid^{13,14}, higher alcohols¹⁵, liquid hydrocarbon fuels^{16,17}, aromatics¹⁸ and light olefins^{7,19,20,21,22}. The importance of light olefin synthesis has been remarked in previous chapters. Currently, light olefins are mainly produced by thermal cracking of naphtha²³, dehydrogenation of light alkanes²⁴ and methanol to olefins (MTO) conversion^{25,26,27}. Recently, novel bifunctional or multifunctional catalysts, which are composed of metal oxide nanoparticles and zeolites have been proposed^{20,28,29,30,31} for hydrogenation of CO₂ into light olefins via so called “methanol-mediated route”. Lower catalytic activity, major amounts of

co-produced CO and insufficient olefin yield represent major drawbacks of this approach. Because of high CO selectivity (>50-80%), the single-pass yield of olefins from CO₂ over the bifunctional metal oxide/zeolite catalysts is usually limited to maximum ~ 7%^{29,30}.

The CO₂ Fischer-Tropsch (CO₂-FT) synthesis, which allows achieving a higher single-pass yield, is an attractive route to transform CO₂ into light olefins³¹. The CO₂ conversion into olefins proceeds via a combination of the reverse water gas shift reaction (RWGS) and FT synthesis:



Due to their high activity in both RWGS and FT reactions, iron-based catalysts remain the principal option for the CO₂-FT synthesis. Nonetheless, iron employment by itself does not result in a sufficiently high light olefin selectivity. The optimization of catalyst chemical composition and structure is therefore required to attain high and selective yield of these products. Most commonly, iron catalysts for CO₂ hydrogenation to light olefins have been supported by oxides or carbon materials. In particular, SiO₂, TiO₂, Al₂O₃, ZrO₂, carbon and carbon nanotubes have been evaluated as supports³². Strong hydrophilicity and instability of alumina support could be detrimental for the CO₂ hydrogenation reactions, which may generate larger amounts of water than CO hydrogenation. Relatively weak hydrophilic character and noticeable basicity favoring CO₂ adsorption seem to be some of the required characteristics for carbon dioxide hydrogenation catalysts. Among the investigated supports, the ZrO₂-supported catalysts have shown³² the highest selectivity and yield of light olefins.

The iron CO₂-FT catalysts are most commonly promoted with alkali metals^{32,33,34,35}, Co^{36,37,38}, Cu^{39,40}, Mn^{34,35,41} and/or Zn^{29,42}. Much less information is available on promotion with other elements. Note that unambiguous identification of the most efficient promoters for iron CO₂ hydrogenation catalysts seems challenging. First, the iron catalysts prepared by different research groups may have different contents of promoters. Second, different catalyst activation and reaction procedures even with the same catalyst may lead to different catalytic performance.

In chapter 3, the HTE strategy was successfully employed for unrevealing novel highly efficient promoters such as soldering metals (Bi, Pb, Sn and Sb) for high temperature FT synthesis using syngas over iron catalysts.

This chapter focuses on the one hand, on selection of most efficient new promoters for iron catalysts and on the other hand, on the elucidation of reaction paths on promoted iron catalysts in CO₂ hydrogenation. The promoters were added in the same molar concentrations; the catalysts were activated and tested under the same conditions. The effects of 15 different elements (K, Cs, Ba, Ce, Nb, Mo, Mn, Cu, Zn, Ga, In, Sn, Sb, Bi, and V) on the Fe/ZrO₂ catalyst structure and CO₂ hydrogenation to light olefins were investigated over zirconia supported iron catalysts using HTE catalytic measurements and a large combination of characterization techniques.

5.2. Results

5.2.1. CO₂ hydrogenation on SiO₂-supported catalysts

In previous chapters we evidenced that iron-based catalysts supported on SiO₂ promoted with different soldering metals (Bi, Pb, Sb and Sn) improve considerably the activity and selectivity to light olefins in FT synthesis. As in the CO₂ hydrogenation process to light olefins one of the possible routes is CO₂ reduction to CO and then CO

can further react to give hydrocarbons, we decided to study some of the catalysts that showed good results in previous chapters for CO₂ hydrogenation reaction.

The catalysts tested for CO₂ hydrogenation reaction were Fe/SiO₂ (reference) and Sb-, Sn-, and Bi-promoted catalysts. **Figure 5-1** shows the stability after 48 h of reaction. These catalysts show no clear deactivation under CO₂ reaction conditions. Even though, stability results are promising, in terms of selectivity the results are not satisfactory. Selectivity to light olefins (target fraction) hardly reaches 2%. Based on this poor selectivity, we decided to choose another support that could help to direct the reaction towards C₂-C₄ olefins production more efficiently. As stated before, the ZrO₂-supported catalysts have shown interesting selectivity and yield of light olefins.

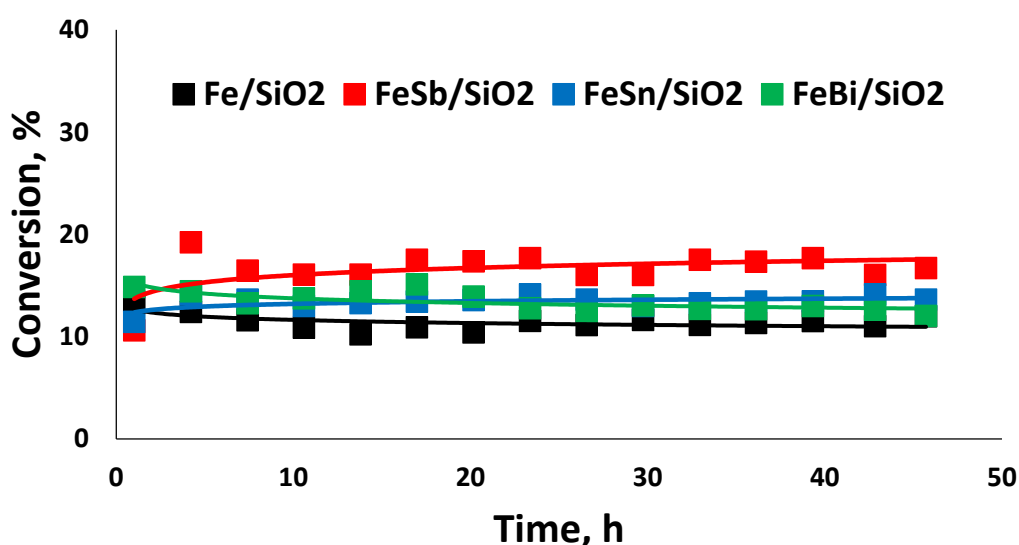


Figure 5-1. CO₂ conversion as a function of time for iron catalysts promoted with Bi, Sn and Sb. Reaction conditions: $T = 350\text{ }^{\circ}\text{C}$, $P = 10\text{ bar}$, $H_2/CO_2 = 3$, $GHSV = 10.2\text{ L/g.h}$.

5.2.2. Optimization of potassium load for iron-based catalysts

It is noted from literature review that the incorporation of alkali metals could improve the C₂-C₄ olefins production from CO₂. In order to design more efficient catalysts, we explore the influence of potassium load on the hydrogenation of CO₂.

Figure 5-2 shows the activity of iron-based catalysts promoted with different potassium content (0.5; 1 and 2 wt.%). It is clear that best activity is obtained for that catalyst containing 1 wt.% of K in its composition. When K load is increased (2 wt.%), activity is negatively affected, probably due to blocking of active sites. Regardless the K content, catalysts remain stable during 48 h of reaction. **Table 5-1** shows a decrease in the CO selectivity for all K promoted catalysts compared to the reference (Fe/ZrO₂). Production of methane drops to ~15% in all cases which represents 60% less methane production compared to Fe/ZrO₂. At the same time the light olefins selectivity improves (10-15 times higher) and the C₂-C₄ paraffins are maintained below 5% when potassium is present. Finally, it is evident the higher production of C₅₊ compounds (above 50%) which is expected due to K capability of improving the C/H ratio on the catalyst surface. Based on activity results obtained from these tests, we decided to synthesize the catalysts for further analysis with a potassium content around 1 wt.%.

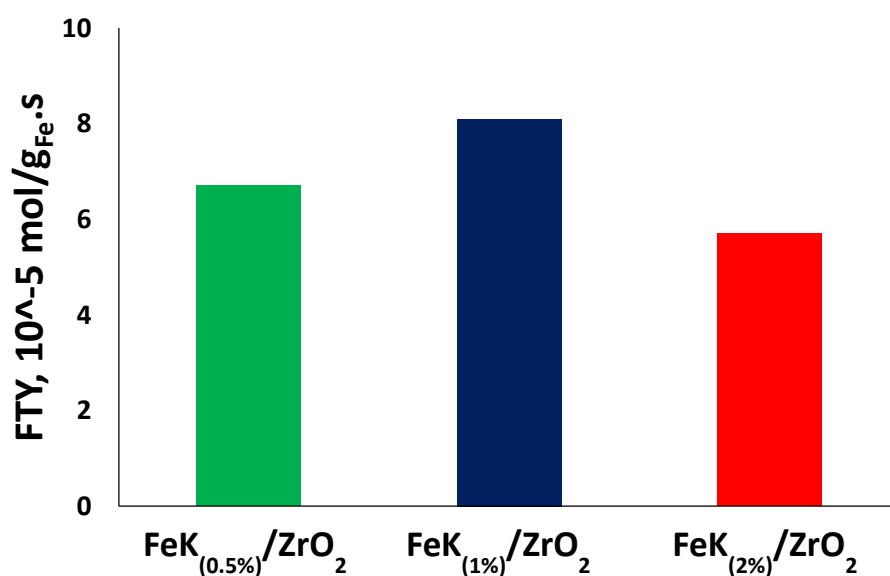


Figure 5-2. Iron-based catalysts activity promoted with different amounts of potassium.

Table 5-1. Catalytic performance of iron catalysts promoted with different K amount for CO₂ hydrogenation reaction (10 bar, 350 °C, H₂/CO₂ = 3, GHSV = 9.25 L/g.h, TOS = 48 h)

Catalysts	FTY 10 ⁻⁵ mol _{CO2} g _{Fe} ⁻¹ s ⁻¹	CO ₂ conv. (%)	CO select. (%)	Hydrocarbon selectivity (%)			
				CH ₄	C ₂₋₄ ⁼	C ₂₋₄ ⁰	C ₅ ⁺
Fe/ZrO ₂	2.2	8	49	75	2	20	3
FeK _(0.5%) /ZrO ₂	6.7	25	22	13	25	5	57
FeK _(1%) /ZrO ₂	8.1	31	19	14	22	5	58
FeK _(2%) /ZrO ₂	5.7	21	19	13	29	4	54

5.2.3. HTE evaluation of the promoted iron catalysts

5.2.3.1. Catalyst activity and iron time yield

Carbon dioxide hydrogenation reaction (H₂/CO₂=3, P=10 bar, T=350 °C) yields methane, C₂-C₄ paraffins and olefins, and C₅⁺ products (until C₁₂). There was no evidence of oxygenated compounds or long-chain liquid hydrocarbons. By adjusting the gas-space velocity, CO₂ conversions in the range from 25 to 45 % were obtained. This conversion range allows accurate measurements of the overall CO₂ hydrogenation rates and product selectivities. The catalytic activity is expressed as iron time yield for each catalyst (**Figure 5-3**). Note that the Sb-, Bi-, and Mo-promoted catalysts seem to have a slightly negative effect on the catalyst activity. All other promoted catalysts exhibit a higher activity than reference unpromoted Fe/ZrO₂. The most pronounced increase in the reaction rate was observed over the potassium and cesium promoted catalysts. The iron time yield almost doubled after addition of 1.5 wt. % of potassium. Interestingly, the combined promotion with potassium and a second element generally leads to higher reaction rates, compared to the promotion without potassium.

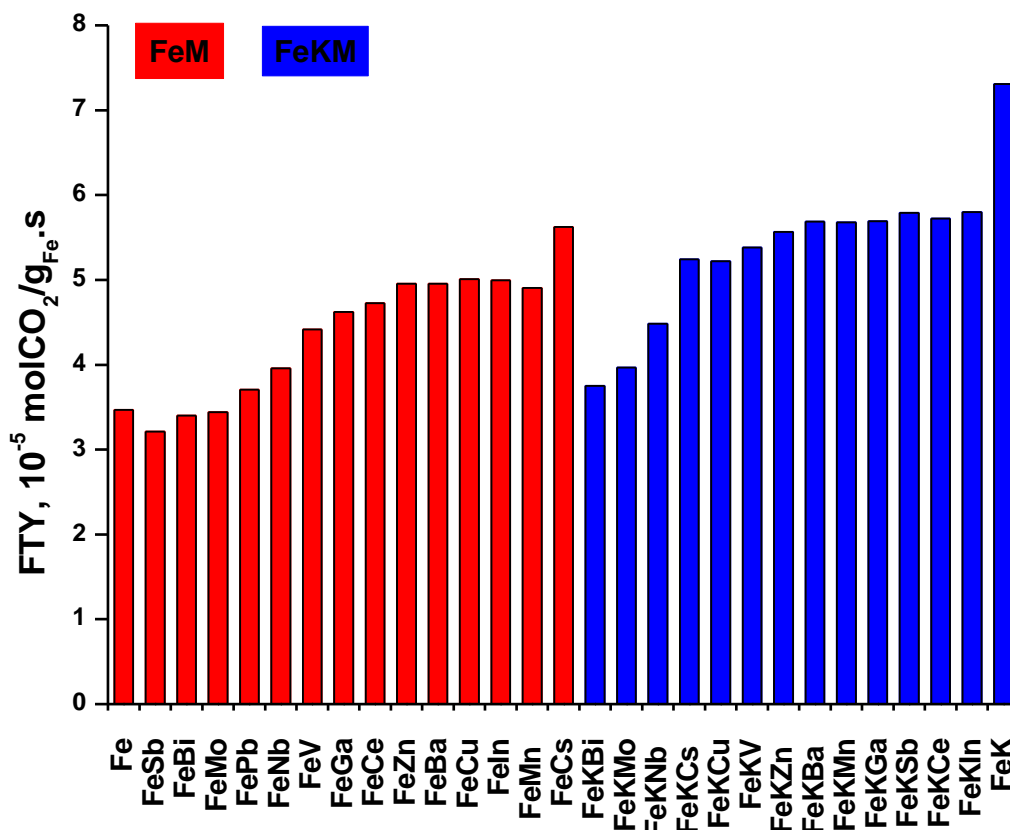


Figure 5-3. Carbon dioxide conversion and activity measured over the promoted zirconia supported iron catalysts $T=350\text{ }^\circ\text{C}$, $\text{H}_2/\text{CO}_2=3$, $p=10\text{ bar}$.

5.2.3.2. Product selectivity at different conversions

The selectivities of CO_2 hydrogenation to carbon monoxide and hydrocarbons measured at different GHSV are shown in **Figures 5-4 to 5-8**. At lower CO_2 conversions, the selectivity to CO is very high; extrapolation of CO selectivity to the zero leads to CO_2 conversion yields almost 100%. The CO selectivity decreases as a function of increase in CO_2 conversion (**Figure 5-4**). The CO selectivity drops to 10% at the CO_2 conversions exceeding 40%. Carbon monoxide seems to be produced by RWGS. Extremely high CO selectivity (>90%) at low CO_2 conversion suggests that the CO_2 -FT synthesis proceeds *via* intermediate formation of carbon monoxide.

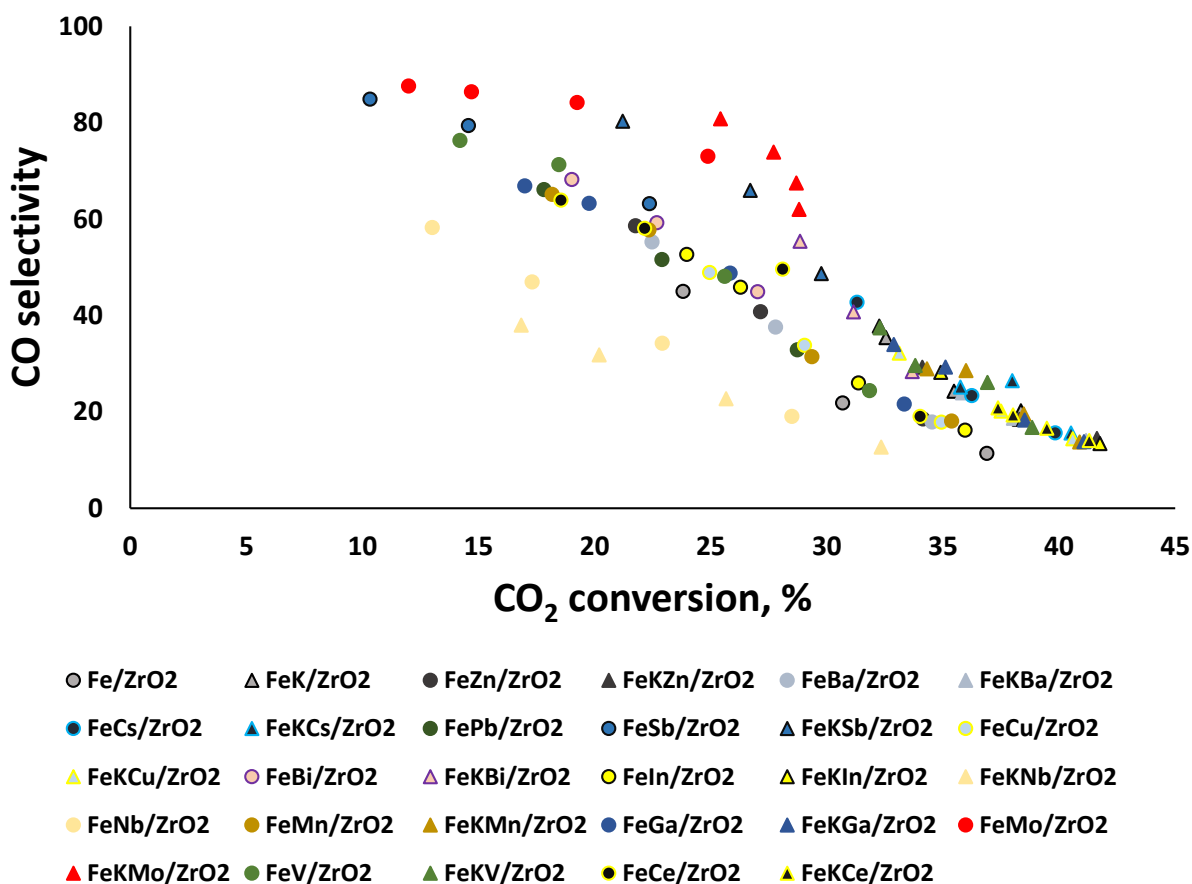


Figure 5-4. CO selectivity versus carbon dioxide conversion for Fe/ZrO₂ promoted catalysts. H₂/CO=3, WHSV=4.67-18.19 L/g.h, P=10 bar.

Note that the CO selectivity at the same conversion varies for different catalysts. The CO selectivity was particularly high over the antimony and molybdenum promoted catalysts, while somewhat lower CO selectivity was observed over the niobium promoted samples. Interestingly, the promoted iron catalysts containing potassium, show higher CO selectivity at the same conversion compared to the promoted iron catalysts without potassium.

A similar trend was observed for the CH₄ selectivity (**Figure 5-5**). The methane selectivity (excluding carbon monoxide) was relatively high at low CO₂ conversion on all catalysts approaching 80% at zero conversion. An increase in the CO₂ conversion results in a drop in the methane selectivity and production of higher hydrocarbons. In

chapter 3 a similar behavior for methane selectivity was observed in the FT synthesis with syngas over promoted iron catalysts. Higher methane selectivity was observed over the FeMo/ZrO₂, FeBi/ZrO₂, FeIn/ZrO₂ and FeSb/ZrO₂ samples (**Figure 5-5**). Addition of potassium as a second promoter to the catalysts results in a decreased methane selectivity over all promoted iron catalysts.

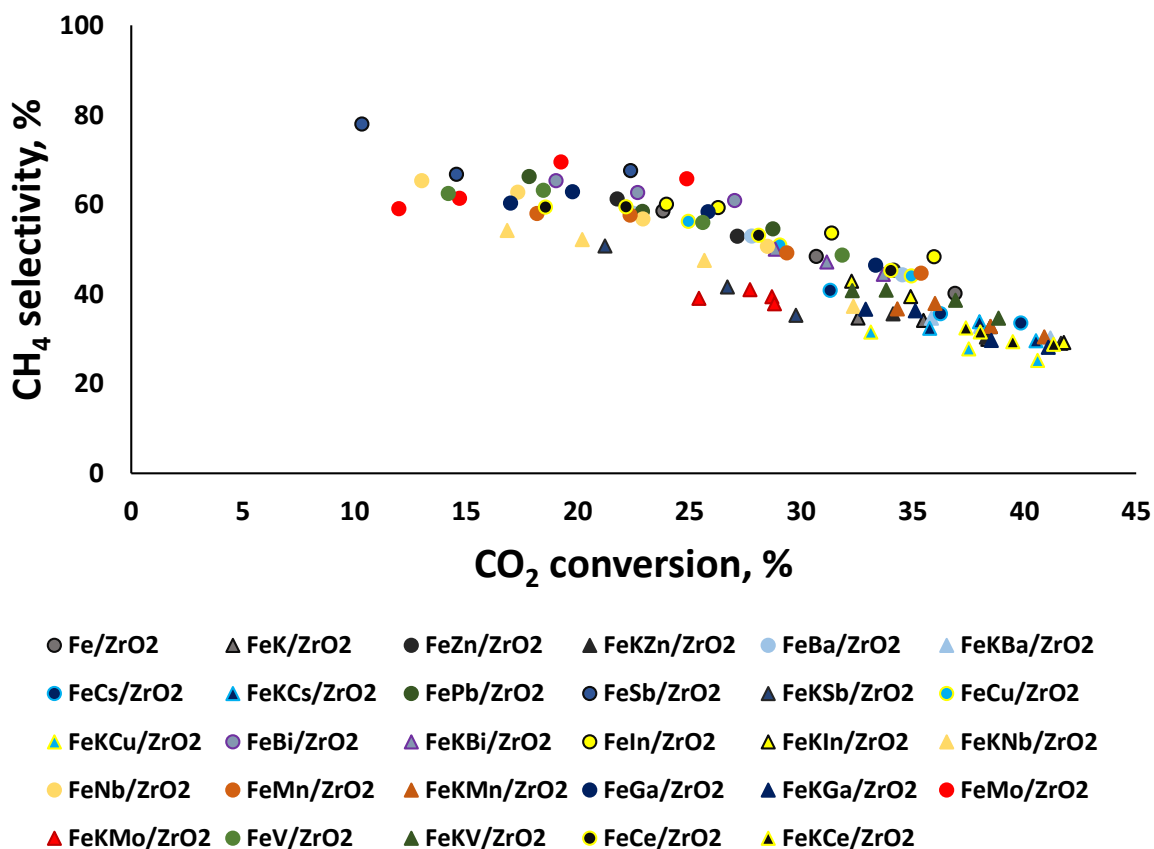


Figure 5-5. Methane selectivity versus carbon dioxide conversion for Fe/ZrO₂ promoted catalysts. H₂/CO₂=3, WHSV=4.67-18.19 L/ g.h, P=10 bar.

The light olefin selectivity data are displayed in **Figure 5-6**. Higher selectivity to light olefin is observed over the promoted iron catalysts containing potassium. Dependence of light olefin selectivity (**Figure 5-6**) on the CO₂ conversion shows two different behaviors. The first trend is observed for the promoted iron catalysts, which do not contain alkaline metals (potassium or cesium). The light olefin selectivity varies between 5 and 15% and is not, to any noticeable extent, affected by the CO₂

conversion. The second trend is seen for the promoted iron catalysts containing potassium or cesium. The light olefin selectivity shows some decrease, when the CO₂ conversion increases. The most efficient promoters for light olefins production on iron catalysts can be identified in **Figure 5-6**. Clearly, the presence of potassium is essential to obtain higher light olefin selectivity. In addition to potassium, Mo, Cu, Cs, Ce and Ga seem to be efficient promoters, further increasing the selectivity of CO₂ hydrogenation to light olefins. The phenomenon is more pronounced for the FeKM_x/ZrO₂ catalyst

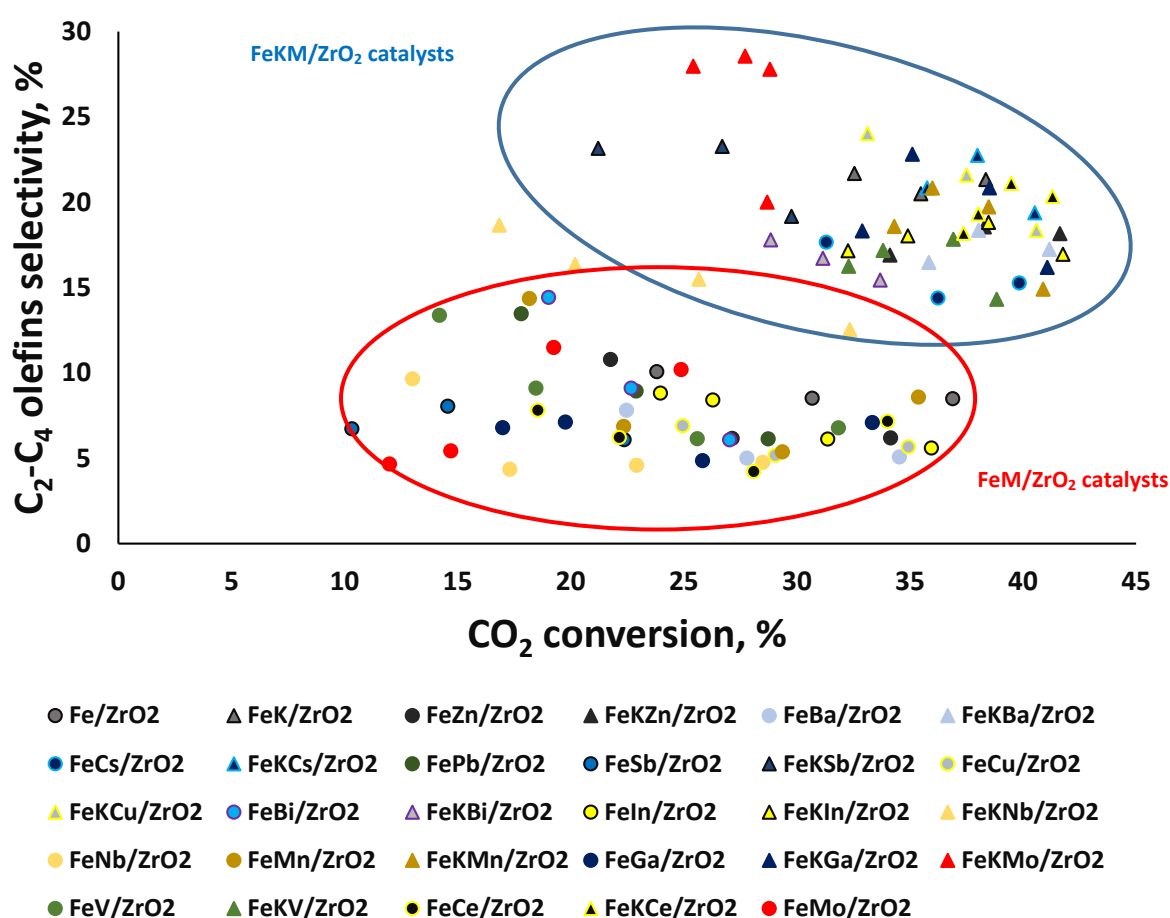


Figure 5-6. Light olefin selectivity versus carbon dioxide conversion for Fe/ZrO₂ promoted catalysts. H₂/CO₂=3, WHSV=4.67-18.19 L/g.h, P=10 bar.

Let us now consider variation of light paraffin and C₅₊ hydrocarbon selectivities with the CO₂ conversion over the promoted iron catalysts. The FeM/ZrO₂ catalysts, which do not contain alkaline metals show a noticeable increase in the C₂-C₄ paraffin

selectivity with CO₂ conversion (**Figure 5-7**). The light paraffin selectivity increases from 0 to 35%, as the CO₂ conversion rises from 10 to 40%. This suggests that on the one hand, C₂-C₄ paraffins seem to be secondary products of CO₂ hydrogenation over iron catalysts. They probably originate from hydrogenation of light olefins or C_nH_m surface species, which can be common precursors of light olefins or paraffins. On the other hand, FeKM/ZrO₂ catalysts, i.e., with potassium, present much smaller variation of the C₂-C₄ paraffin selectivity with conversion (**Figure 5-7**). This suggests that secondary hydrogenation of light olefins or common surface precursors would be less significant. Instead, over the latter catalysts, higher CO₂ conversion results in the increase in the selectivity to the C₅₊ hydrocarbons (**Figure 5-8**). Finally, in contrast to FeKM/ZrO₂ catalysts, for FeM/ZrO₂ catalysts the C₅₊ production seems to be less dependent of CO₂ conversion varying between 5 and 20%.

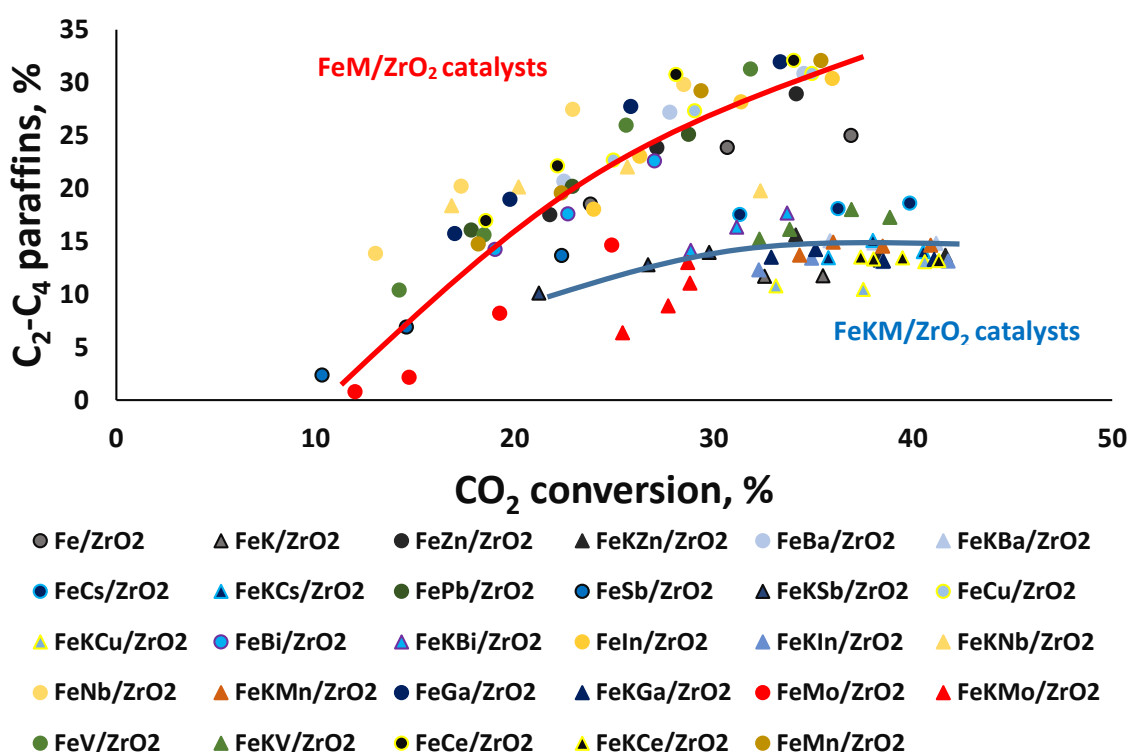


Figure 5-7. C₂-C₄ paraffins selectivity versus carbon dioxide conversion for Fe/ZrO₂ promoted catalysts. H₂/CO₂=3, WHSV=4.67-18.19 L/g.h, P=10 bar.

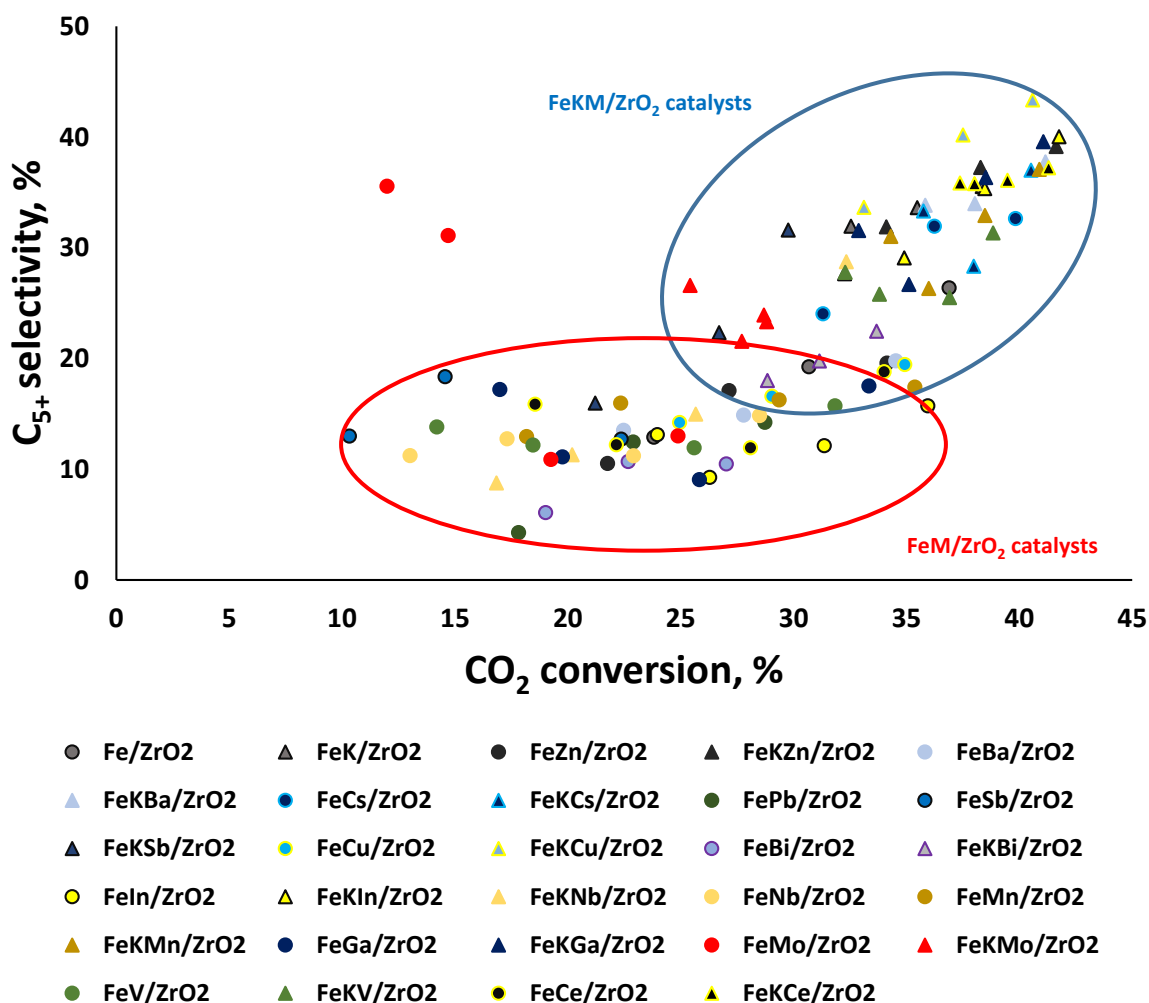


Figure 5-8. *C₅₊ selectivity versus carbon dioxide conversion for Fe/ZrO₂ promoted catalysts. H₂/CO₂=3, WHSV=4.67-18.19 L/g.h, P=10 bar.*

HTE tests allowed the identification of suitable promoters such as K, Mo, Ce, Cu, Cs and Ga for CO₂ hydrogenation to light olefins. Then, the catalyst stability was further tested in a fixed bed reactor using similar condition to those used in HTE (**Table 5-2**). The catalyst results obtained with the laboratory fixed bed reactor are consistent with the HTE tests. **Figure 5-9** shows the CO₂ conversion as a function of time-on-stream during 48 h of reaction. It is clear that the Fe/ZrO₂ reference catalyst deactivates with the reaction time, the CO₂ conversion drops from 20 to 8%. All the promoted catalysts showed higher activity than the reference catalyst (up to 7 times higher). In the case of the catalyst promoted only with K, the activity increases up to 4 times

compared to the reference Fe/ZrO₂ catalyst, while the addition of a second promoter can further enhance the activity compared to the catalysts promoted solely with an alkaline metal. Note that not only the activity but also the stability was also enhanced in the presence of these promoters. The light olefins selectivity did not significantly change during the reaction with the exception of FeKMo/ZrO₂, which shows a steady increase in the light olefin selectivity with the reaction time.

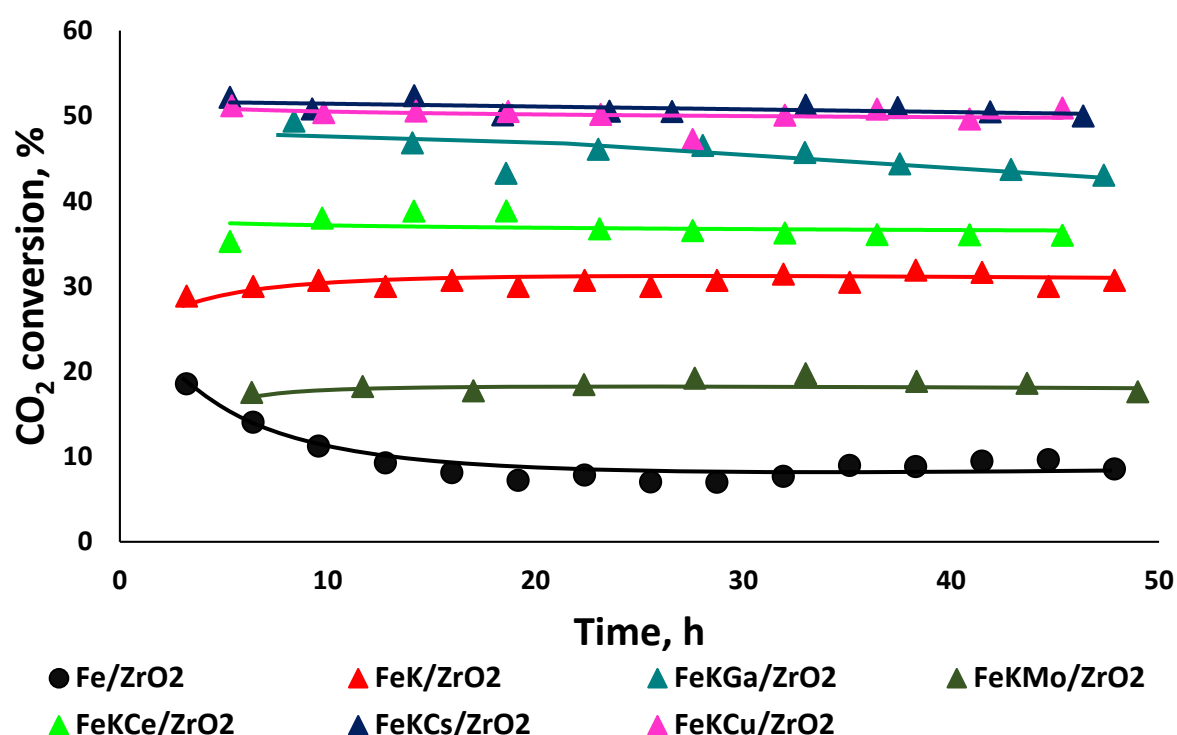


Figure 5-9. CO₂ conversion as a function of time for iron catalysts promoted with K, Ga, Mo, Ce, Cs, and Cu. Reaction conditions: T = 350 °C, P = 10 bar, H₂/CO₂ = 3, WHSV = 9.25 L/g.h.

Table 5-2. Catalytic performance of iron catalysts promoted with K, Cs, Cu, Ga, Mo and Ce for CO₂ hydrogenation reaction measured in a fixed bed reactor (10 bar, 350 °C, H₂/CO₂ = 3, GHSV = 9.25 L/g.h, TOS = 48 h)

Catalysts	FTY 10 ⁻⁵ mol _{CO2} g _{Fe} ⁻¹ s ⁻¹	CO ₂ conv. (%)	CO select. (%)	Hydrocarbon selectivity (%)			
				CH ₄	C ₂₋₄ ⁼	C ₂₋₄ ⁰	C ₅ ⁺
Fe/ZrO ₂	2.16	8	49	75	2	20	3
FeK/ZrO ₂	8.10	31	19	14	22	6	58
FeKCs/ZrO ₂	14.26	51	29	17	30	6	47
FeKCu/ZrO ₂	13.52	50	37	23	25	8	44
FeKGa/ZrO ₂	12.21	46	32	19	28	10	43

FeKMo/ZrO₂	4.69	18	37	28	33	5	34
FeKCe/ZrO₂	9.26	37	23	23	22	8	47

In order to provide further insights into the enhancement of the reaction rate and light olefins selectivity on the promotion, the Fe/ZrO₂ (reference), FeK/ZrO₂, FeKMo/ZrO₂, FeKCu/ZrO₂, FeKCs/ZrO₂, FeKCe/ZrO₂ and FeKGa/ZrO₂ catalysts have been investigated by a combination of characterization techniques.

5.3. Catalyst characterization

The XRF elemental analysis data for selected iron catalysts are displayed in Table 5-3. All the catalysts have similar iron contents close to nominal value (around 10 wt. %). At the same time, the potassium content was slightly higher than expected (1 wt.%) and the amount of Cs, Ce, Cu and Ga was as expected, 50:1 in molar ratio relative to iron. Only the Mo promoted catalyst shows a higher Fe/Mo ratio. The calcined catalysts display the characteristic XRD peaks (**Figure 5-10**) attributed to the zirconia support^{43,44}. The XRD peaks located at 28.2 and 31.5° are assigned to monoclinic zirconia (JCPDS 37-1484), while the peak at 50.3° reveals the presence of tetragonal zirconia (JCPDS 17-0923). Even though some broad hematite (Fe₂O₃, JCPDS13-0534) peaks were detected, the intensity of them was rather low. Significant broadening of these peaks indicates small size of iron oxide nanoparticles (below 5 nm). No diffraction peaks assignable to the crystalline phases of the promoters were observed, which is attributed to their low content in the catalysts.

Table 5-3. Physical properties of supported Fe catalysts.

Sample	Fe content ^a (wt%)	K content ^a (wt%)	Promoter content ^a (wt%)	Total H ₂ consum ^b (mmol/g)	S _{BET} ^c (m ² /g)	V _{tot} ^d (cm ³ /g)	CO ₂ ads. from TPD (μmol/g)
ZrO ₂	-	-	-	-	95.6	0.286	195.7
Fe/ZrO ₂	10.09	-	-	1.81	70.0	0.212	46.9
FeK/ZrO ₂	10.35	1.51	-	2.01	57.6	0.171	388.2
FeKCs/ZrO ₂	9.66	1.11	1.05	2.45	58.4	0.173	474.4
FeKCu/ZrO ₂	10.22	1.56	0.77	2.16	66.8	0.200	342.0
FeKGa/ZrO ₂	10.38	1.46	0.33	2.62	47.6	0.174	312.9
FeKMo/ZrO ₂	10.36	1.53	2.87	2.86	64.3	0.185	102.3
FeKCe/ZrO ₂	11.01	1.47	0.97	2.70	65.4	0.176	246.0

^aFe and promoter content from XRF.

^bThe total H₂ consumption from TPR analysis.

^cBET surface area.

^dSingle point desorption total pore volume of pores, $P/P_0=0.975$.

We also performed XRD measurements (**Figure 5-10b**) for reference and promoted catalysts after conducting the CO₂ hydrogenation reaction. The spent FeKCs/ZrO₂, FeKCu/ZrO₂, FeKGa/ZrO₂, and FeKMo/ZrO₂ catalysts exhibit diffraction peaks at 2θ angle of 43.4 and 44.1° that can be attributed to the iron carbide phases such as Hägg iron carbide (Fe₅C₂, JCPDS20-0509) formed during reaction. Because of similarity of XRD patterns attributed to different iron carbide, identification of individual iron carbide phases by means of XRD analysis is challenging.

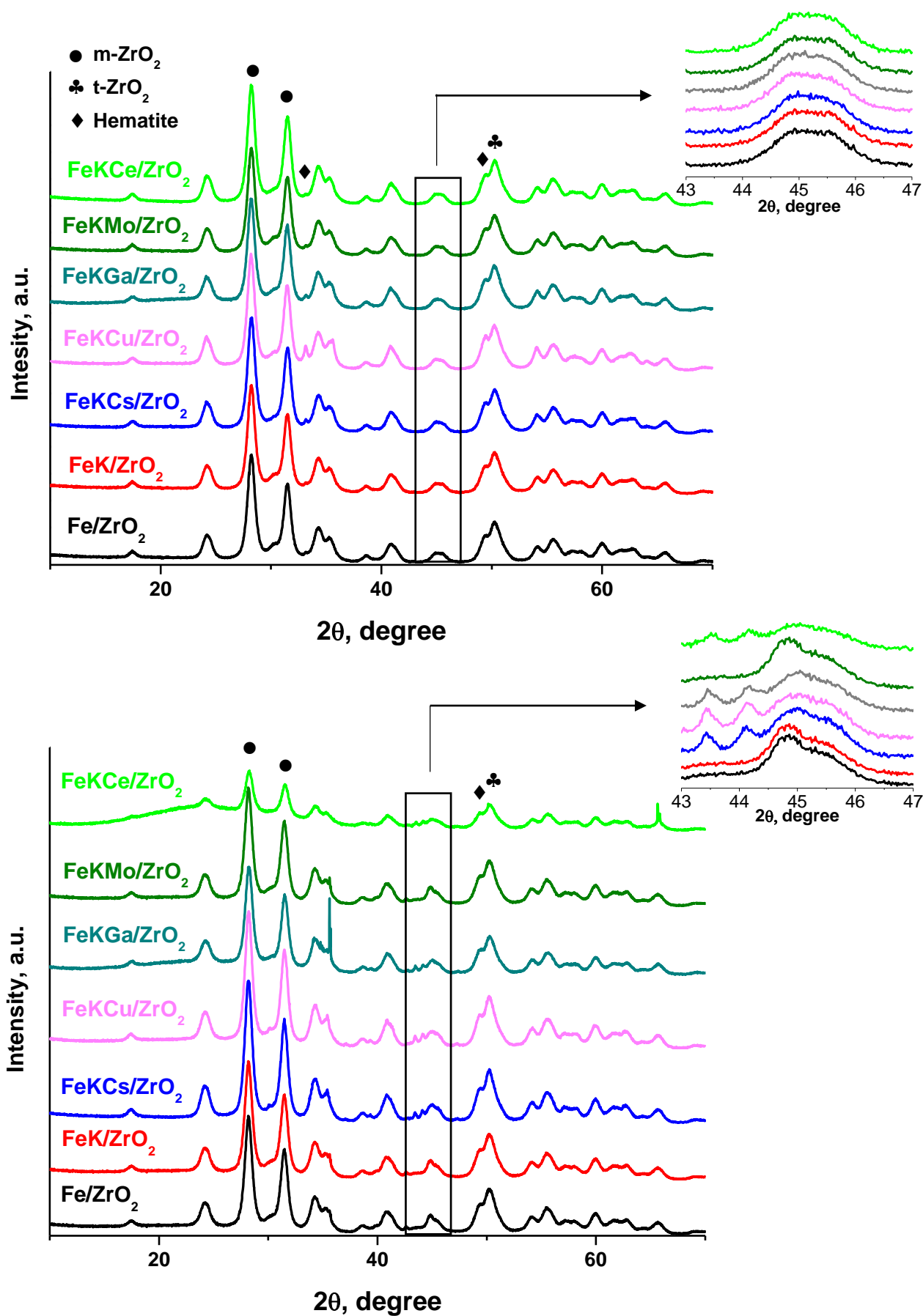


Figure 5-10. XRD patterns of the catalysts after calcination (a) and after reaction (b).

Figure 5-11 shows the CO₂-TPD curves for promoted iron catalysts, the amount of CO₂ adsorbed over the catalyst is shown in **Table 5-3**. The profiles exhibit three peaks: the first one located at 80-100 °C, corresponding to weak basic sites, the second one at 150-200 °C assigned to medium basic sites and the third one at 350 °C attributed to strong basic sites.

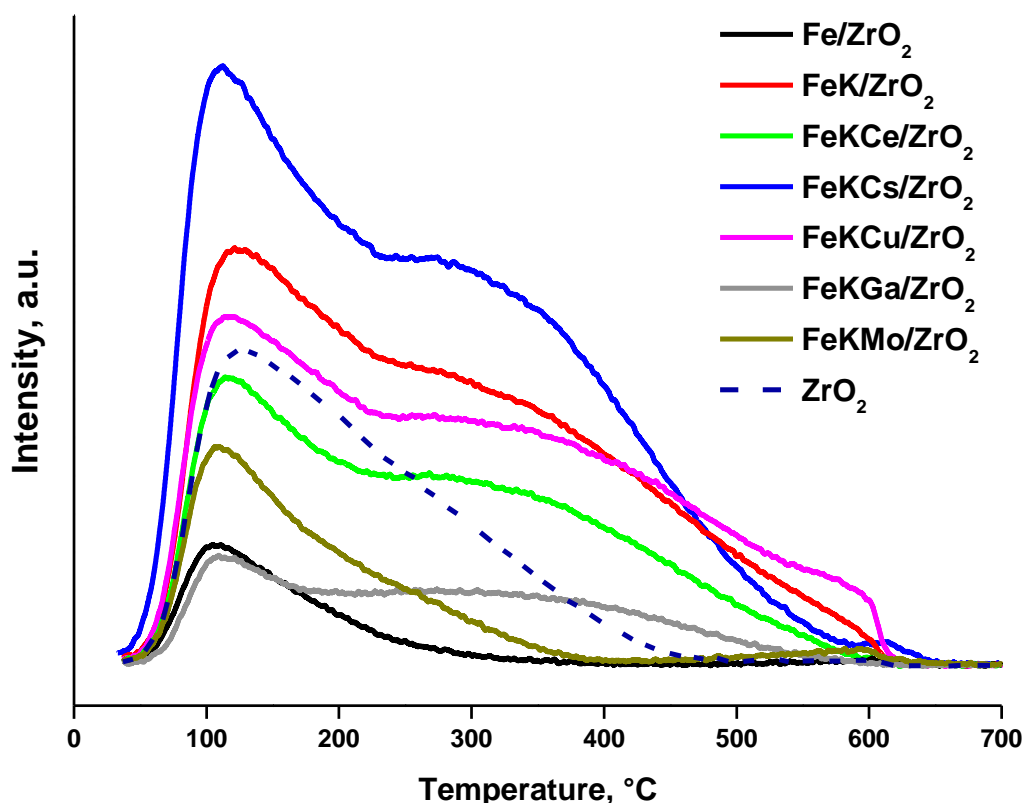


Figure 5-11. CO₂ TPD profiles adsorbed over ZrO₂ and iron catalysts.

The deconvolution of the CO₂-TPD profiles is illustrated by **Figure 5-12**. ZrO₂ is a basic oxide and the TPD profile of pure zirconia is similar to that previously reported in the literature^{45,46}. It displays two broad CO₂ TPD peaks at 100°C and 220°C. This suggests the presence of a wide range of relatively weak and medium basic sites. Addition of iron reduces the CO₂-TPD peak intensity. It seems that some medium basic sites of zirconia are neutralized by interaction with the added iron oxides. The promotion with potassium and cesium leads to an increase in the number of adsorbed

CO₂ and results in two distinct peaks, the first at 120°C corresponding to the weak basicity and the second at 300-420°C corresponding to stronger basicity. The intensity of these peaks correlates with the amount of alkaline metals in the catalysts. Addition of the second promoter results in a decreasing concentration of basic sites, indicating some interaction of the promoter with potassium and zirconia. Such a lower concentration of basic sites has been observed in the iron catalyst simultaneously promoted with potassium and molybdenum (Figure 5-11).

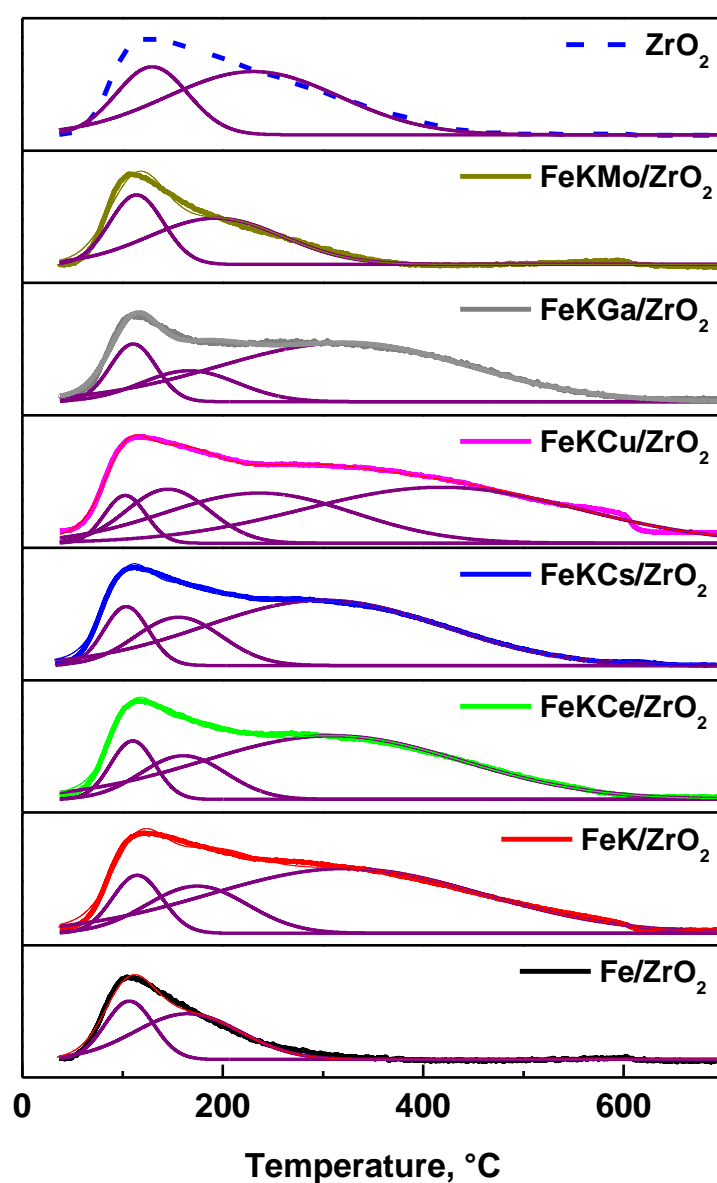


Figure 5-12. CO₂-TPD curves deconvolution for different ZrO₂-supported catalysts.

The TPR profiles of the reference Fe/ZrO₂ and FeK/ZrO₂, FeKCs/ZrO₂, FeKCe/ZrO₂, FeKGa/ZrO₂ catalysts are displayed in **Figure 5-13**. The amount of hydrogen consumed is given in **Table 5-3**. A first reduction peak at ~380 °C is observed, which can be attributed to the hematite reduction to magnetite, Fe₂O₃ → Fe₃O₄,⁴⁷ and a second broader peak related to the successive reduction of iron oxides, Fe₃O₄ → FeO → Fe^{48,49}. This second peak is centered at ~500 °C for the reference Fe/ZrO₂ and FeK/ZrO₂ catalysts. For the FeKCs/ZrO₂, FeKCe/ZrO₂ and FeKGa/ZrO₂ catalysts, this peak shifts toward higher temperatures. Addition of Cs, Ga, Ce seems to give place to a strong interaction of iron oxide with the promoters⁵⁰ and hinders reduction of the magnetite phase. Note that these promoters do not affect the reduction of Fe₂O₃ to Fe₃O₄. On the other hand, the H₂-TPR profile of FeKMo/ZrO₂ shows a shift to higher temperatures for both peaks. So, the molybdenum presence clearly affects the different iron oxide reduction steps. Finally, the H₂-TPR profile of FeKCu/ZrO₂ displays two reduction peaks at ~250 and 298 °C, which shift to lower temperatures compared to the reference Fe/ZrO₂ sample, which is in agreement with the literature⁵¹. The intensity of peak at 250°C can also contribute from the reduction of copper. Indeed, the presence of copper in the catalyst facilitates iron oxide reduction. Interestingly, addition of promoters results in higher amount of consumed hydrogen (Table 5-3). It seems that the promotion slows down interaction of iron with zirconia and increases the amount of reducible iron. Note that the amount of incorporated promoters compared to iron is rather small to significantly contribute to the intensity of the TPR peaks.

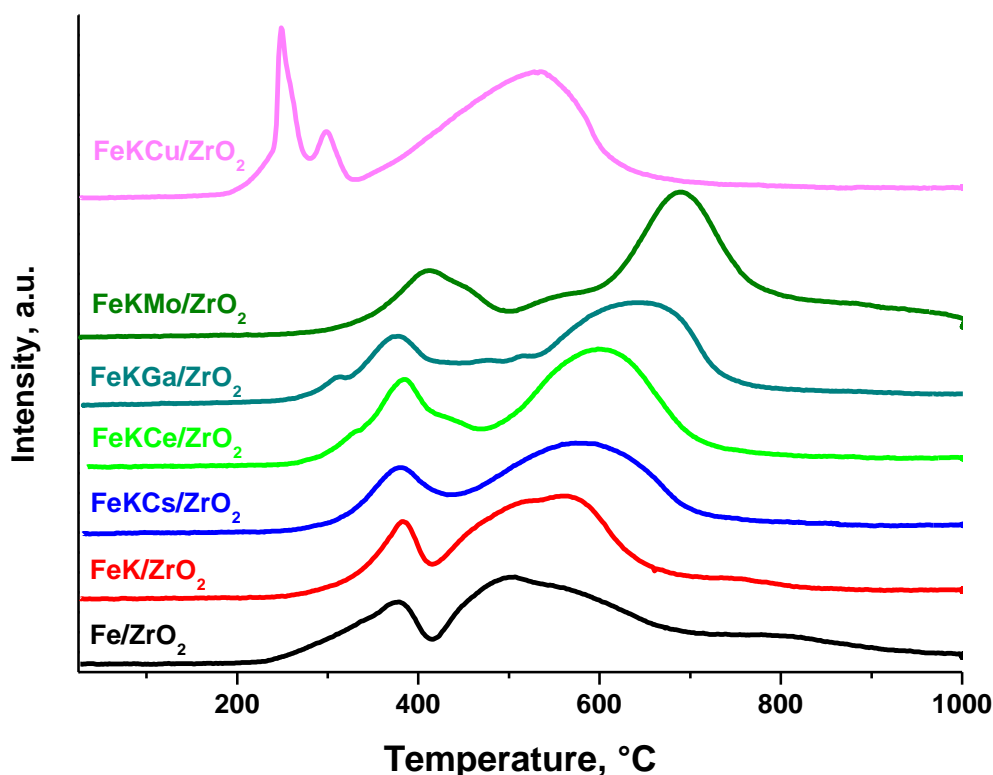
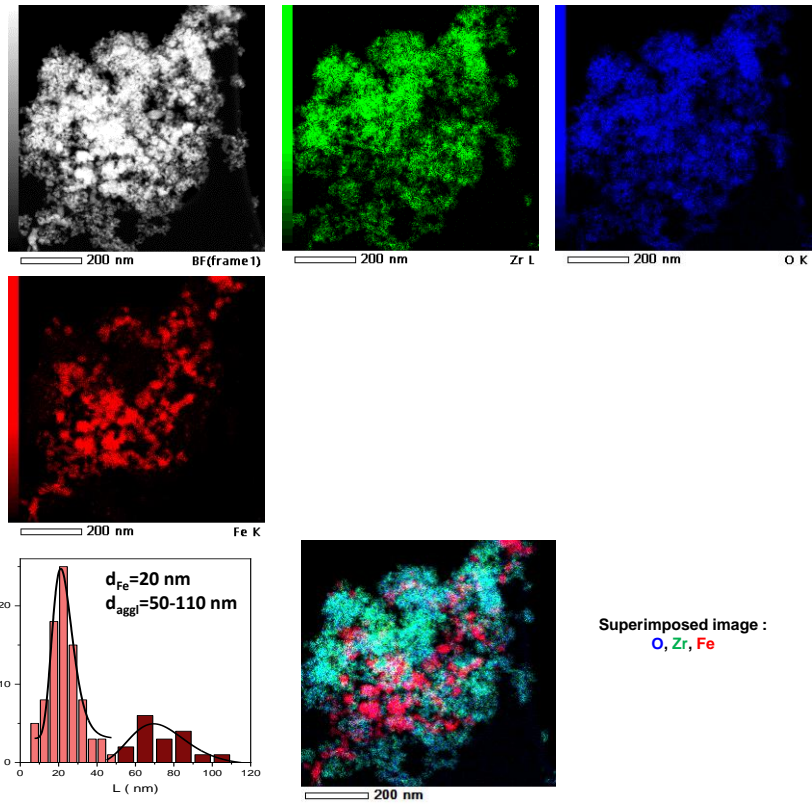


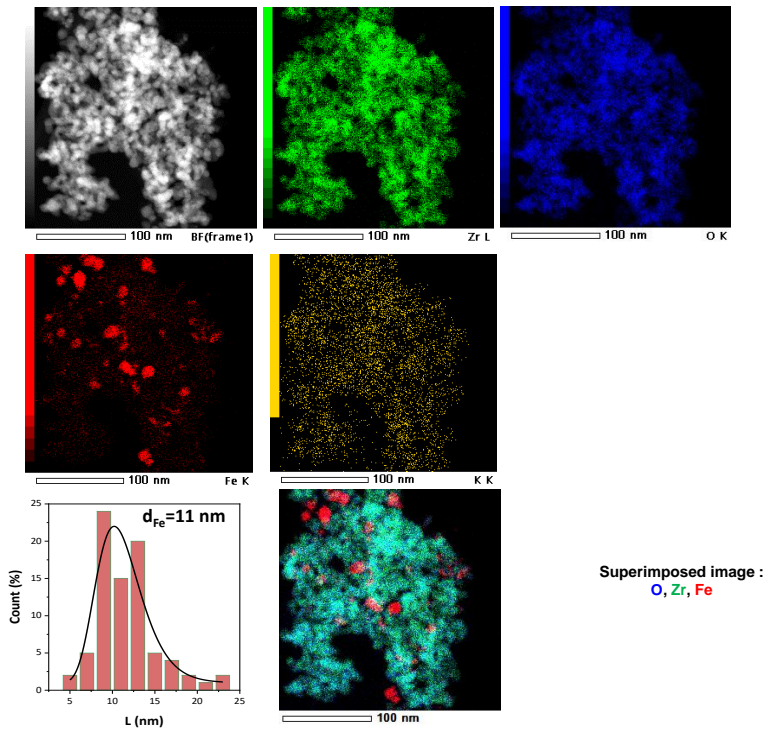
Figure 5-13. *H₂-TPR profiles of reference and promoted catalysts with K, Cs, Ce, Ga, Mo, and Cu.*

STEM-HAADF and STEM-EDS images have provided further information about iron particle sizes and promoter localization in the supported catalysts (**Figure 5-14**). The histograms of iron nanoparticle sizes were calculated from STEM-HAADF. In the reference Fe/ZrO₂ sample, iron nanoparticles of 20 nm mean diameter were dispersed in ZrO₂ matrix with a rather homogenous distribution. The agglomeration of iron nanoparticles was also uncovered, which is most probably due to the nanoparticle superposition in the projection of the volume. The promoted FeK/ZrO₂, FeKGa/ZrO₂ and FeKMo/ZrO₂ catalysts exhibited much smaller iron nanoparticles of 11-14 nm homogeneously dispersed within the ZrO₂ matrix, without any Fe nanoparticles agglomeration (**Figure 5-14**). The promoters (K, Ga and Mo) appear to be homogeneously distributed.

a



b



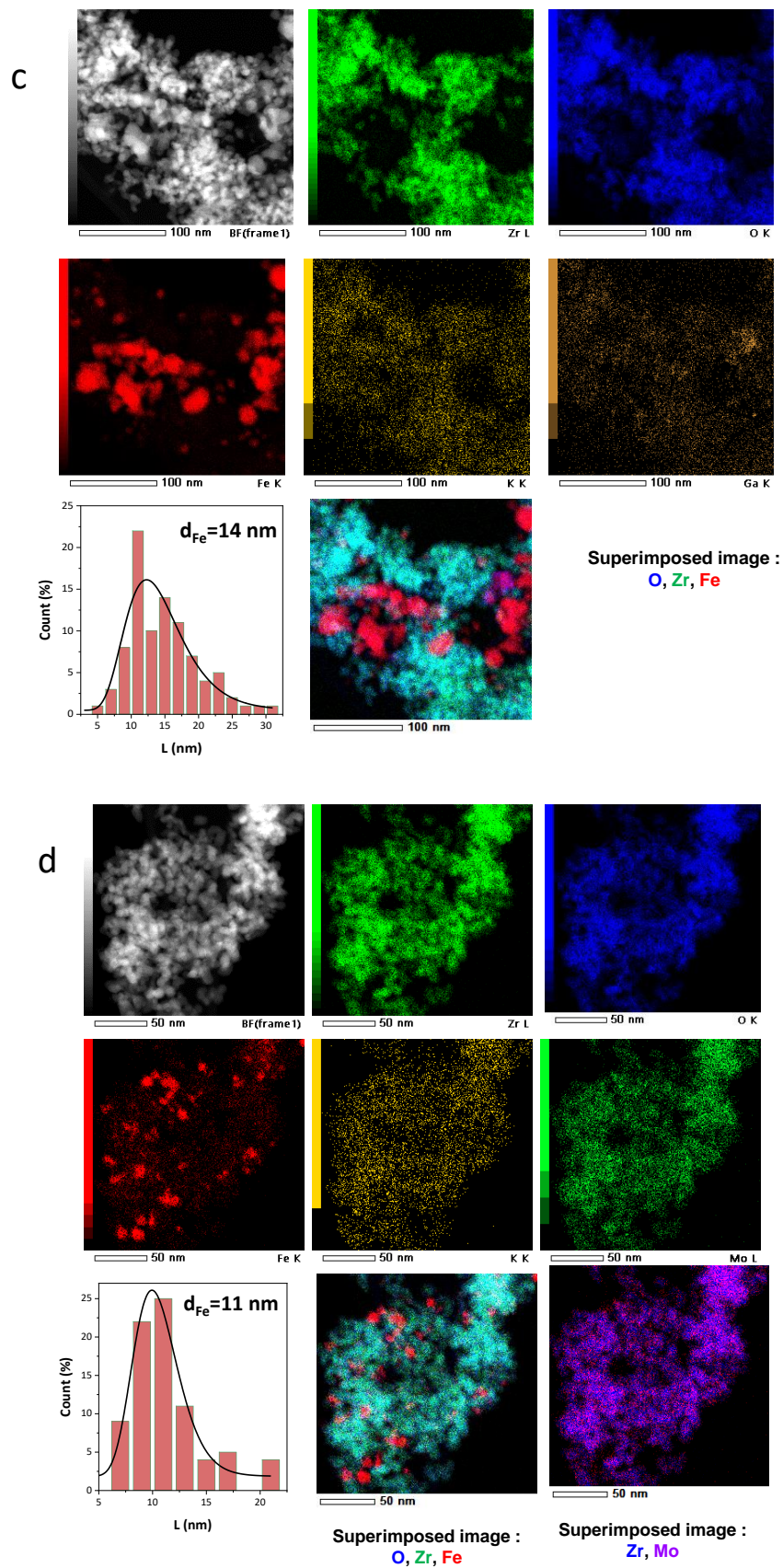


Figure 5-14. STEM-HAADF, SEM-EDX mapping and histograms of iron nanoparticle sizes for the activated Fe/ZrO_2 (a), FeK/ZrO_2 (b), $FeKGa/ZrO_2$ (c) and $FeKMo/ZrO_2$ (d) catalysts.

In order to get a deeper understanding of the catalytic performance, the reference and promoted iron catalysts were characterized using *in-situ* Mössbauer spectrometry under the flow of CO and reaction mixture (CO₂ + H₂). After the CO activation at 350 °C (**Figure 5-15**), the presence of iron Hägg carbide and wüstite (FeO) was observed in all samples.

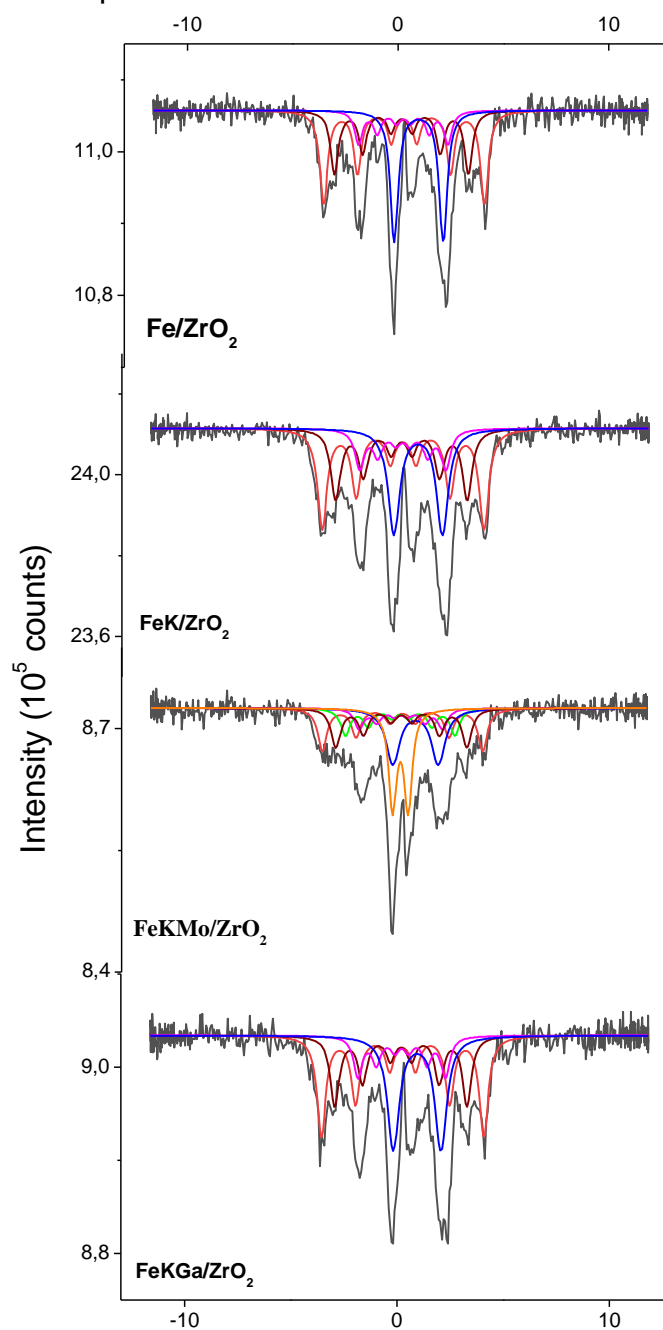


Figure 5-15. Mössbauer spectra after activation measured at -153 °C.

The promotion of Fe/ZrO₂ catalyst with K and Mo results in a higher fraction of iron carbide (**Table 5-4**). A noticeable concentration of metastable (ϵ' -Fe_{2.2}C) carbide was observed in the FeKMo/ZrO₂ catalyst after the activation. **Figure 5-16** shows the *in-situ* Mössbauer spectra after catalyst exposure to the reaction conditions (H₂/CO₂ = 3, 350 °C and 10 bar). Two types of Mössbauer spectra modification were observed. On the one hand, there is a slight improvement in the crystallinity of the Hägg iron carbide species. In the Mössbauer spectroscopy, the crystallinity is reflected by the linewidth of the measured signal. The reference Fe/ZrO₂ catalyst after the 24 h of reaction exhibits better defined Hägg structures. The linewidth of Mössbauer signals decreases from 0.45 to 0.42 mm/s (**Table 5-4**).

Table 5-4. The Mössbauer fitted parameters of the ZrO₂-based catalysts, obtained at 120 K.

Sample/ Treatment	IS (mm·s ⁻¹)	QS (mm·s ⁻¹)	Hyperfine field (T)	Γ (mm·s ⁻¹)	Phase	Spectral contribution (%)
Fe/ZrO ₂ CO, 350 °C	0.28	-	23.7	0.45	χ -Fe ₅ C ₂ (I)	36
	0.16	-	19.7	0.45	χ -Fe ₅ C ₂ (II)	25
	0.24	-	13.2	0.45	χ -Fe ₅ C ₂ (III)	13
	0.98	2.32	-	0.45	Fe _{1-x} O (SPM ^a)	26
Fe/ZrO ₂ H ₂ /CO ₂ =3 350 °C, 10 bar	0.28	-	23.7	0.42	χ -Fe ₅ C ₂ (I)	37
	0.15	-	19.8	0.42	χ -Fe ₅ C ₂ (II)	27
	0.17	-	13.6	0.42	χ -Fe ₅ C ₂ (III)	12
	1.00	2.35	-	0.47	Fe _{1-x} O (SPM)	24
FeK/ZrO ₂ CO, 350 °C	0.26	-	23.7	0.54	χ -Fe ₅ C ₂ (I)	37
	0.18	-	19.3	0.54	χ -Fe ₅ C ₂ (II)	26
	0.24	-	12.6	0.54	χ -Fe ₅ C ₂ (III)	14
	0.96	2.28	-	0.65	Fe _{1-x} O (SPM)	23
FeK/ZrO ₂ H ₂ /CO ₂ =3 350 °C, 10 bar	0.27	-	23.8	0.47	χ -Fe ₅ C ₂ (I)	36
	0.17	-	19.9	0.47	χ -Fe ₅ C ₂ (II)	29
	0.24	-	12.8	0.47	χ -Fe ₅ C ₂ (III)	16
	1.00	2.31	-	0.58	Fe _{1-x} O (SPM)	19
FeKMo/ZrO ₂ CO, 350 °C	0.28	-	23.5	0.53	χ -Fe ₅ C ₂ (I)	20
	0.23	-	19.2	0.53	χ -Fe ₅ C ₂ (II)	18
	0.20	-	11.2	0.53	χ -Fe ₅ C ₂ (III)	10
	0.17	-	16.1	0.53	ϵ' -Fe _{2.2} C	13
	0.17	0.74	-	0.45	Fe _x C (SPM)	20
	0.90	2.15	-	0.77	Fe _{1-x} O (SPM)	19
FeKMo/ZrO ₂ H ₂ /CO ₂ =3 350 °C, 10 bar	0.27	-	23.7	0.49	χ -Fe ₅ C ₂ (I)	25
	0.21	-	19.6	0.49	χ -Fe ₅ C ₂ (II)	24
	0.20	-	10.9	0.49	χ -Fe ₅ C ₂ (III)	11
	0.22	-	16.6	0.49	ϵ' -Fe _{2.2} C	14
	0.14	0.70	-	0.28	Fe _x C (SPM)	10
	1.02	2.35	-	0.61	Fe _{1-x} O (SPM)	16
FeKGa/ZrO ₂ CO, 350 °C	0.26	-	23.8	0.50	χ -Fe ₅ C ₂ (I)	35
	0.19	-	19.3	0.50	χ -Fe ₅ C ₂ (II)	24
	0.22	-	12.3	0.50	χ -Fe ₅ C ₂ (III)	14

	0.95	2.24	-	0.67	Fe _{1-x} O (SPM)	27
FeKGa/ZrO ₂	0.28	-	23.9	0.43	χ-Fe ₅ C ₂ (I)	36
H ₂ /CO ₂ =3	0.19	-	20.0	0.43	χ-Fe ₅ C ₂ (II)	29
350 °C, 10	0.26	-	12.7	0.43	χ-Fe ₅ C ₂ (III)	17
bar	0.99	2.38	-	0.57	Fe _{1-x} O (SPM)	18

Experimental uncertainties: Isomer shift: I.S. ± 0.02 mm s⁻¹; Quadrupole splitting: Q.S. ± 0.02 mm s⁻¹; Line width: $\Gamma \pm 0.03$ mm s⁻¹; Hyperfine field: ± 0.1 T; Spectral contribution: $\pm 3\%$; ^aVery small, superparamagnetic (SPM) structures.

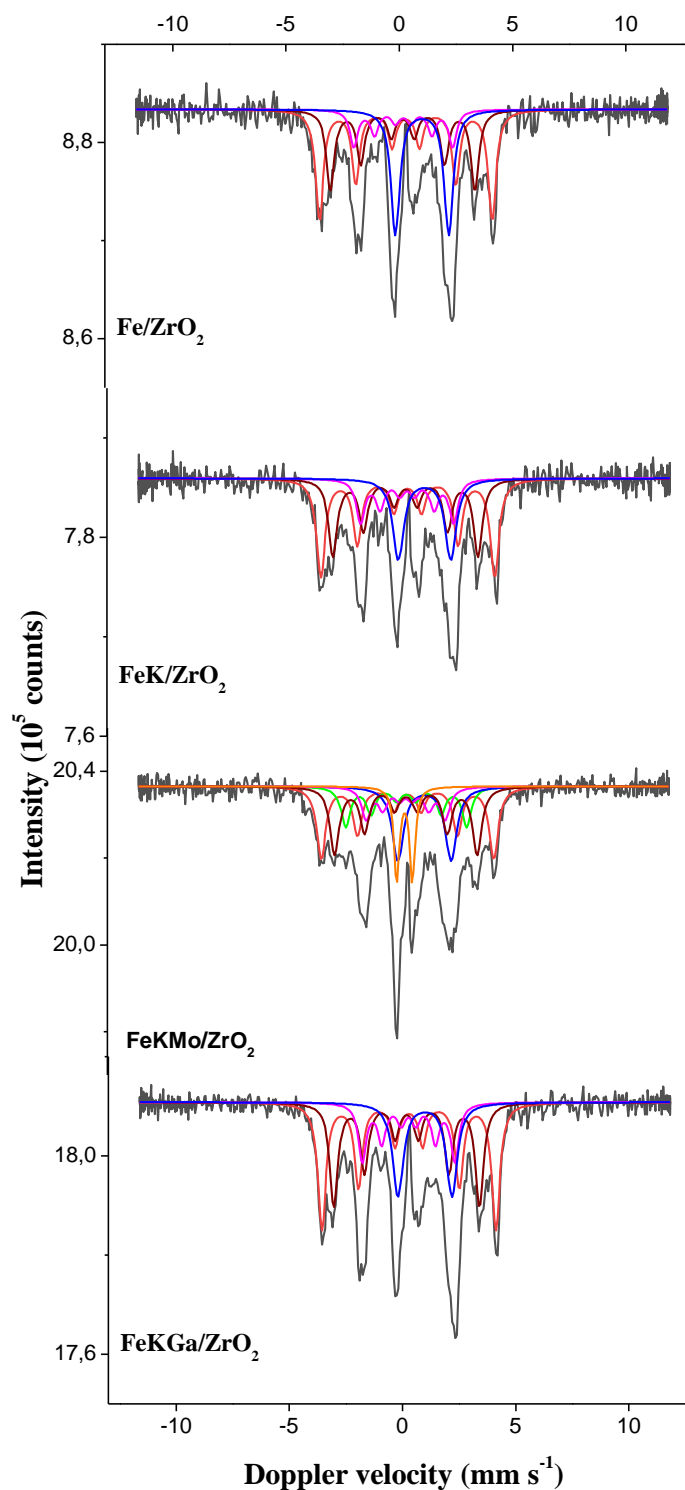


Figure 5-16. Mössbauer spectra after reaction measured at -153 °C.

The same tendency is observed for all promoted catalysts. On the other hand, the fraction of iron carbide seems to further increase after conducting the CO₂ hydrogenation. This is shown by the lower amount of unreduced wüstite species in the spent catalysts compared to that in the counterparts activated in CO. In contrast to other catalysts, FeKGa/ZrO₂ after reaction does not show any increase in the iron carbide content, indicating a smaller effect of Ga addition to iron carbidisation. Only the slightly smaller linewidth values indicate the presence of better defined Hägg carbide species in FeKGa/ZrO₂ compared to FeK/ZrO₂. Note that the FeKMo/ZrO₂ catalyst showed the higher fraction of iron carbide among all studied promoted iron catalysts after conducting CO₂ hydrogenation.

Carbon deposition is a major limitation of CO₂ hydrogenation resulting in a loss of catalytic activity. **Figure 5-17** shows the thermogravimetric analysis (TGA) data for the spent ZrO₂-supported catalysts. The first small loss around 150 °C is normally generated by the water elimination and possible dehydration of iron oxyhydroxide (FeOOH). Above 300 °C, significant weight losses produced by the combustion of carbon deposits can be observed. Interestingly, the reference catalyst presents a smaller weight loss. So the enhancement in stability observed during the CO₂ hydrogenation reaction over the promoted catalysts (**Figure 5-9**) seems not to be related to the catalyst ability to avoid carbon deposition and can possibly be assigned to other phenomena.

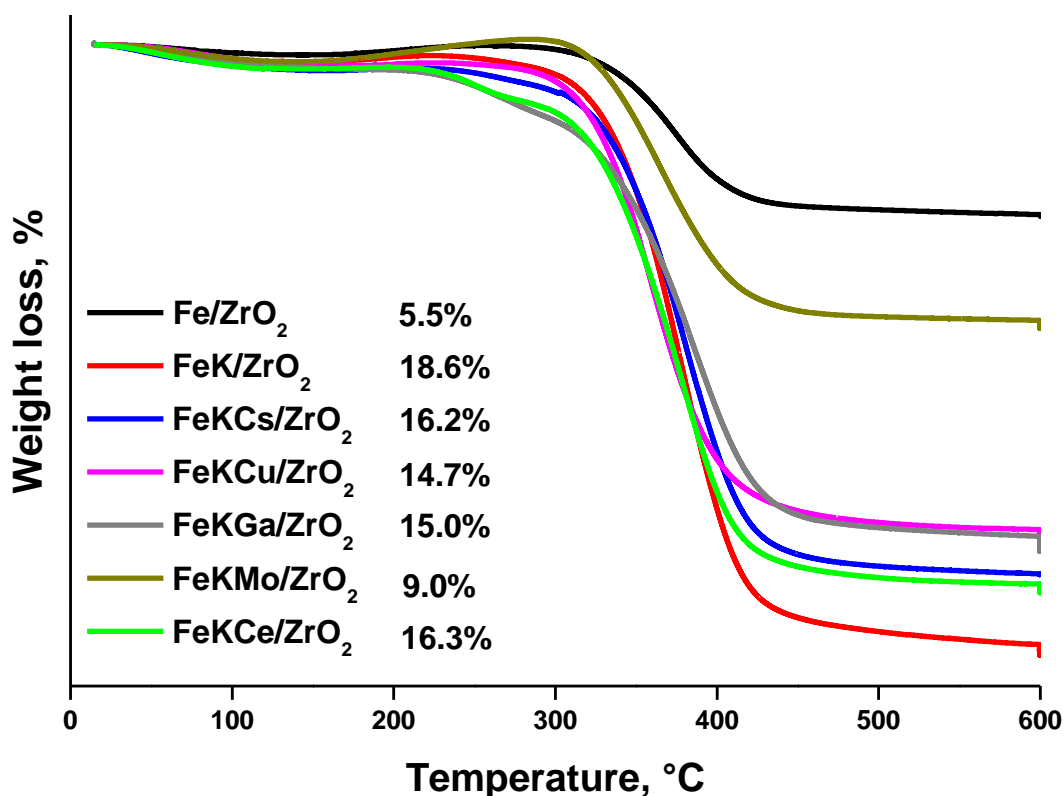


Figure 5-17. Thermogravimetric analysis (TGA) curves of the spent catalysts.

5.4. Discussion

CO₂-FT synthesis occurs at 300-350 °C and is focused on the production of light olefins. Compared to the “methanol-mediated” processes occurring over metal-oxide/zeolite catalysts, CO₂-FT synthesis exhibits higher yields of olefins and lower selectivity to CO^{29,30}. Iron catalysts are the catalysts of choice for light olefin synthesis from CO₂ via the FT route. The selection of efficient promoters for iron catalysts seems to be the key for the selectivity control of this reaction. Alkaline metals, copper, manganese, zinc and cobalt have been the most investigated promoters for iron CO₂-FT catalysts. At the same time, very limited attention has been paid to the promotion of iron CO₂-FT catalysts with other elements. In this chapter, HTE combined with catalyst characterization have allowed identification of new efficient promoters and also provided important information about the influence of these promoters on different reaction elementary steps.

CO₂-FT synthesis is a complex multi-stage reaction^{7,21,22,35}. It can be therefore suggested that different reaction stages can be affected to a different extent by the promotion. The experimental results shown in **Figures 5-4 to 5-8** illustrate the effects of added promoters on different reactions steps.

Figure 5-4 shows higher CO selectivity at low CO₂ conversion. CO seems indeed, to be the primary product of CO₂ hydrogenation over iron catalysts. Important, the experimental results obtained for numerous promoted iron catalysts exhibit a similar trend. RWGS is a fast reaction and is readily catalyzed by iron oxides (e. g. Fe₃O₄)^{29,52}. The presence of considerable concentrations of iron oxide species in the working catalysts has been identified by Mössbauer spectrometry. This explains rather similar behavior of all promoted catalysts in the CO₂ hydrogenation to CO. Interestingly, almost all promoted catalysts showed much higher CO selectivity at the same CO₂ conversion compared to the reference Fe/ZrO₂ catalyst. The added promoters could therefore contribute to RWGS. This also coincides with higher activity (FTY) of the promoted catalysts compared to the reference one (**Figure 5-3**).

The methane selectivity versus conversion curve (**Figure 5-5**) also agrees with the suggested reaction sequence (**Figure 5-18**). Higher methane selectivity is observed at lower CO₂ conversion, then the methane selectivity drops at higher conversion. At low conversion hydrogenation of C₁ monomer seems to prevail over its oligomerization. At higher CO₂ conversion and higher surface concentration of C₁ monomers, their oligomerization becomes more favorable and leads to adsorbed C₂-C₄ species. This trend has been seen for all catalysts, with somewhat lower methane selectivity at the same conversions observed for FeMo/ZrO₂, FeKMo/ZrO₂ and FeKSb/ZrO₂.

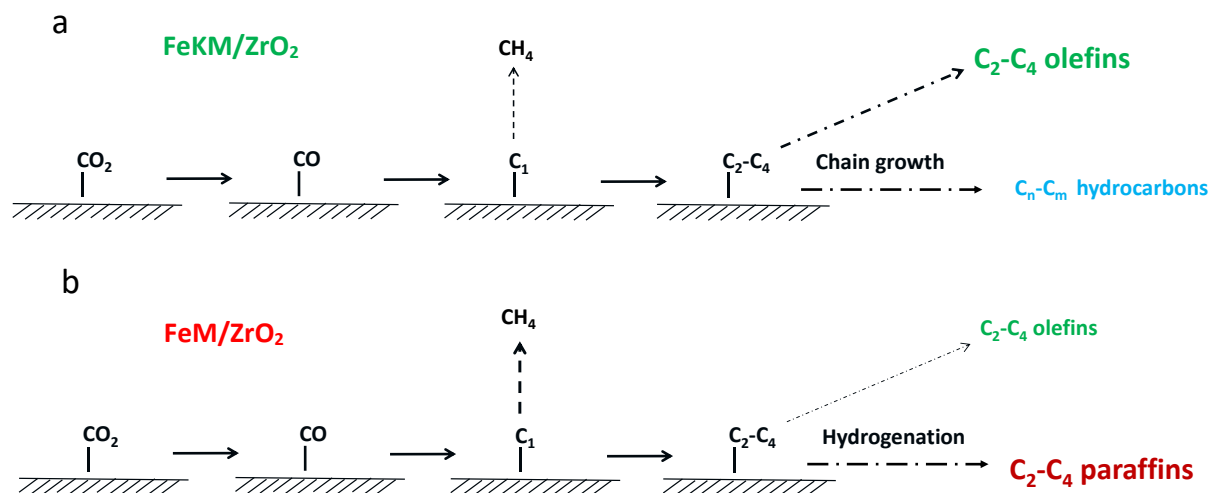


Figure 5-18. Reaction paths in CO₂ hydrogenation over promoted iron catalysts with (a) and without (b) potassium.

Very different correlations between light olefin selectivity and conversion have been observed for the catalysts with and without alkaline metals (**Figure 5-6**). The light olefin selectivity over FeM/ZrO₂ (without alkaline metals) was much lower compared to the FeKM/ZrO₂ catalysts promoted with potassium and it does not noticeably vary as a function of CO₂ conversion. The higher selectivity to light olefins over the FeKM/ZrO₂ catalysts decreases as a function of CO₂ conversion. For the catalysts without alkaline promoters, increased CO₂ conversion results in higher selectivity to C₂-C₄ hydrocarbons, while for the catalysts containing alkaline metals, higher selectivity for C₅₊ hydrocarbons was measured at higher CO₂ conversions. Higher conversion therefore leads to a higher chain growth rate, which can be attributed to enhanced surface oligomerization of C₁ monomeric species and light olefin readsorption⁵³, which may reinitialize oligomerization on iron catalysis, both phenomena favoring production of longer chain hydrocarbons.

The possible reaction paths of CO₂-FT synthesis over iron catalysts have been summarized in **Figure 5-18**. The first step in CO₂-FT synthesis over iron catalysts is CO₂ hydrogenation to CO followed by formation of C₁ adsorbed monomers. Then, the

adsorbed C_1 monomers can be either hydrogenated to yield methane or to undergo oligomerization to different C_n adsorbed species. Desorption of C_2 - C_4 adsorbed species should produce light olefins (ethylene, propylene or butylene), while their hydrogenation leads to light paraffins, the latter also possibly be produced via olefin re-adsorption (and subsequent hydrogenation)^{54,55,56}. Further reactions of adsorbed C_2 - C_4 species with C_1 monomer produce longer-chain hydrocarbons.

The rates of hydrogenation of adsorbed C_2 - C_4 species and rates of oligomerization seem to be different over the catalysts with (**Figure 5-18 a**) and without potassium (**Figure 5-18 b**). These phenomena also explain the role of alkaline promoters. The promotion with alkaline metals results in a decrease in the catalyst hydrogenation ability and at the same time, increases the rate of oligomerization of C_1 surface monomers. Thus, over the catalysts containing alkaline metals, the oligomerization limits the light olefin selectivity, while the contribution of hydrogenation of adsorbed C_2 - C_4 species or secondary hydrogenation of light olefins is not significant. This suggests that, in order to boost the light olefin selectivity over the catalysts promoted with alkaline metals, the surface oligomerization should be hindered after the formation of the C_4 surface fragments. Similar effects were previously observed in chapter 3. The second promoter should therefore, slow down chain growth without any major enhancement of the hydrogenation rate of surface species.

The key issue in the catalyst design for CO_2 -FT synthesis is therefore light olefin selectivity and the role of specific promoters in there. **Figure 5-6** shows the light olefin selectivity versus conversion, and it enables identification of the most efficient second promoters such as Mo, Cs, Ga, Ce and Cu. Note that in order to reach higher selectivity to light olefins, these promoters should be used in combination with potassium.

Several phenomena can be responsible for the observed increase in CO₂ hydrogenation rate and light olefin selectivity over the catalysts promoted simultaneously with potassium and other elements. First, the STEM and STEM-EDS of the promoted catalysts (**Figure 5-14**) showed noticeable increase in the iron dispersion in activated catalysts compared to the reference Fe/ZrO₂ counterpart. Consequently, higher iron dispersion can contribute to the increase in FT reaction rate and light olefin selectivity. Second, addition of the promoters can modify the extent of iron carbidization and reduction. The in-situ Mössbauer data (**Table 5-4**) show that the presence of the promoters such as Mo, K and Ga results in a higher fraction of iron carbide. For the FeKMo/ZrO₂ catalyst promoted with potassium and molybdenum, the increase in iron carbidization during the reaction coincides with the continuous increase in light olefin selectivity. TPR results (**Figure 5-13**) show easier iron reduction in the copper-promoted catalysts. Third, the promotion enhances the RWGS reaction, which is an important step in CO₂-FT synthesis and often affects the overall activity. Indeed, most of the promoted catalysts showed higher CO selectivity at a given CO₂ conversion compared to the reference Fe/ZrO₂. Four, the promotion affects the catalyst basicity and, hence, adsorption of CO₂, which is an acid molecule. The promotion with potassium principally results in the buildup of strong basic sites (**Figure 5-11 and Figure 5-12**). Note that extremely strong basicity and strong CO₂ adsorption do not seem to be optimal for obtaining high concentrations of reactive CO₂ adsorbed molecules. Addition of the second promoter mediates the basicity of FeK/ZrO₂ catalysts and thus, favors the CO₂ activation. Finally, the promotion affects the rate of hydrogenation and surface chain growth (**Figure 5-18**). The promotion of iron catalysts with potassium reduces the rate of hydrogenation and favors chain growth. Addition of the second promoter can further tune the hydrogenation and chain growth rates, which should

hinder formation of paraffins and longer chain hydrocarbons and thus, can lead to higher light olefin selectivity.

5.5. Conclusions

HTE tests allowed the identification of new suitable promoters of zirconia supported iron catalysts for CO₂ hydrogenation to light olefins. The presence of alkaline promoters seems to be indispensable for the selectivity enhancement towards light olefins over iron catalysts. Complementary to potassium, the promotion of ZrO₂-supported catalysts with Cs, Mo, Cu, Ga, and Ce resulted in further increase in the light olefin selectivity. The promotion seems to lead to better iron dispersion and more pronounced iron carbidization. The catalyst basicity required for CO₂ adsorption is enhanced by the promotion with alkaline metals and mediated by the second promoter.

CO₂-FT synthesis proceeds via intermediate production of carbon monoxide. The dependence of light olefin selectivity on the CO₂ conversion exhibits two different trends, depending on potassium promotion. Without potassium as promoter, the relatively low selectivity to light olefins is practically independent from the CO₂ conversion. The second trend is identified for the iron catalysts containing simultaneously alkaline and second promoter. Over those catalysts much higher selectivity to light olefins shows a noticeable decrease with the increase in CO₂ conversion. Over the catalysts without alkaline metals, higher CO₂ conversion favors production of light paraffins, while the presence of potassium leads to higher selectivity towards longer chain hydrocarbons at higher conversion level. The second promoter, complementary to an alkaline metal, should hinder chain growth rates without any increase in hydrogenation rate of surface intermediate species.

5.6. Reference

1. D'Alessandro, D. M., Smit, B. & Long, J. R. Carbon dioxide capture: Prospects for new materials. *Angew. Chemie - Int. Ed.* **49**, 6058–6082 (2010).
2. Aresta, M., Dibenedetto, A. & Angelini, A. Catalysis for the valorization of exhaust carbon: From CO₂ to chemicals, materials, and fuels. technological use of CO₂. *Chem. Rev.* **114**, 1709–1742 (2014).
3. Goeppert, A., Czaun, M., Jones, J. P., Surya Prakash, G. K. & Olah, G. A. Recycling of carbon dioxide to methanol and derived products-closing the loop. *Chem. Soc. Rev.* **43**, 7995–8048 (2014).
4. Ordonsky, V. V., Dros, A.-B., Schwiedernoch, R. & Khodakov, A. Y. Challenges and Role of Catalysis in CO₂ Conversion to Chemicals and Fuels. in *Nanotechnology in Catalysis* 803–850 (Wiley-VCH Verlag GmbH & Co. KGaA, 2017). doi:10.1002/9783527699827.ch30.
5. Porosoff, M. D., Yan, B. & Chen, J. G. Catalytic reduction of CO₂ by H₂ for synthesis of CO, methanol and hydrocarbons: Challenges and opportunities. *Energy Environ. Sci.* **9**, 62–73 (2016).
6. Posada-Pérez, S. *et al.* Highly Active Au/δ-MoC and Cu/δ-MoC Catalysts for the Conversion of CO₂: The Metal/C Ratio as a Key Factor Defining Activity, Selectivity, and Stability. *J. Am. Chem. Soc.* **138**, 8269–8278 (2016).
7. Ye, R. P. *et al.* CO₂ hydrogenation to high-value products via heterogeneous catalysis. *Nat. Commun.* **10**, (2019).
8. Navarro-Jaén, S. *et al.* Highlights and challenges in the selective reduction of carbon dioxide to methanol. *Nat. Rev. Chem.* **0123456789**, (2021).
9. Graciani, J. *et al.* Highly active copper-ceria and copper-ceria-titania catalysts for methanol synthesis from CO₂. *Science (80-.)*. **345**, 546–550 (2014).
10. Rodriguez, J. A. *et al.* Hydrogenation of CO₂ to Methanol: Importance of Metal-Oxide and Metal-Carbide Interfaces in the Activation of CO₂. *ACS Catal.* **5**, 6696–6706 (2015).
11. Frusteri, F., Cordaro, M., Cannilla, C. & Bonura, G. Multifunctionality of Cu-ZnO-ZrO₂/H-ZSM5 catalysts for the one-step CO₂-to-DME hydrogenation reaction. *Appl. Catal. B Environ.* **162**, 57–65 (2015).
12. Bonura, G. *et al.* Catalytic behaviour of a bifunctional system for the one step synthesis of DME by CO₂ hydrogenation. *Catal. Today* **228**, 51–57 (2014).
13. Mori, K., Taga, T. & Yamashita, H. Isolated Single-Atomic Ru Catalyst Bound on a Layered Double Hydroxide for Hydrogenation of CO₂ to Formic Acid. *ACS Catal.* **7**, 3147–3151 (2017).
14. Xu, Z., Mcnamara, N. D., Neumann, G. T., Schneider, W. F. & Hicks, J. C. Catalytic hydrogenation of CO₂ to formic acid with silica-tethered iridium catalysts. *ChemCatChem* **5**, 1769–1771 (2013).
15. Luk, H. T. *et al.* CO₂-Promoted Catalytic Process Forming Higher Alcohols with Tunable Nature at Record Productivity. *ChemCatChem* **12**, 2732–2744 (2020).
16. Dorner, R. W., Hardy, D. R., Williams, F. W. & Willauer, H. D. Heterogeneous catalytic CO₂ conversion to value-added hydrocarbons. *Energy Environ. Sci.* **3**, 884–890 (2010).
17. Rodemerck, U. *et al.* Catalyst development for CO₂ hydrogenation to fuels. *ChemCatChem* **5**, 1948–1955 (2013).
18. Wang, Y. *et al.* Direct and Oriented Conversion of CO₂ into Value-Added Aromatics. *Chem. - A Eur. J.* **25**, 5149–5153 (2019).
19. Li, Z. *et al.* Highly Selective Conversion of Carbon Dioxide to Lower Olefins. *ACS Catal.* **7**, 8544–8548 (2017).
20. Gao, P. *et al.* Direct Production of Lower Olefins from CO₂ Conversion via Bifunctional Catalysis. *ACS Catal.* **8**, 571–578 (2018).
21. Li, W. *et al.* A short review of recent advances in CO₂ hydrogenation to hydrocarbons over heterogeneous catalysts. *RSC Adv.* **8**, 7651–7669 (2018).
22. Ojelade, O. A. & Zaman, S. F. A review on CO₂ hydrogenation to lower olefins: Understanding the structure-property relationships in heterogeneous catalytic systems. *J. CO₂ Util.* **47**, 101506 (2021).
23. Corma, A., Melo, F. V., Sauvanaud, L. & Ortega, F. Light cracked naphtha processing: Controlling chemistry for maximum propylene production. *Catal. Today* **107–108**, 699–706 (2005).
24. Sattler, J. J. H. B., Ruiz-Martinez, J., Santillan-Jimenez, E. & Weckhuysen, B. M. Catalytic Dehydrogenation of Light Alkanes on Metals and Metal Oxides. *Chem. Rev.* **114**, 10613–10653 (2014).
25. Tian, P., Wei, Y., Ye, M. & Liu, Z. Methanol to olefins (MTO): From fundamentals to

- commercialization. *ACS Catal.* **5**, 1922–1938 (2015).
26. Stöcker, M. Methanol-to-hydrocarbons: catalytic materials and their behavior. *Microporous Mesoporous Mater.* **29**, 3–48 (1999).
 27. Goud, D., Gupta, R., Maligal-Ganesh, R. & Peter, S. C. Review of Catalyst Design and Mechanistic Studies for the Production of Olefins from Anthropogenic CO₂. *ACS Catal.* **10**, 14258–14282 (2020).
 28. Zhou, W. *et al.* New horizon in C1 chemistry: Breaking the selectivity limitation in transformation of syngas and hydrogenation of CO₂ into hydrocarbon chemicals and fuels. *Chem. Soc. Rev.* **48**, 3193–3228 (2019).
 29. Zhang, Z. *et al.* Selective hydrogenation of CO₂ and CO into olefins over Sodium- and Zinc-Promoted iron carbide catalysts. *J. Catal.* **395**, 350–361 (2021).
 30. Ronda-Lloret, M., Rothenberg, G. & Shiju, N. R. A Critical Look at Direct Catalytic Hydrogenation of Carbon Dioxide to Olefins. *ChemSusChem* **12**, 3896–3914 (2019).
 31. Liu, R. *et al.* Selective hydrogenation of CO₂ and CO over potassium promoted Co/ZSM-5. *Appl. Catal. B Environ.* **284**, 119787 (2021).
 32. Wang, J., You, Z., Zhang, Q., Deng, W. & Wang, Y. Synthesis of lower olefins by hydrogenation of carbon dioxide over supported iron catalysts. *Catal. Today* **215**, 186–193 (2013).
 33. Ramirez, A. *et al.* Tandem Conversion of CO₂ to Valuable Hydrocarbons in Highly Concentrated Potassium Iron Catalysts. *ChemCatChem* **11**, 2879–2886 (2019).
 34. Dorner, R. W., Hardy, D. R., Williams, F. W. & Willauer, H. D. K and Mn doped iron-based CO₂ hydrogenation catalysts: Detection of KAlH₄ as part of the catalyst's active phase. *Appl. Catal. A Gen.* **373**, 112–121 (2010).
 35. Liu, B. *et al.* Unravelling the New Roles of Na and Mn Promoter in CO₂ Hydrogenation over Fe₃O₄-Based Catalysts for Enhanced Selectivity to Light α -Olefins. *ChemCatChem* **10**, 4718–4732 (2018).
 36. Xu, Q., Xu, X., Fan, G., Yang, L. & Li, F. Unveiling the roles of Fe-Co interactions over ternary spinel-type Zn_xCo_{1-x}Fe₂O₄ catalysts for highly efficient CO₂ hydrogenation to produce light olefins. *J. Catal.* **400**, 355–366 (2021).
 37. Yuan, F. *et al.* Boosting light olefin selectivity in CO₂ hydrogenation by adding Co to Fe catalysts within close proximity. *Catal. Today* **371**, 142–149 (2021).
 38. Numpilai, T. *et al.* Tuning Interactions of Surface-adsorbed Species over Fe-Co/K-Al₂O₃ Catalyst by Different K Contents: Selective CO₂ Hydrogenation to Light Olefins. *ChemCatChem* **12**, 3306–3320 (2020).
 39. Gong, W. *et al.* Effect of copper on highly effective Fe-Mn based catalysts during production of light olefins via Fischer-Tropsch process with low CO₂ emission. *Appl. Catal. B Environ.* **278**, 119302 (2020).
 40. Choi, Y. H. *et al.* Carbon dioxide Fischer-Tropsch synthesis: A new path to carbon-neutral fuels. *Appl. Catal. B Environ.* **202**, 605–610 (2017).
 41. Hu, B. *et al.* Selective hydrogenation of CO₂ and CO to useful light olefins over octahedral molecular sieve manganese oxide supported iron catalysts. *Appl. Catal. B Environ.* **132–133**, 54–61 (2013).
 42. Zhang, J. *et al.* Selective formation of light olefins from CO₂ hydrogenation over Fe-Zn-K catalysts. *J. CO₂ Util.* **12**, 95–100 (2015).
 43. Wang, S., Zhai, Y., Li, X., Li, Y. & Wang, K. Coprecipitation synthesis of MgO-doped ZrO₂ nano powder. *J. Am. Ceram. Soc.* **89**, 3577–3581 (2006).
 44. Gusain, D., Singh, P. K. & Sharma, Y. C. Kinetic and equilibrium modelling of adsorption of cadmium on nano crystalline zirconia using response surface methodology. *Environ. Nanotechnology, Monit. Manag.* **6**, 99–107 (2016).
 45. Su, C., Li, J., He, D., Cheng, Z. & Zhu, Q. Synthesis of isobutene from synthesis gas over nanosize zirconia catalysts. *Appl. Catal. A Gen.* **202**, 81–89 (2000).
 46. Zhang, Z., Zhang, L., Hülsey, M. J. & Yan, N. Zirconia phase effect in Pd/ZrO₂ catalyzed CO₂ hydrogenation into formate. *Mol. Catal.* **475**, (2019).
 47. Chernavskii, P. A. *et al.* Influence of copper and potassium on the structure and carbidisation of supported iron catalysts for Fischer-Tropsch synthesis. *Catal. Sci. Technol.* **7**, 2325–2334 (2017).
 48. Subramanian, V. *et al.* Design of iron catalysts supported on carbon-silica composites with enhanced catalytic performance in high-temperature Fischer-Tropsch synthesis. *Catal. Sci. Technol.* **6**, 4953–4961 (2016).
 49. Mai, K., Elder, T., Groom, L. H. & Spivey, J. J. Fe-based Fischer Tropsch synthesis of biomass-derived syngas: Effect of synthesis method. *Catal. Commun.* **65**, 76–80 (2015).

50. Beasley, C., Gnanamani, M. K., Hamdeh, H. H., Martinelli, M. & Davis, B. H. Effect of Gallium Additions on Reduction, Carburization and Fischer–Tropsch Activity of Iron Catalysts. *Catal. Letters* **148**, 1920–1928 (2018).
51. Chernavskii, P. A. *et al.* Influence of copper and potassium on the structure and carbidisation of supported iron catalysts for Fischer-Tropsch synthesis. *Catal. Sci. Technol.* **7**, 2325–2334 (2017).
52. Visconti, C. G. *et al.* CO₂ hydrogenation to lower olefins on a high surface area K-promoted bulk Fe-catalyst. *Appl. Catal. B Environ.* **200**, 530–542 (2017).
53. Schulz, H. & Claeys, M. Kinetic modelling of Fischer–Tropsch product distributions. *Appl. Catal. A Gen.* **186**, 91–107 (1999).
54. Yang, J., Ma, W., Chen, D., Holmen, A. & Davis, B. H. Fischer-Tropsch synthesis: A review of the effect of CO conversion on methane selectivity. *Appl. Catal. A Gen.* **470**, 250–260 (2014).
55. Govender, N. S., Botes, F. G., de Croon, M. H. J. M. & Schouten, J. C. Mechanistic pathway for C₂₊ hydrocarbons over an Fe/K catalyst. *J. Catal.* **312**, 98–107 (2014).
56. Olewski, T., Todic, B., Nowicki, L., Nikacevic, N. & Bukur, D. B. Hydrocarbon selectivity models for iron-based Fischer–Tropsch catalyst. *Chem. Eng. Res. Des.* **95**, 1–11 (2015).

Chapter 6 General conclusions and perspectives

Valorization of CO and CO₂ are crucial processes as they are plausible carbon resources that can substitute petroleum derivate products. At the same time, they allow the synthesis of clean building block chemicals for chemical industry. Most investigations on this area focus on developing highly active, selective and stable catalysts which to day continues to be a great challenge. In addition to develop catalysts with these characteristics, it is important to have deeper insights in understanding the factors playing a role in catalysts performance. The main goals of this thesis were to design efficient, stable and active catalysts for CO and CO₂ hydrogenation.

6.1. General conclusion

Among all promoters tested for direct conversion of CO to light olefins, bismuth, lead, tin and antimony resulted to be the most active catalysts (up to 5 times) compared to reference Fe/SiO₂ catalyst. These metals showed two different types of promotion. On the one hand, Bi and Pb enhanced the reaction rate, at the same time the light olefin selectivity increased. On the other hand, Sn and Sb just had a clear effect on the reaction rate. Deeper insights on the active phases for Sb and Sn-promoted catalysts were provided. The turnover frequency was improved 7-10 times. It was demonstrated by different characterization techniques that Sb-promoted catalyst is more easily carbidized while the Sn-promotion did not show a clear influence on this aspect. However, its better activity was attributed to close localization of Sn particles to Fe species. XAS experiments allow the identification of in-situ formation of Fe-Sb alloy which was also confirmed by core-shell structures seen by TEM images.

For CO₂-FT process, different ZrO₂-supported catalysts were studied. CO₂-FT synthesis occurs *via* intermediate production of carbon monoxide. Alkali promoters resulted to be crucial to increase activity and light olefins production. Light olefins selectivity can be further increased in the presence of Mo. In general, the promoted catalysts show a higher extent of iron carbidization compared to on-promoted Fe/ZrO₂ being the Hägg Carbide the main specie formed during the activation process. Copper introduction resulted in better iron reducibility which can be translated into an easier carbidization of iron nanoparticles (improving activity).

Globally, results of CO and CO₂-FT process indicate key points to address for catalyst design in both reactions. CO conversion needs a close interaction of Fe-promoter like allow formation or core-shell structures attributing the highest activity to higher carbidization and the electronic effects arising from the promoters localized in close proximity to the iron carbide nanoparticles. On the other hand, for CO₂-FT process, basicity together with better iron carbidization are the crucial points to direct the selectivity towards light olefins production. However, this basicity needs to be mediated (by introduction of second promoter like Mo) in order to improve light olefins production and avoid excessive C₅₊ production.

Even though CO and CO₂-FT are similar processes, different mechanisms seem to be ruling these reactions. In CO₂-FT, at higher CO₂ conversions, the selectivities to CO and CH₄ decrease considerably, while for CO hydrogenation the selectivities to CO₂ selectivity increases with the conversion and then reaches 50% and CH₄ remain constant with the CO conversion. Additionally, lower olefins and C₅₊ selectivity have a different behavior with CO₂ conversion depending on K presence. Those catalysts with K in their composition show lower olefins selectivity decrease with increasing in CO₂ conversion which is similar for CO hydrogenation (no matter the

promoter). However, the CO₂ conversion level in the catalysts without potassium has no effect on relatively low light olefin production. The C₅₊ selectivity varies similarly with the conversion in CO₂ (potassium promoted) and CO hydrogenation catalysts. At higher conversions, the potassium-promoted catalysts exhibit higher selectivities to this fraction, while the non K-promoted catalysts in CO₂ reaction have no effect on C₅₊ production. Finally, light paraffins seem to be promoted at the higher conversion over the CO₂ hydrogenation catalysts without K. In contrast, K-promoted CO₂ hydrogenation and CO hydrogenation catalyst have no clear changes in light paraffin selectivity with conversion.

6.2. Perspectives

Even though FT synthesis to light olefins have been widely studied, there still exists the necessity to have a better balance between the activity and selectivity of the catalysts. For this reason, further studies need to address the optimization of catalyst preparation and reaction conditions. For example, a starting point could be the improvement of the optimal load of promoter (Bi, Pb, Sb, and Sn). In a preliminary test, we found the activity of Sb-promoted catalysts seems to be ideal when 1.6% of antimony is load in iron-based catalysts supported on silica (as shown in **Figure 6-1**).

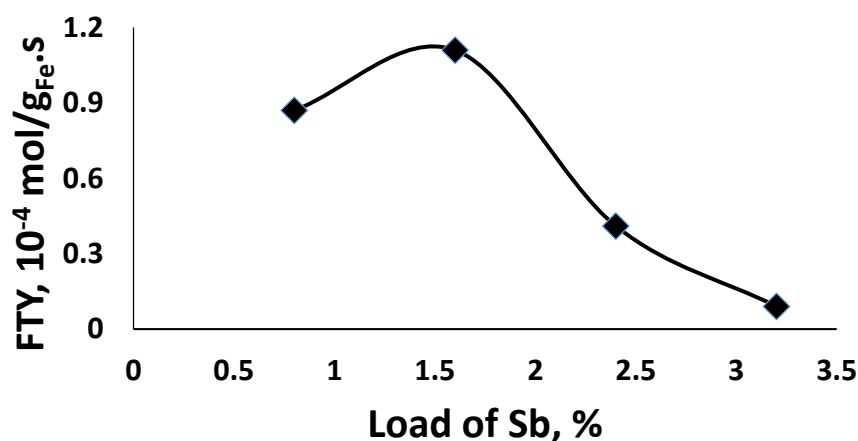


Figure 6-1. Activity of iron-promoted catalysts with different load of Sb.

During last years, there has been a growing interest on taking advantage of the huge amount of CO₂ available. The catalysts designed in this thesis show interesting light olefins production. However, they need to be further studied and optimized. As in the case of CO hydrogenation, it would be interesting to have the best ratio iron/promoter (Cu, Mo, Ga, etc.).

Also, it is important to study about the mechanistic aspects of CO₂ hydrogenation that, so far, continue to be not fully understood. In this regard, steady state isotopic transient kinetic analysis (SSITKA), among other techniques, is an exciting opportunity to obtain more details on reaction mechanisms. Another approach that can be followed in order to improve the activity of the catalyst is synthesizing mixed oxide supports that could improve the catalyst basicity like MgO-ZrO₂ or MgO-Al₂O₃.

One important parameter is the stability. Although, we improved the catalyst stability for both CO and CO₂ hydrogenation reactions, a complete study on how much time these catalysts are stable and deactivation mechanisms should be addressed in further investigations together with catalyst regeneration.

Finally, as we worked in the framework of the Interreg PSYCHE Project, and the plastic gasification generates syngas together with a considerable amount of CO₂. One of the most important outlooks of this thesis is the development of catalysts that can work for both CO and CO₂ hydrogenation at the same time. On the other hand, study the process development in which CO₂ can be first converted to CO *via* RWGS and then the CO generated converted to Light olefins using soldering metals as promoters.

List of published papers

1. **Barrios Alan J.**, Bang Gu, Yuan Luo, Deizi V. Peron, Petr. A. Chernavskii, Mirella Virginie, Robert Wojcieszak, Joris W. Thybaut, Vitaly V. Ordonsky, Andrei Y. Khodakov. *Identification of efficient promoters and selectivity trends in high temperature Fischer-Tropsch synthesis over supported iron catalysts.* Applied Catalysis B: Environmental, 2020, 273.
2. Peron Deizi V., **Barrios Alan J.**, Taschin Alan, Dugulan Iulian, Marini Carlo, Gorni Giulio, Moldovan Simona, Koneti Siddardha, Wojcieszak Robert, Thybaut Joris W., Virginie Mirella, Khodakov Andrei Y. *Active phases for high temperature Fischer-Tropsch synthesis in the silica supported iron catalysts promoted with antimony and tin.* Applied Catalysis B: Environmental, pg. 120-141 (2021). D.V. Peron and A. J. Barrios contributed equally to this work.
3. **Barrios Alan J.**, Peron Deizi V., Chakkingal Anoop, Dugulan Iulian, Thuriot-Roukos Joëlle, Wojcieszak Robert, Thybaut Joris W., Virginie Mirella, Khodakov Andrei Y. *Efficient promoters and reaction paths in the CO₂ hydrogenation to light olefins over zirconia supported iron catalysts.* Submitted in Applied Catalysis B: Environmental, 2021.
4. Bang Gu, Deizi V. Peron, **Alan J. Barrios**, Mirella Virginie, Camille La Fontaine, Valérie Briois, Mykhailo Vorokhta, Břetislav Šmíd, Simona Moldovan, Siddardha Koneti, Thobani G. Gambu, Mark Saeys, Vitaly V. Ordonsky, Andrei Y. Khodakov. *Bismuth mobile promoter and cobalt-bismuth nanoparticles in carbon nanotube supported Fischer-Tropsch catalysts with enhanced stability.* Journal of Catalysis, (2021).
5. Chakkingal Anoop, Pirro Laura, Costa da Cruz A.R., **Barrios Alan J.**, Virginie Mirella, Khodakov Andrei Y., Thybaut Joris W. *Unravelling the influence of*

catalyst properties on light olefin production via Fischer–Tropsch synthesis: A descriptor space investigation using Single-Event MicroKinetics. Chemical Engineering Journal, vol. 419, (2021).

6. Bang Gu, **Barrios Alan J.**, Deizi V. Peron, Mounib Bahri, Ovidiu Ersen, Mykhailo Vorokhta, Břetislav Šmíd, Dipanjan Banerjee, Mirella Virginie, Eric Marceau, Robert Wojcieszak, Vitaly V. Ordomsky and Andrei Y. Khodakov. *Mobility and versatility of the liquid bismuth promoter in the working iron catalysts for light olefin synthesis from syngas*. Chemical Science, 2020, 11, 6167-6182.
7. Aleksandra S. Peregudova, **Barrios Alan J.**, Vitaly V. Ordomsky, Nataliya E. Borisova, and Andrei Y. Khodakov. *The Fischer–Tropsch reaction in the aqueous phase over rhodium catalysts: a promising route to selective synthesis and separation of oxygenates and hydrocarbons*. Chemical Communications, 2019, 56, 277-280.

Conferences

1. **Alan J. Barrios**, Deizi Peron, Mirella Virginie, Robert Wojcieszak, Joris Thybaut, and Andrei Khodakov. Recognition of efficient promoters for light olefin production from CO₂ hydrogenation reaction over zirconia supported iron catalysts using high throughput experimentation. First international symposium on High-Throughput Catalysts Design, Lille, 2021, oral presentation.
2. **Alan J. Barrios**, Bang Gu, Deizi V. Peron, Mirella Virginie, Robert Wojcieszak, Vitaly V. Ordomsky, Ersen O. and Andrei Y. Khodakov. Gaseous Phase Fischer-Tropsch Synthesis on Solid Iron Catalysts Promoted with Liquid Metals. Camure11-ISMR10 Conference, Milan, 2021, oral presentation.

3. **Alan J. Barrios**, Anoop Chakkingal, Deizi V. Peron, Mirella Virginie, Robert Wojcieszak, Vitaly V. Ordonsky, Joris Thybaut, and Andrei Y. Khodakov. Direct synthesis of light olefins in CO hydrogenation over iron catalysts improved with mobile promoters. The Netherlands' Catalysis and Chemistry Conference, 2020, oral presentation.
4. **Alan J. Barrios**, Bang Gu, Virginie Mirella, Robert Wojcieszak, Vitaly V. Ordonsky, Joris Thybaut and Andrei Y. Khodakov. Direct synthesis of light olefins in CO and CO₂ hydrogenation over promoted iron catalysts. Chemical Research in Flanders, Blankenberge, 2019, poster presentation.

Acknowledgments

First of all, I would like to thank to my supervisors Dr. Andrei Khodakov, Dr. Mirella Virginie and Dr. Joris Thybaut for giving me the opportunity of taking part of this project, their guidance and advice during these three years of PhD. Equally, I want to thank for the financial support from European Union (Interreg V project PSYCHE).

I thank my family, especially my parents, Juan Barrios and Yoli Medina, for giving me all the best of them, for all their sacrifices and the great effort made that allowed me to be here today. For that and many other things I will always be indebted to them. Also I want to say thank you to my sister Alana and my aunt Maria Elena for their support not just during the last three years but during my life. Thank you.

To my wife, María Gabriela Marin, the best that has happened to me in life, who has always been with me through thick and thin. Always being my counselor, my friend and My Love. I love you immensely and every day more, of that you can always be sure. I have missed you every day.

To the Marín Escalante family, for allowing me to be part of their family and for all the help they have given me over the years. Especially to Mrs. Edilia who has treated me like a son and to Emely who makes the best cakes I have ever eaten.

To all the people from laboratory 152 in Venezuela: professor Carmelo Bolivar, Gabriel, Francisco, Manuel, Nelson, Roger and specially to professor Mireya Goldwasser and professor Juan Alvarez who help me to give my first steps in heterogeneous catalysis.

I would like to express my gratitude to all people who collaborated in this work: Robert Wojcieszak, Pardis Simon, Olivier Gardoll, Joëlle Thuriot-Roukos, Stephane

Chambrey, Svetlana Heyte, Simona Moldovan, Cristophe Dujardin, Vitaly Ordonsky and others that right now I cannot remember.

Also, I want to thank to the good friends I met during these three years, specially to Benoît Boussemart, Ana Fellenberg (who taught me to speak Portuguese by force), Paola Arango, Sara Navarro-Jaen, Tiago Rossi, Yamid Gomez, Andrea Forero, Anoop Chakkingal and to all the people from UCCS laboratory and our group: Melissa de la Rocha, Max, Debora Strossi, Deizi Peron, Aleksandra Peregudova, Bang Gu, Qiyang, Hu Di, Dan Wu, Shilpa, Grece, My Nghe Tran, Dong, Yong, Shreya Nandi, Nassim Bachoul, Ying, Alan Taschin, and all UCCS staff. Thank you for all.

Synthèse Directe d'Oléfines Légères par des Réactions d'Hydrogénation du CO et du CO₂

Résumé : L'hydrogénation du CO et du CO₂ sont une voie intéressante de conversion des matières premières non pétrolières et renouvelables tels que la biomasse, le plastique et les déchets organiques, en carburant et en produits chimiques. L'activité, la sélectivité vers la production d'oléfines légères et la stabilité sont des défis majeurs de ces réactions sur les catalyseurs à base de fer. Dans cette thèse, nous avons synthétisé différents catalyseurs à base de fer pour l'hydrogénation du CO et du CO₂ afin d'obtenir des catalyseurs hautement sélectifs, actifs et stables. Pour l'hydrogénation du CO, SiO₂ a été utilisée comme support tandis que pour la réaction d'hydrogénation du CO₂, les catalyseurs supportés par de la ZrO₂ ont présenté les résultats les plus encourageants. Les résultats sont appuyés sur l'expérimentation à haut débit (EHD) pour identifier parmi 27 promoteurs les plus efficaces pour la synthèse de FT en évaluant également les différentes tendances de sélectivité en la réaction FT. Les tests EHD nous ont permis d'identifier clairement Sn, Sb, Bi et Pb comme les promoteurs les plus prometteurs afin d'obtenir des catalyseurs de Fe avec une plus grande activité. Après, nous nous sommes concentrés sur l'étude des promoteurs Sb et Sn, sur la performance catalytique des catalyseurs à base de fer supportés sur SiO₂, en utilisant une combinaison de techniques avancées et in-situ. Les images MET du catalyseur FeSn/SiO₂ activé ont montré des nanoparticules de Sn hautement dispersées sur le support de silice. D'autre part, le catalyseur FeSb/SiO₂ activé a montré une morphologie cœur-coquille. Plus petite quantité de dépôt de carbone détectée est cruciale pour une meilleure stabilité des catalyseurs promus par Sn- et Sb dans la réaction FT. Finalement, nous nous sommes concentrés sur l'identification des promoteurs pour les catalyseurs de fer supportés sur ZrO₂ pour la réaction d'hydrogénation du CO₂. Nous avons observé une nette augmentation de la vitesse de réaction pour les catalyseurs promus par le K et le Cs. L'EHD a clairement montré que la présence de K est essentielle pour obtenir une plus grande sélectivité en oléfines légères. En plus, le Mo, Cu, Cs, Ce et Ga ont été identifiés comme des promoteurs capables d'augmenter encore la sélectivité en oléfines. Le travail effectué au cours de cette thèse a permis de concevoir de nouveaux catalyseurs pour la réaction d'hydrogénation du CO et du CO₂ qui pourraient être facilement mis en œuvre au niveau industriel. Les catalyseurs étudiés pour les deux réactions ont montré une amélioration de trois aspects clés : l'activité, la sélectivité et la stabilité.

Mots clés : Synthèse de Fischer-Tropsch, hydrogénation du CO₂, catalyseurs à base de fer, oléfines légères, expérimentation à haut débit, promoteur.

Direct Synthesis of Light Olefins Using CO and CO₂ Hydrogenation Reactions

Abstract: CO and CO₂ Hydrogenation are an attractive way to convert non-petroleum and renewable feedstocks such as biomass, plastic and organic waste into fuels and chemicals. Activity, selectivity to light olefins and stability are major challenges of these reactions over Fe catalysts. In this thesis, we synthesized different iron-based catalysts for both CO and CO₂ hydrogenation in order to get highly selective, active and stable catalysts. For CO hydrogenation SiO₂ was used as support while for CO₂ hydrogenation reaction ZrO₂ supported catalysts presented the most encouraging results. We relied on High Throughput Experimentation (HTE) to identify among 27 promoters the most efficient ones for FT synthesis at the same time that different selectivity trends were evaluated. HTE tests allowed us to clearly identify Sn, Sb, Bi and Pb as the most promising promoters in order to obtain Fe catalysts with higher activity in FT synthesis. Then, we focused on studying the strong promoting effects of Sb and Sn on the catalytic performance of SiO₂ supported iron Fischer Tropsch catalysts using a combination of advanced and in-situ techniques. TEM in the activated FeSn/SiO₂ catalyst showed highly dispersed Sn nanoparticles on the silica support. On the other hand, activated FeSb/SiO₂ catalyst showed a core-shell morphology. Additionally, smaller amount of carbon deposition detected is crucial for better stability of the Sn- and Sb-promoted catalysts in FT reaction. Finally, we focused on the identification of efficient promoters for ZrO₂ supported iron catalysts in CO₂ hydrogenation reaction. We observed the most pronounced increase in the reaction rate for the K and Cs promoted catalysts. HTE clearly showed that the presence of K was essential to achieve higher light olefin selectivity. Additionally, Mo, Cu, Cs, Ce and Ga were identified as possible promoters to further increase the selectivity of CO₂ hydrogenation to this fraction. The work performed during this thesis allowed to design new catalysts for CO and CO₂ hydrogenation reaction that could be easily implemented at industrial level. Catalysts studied for both reactions showed improvement three key aspects: activity, selectivity, and stability.

Key words: Fischer-Tropsch synthesis, CO₂ hydrogenation, iron catalysts, light olefins, High Throughput Experimentation, promoter.

Corrections 07/04/2022

Page 108, Figure 3.2. The “X” axe legend is referring to “CO conversion” not “CO₂ conversion.”

Page 125, paragraph 1, line 6: “At the same time could Iron time yield (FTY) in the catalysts promoted with Bi, Pb, Sn and Sb increased 3-5 times.” should write “At the same time, iron time yield (FTY) in the catalysts promoted with Bi, Pb, Sn and Sb increased 3-5 times.”

Page 189, paragraph 1, line 18: “It seels that the promotion slows down interaction of iron with zirconia an increases the amount of reducible iron.” Should write “It seems that the promotion slows down interaction of iron with zirconia and increases the amount of reducible iron.”